HADRON MASS CALCULATIONS IN QUENCHED QCD

Thesis
submitted by

Catherine Bruce Chalmers

for the degree of

Doctor of Philosophy

Department of Physics
University of Edinburgh
October 1986

To Mum and Dad

and in loving memory of Grandad

DECLARATION

Some of the work of chapter three was done with Richard Kenway and Duncan Roweth and that of chapter four was done as part of a collaborative project [Bowler et al. (1986b,1986c)]. All other work in this thesis is entirely my own unless otherwise stated. Work to be published includes :

Bowler, K.C., C.B. Chalmers, R.D. Kenway, G.S. Pawley and D. Roweth, Edinburgh preprint 86/369, to appear in Nucl. Phys. B

Chalmers, C.B., R.D. Kenway and D. Roweth, Edinburgh preprint 86/361, to appear in J. Comput. Phys.

Chalmers, C.B., R.D. Kenway and D. Roweth, Edinburgh preprint 86/386, submitted to Phys. Lett.

ACKNOWLEDGEMENTS

I would like to thank my supervisor Richard Kenway for his generous help and encouragement during the course of this work. Thanks are also due to Ken Bowler for valuable help and Duncan Roweth for many useful discussions during our work together.

I acknowledge the award of a Vans Dunlop Scholarship from the University of Edinburgh, and the support of the Edinburgh Regional Computing Centre in the computing involved in this work.

It is with great pleasure that I thank the other members of the Physics department for their friendship over the past three years; in particular Andy Brass,Duncan Roweth, Dave Scott and my office-mates Clive Baillie and Simon Hands. Finally, I would also like to thank Peter Gibbons for his friendship and encouragement.

ABSTRACT

Numerical estimates for the low lying hadron mass spectrum are obtained in the Quenched Approximation of lattice QCD using the standard Wilson pure gauge action and the Susskind fermionic action.

The numerical techniques used are discussed and an Iterative Block SOR algorithm is found to be optimal for inverting the fermion matrix using the DAP. Block Gauss Elimination is found to be impractical. The Distant Source Method for extending quark propagators in time is also tested and found to be of use where finite-size-effects are small.

High statistics measurements of hadron masses are performed in the range $5.7 \leqslant \beta \leqslant 6.3$ on 16^4 and $16^3 \times 24$ lattices. Restoration of flavour symmetry in the meson sector occurs at around $\beta = 6.0$, improving as β increases further, suggesting the possibility of observing continuum behaviour in this range. Finite size effects for mesons become significant for small quark masses at $\beta = 6.3$.

A comparison of baryon propagators with different spatial boundary conditions is made at $\beta = 6.15$ and reveals finite size effects at small quark masses. Using antiperiodic spatial boundary conditions, the finite size effects are manifested as a discrepancy between two baryon propagators, EVEN and ALL, which should be equal on an infinite lattice. This discrepancy persists at $\beta = 6.3$.

Mass ratios obtained at $\beta = 6.0$ and 6.15 are compared and found to be in good agreement, suggesting that there may be a scaling 'window' in this range of β.

CONTENTS

CONTENTS(contd.)

CHAPTER ONE

Introduction

Quantum Chromodynamics (QCD) is widely believed to be the theory which describes the strong interaction. Its formulation is straightforward : it is a non-Abelian gauge field theory of quarks and gluons, analogous to the well-established Abelian theory QED of electrons and photons. However, the dynamics resulting from the non-Abelian structure are quite different, encompassing all the complex phenomena of the strong force. from jets to nuclear energy levels. The work presented here is an attempt to extract one aspect of this complex dynamics, namely the spectrum of quark bound states, and hence to predict hadron masses, using numerical techniques based on the lattice approximation to QCD. In this chapter we shall outline the framework for this calculation by discussing gauge theories, the development of QCD and the implementation of the lattice theory.

1.1 QCD as a Gauge Theory

Present day particle physics is dominated by gauge theories : the discovery of the W and Z bosons at CERN [Arnison et al (1983abc), Bagnaia et al. (1983) and Banner et al. (1983)] justified acceptance of the electroweak theory proposed by Glashow, Weinberg and Salam [Glashow (1961), Weinberg (1967) and Salam (1968)] and the theory of quantum electrodynamics (QED) is in astonishingly good agreement with experiment. Before discussing QCD in more detail, let us first look at the concept of gauge theories.

A gauge theory can be constructed by imposing local symmetry conditions on a Lagrangian. Taking as an example the Lagrangian for a free electron field,

$$\mathcal{L}_0 = \bar{\psi}(x)\left\{ i\gamma^\mu \partial_\mu - m \right\}\psi(x) \qquad (1.1)$$

This has a global U(1) symmetry under

$$\begin{aligned} \psi(x) &\longrightarrow e^{-i\alpha}\,\psi(x) \\ \bar{\psi}(x) &\longrightarrow e^{i\alpha}\,\bar{\psi}(x) \end{aligned} \qquad (1.2)$$

We wish to elevate this to a *local* space-time dependent symmetry namely

$$\begin{aligned} \psi(x) &\longrightarrow e^{-i\alpha(x)}\,\psi(x) \\ \bar{\psi}(x) &\longrightarrow e^{i\alpha(x)}\,\bar{\psi}(x) \end{aligned} \tag{1.3}$$

Now when we substitute these into the Lagrangian, the derivative term $\psi(x)\partial_\mu\psi(x)$ becomes

$$\begin{aligned} &\bar{\psi}(x)\, e^{i\alpha(x)}\,\partial_\mu\left[e^{-i\alpha(x)}\,\psi(x)\right] \\ &= \bar{\psi}(x)\left\{\partial_\mu - i\,\partial_\mu\alpha(x)\right\}\psi(x) \end{aligned} \tag{1.4}$$

The second term spoils the gauge invariance, so we replace ∂_μ in the Lagrangian by $\mathcal{D}_\mu$, a covariant derivative, which must transform as

$$\mathcal{D}_\mu\,\psi(x) \longrightarrow \left[\mathcal{D}\,\psi(x)\right]' = e^{-i\alpha(x)}\,\mathcal{D}_\mu\,\psi(x) \tag{1.5}$$

For this to hold we must introduce a new vector field $A_\mu(x)$, the gauge field, where A_μ has the property

$$A_\mu \rightarrow A'_\mu(x) = A_\mu(x) + \frac{1}{e}\,\partial_\mu\,\alpha(x) \tag{1.6}$$

and

$$\mathcal{D}_\mu = \partial_\mu + ie\,A_\mu \tag{1.7}$$

Then (1.5) holds. So now $\mathcal{L}_0$ reads

$$\mathcal{L}_0 = \bar{\psi}\; i\gamma^\mu\left\{\partial_\mu + ie\,A_\mu\right\}\psi - m\bar{\psi}\psi \tag{1.8}$$

However we should also include a term involving the derivatives of A_μ if we want A to have non-trivial dynamics. The simplest term which is gauge invariant is

$$\mathcal{L}_A = -\frac{1}{4} F_{\mu\nu} F^{\mu\nu} \tag{1.9}$$

where

$$F_{\mu\nu} = \partial_\mu A_\nu - \partial_\nu A_\mu \tag{1.10}$$

$F_{\mu\nu}$ is related to $\mathcal{D}_\mu$:

$$(\mathcal{D}_\mu \mathcal{D}_\nu - \mathcal{D}_\nu \mathcal{D}_\mu)\,\psi = ie\, F_{\mu\nu}\, \psi \tag{1.11}$$

From (1.5) we see that

$$[(\mathcal{D}_\mu \mathcal{D}_\nu - \mathcal{D}_\nu \mathcal{D}_\mu)\,\psi]' = e^{-i\alpha}\,[(\mathcal{D}_\mu \mathcal{D}_\nu - \mathcal{D}_\nu \mathcal{D}_\mu)\,\psi] \tag{1.12}$$

so

$$F'_{\mu\nu}\,\psi' = (F_{\mu\nu}\,\psi)\, e^{-i\alpha} \tag{1.13}$$

i.e.

$$F'_{\mu\nu} = F_{\mu\nu}$$

The final form of the gauge invariant Lagrangian is then

$$\mathcal{L} = -\frac{1}{4} F_{\mu\nu} F^{\mu\nu} + \bar{\psi}\, i\gamma^\mu (\partial^\mu + ieA^\mu)\,\psi - m\bar{\psi}\psi \tag{1.14}$$

This Lagrangian has no gauge field self-coupling as we cannot write down a gauge-invariant interaction and because the photon has no electric charge.

The Lagrangian for a non-Abelian gauge theory on the other hand does contain gauge field self-couplings as we now show. Yang and Mills [Yang and Mills (1954)] developed the gauge principle to include non-Abelian symmetry groups. Let us look at the formulation for SU(N). The form of the free Lagrangian is (1.1) as before but now

$$\Psi = \begin{pmatrix} \Psi_1 \\ \vdots \\ \Psi_N \end{pmatrix} \tag{1.16}$$

an N-component object. Under the group transformation we have

$$\Psi(x) \longrightarrow \Psi'(x) = U(\theta)\,\Psi(x) = \exp(-i\,\frac{\underline{\lambda}}{2}.\underline{\theta})\,\Psi(x) \tag{1.17}$$

where $\lambda_a/2$ a = 1...n_g, are the generators of SU(N) (for N=2 λ_a,a = 1,2,3 are the Pauli matrices, for N=3 they are the Gell-Mann matrices, a = 1,..8). The λ_a obey

$$\left[\frac{\lambda_a}{2}, \frac{\lambda_b}{2}\right] = i f_{abc}\,\frac{\lambda_c}{2} \tag{1.18}$$

where f_{abc} are the structure constants of SU(N). When the θ_a are space-time independent, this global transformation leaves the Lagrangian invariant. Under the local gauge transformation

$$\Psi(x) \longrightarrow \exp(-i\,\frac{\underline{\lambda}}{2}.\underline{\theta}(x))\,\Psi(x) \tag{1.19}$$

$\mathcal{L}_0$ is not invariant, due to the derivative term which gives

$$\bar{\Psi}(x)\left[\partial_\mu + U^{-1}(\theta)\,\partial_\mu\,U(\theta)\right]\Psi(x) \tag{1.20}$$

We introduce the vector gauge fields A^a_μ, a = 1,..n_g one for each group generator, and covariant derivative

$$\mathcal{D}_\mu\,\Psi = \left\{\partial_\mu - i g\,\frac{\underline{\lambda}}{2}.\underline{A}_\mu\right\}\Psi \tag{1.21}$$

Then for the Lagrangian to be invariant, where g is a coupling constant,

$$(\mathcal{D}_\mu \Psi) \rightarrow (\mathcal{D}_\mu \Psi)' = U(\theta)\, \mathcal{D}_\mu \Psi \tag{1.22}$$

or

$$(\partial_\mu - i g \frac{\underline{\lambda}}{2} \cdot \underline{A}'_\mu)(U(\theta)\Psi) = U(\theta)(\partial_\mu - i g \frac{\underline{\lambda}}{2} \cdot \underline{A}_\mu)\Psi \tag{1.23}$$

$$\Rightarrow$$

$$\left(\partial_\mu U(\theta) - i g \frac{\underline{\lambda}}{2} \cdot \underline{A}'_\mu\, U(\theta)\right)\Psi = U(\theta)\left[-i g \frac{\underline{\lambda}}{2} \cdot \underline{A}_\mu\right]\Psi \tag{1.24}$$

ie

$$\frac{\underline{\lambda}}{2} \cdot \underline{A}'_\mu = U(\theta) \frac{\underline{\lambda}}{2} \cdot \underline{A}_\mu\, U^{-1}(\theta) - \frac{i}{g}\left[\partial_\mu U(\theta)\right] U^{-1}(\theta) \tag{1.25}$$

For an infinitesimal transformation

$$U(\theta) \sim 1 - i \frac{\underline{\lambda}}{2} \cdot \underline{\theta}(x) \tag{1.26}$$

and (1.25) is

$$\frac{\underline{\lambda}}{2} \cdot \underline{A}'_\mu = \frac{\underline{\lambda}}{2} \cdot \underline{A}_\mu - i \theta^b A_\mu^c \left[\frac{\lambda^b}{2}, \frac{\lambda^c}{2}\right] - \frac{1}{g} \frac{\underline{\lambda}}{2} \cdot \partial_\mu \underline{\theta} \tag{1.27}$$

$$= \frac{\underline{\lambda}}{2} \cdot \underline{A}_\mu + \frac{1}{2} f^{abc} \lambda^a \theta^b A_\mu^c - \frac{1}{g} \frac{\underline{\lambda}}{2} \cdot \partial_\mu \underline{\theta} \tag{1.28}$$

i.e.

$$A_\mu^{a\prime} = A_\mu^a + f^{abc} \theta^b A_\mu^c - \frac{1}{g} \partial_\mu \theta^a \tag{1.29}$$

This defines the transformation law for the gauge fields. Following (1.11) we look at

$$(\mathcal{D}_\mu \mathcal{D}_\nu - \mathcal{D}_\nu \mathcal{D}_\mu)\,\psi \equiv ig\left(\frac{\lambda^a}{2} F_{\mu\nu}^a\right)\psi \qquad (1.30)$$

where

$$F_{\mu\nu}^a = \partial_\mu A_\nu^a - \partial_\nu A_\mu^a + g f^{abc} A_\mu^b A_\nu^c \qquad (1.31)$$

$$\left[(\mathcal{D}_\mu \mathcal{D}_\nu - \mathcal{D}_\nu \mathcal{D}_\mu)\psi\right]' = U(\theta)\left[\mathcal{D}_\mu \mathcal{D}_\nu - \mathcal{D}_\nu \mathcal{D}_\mu\right]\psi \qquad (1.32)$$

$$\underline{\lambda} \cdot F_{\mu\nu}'\, U(\theta)\,\psi = U(\theta)\, \underline{\lambda} \cdot F_{\mu\nu}\,\psi \qquad (1.33)$$

$$\underline{\lambda} \cdot F_{\mu\nu}' = U(\theta)\,(\underline{\lambda} \cdot F_{\mu\nu})\,U^{-1}(\theta) \qquad (1.34)$$

so that in the infinitesimal case $\theta^a < 1$

$$F_{\mu\nu}'^a = F_{\mu\nu}^a + f^{abc}\,\theta^b\,F_{\mu\nu}^c \qquad (1.35)$$

Thus $F_{\mu\nu}$ has a non-trivial transformation, unlike the Abelian case, while $F_{\mu\nu}$ $F^{\mu\nu}$ is gauge invariant. The final form for the gauge invariant Lagrangian is

$$\mathcal{L} = -\frac{1}{4} F_{\mu\nu}^a F^{\mu\nu a} + \bar{\psi}\, i\gamma_\mu \mathcal{D}_\mu \psi - m\bar{\psi}\psi \qquad (1.36)$$

where

$$F_{\mu\nu}^a = \partial_\mu A_\nu^a - \partial_\nu A_\mu^a + g f^{abc} A_\mu^b A_\nu^c \qquad (1.37)$$

and

$$\mathcal{D}_\mu = \partial_\mu - ig\,\frac{\underline{\lambda}}{2} \cdot \underline{A}_\mu \qquad (1.38)$$

The Yang-Mills term $F_{\mu\nu} F^{\mu\nu}$ contains factors which are trilinear and quadrilinear in A_μ corresponding to the fact that the gauge fields are self-interacting.

We now briefly follow the development of QCD. Quarks were first postulated by Gell-Mann and Zweig in 1964. At that time they were widely viewed only as algebraic entities, serving as the building blocks of an observed internal symmetry SU(3). This symmetry was seen as that of three quarks : u(p),d(own) and s(trange). Today we know that five quarks exist - c(harm) was discovered in 1974 and b(ottom) in 1977 - and a sixth, the t(op), is also postulated to exist. However, we believe that the number of such types of quark does not have a fundamental meaning in strong interaction physics : the basic dynamics of quarks and gluons do not depend on the flavour (which is in fact a broken symmetry) provided the number of flavours is sufficiently small not to spoil asymptotic freedom.

In 1965 Han and Nambu [Han and Nambu (1965)] proposed that each quark occurred in three different types or *colours* . This solved the spin-statistics puzzle of the Δ^{++} - a fermion which, in the absence of an extra degree of freedom, appeared to have an overall symmetric wave function - since bound states of three quarks could be overall anti-symmetric in colour. However, their quarks had integer electric charge (the non-integral charge of Gell-Mann and Zweig being obtained by averaging over the colour index) and the scheme mixed the electroweak interaction with the colour degree of freedom so had not yet acheived a description of the strong force alone.

By the early seventies much work had been done on chiral symmetry and its breaking. The electromagnetic decay rate of the neutral pion was expressed in terms of the charges of the fundamental particles carrying the isospin charges, which annihilated via a triangle diagram. The experimental rate implied that the fundamental particles were non-integrally charged quarks occurring with three colours. Thus in 1972, the idea took shape of interpreting the colour quantum number as a 'hidden variable' so that quarks were tricoloured objects existing only inside hadrons. In order not to thereby introduce an extra multiplicity in the hadron spectrum it was postulated that quarks could only exist in colour singlet combinations. Thus quarks are presumed not to exist as free particles but are confined as colour singlet combinations inside hadrons. The group SU(3) describes the exact colour symmetry. Baryons are composed of three quarks and mesons of a quark and an anti-quark. The theory was supported by measurements of the ratio R

$$R = \frac{\sigma(e^+e^- \longrightarrow \text{hadrons})}{\sigma(e^+e^- \longrightarrow \mu^+\mu^-)} \qquad (1.39)$$

at energies corresponding to the production of u,d and s quarks. Again the factor of three from having three colours is necessary for agreement between theory and experiment. Another important experimental result was that quarks only contribute about 50% of the momentum of a nucleon. The remaining 50% must be carried by electrically neutral objects - the particles responsible for binding the quarks, the gluons.

Deep inelastic scattering revealed that although the quark constituents of hadrons are not produced as free particles in the final states, they behave at short distances if they were weakly bound inside the target nucleons. The field theory must take account of all these features, particularly free propagation at short distance and confinement at long distance. In 1973 the discovery of asymptotic freedom marked an important step in the development of QCD - already it was known that the effective coupling between the particles of an interacting field theory is not a constant but depends on the energy scale involved. The functional dependence of the coupling constant on energy and distance scale is prescribed by the renormalisation group β-function,

$$\beta(g) = -\frac{d\,g}{d(\ln a)} \qquad (1.40)$$

which can be calculated in perturbation theory to be

$$\beta(g) = -\beta_0 g^3 - \beta_1 g^5 + O(g^7) \qquad (1.41)$$

with

$$\beta_0 = \frac{11}{3}\left(\frac{N}{16\pi^2}\right) \quad \text{for } SU(N) \qquad (1.42)$$

$$\beta_1 = \frac{34}{3}\left(\frac{N}{16\pi^2}\right)^2$$

Higher order terms are regularisation-scheme dependent but these are universal. It turns out that for Yang-Mills theories the slope of the β-function at the origin is negative. Theories with this property are *asymptotically free*, i.e. the effective coupling decreases at short distances (as found in the deep inelastic scattering of leptons on nucleons). The only renormalisable theories

in four dimensions which are asymptotically free are non-Abelian gauge theories. The effect of asymptotic freedom also allows for the opposite effect at long distances : 'infrared slavery' whereby the force between quarks becomes stronger at large distances, potentially giving rise to quark confinement, although for precisely this reason perturbation theory breaks down so that a non-perturbative approach is essential if we are to understand how hadronic bound states are formed.

To account for all the above features, QCD is thus a non-Abelian gauge field theory with SU(3) as its gauge group, describing the interactions between three colours of quarks (in the fundamental representation) and eight types of massless gluons (in the adjoint representation). So

$$\mathcal{L}_{QCD} = -\frac{1}{4} F_{\mu\nu}^{a} F^{\mu\nu a} + \bar{\psi}(x)(i\gamma^{\mu}\partial_{\mu} - m)\psi(x) - m\bar{\psi}\psi \qquad (1.43)$$

with

$$\partial_{\mu} = \partial_{\mu} - igA_{\mu} \qquad (1.44)$$

$$F_{\mu\nu} = \partial_{\mu}A_{\nu} - \partial_{\nu}A_{\mu} + g f^{abc} \lambda^{a} A_{\mu}^{b} A_{\nu}^{c} \qquad (1.45)$$

$$A_{\mu} = \sum_{a=1}^{8} A_{\mu}^{a} \frac{\lambda}{2}^{a} \qquad (1.46)$$

and

$$\left[\frac{\lambda_a}{2}, \frac{\lambda_b}{2}\right] = \frac{i}{2} f_{abc} \lambda_c \qquad (1.47)$$

where the λ_a are now the Gell-Mann matrices and f_{abc} the structure constants of SU(3).

Predictions based on QCD perturbation theory have been tested experimentally : through deep inelastic lepton-nucleon scattering, quarkonium physics and quark-gluon jets. However these only probe the short distance regime where the bare coupling g is small, whereas the directly observable particles, the hadrons, are the product of non-perturbative effects where g is large. Lattice QCD is a non-perturbative formulation of the theory which permits the study of effects like confinement of quarks, chiral symmetry breaking, hadron masses, meson and baryon coupling constants and so on. Within the approximations it makes, it provides a means of calculating

non-perturbative quantities and checking the results of the theory with experiment. We now discuss lattice theories.

1.2 Lattice Gauge Theory

A quantum field theory on a Euclidean lattice of discrete space-time points becomes mathematically well-defined. Wilson (1974) showed that it is possible to make gauge theories discrete in this way and still maintain exact gauge-invariance, though, of course breaking Euclidean invariance. Hence a space-time lattice provides a non-perturbative cut-off which removes the ultra-violet divergences by eliminating all wavelengths less than twice the lattice spacing. As with any regulator, it must be removed after renormalisation so that physics results can only be extracted in the continuum limit where the lattice spacing is taken to zero. Here also, we expect Euclidean invariance to be restored.

As an illustration, consider a free scalar field $\phi(x)$. Working in Euclidean space-time, the Lagrangian is

$$\mathcal{L}_E = \frac{1}{2} (\partial_\mu \varphi)^2 + \frac{1}{2} m^2 \varphi^2 \qquad (1.48)$$

and we can write down the action :

$$S[\varphi] = \int d^4x \; \mathcal{L}_E(\partial_\mu \varphi, \varphi) \qquad (1.49)$$

for a given field configuration. In the Feynman Path Integral formulation [Feynman (1948)], the matrix element $\langle \phi' t' | \phi t \rangle$ is written as a functional integral : Z,

$$= \langle \phi' t' \mid \phi t \rangle = N \int [d\varphi] \exp i \int_t^{t'} L \, dt \qquad (1.50)$$

where

$$L = \int d^3x \; \mathcal{L}(\partial_\mu \varphi, \varphi) , \qquad (1.51)$$

represents the sum of contributions over all paths connecting the initial and final states, weighted by the exponential of i times the action. Here the generating functional

$$Z = \int \{d\varphi\} \exp - S[\varphi] \tag{1.52}$$

where the functional integral over field configurations requires careful definition. Expectation values are given by

$$\langle \phi_1 \phi_2 \cdots \rangle = \frac{1}{Z} \int \{d\phi\} \; \phi_1 \phi_2 \cdots \exp - S[\phi] \tag{1.53}$$

Introducing a regular hypercubic lattice (there are other possibilities e.g. triangular or random lattices) of spacing a and extent La with sites n,

$$n = (n_1, n_2, n_3, n_4) \tag{1.54}$$

we make the substitutions

$$\begin{aligned} \phi(x) &\longrightarrow \phi(n) \\ \partial_\mu \phi(x) &\longrightarrow \frac{\varphi(n+\hat{\mu}) - \varphi(n)}{a} \\ \int d^4x &\longrightarrow a^4 \sum_n \end{aligned} \tag{1.55}$$

where $\hat{\mu}$ is a unit vector in the μ-direction, μ=1,2,3,4. The lattice action is then a sum

$$a^4 \sum_n \left\{ \sum_{\mu=1}^{4} \frac{1}{2} \frac{(\phi(n+\hat{\mu}) - \phi(n))^2}{a^2} + \frac{1}{2} m^2 \phi^2(n) \right\} \tag{1.56}$$

and we can write down the Feynman Path Integral

$$Z = \int \left(\prod_n d\phi(n) \right) \exp - S[\phi] \tag{1.57}$$

which is now perfectly well defined mathematically : the functional integrals are now multiple integrals since the total volume of the system is finite.

If we add an interaction term $g^2\phi^4$ to the Lagrangian, we see that if we rescale the fields

$$\phi_n' = g\,\phi_n \tag{1.58}$$

then

$$S[\phi] = S\left[\frac{\phi'}{g}\right] \equiv \frac{1}{g^2} S'[\phi'] \tag{1.59}$$

i.e. the coupling constant g appears as an overall factor in the action, and rewriting (1.57)

$$Z' = \int \left(\prod_n d\phi_n'\right) \exp -\frac{1}{g^2} S'[\phi'] \tag{1.60}$$

This has the same form as the partition function for a statistical spin system where instead of S/g^2 in the exponential there would be E/kT. Thus we may consider g^2 to be the analogue of temperature so that strong and weak coupling can be equated with high and low temperature respectively. This correspondence between lattice field theories and spin systems means statistical mechanics techniques can be applied to both : a particular example of this as we shall see in chapter 3 is Monte Carlo techniques.

Let us now move on to look at Wilson's formulation of an SU(3) pure gauge theory on the lattice [Wilson 1974]. The continuum action is

$$S = -\int d^4x \; \frac{1}{4} F_{\mu\nu}^{\;a} \; F^{\mu\nu\,a} \tag{1.61}$$

We work with a Euclidean lattice (the connection with Minkowski space is made by a Wick rotation of the time variable $t \rightarrow i\tau$. On the lattice, the gauge fields A_μ are replaced by elements of the gauge group :

$$U = \exp iga\,A_\mu = \exp iga\,\lambda^a\,A_\mu^a \tag{1.62}$$

where $\lambda_a/2$ are the generators of the gauge group (SU(3) in this case) on the links between the sites. (1.62) is the discretised form of the connection $P \exp ig\int_x^y A_\mu^a \lambda^a dx_\mu$ which transports colour from x to y with $x = y + a$ and hence it is naturally associated with the link from x to $x+a$ So we have on each link a matrix U_{ab} where a and b are colour labels associated with the sites at each end of the link. We make the assignment

$$U_{-\mu}(n+\hat{\mu}) = U_\mu^{-1}(n) \tag{1.63}$$

and we can perform discrete elementary transports

$$\Psi_b = U_{ab}\,\Psi_a \tag{1.64}$$

of the colour vector ψ equivalent to infinitesimal displacements in the continuum. For local gauge invariance, we allow an arbitrary group rotation at each site of the lattice and assume the same transformation law as for the line integral of the gauge field in the continuum:

$$U_\mu(n) \longrightarrow U'_\mu(n) = \Omega(n)\, U_\mu(n)\, \Omega^{-1}(n+\hat{\mu}) \tag{1.65}$$

Thus $\Omega(n)$ defines the orientation of a local colour frame at each site n, whereas $U_\mu(n)$ provides the transport from one frame to the next in the direction μ. From (1.65) the trace of the product of U matrices round a closed path is a gauge invariant quantity and Wilson proposed constructing the action from the simplest such products, round the elementary squares on the lattice called plaquettes.

$$S = \frac{1}{2g^2} \sum_{n\mu\nu} \mathrm{Tr}\, U_\square + \mathrm{Tr}\, U_\square^\dagger \tag{1.66}$$

where

$$U_\square = U_\mu(n)\, U_\nu(n+\hat{\mu})\, U_\mu^\dagger(n+\hat{\nu})\, U_\nu^\dagger(n) \tag{1.67}$$

This must have (1.61) as its continuum limit; indeed it does as we now show. Since

$$U = \exp iga A_\mu \equiv \exp i B_\mu \tag{1.68}$$

writing (1.67) out in full gives

$$U_\square = \exp i B_\mu(n) \cdot \exp i \{ B_\nu(n) + a \partial_\mu B_\nu(n) \} \cdot \times \exp -i \{ B_\mu(n) - a \partial_\nu B_\mu(n) \} \cdot \exp -i B_\nu(n) \tag{1.69}$$

where we have used

$$B_\nu(n+\hat{\mu}) = B_\nu(n) + a \partial_\mu B_\nu(n) \tag{1.70}$$

We now use the Baker-Campbell-Hausdorff relation

$$\exp A \exp B = \exp [A + B + \tfrac{1}{2}[A,B] \cdots] \tag{1.71}$$

to obtain

$$U_\square = \exp\left(ia \{ \partial_\mu B_\nu - \partial_\nu B_\mu \} + [B_\mu, B_\nu] + \text{higher order terms} \right) \tag{1.72}$$

$$= \exp\left(ia^2 g (\partial_\mu A_\nu - \partial_\nu A_\mu) + [A_\mu, A_\nu] + \text{higher order terms} \right) \tag{1.73}$$

$$U_{\square} = \exp i a^2 g F_{\mu\nu} \tag{1.74}$$

as $a \to 0$

$$U_{\square} = 1 + i a^2 g F_{\mu\nu} - \frac{a^4}{2} g F_{\mu\nu} F^{\mu\nu} \tag{1.75}$$

Since $F_{\mu\nu} = \lambda^a F^a_{\mu\nu}$ is linear in the generators, its trace is zero so we look at the next term $F_{\mu\nu}F^{\mu\nu}$:

$$\mathrm{Tr}\ F_{\mu\nu} F^{\mu\nu} \sim \mathrm{Tr}\ F^a_{\mu\nu} \frac{\lambda^a}{2} F^b_{\mu\nu} \frac{\lambda^b}{2} \tag{1.76}$$

where

$$\mathrm{Tr}\ \frac{\lambda^a}{2} \frac{\lambda^b}{2} = \frac{\delta^{ab}}{2} \tag{1.77}$$

so making the equivalence

$$\sum_{n\,\mu\nu} \longrightarrow \int \frac{d^4x}{a^4} \sum_{\mu\nu} \tag{1.78}$$

we have

$$\frac{1}{2g^2} \sum_{n\mu\nu} \mathrm{Tr}\, U_{\square} + \text{hermitian conjugate} = \tag{1.79}$$

$$2\left\{ \frac{1}{2g^2} \int \frac{d^4x}{a^4} \sum_{\mu\nu} \tfrac{1}{2} (F^a_{\mu\nu} F^{\mu\nu a})(-\tfrac{1}{2} a^4 g^2) \right\}$$

$$= \text{/ contd}$$

$$= -\frac{1}{4} \int d^4x \sum_{\mu\nu} F_{\mu\nu}^{\ a} F^{\mu\nu\, a} \qquad (1.80)$$

Thus we recover the Yang-Mills action of (1.61)

The lattice theory provides a precise mathematical meaning for any quantity we wish to measure, but we must remember that we need to take the limit of zero lattice spacing to recover the physical value. Consider some physical quantity q with dimension -d in lattice units. In a lattice calculation it takes the form

$$q = a^{-d} f(g) \qquad (1.81)$$

The dimensionless function f(g) contains all the physical information. (g is a dimensionless coupling constant in four dimensions). If q=m is a mass

$$m = \frac{1}{a} f(g) \qquad (1.82)$$

where f(g) will give the mass in terms of the number of lattice spacings. Letting $a \to 0$ will not produce a sensible limit unless g is also tuned towards some value g_{cr} (i.e. g is renormalised) so that quantities like m approach well defined finite values : as $a \to 0$ we need $f(g) \to 0$. This implies

$$g = g(a) \qquad (1.83)$$

and g_{cr} is such that

$$\lim_{g \to g_{cr}} f(g) = 0 \qquad (1.84)$$

This critical point g_{cr} must have scaling properties - once the functional

relationship between g and a is established from one particular observable, the same relation must also give the correct, well-defined values for all other observables as $a \to 0$. For non-Abelian gauge theories, $g_{cr} = 0$.

We also have, for small enough a,

$$\frac{dm}{da} = 0 \tag{1.85}$$

so from (1.82)

$$-\frac{1}{a^2} f(g) + \frac{1}{a} f'(g) \frac{\partial g}{\partial a} = 0 \tag{1.86}$$

$$\Rightarrow \quad f(g) = f'(g)\, a \frac{\partial g}{\partial a} \tag{1.87}$$

Near g=0

$$-a \frac{\partial g}{\partial a} = \beta(g), \tag{1.88}$$

the β-function of (1.40),which may be expressed as in (1.41) We thus have

$$f(g) = \exp - \int^{g} \frac{dg'}{\beta(g')} \tag{1.89}$$

$$\propto (\beta_0 g^2)^{-\beta_1/2\beta_0^2} \exp(-1/2\beta_0 g^2) \left[1 + O(g^2)\right] \tag{1.90}$$

We may write

$$\Lambda = \frac{1}{a} f(g) \tag{1.91}$$

where Λ is a dimensionful constant of integration which sets the scale for all masses in the theory. (1.91) may thus be written

$$\Lambda^{latt} = \frac{1}{a} (\beta_0 g^2)^{-\beta_1/2\beta_0^2} \exp(-1/2\beta_0 g^2) \left[1 + O(g^2)\right] \tag{1.92}$$

and all masses in the theory may be expressed

$$m_i = c_i \Lambda^{latt} \qquad (1.93)$$

So masses are given by expressions like (1.92) which are non-analytic at g=0 meaning the masses are therefore non-perturbative quantities. Mass ratios are independent of Λ and become constant in the asymptotic scaling regime where both have the same g dependence (where only the two-loop β function is required). It is crucial to establish numerically how close to g = 0 the scaling regime (in which all masses have the same g dependence) sets in, because it will not be necessary to reduce the lattice spacing further in order to make continuum predictions. Asymptotic scaling (in which the g dependence is given by the two-loop β-function) may set in at this value of g or at a smaller value. All existing lattice gauge theory calculations have been done in the hope that scaling sets in for g^2 not very much smaller than 1, although the evidence for this is not yet conclusive. Monte Carlo Renormalisation Group analysis has been used to discover at which values of $\beta = 6/g^2$ asymptotic scaling sets in. The latest results [Bowler et al. (1986a)] at high β (6.9 and 7.2) are inconclusive, indicating that whereas previous calculations of the parameter $\Delta\beta$ at lower values of β seemed to be approaching the asymptotic value of 0.58, the 6.9 and 7.2 results seem to have levelled off at 0.51, albeit with high errors (0.51 ± 0.07 at $\beta = 7.2$) On the other hand, recent work in finite temperature QCD shows asymptotic scaling setting in at $\beta = 6.15$ [Kennedy (1986)].

Quark confinement is exact on the lattice [Tomboulis (1983)] but it has not been shown to persist as the lattice spacing $a \to 0$. Lattices have been used to obtain the string tension σ. Consider a $q\text{-}\bar{q}$ pair adiabatically separated to a distance R, held for a time T and then adiabatically brought together again and annihilated. The Euclidean amplitude is

$$\langle \text{final state} \mid e^{-Ht} \mid \text{initial state} \rangle \qquad (1.94)$$

On the lattice this process is represented by the Wilson loop

$$W(R,T) = \mathrm{Tr} \prod_{\mu,n \in C} U_\mu(n) \qquad (1.95)$$

where C is the path described by the R×T loop. If the energy of our $q\bar{q}$ system is V(R), we expect

$$W(R,T) \underset{T\to\infty}{\sim} \exp -TV(R) \qquad (1.96)$$

Using

$$V(R) \sim \sigma R + \frac{a}{R} \qquad (1.97)$$

ratios of measurements of Wilson loops W(R,T) may be used to extract estimates for the string tension σ.

So we have a lattice theory which is confining at strong coupling, and whose continuum limit is the g->0 limit. As long as there is no deconfining transition in the intermediate coupling region, we can proceed with simulations and extract physical results. Studies of both the SU(2) and SU(3) theory using discrete subgroups have indicated that there is no such transition in four dimensions, so that quarks are confined at all couplings. Other quantities have been investigated in the pure gauge theory such as the mass gap and topological effects. These will not be discussed here but details may be found in for example [Kogut (1983) and references therein]. We now move on from the pure gauge sector to discuss in chapter two how to include fermions in the lattice theory and how to construct hadronic states, so that we may calculate hadron masses.

CHAPTER TWO

The Hadronic Spectrum from a Lattice

In the previous chapter, it was shown how to set up a pure non-Abelian gauge theory on a lattice. If we wish to calculate the particle spectrum, we must further introduce fermions since the observed low-lying hadrons are bound states of quarks. This chapter is concerned with formulating fermionic fields on the lattice and then using the quark propagator to obtain mesonic and baryonic propagators from which hadron masses may be extracted. In the final section of this chapter, we review lattice hadron mass calculations to date.

2.1 Susskind Fermions

The fermionic part of the QCD Lagrangian in Euclidean space is

$$\bar{q}\,\gamma_\mu\,\mathcal{D}_\mu\,q \;+\; m\bar{q}\,q \qquad (2.1)$$

where

$$\mathcal{D}_\mu \;=\; \partial_\mu + ig\,A_\mu \qquad (2.2)$$

and

$$\{\gamma_\mu, \gamma_\nu\} \;=\; \delta_{\mu\nu} \qquad (2.3)$$

$$\gamma_\mu^{\dagger} \;=\; \gamma_\mu$$

The most obvious method of formulating fermions on the lattice is to use the 'naive lattice action' :

$$S_W = \frac{1}{2a} \sum_{n,\mu} \bar{\Psi}(n) \left[\gamma_\mu U_\mu(n) \Psi(n+\hat{\mu}) - \gamma_\mu U_\mu^+(n-\mu) \Psi(n-\hat{\mu}) \right] + \sum_n m \bar{\Psi}(n) \Psi(n) \tag{2.4}$$

where the $\psi(n)$ fermionic fields are associated with lattice sites n, and the ∂_μ has been evaluated using a central difference operator. The point-splitting has been rendered gauge invariant by including the appropriate link variable. It is straightforward to demonstrate that this reduces to (2.1) in the naive continuum limit.

However, if we look at this expression in more detail we discover things are not as straightforward as we would like; the continuum limit actually leads to a multiplicity of fermionic modes which cannot be ignored in the interacting theory. The existence of these extra degrees of freedom can most easily be demonstrated in the free theory. Using the central difference approximation as above,

$$\gamma_\mu \partial_\mu \longrightarrow \frac{1}{2a} \sum_\mu \gamma^\mu \left[\Psi(n+\hat{\mu}) - \Psi(n-\hat{\mu}) \right] \tag{2.5}$$

so that the lattice Green function in a finite box of side L satisfies (for $a = 1$)

$$\frac{1}{2} \sum_\mu \gamma^\mu \left\{ G(n+\hat{\mu},0) - G(n-\hat{\mu},0) \right\} + G(n,0) = \delta_{n,0} \tag{2.6}$$

Using the Fourier transform

$$G(n,0) = \sum_{\{p\}} e^{ip\cdot n} \tilde{G}(p) \qquad p = \frac{2\pi\ell}{L} \quad \ell = 0,\ldots,L-1 \tag{2.7}$$

$$\tilde{G}(p) = \frac{1}{L^4} \sum_{\{n\}} e^{-ip\cdot n} G(n,0)$$

we have

$$\frac{1}{2}\sum_{r}\gamma^{r}\left(e^{ipr}-e^{-ipr}\right)\tilde{G}(p)+m\tilde{G}(p)=\frac{1}{L^4} \qquad (2.8)$$

For m=0, $\tilde{G}(p)$ has poles at $\sum \sin^2 p_\mu = 0$. This happens not only when $p_\mu = \underline{0}$, but also when one or more component of $p_\mu = \pi$ with the other components 0. Thus in four dimensions there are $2^4 = 16$ poles, corresponding to 16 degenerate fermions. This is of no consequence if there are no interactions, but in the presence of interactions the fermion species mix [Guerin and Kenway (1980)]. This is known as the 'fermion doubling problem '.

The naive lattice action is not, however, the only possible action we could use and we might think that another choice could circumvent the problem of these 15 unwanted species. In fact, it has been shown [Nielsen and Ninomiya (1981)] that a fermionic lattice action cannot reproduce all the features of the continuum : if we want a local description of fermions on the lattice, either we must give up chiral symmetry as m -> 0 or we will have cancellation of the anomaly in the currents associated with the chiral symmetries. Chiral symmetry is important for the low-lying hadron spectrum so we are reluctant to give that up. The two most commonly used fermion formulations are Wilson fermions [Wilson (1975,1977)] and Susskind fermions [Kogut and Susskind (1975); Susskind (1977); Kawamoto and Smit (1981)]. The Wilson formulation introduces a new term to the action which causes a splitting between the sixteen species, so that in the continuum limit $a -> 0$, fifteen of them become infinitely heavy leaving a single fermion species with zero mass. However, the extra term explicitly breaks chiral symmetry. Aside from this undesirable feature, at finite lattice spacing the 15 unwanted species must be retained in the computer simulation even though it is hoped that they are approximately decoupled from the low-lying spectrum : their presence is an unnecessary burden on computation and memory.

For this technical reason, and because it is important to retain a remnant of the chiral symmetry of the continuum theory, we choose to work with the Susskind formulation. Here some of the unwanted fermion degrees of freedom are explicitly decoupled on the lattice via the transformation

$$\psi(n) = T(n)\,\chi(n)$$

$$\bar{\psi}(n) = \bar{\chi}(n)\,T^{+}(n) \qquad (2.9)$$

where

$$T(n) = \gamma_1^{n_1} \gamma_2^{n_2} \gamma_3^{n_3} \gamma_4^{n_4} \tag{2.10}$$

Then the naive free action becomes

$$S = \frac{1}{2} \sum_{n,\mu} \bar{\chi}(n) T^{+}(n) \gamma^{\mu} \left[T(n+\hat{\mu}) \chi(n+\hat{\mu}) - T(n-\hat{\mu}) \chi(n-\hat{\mu}) \right] + \sum_{n} m \bar{\chi}(n) \chi(n) \tag{2.11}$$

Let us look at the cases $\mu = 1$ and 2

$$\begin{aligned} \bar{\psi}(n) \gamma_1 \psi(n+\hat{1}) &= \bar{\chi}(n) T^{+}(n) \gamma_1 T(n+\hat{1}) \chi(n+\hat{1}) \\ &= \bar{\chi}(n) \gamma_4^{n_4} \gamma_3^{n_3} \gamma_2^{n_2} \gamma_1^{n_1} \gamma_1 \gamma_1^{n_1+1} \gamma_2^{n_2} \gamma_3^{n_3} \gamma_4^{n_4} \chi(n+\hat{1}) \\ &= \bar{\chi}(n) \chi(n+\hat{1}) \end{aligned} \tag{2.12}$$

$$\begin{aligned} \bar{\psi}(n) \gamma_2 \psi(n+\hat{2}) &= \bar{\chi}(n) T^{+}(n) \gamma_2 T(n+\hat{2}) \chi(n+\hat{2}) \\ &= \bar{\chi}(n) \gamma_4^{n_4} \gamma_3^{n_3} \gamma_2^{n_2} \gamma_1^{n_1} \gamma_2 \gamma_1^{n_1} \gamma_2^{n_2+1} \gamma_3^{n_3} \gamma_4^{n_4} \chi(n+\hat{2}) \\ &= (-1)^{n_1} \bar{\chi}(n) \chi(n+\hat{2}) \end{aligned} \tag{2.13}$$

so the free action becomes

$$S = \frac{1}{2} \sum_{n,\mu} \alpha_{\mu}(n) \bar{\chi}(n) \left[\chi(n+\hat{\mu}) - \chi(n-\hat{\mu}) \right] + \sum_{n} m \bar{\chi}(n) \chi(n) \tag{2.14}$$

where

$$\alpha_{\mu}(n) = \begin{cases} 1 & \mu = 1 \\ (-1)^{n_1} & \mu = 2 \\ (-1)^{n_1+n_2} & \mu = 3 \\ (-1)^{n_1+n_2+n_3} & \mu = 4 \end{cases} \tag{2.15}$$

This is diagonal in the spinor indices : we have four identical copies and so only need consider one of them. Dropping three of the copies reduces the degeneracy from sixteen to four, which are sometimes considered as four different flavours. At non-zero lattice spacing a there is a continuous U(1)⊗U(1) symmetry for m -> 0 ,which is a remnant of the full U(4)⊗U(4) chiral symmetry of the continuum. This will be discussed in section 2.5. In this formulation, there are two Grassmann variables per lattice site, χ and $\overline{\chi}$. This action should describe $2^{d/2} = 4$ Dirac fermions in the continuum limit, but these 'flavours' are not apparent in (2.14). Kluberg-Stern, Morel, Napoly and Petersson have proposed a method of identifying them [Kluberg-Stern et al. (1983)] which defines the quark fields on hypercubes of side $2a$ Each lattice site can be written

$$x_\mu = 2y_\mu + \eta_\mu \qquad \eta_\mu = 0 \text{ or } 1 \tag{2.16}$$

where the x_μ describe a lattice with spacing $2a$ and $1/2^d$ times the number of sites of the y_μ lattice. We may then define the quark fields by

$$\begin{aligned} q^{\alpha a}(y) &= \sum_\eta \Gamma^{\alpha a}_\eta \, \chi(2y+\eta) \\ \bar{q}^{\alpha a}(y) &= \sum_\eta \bar{\chi}(2y+\eta) \, \Gamma^{*\alpha a}_\eta \end{aligned} \tag{2.17}$$

where

$$\Gamma^{\alpha a}_\eta = \gamma_1^{\eta_1} \gamma_2^{\eta_2} \gamma_3^{\eta_3} \gamma_4^{\eta_4} \tag{2.18}$$

The α indices are interpreted as Dirac indices and the a indices as flavour. This comes from rewriting the free action for F flavours as

$$\begin{aligned} S_F = a^d \sum_{y,\mu} \sum_{\eta\eta'} \{ & \bar{\chi}(2y+\eta) \, \Gamma^\mu_{\eta,\eta'} \, \Delta_\mu \, \chi(2y+\eta') \\ & + a \, \bar{\chi}(2y+\eta) \, \tilde{\Gamma}^\mu_{\eta,\eta'} \, \delta_\mu \, \chi(2y+\eta') \} \end{aligned} \tag{2.19}$$

where

$$\Delta_\mu q(y) = \frac{1}{4a} \left[q(y+\hat{\mu}) - q(y-\hat{\mu}) \right] \xrightarrow{a \to 0} \partial_\mu q(y) \tag{2.20}$$

and

$$\delta_\mu q(y) = \frac{1}{4a^2}\left[q(y+\hat{\mu}) + q(y-\hat{\mu}) - 2q(y)\right] \xrightarrow{a \to 0} \partial_\mu^2 q(y) \qquad (2.21)$$

are defined on the 2y lattice of spacing $2a$, with μ now of length $2a$. We have defined

$$\Gamma^{\mu}_{\eta,\eta'} = \frac{1}{F} Tr\left(\Gamma^{\dagger}_{\eta} \gamma_\mu \Gamma_{\eta'}\right) \qquad (2.22)$$

and

$$\tilde{\Gamma}^{\mu}_{\eta,\eta'} = \frac{1}{F} Tr\left(\Gamma^{\dagger}_{\eta} \gamma_\mu \Gamma_{\eta'}\right)\left\{\delta_{\eta',\eta-\hat{\mu}} - \delta_{\eta',\eta+\hat{\mu}}\right\} \qquad (2.23)$$

where

$$\delta_{\eta',\eta-\hat{\mu}} = \begin{cases} 1 & \text{if } \eta'_\mu = \eta_\mu - \hat{\mu} \quad \forall\mu \\ 0 & \text{otherwise} \end{cases} \qquad (2.24)$$

This follows from the fact that we may write

$$\alpha_\mu(n) = \frac{1}{F} Tr\left(\Gamma^{\dagger}_{\eta} \gamma_\mu \Gamma_{\eta+\hat{\mu}}\right) \qquad (2.25)$$

With the relations (2.17) we have,

$$S_F = (2a)^d \sum_{y,\mu} \bar{q}(y)(\gamma_\mu \otimes \mathbb{1})\, \Delta_\mu q(y) + a\, \bar{q}(y)(\gamma_5^{\dagger} \otimes t_\mu^{\dagger} t_5^{\dagger})\, \delta_\mu q(y) \qquad (2.26)$$

where we use t_μ to represent γ_μ acting in flavour space. The first term is the naive action for F free Dirac fermions on a lattice of spacing $2a$, and suggests the flavour interpretation of the second index. It has the full U(F)⊗U(F) symmetry of the continuum. The second term, involving second order lattice derivatives, is $O(a)$ with respect to the first and is responsible for lifting the fermion degeneracy. It explicitly breaks the Lorentz and flavour symmetry, and only the U(1)⊗U(1) generators are conserved. Generalising (2.14) and (2.17) to the interacting theory, we use

$$q_\mu^{\alpha a}(n) = \sum_\eta \Gamma_\eta^{\alpha a} U_\eta(n) \chi(2y+\eta)$$

$$\bar{q}_\mu^{\alpha a}(n) = \sum_\eta \bar{\chi}(2y+\eta) U_\eta^+(n) \Gamma_\eta^{*\alpha a} \qquad (2.27)$$

where

$$U_\eta(n) = [U_1(2y)]^{\eta_1} [U_2(2y+\eta_1)]^{\eta_2} \cdots [U_d(2y+\eta_1+\cdots\eta_{d-1})]^{\eta_d} \qquad (2.28)$$

to relate the q-fields and the χ fields. The Susskind action is

$$S = \frac{1}{2} \sum_{n,\mu} \bar{\chi}(n) \alpha_\mu(n) [U_\mu(n) \chi(n+\hat{\mu}) - U_\mu^+(n-\hat{\mu}) \chi(n-\hat{\mu})] + \sum_n m \bar{\chi}(n) \chi(n) \qquad (2.29)$$

2.2 Quark Propagators in the Quenched Approximation

We now show how to use the action discussed in the previous section to calculate expressions for expectation values of operators on the lattice. The expectation values for operators involving quark fields, such as the meson and baryon propagators are expressed in terms of the elementary quark propagators.

The general expression for the expectation value of an operator is

$$\langle O \rangle = \int [dU][d\chi][d\bar{\chi}] \, O \exp -S(U,\chi,\bar{\chi}) \qquad (2.30)$$

where

$$S = S_G + S_F \qquad (2.31)$$
$$= -3\beta \sum \mathrm{Tr}\, U_\Box + \mathrm{h.c.} + \frac{1}{2} \sum_{ij} \bar{\chi}(i) \left(\mathbb{D}_{ij} + M \right) \chi(j)$$

with **D** defined as

$$\mathbb{D}_{ij} = \alpha_\mu(i) \left[U_\mu(i)\, \delta_{i+1,j} - U_\mu^\dagger(i-1)\, \delta_{i-1,j} \right] \qquad (2.32)$$

and **M** = mI. The quark propagator is

$$\langle \chi \bar{\chi} \rangle = \int [dU][d\chi][d\bar{\chi}]\ \chi \bar{\chi}\ \exp -(S_G + S_F) \qquad (2.33)$$

Because the fermionic part of the action is bilinear in the quark fields, we can integrate out the χ and $\bar{\chi}$ degrees of freedom [Matthews and Salam (1954,1955), see Cheng and Li (1984)], to obtain

$$\int [dU] \left\{ \det(\mathbb{D}+M) \right\} \left[\mathbb{D}+M \right]^{-1} \exp -S_G \qquad (2.34)$$

The integral over the bosonic gauge fields must be performed numerically, and so is replaced by a finite sum over configurations of gauge fields :

$$\sum_{\{c\}} \det(\mathbb{D}+M) \left[\mathbb{D}+M \right]^{-1} \exp -S_G(c) \qquad (2.35)$$

Since det (**D**+**M**) > 0, a Monte-Carlo technique (see chapter three) may in principle be used to generate a sequence of pure gauge configurations, each occurring with probability {det(**D**+**M**)exp(-S_G)} We may then approximate expectation values by the corresponding quantities averaged over a finite sized sample, which ideally should be as large as possible. Thus :

$$\frac{1}{N} \sum_{c=1}^{N} \left\{ \left[D+M \right]^{-1} \right\}_c \qquad (2.36)$$

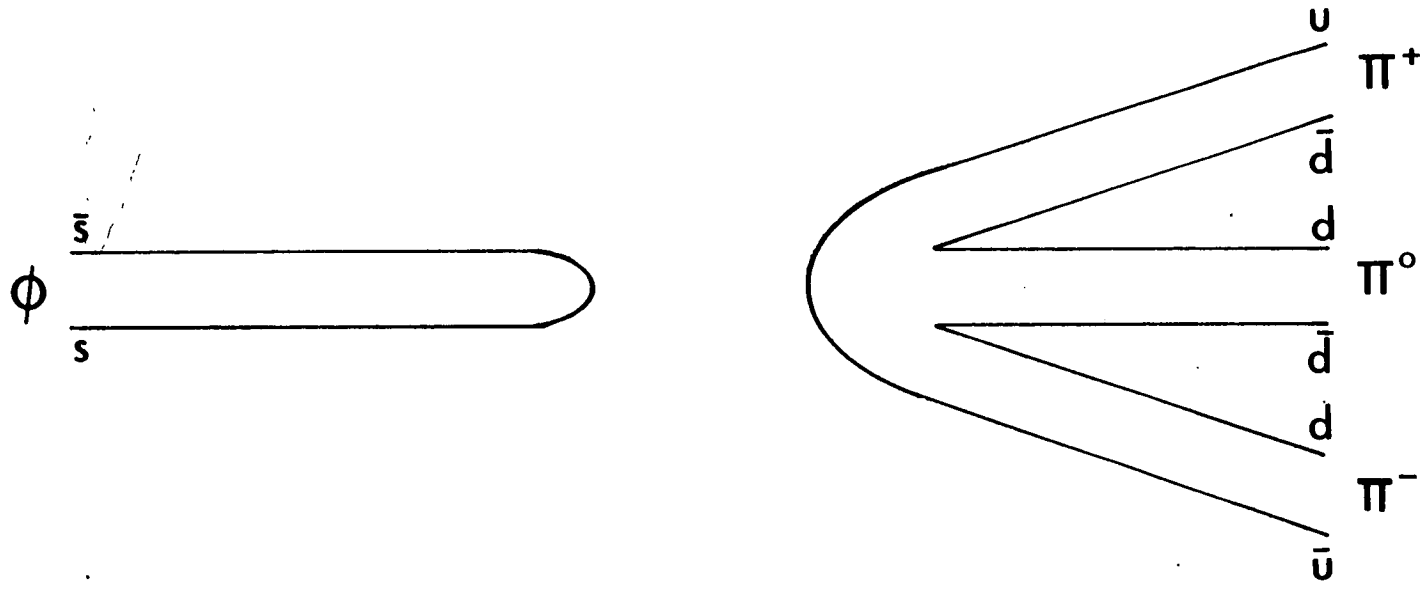

Figure 2.1 This decay of the $\phi \rightarrow 3\pi$ involves unconnected quark lines and is suppressed. This suppression is known as the Zweig rule and is seen in terms of a multi-gluon intermediate state.

On a $16^3 \times 24$ lattice the matrix **D+M** is of dimension $16^3 \times 24 \times 3$, and to calculate det(**D+M**) for a given (**D+M**) would be computationally very intensive. Furthermore, during the Monte-Carlo updating described in chapter three, it would be necessary to recalculate the determinant at each sweep as **D** is updated. This would not be practical on currently available computers if we wish to work with large lattices. Instead, we choose to work in the 'Quenched Approximation', which neglects the effect of the determinant by setting it to unity. This is equivalent to ignoring quark loops in perturbation theory and hence we only have valence quarks in our hadrons. We are solving the problem of quark propagation in a background gauge field, ignoring the back reaction of the quarks on the gauge fields themselves. This is certainly a good approximation for high quark mass, but it is not known at what point it breaks down as $m \rightarrow 0$. Determining this is one of the aims of this study. The quenched approximation effectively enforces the Zweig rule for all flavours. Several authors have used this as a justification for using the quenched approximation - Zweig suppression of diagrams like fig 2.1 is indeed observed in nature. These approximations mean we have nonet symmetry, since we do not measure any diagrams which would remove the π-η' degeneracy. Weingarten [1982a] has also used the following argument. Removing closed quark loops inside diagrams should result in the gauge fields between a valence quark and anti-quark in a meson being string-like, with a string tension T. If the determinant is restored it is plausible that the field in the meson remains string-like but now with breaks at various points where there is a quark loop. This string will have a new string tension T' with a real part $\mathrm{re}\ T' < T$. In fact, in nature meson Regge trajectories <u>are</u> nearly linear. If we can shift β so that $T = \mathrm{Re}\ T'$, we might thus hope that the behaviour of the quenched and unquenched theories to be (qualitatively at least) the same. This effect has recently been confirmed in a study on a $9^3 \times 18$ lattice [Fukugita et al. (1986)]. What we use, then, to calculate the quark propagator is (2.36), an average over independent configurations distributed according to the pure gauge action. We must calculate the Green function $[\mathbf{D+M}]^{-1}$ for the lattice Dirac equation :

$$(D + M)\ G = \delta \qquad (2.37)$$

for a large number of configurations, and having done so , we can then build

up meson and baryon propagators from it.

2.3 Local Lattice Operators for Mesons and Identification of Quantum Numbers

We will now show how, using Susskind fermions, a range of operators can be constructed to create mesonic bound states which may be identified in the continuum limit with the pion, rho, B, A_1 and δ states etc.

A general meson operator at a site y is

$$J_{\lambda\delta}(y) = \sum_{A} \bar{q}_A(y)(\Gamma_\lambda \otimes \Gamma_\delta^*) q_A(y) \qquad (2.38)$$

where A is a colour index, λ a spinor index and δ a flavour index. The Γ_λ are the appropriate Gamma matrices (λ = 1,16). The $q_A(y)$ fermionic fields are related to the one component Susskind fields by (2.27).
Thus

$$J_{\lambda\delta}(y) = \sum_{A\eta\eta'} \bar{\chi}(2y+\eta) U^{\dagger}_{\eta}(y) \Gamma^{*da}_{\eta} (\Gamma^{\alpha\beta}_{\lambda} \otimes \Gamma^{*ab}_{\delta}) \Gamma^{\beta b}_{\eta'} U_{\eta'}(y) \chi(2y+\eta') \qquad (2.39)$$

Because the solution of (2.37) is so computationally demanding on large lattices, and must be performed for as large a set of gauge configurations as possible, we prefer to solve it for just one origin per configuration and hence work with hadron operators which are <u>local</u> ,i.e. we require $2y+\eta$ and $2y+\eta'$ to be the same site. If we put $\eta=\eta'$ in the above equation we have

$$J_{\lambda\delta}(y) = \sum_{A\eta} \bar{\chi}(2y+\eta) \, Tr\left[\Gamma^{\dagger}_{\eta} \Gamma_\lambda \Gamma_\eta \Gamma^{\dagger}_{\delta}\right] \chi(2y+\eta) \qquad (2.40)$$

which requires $\lambda=\delta$ for a non-zero trace. So, the general local meson operator is

$$J_{\lambda}(y) = \sum_{A\eta} \bar{\chi}(2y+\eta) \chi(2y+\eta) \, Tr\left[\Gamma^{\dagger}_{\eta} \Gamma_\lambda \Gamma_\eta \Gamma^{\dagger}_{\lambda}\right] \qquad (2.41)$$

To calculate mesonic rest-frame propagators , we must evaluate

$$M_\lambda(y_4=t) = \sum_{\underline{y}} \langle J_\lambda(y)\, J_\lambda(0)\rangle \qquad (2.42)$$

for a range of Γ_λ. We have $\Gamma_\lambda = 1$, γ_5 , $\gamma_0\gamma_5$, γ_μ , $\gamma_0\gamma_\mu$, $\gamma_5\gamma_\mu$ and $\gamma_\mu\times\gamma_\mu$. We define the parity operation as follows :

$$\mathcal{P}\, q(y)\, \mathcal{P}^{-1} = P\, q(-\underline{y}, y_4) \qquad (2.43)$$

$$P = \gamma_4 \otimes 1 \qquad (2.44)$$

where the γ_4 acts in spinor space and the 1 in flavour space, and use it to operate on $J_\lambda(y)$ in (2.41) for each value of λ, to obtain the following (continuum) parity identifications :

Γ_λ	J^P
1	0^+
γ_5	0^-
$\gamma_4\gamma_5$	0^-
γ_μ	1^-
$\gamma_4\gamma_\mu$	1^-
$\gamma_5\gamma_\mu$	1^+
$\gamma_\mu\otimes\gamma_\mu$	1^+

(2.45)

The meson timeslice propagator

$$G_M(y_4=t) = \sum_{\underline{y}} G_M(0,\underline{y}) \qquad (2.46)$$

where

$$G_M(y_4=t) \equiv M_\lambda(y_4=t) \qquad (2.47)$$

is expected to be an exponential function of time :

$$G_M(t) \sim A \exp -m_\lambda t \qquad (2.48)$$

So we make the identifications of table 2.1, between the lattice states and the lowest lying continuum states.

M_λ	J^{PC}	meson	$G_m(t')$
$M_{\mathbb{1}}$	0^{++}	$\delta(980)$	$K_\delta \exp -m_\delta t'$
$M_{\gamma_5}, M_{\gamma_4\gamma_5}$	0^{-+}	$\pi(140)$	$K_\pi \exp -m_\pi t'$
$M_{\gamma_\mu}, M_{\gamma_4\gamma_\mu}$	1^{--}	$\varrho(770)$	$K_\varrho \exp -m_\varrho t'$
$M_{\gamma_\mu \times \gamma_\mu}$	1^{+-}	$B(1235)$	$K_B \exp -m_B t'$
$M_{\gamma_5\gamma_\mu}$	1^{++}	$A_1(1270)$	$K_{A_1} \exp -m_{A_1} t'$

Table 2.1 Identification of continuum quantum numbers for the lowest lying states in local meson timeslice propagators.

Let us look, for example, at M_{γ_5} in more detail.

$$M_{\gamma_5}(t) = \sum_{\underline{y}} \langle J_{\gamma_5}(y)\ J(0) \rangle$$

$$= \sum_{\underline{y}} \sum_{AB\eta\eta'} \mathrm{Tr}\left[\Gamma_\eta^\dagger \gamma_5 \Gamma_\eta \gamma_5\right] \mathrm{Tr}\left[\Gamma_{\eta'}^\dagger \gamma_5 \Gamma_{\eta'} \gamma_5\right] \qquad (2.49)$$

$$\times \bar{\chi}_A(2y+\eta)\, \chi_A(2y+\eta)\, \bar{\chi}_B(\eta')\, \chi_B(\eta')$$

since

$$J_{\gamma_5}(y) = \sum_{A\eta} \mathrm{Tr}\left[\Gamma_\eta^\dagger \gamma_5 \Gamma_\eta \gamma_5\right] \bar{\chi}_A(2y+\eta)\, \chi_A(2y+\eta) \qquad (2.50)$$

We take $\eta' = (\underline{0}, \eta_4)$ so that the origin is at $\underline{0}$. We must therefore sum over η_4' = 0,1 and η_μ = 0,1. Considering η_4, η_4' = 0 and 1 separately, we need the following four traces :

$$1.\ \mathrm{Tr}\left(\Gamma_\eta^\dagger \gamma_5 \Gamma_\eta \gamma_5\right)\Big|_{\eta_4=0} = \mathrm{Tr}\ \gamma_3^{\eta_3}\gamma_2^{\eta_2}\gamma_1^{\eta_1}\gamma_5\gamma_1^{\eta_1}\gamma_2^{\eta_2}\gamma_3^{\eta_3}\gamma_5 = F\,(-1)^{\eta_1+\eta_2+\eta_3}$$

$$2.\ \mathrm{Tr}\left(\Gamma_\eta^\dagger \gamma_5 \Gamma_\eta \gamma_5\right)\Big|_{\eta_4=1} = \mathrm{Tr}\ \gamma_4\gamma_3^{\eta_3}\gamma_2^{\eta_2}\gamma_1^{\eta_1}\gamma_5\gamma_1^{\eta_1}\gamma_2^{\eta_2}\gamma_3^{\eta_3}\gamma_4\gamma_5 = -F\,(-1)^{\eta_1+\eta_2+\eta_3}$$

$$3.\ \mathrm{Tr}\left(\Gamma_{\eta'}^\dagger \gamma_5 \Gamma_{\eta'} \gamma_5\right)\Big|_{\eta_4'=0} = \mathrm{Tr}\ \gamma_5\gamma_5 = F \qquad (2.51)$$

$$4.\ \mathrm{Tr}\left(\Gamma_{\eta'}^\dagger \gamma_5 \Gamma_{\eta'} \gamma_5\right)_{\eta_4'=1} = \mathrm{Tr}\ \gamma_4\gamma_5\gamma_4\gamma_5 = -F$$

so that

$$M_{\gamma_5}(t) = F^2 \sum_{\underline{y}} \sum_{AB\eta} (-1)^{\eta_1+\eta_2+\eta_3} \times$$

$$\Big\{ \bar{\chi}_A(\underline{x},2t)\chi_A(\underline{x},2t)\,\bar{\chi}_B(0)\chi_B(0) - \bar{\chi}_A(\underline{x},2t)\chi_A(\underline{x},2t)\,\bar{\chi}_B(t=1)\chi_B(t=1) - \bar{\chi}_A(\underline{x},2t+1)\chi_A(\underline{x},2t+1)\,\bar{\chi}_B(0)\chi_B(0) + \bar{\chi}_A(\underline{x},2t+1)\chi_A(\underline{x},2t+1)\,\bar{\chi}_B(t=1)\chi_B(t=1)\Big\} \qquad (2.52)$$

With $G^{AB}_{\eta\eta'}(y,0) = \langle \chi_A(2y+\eta)\bar{\chi}_B(\eta')\rangle$ and using

$$G^{AB\,\dagger}_{\eta\eta'}(y,0) = (-1)^{\eta_1+\eta_2+\eta_3+\eta_4+\eta_4'} G^{BA}_{\eta\eta'}(0,y) \qquad (2.53)$$

and translational invariance, we have

$$M_{\gamma_5}(t) = F^2 \sum_{\underline{x},AB} 2\,\langle|\chi_A(\underline{x},2t)\,\bar{\chi}_B(0)|^2\rangle + \langle|\chi_A(\underline{x},2t+1)\,\bar{\chi}_B(0)|^2\rangle + \langle|\chi_A(\underline{x},2t-1)\,\bar{\chi}_B(0)|^2\rangle \qquad (2.54)$$

The relation (2.53) changes the relative signs of the terms in (2.52) because of the η_4 and η_4'. Following the same procedure for the other choices of λ

$$M_{\mathbb{1}}(t) = F^2 \sum_{\underline{x},AB} (-1)^{x_1+x_2+x_3+x_4} 2\langle|\chi_A(x,2t)\,\bar{\chi}_B(0)|^2\rangle - \langle|\chi_A(x,2t+1)\,\bar{\chi}_B(0)|^2\rangle - \langle|\chi_A(x,2t-1)\,\bar{\chi}_B(0)|^2\rangle$$

$$M_{\gamma_4\gamma_5}(t) = F^2 \sum_{\underline{x},AB} 2\langle|\chi_A(x,2t)\,\bar{\chi}_B(0)|^2\rangle - \langle|\chi_A(x,2t+1)\,\bar{\chi}_B(0)|^2\rangle - \langle|\chi_A(x,2t-1)\,\bar{\chi}_B(0)|^2\rangle$$

$$M_{\gamma_\mu}(t) = F^2 \sum_{\underline{x},AB} \{(-1)^{x_1}+(-1)^{x_2}+(-1)^{x_3}\}\, 2\langle|\chi_A(x,2t)\,\bar{\chi}_B(0)|^2\rangle + \langle|\chi_A(x,2t+1)\,\bar{\chi}_B(0)|^2\rangle + \langle|\chi_A(x,2t-1)\,\bar{\chi}_B(0)|^2\rangle \qquad (2.55a\text{-}f)$$

$$M_{\gamma_4\gamma_\mu}(t) = F^2 \sum_{\underline{x},AB} \{(-1)^{x_1+x_2}+(-1)^{x_1+x_3}+(-1)^{x_2+x_3}\}\, 2\langle|\chi_A(x,2t)\,\bar{\chi}_B(0)|^2\rangle + \langle|\chi_A(x,2t+1)\,\bar{\chi}_B(0)|^2\rangle + \langle|\chi_A(x,2t-1)\,\bar{\chi}_B(0)|^2\rangle$$

$$M_{\gamma_5\gamma_\mu}(t) = F^2 \sum_{\underline{x},AB} \{(-1)^{x_1+x_2}+(-1)^{x_1+x_3}+(-1)^{x_2+x_3}\}\, 2\langle|\chi_A(x,2t)\,\bar{\chi}_B(0)|^2\rangle - \langle|\chi_A(x,2t+1)\,\bar{\chi}_B(0)|^2\rangle - \langle|\chi_A(x,2t-1)\,\bar{\chi}_B(0)|^2\rangle$$

$$M_{\gamma_\mu\times\gamma_\mu}(t) = F^2 \sum_{\underline{x},AB} \{(-1)^{x_1}+(-1)^{x_2}+(-1)^{x_3}\}\, 2\langle|\chi_A(x,2t)\,\bar{\chi}_B(0)|^2\rangle - \langle|\chi_A(x,2t+1)\,\bar{\chi}_B(0)|^2\rangle - \langle|\chi_A(x,2t-1)\,\bar{\chi}_B(0)|^2\rangle$$

However these operators M(t) are expressed as functions of 2t. Let us also define the following set of operators :

$$M_{PS}(t) = \sum_{\underline{x}} \sum_{AB} \langle |\chi_A(\underline{x},t)\, \bar{\chi}_B(0)|^2 \rangle$$

$$M_{SC}(t) = \sum_{\underline{x}} \sum_{AB} (-1)^{x_1+x_2+x_3+t} \langle |\chi_A(x,t)\, \bar{\chi}_B(0)|^2 \rangle \qquad (2.56a\text{-}d)$$

$$M_{VT}(t) = \sum_{\underline{x}} \sum_{AB} \{(-1)^{x_1} + (-1)^{x_2} + (-1)^{x_3}\} \langle |\chi_A(x,t)\, \bar{\chi}_B(0)|^2 \rangle$$

$$M_{PV}(t) = \sum_{\underline{x}} \sum_{AB} \{(-1)^{x_1+x_2} + (-1)^{x_1+x_3} + (-1)^{x_2+x_3}\} \langle |\chi_A(x,t)\, \bar{\chi}_B(0)|^2 \rangle$$

The seven correlation functions defined in (2.54) and (2.55a-f) are related to the four defined above as follows :

$$M_{\mathbb{1}}(t) = F^2 (2 M_{SC}(2t) + M_{SC}(2t+1) + M_{SC}(2t-1))$$

$$M_{\gamma_5}(t) = F^2 (2 M_{PS}(2t) + M_{PS}(2t+1) + M_{PS}(2t-1))$$

$$M_{\gamma_4\gamma_5}(t) = F^2 (2 M_{SC}(2t) - M_{SC}(2t+1) - M_{SC}(2t-1))$$

$$M_{\gamma_\mu}(t) = F^2 (2 M_{VT}(2t) + M_{VT}(2t+1) + M_{VT}(2t-1))$$

$$M_{\gamma_4\gamma_\mu}(t) = F^2 (2 M_{PV}(2t) - M_{PV}(2t+1) - M_{PV}(2t-1))$$

$$M_{\gamma_5\gamma_\mu}(t) = F^2 (2 M_{PV}(2t) + M_{PV}(2t+1) + M_{PV}(2t-1))$$

$$M_{\gamma_\mu \times \gamma_\mu}(t) = F^2 (2 M_{VT}(2t) - M_{VT}(2t+1) - M_{VT}(2t-1)) \qquad (2.57a\text{-}g)$$

Now we use table 2.1 and also make the approximation

$$M_{PS}(2t+1) \sim \exp(-m_\pi a)\, M_{PS}(2t) \qquad (2.58)$$

and similarly for the other states of (2.56). This comes from the fact that the PS propagator is decaying exponentially in time. We then obtain

$$F^2 M_{PS}(t) = \frac{1}{1+\cosh m_\pi a} K_\pi \exp(-m_\pi t) + \ldots$$

$$F^2 M_{SC}(t) = \frac{1+\cosh m_\pi a}{8\cosh m_\pi a} K'_\pi \exp(-m_\pi t) - \frac{1-\cosh m_\delta a}{8\cosh m_\delta a} K_\delta \exp(-m_\delta t) + \ldots$$

$$(-1)^t \begin{cases} \dfrac{1+\cosh m_\delta a}{8\cosh m_\delta a} K_\delta \exp(-m_\delta t) \\ -\dfrac{(1-\cosh m_\pi a)}{8\cosh m_\pi a} K'_\pi \exp(-m_\pi t) + \ldots \end{cases}$$

$$F^2 M_{VT}(t) = \frac{1+\cosh m_\rho a}{8\cosh m_\rho a} K_\rho \exp(-m_\rho t) - \frac{1-\cosh m_B a}{8\cosh m_B a} K_B \exp(-m_B t) + \ldots \qquad (2.59\,a\text{-}d)$$

$$(-1)^t \begin{cases} \dfrac{1+\cosh m_B a}{8\cosh m_B a} K_B \exp(-m_B t) \\ -\dfrac{(1-\cosh m_\rho a)}{8\cosh m_\rho a} K_\rho \exp(-m_\rho t) + \ldots \end{cases}$$

$$F^2 M_{PV}(t) = \frac{1+\cosh m_\rho a}{8\cosh m_\rho a} K'_\rho \exp(-m_\rho t) - \frac{1-\cosh m_{A_1} a}{8\cosh m_{A_1} a} K_{A_1} \exp(-m_{A_1} t)$$

$$(-1)^t \begin{cases} \dfrac{1+\cosh m_{A_1} a}{8\cosh m_{A_1} a} K_{A_1} \exp(-m_{A_1} t) \\ -\dfrac{1-\cosh m_\rho a}{8\cosh m_\rho a} K'_\rho \exp(-m_\rho t) \end{cases}$$

For the lowest order in a these equations can be rewritten as below

$$M_{PS}(t) \sim A_\pi \exp -m_\pi t$$
$$M_{SC}(t) \sim A'_\pi \exp -m_\pi t + (-1)^t A_\delta \exp -m_\delta t$$
$$M_{VT}(t) \sim A_\rho \exp -m_\rho t + (-1)^t A_B \exp -m_B t \quad (2.60a\text{-}d)$$
$$M_{PV}(t) \sim A'_\rho \exp -m_\rho t + (-1)^t A_{A_1} \exp -m_{A_1} t$$

These then are the functions we will use to fit the data from measurements of M_{PS}, M_{SC}, M_{VT}, M_{PV} on the lattice. We see from equations (2.60) that each operator we measure on the lattice is a mixture of continuum states with opposite parities (with the exception of M_{PS}). This makes the fitting procedure more difficult as we must use at least two exponentials merely to extract the ground state, and contamination from higher excited states is likely at short times. It is consequently particularly important when using local Susskind operators to have lattices of large extent in the time direction in order to expose the asymptotic decay. More details of the method of fitting will be given in chapter three.

2.4 Local Lattice operators for Baryons

In the same way as we did for the mesons, we wish to work with local fields and so following Kluberg-Stern et al [Kluberg-Stern et al. (1983)] we define

$$B(2y+\eta) = \frac{1}{3!} \varepsilon_{ABC} \chi_A(2y+\eta) \chi_B(2y+\eta) \chi_C(2y+\eta) \quad (2.61)$$

We must relate this to a general baryonic field in terms of q-fields. If we define

$$B^{\alpha a}(y) = \sum_\eta \Gamma_\eta^{\alpha a} B(2y+\eta) \quad (2.62)$$

we can see that $B^{\alpha a}$ depends on B the same way $q^{\alpha a}$ depends on χ, and we also have the result that $B^{\alpha a}(y)$ transforms in the same way as $q^{\alpha a}(y)$ i.e. as a spin 1/2 field on the lattice. Using equations (2.27) and (2.61), we have

$$B^{\alpha a}(y) = \frac{1}{3!} \sum_{ABC} \varepsilon_{ABC} \Gamma_\lambda^{\alpha\beta} q_A^{\beta b} \Gamma_\lambda^{+ba} \left[q_B^{\gamma c}(y) \left(C\Gamma_\lambda^{\gamma\delta} \otimes C^* \Gamma_\lambda^{cd} \right) \right] q_C^{\delta d}(y) \quad (2.63)$$

where C, the charge conjugation matrix is defined by

$$C\gamma_\mu C^\dagger = \gamma_\mu^T \quad ; \quad C^T = -C \tag{2.64}$$

Looking now at the propagator, we have

$$\langle B^{\alpha a}(y)\, \bar{B}^{\beta b}(0)\rangle = \sum_{\eta\eta'} \Gamma_\eta^{\alpha a}\, \Gamma^{*\beta b}_{\eta'} \langle B(2y+\eta)\, \bar{B}(\eta')\rangle \tag{2.65}$$

Morel and Rodrigues [Morel and Rodrigues (1984)] use the Fierz transformation

$$\langle B^{\alpha a}(y)\, B^{\beta b}(0)\rangle = \sum_{\delta\varepsilon} \Gamma_\delta^{\alpha\beta}\, \Gamma_\varepsilon^{+ba}\, X_{\delta\varepsilon}(y) \tag{2.66}$$

$$\text{for } X_{\delta\varepsilon}(y) = \Gamma_\delta^{+\mu\lambda} \langle B^{\lambda\ell}(y)\, \bar{B}^{\mu m}(0)\rangle \Gamma_\varepsilon^{\ell m}$$

to rewrite (2.65) as

$$\langle B^{\alpha a}(y)\, \bar{B}^{\beta b}(0)\rangle = \sum_{\delta\varepsilon\eta} \Phi \langle B(2y+\rho-2\rho.\eta)\, \bar{B}(0)\rangle \Gamma_\delta^{\alpha\beta}\, \Gamma_\varepsilon^{+ba} \tag{2.67}$$

where $\rho_\mu = \delta_\mu + \varepsilon_\mu \mod 2$, and Φ is a phase, dependent on η, δ and ε.

Then using Fourier transforms on an infinite lattice

$$f(P) = \sum_y \exp(2iP.y)\, f(y)$$

$$f(y) = \int_{-\pi/2}^{\pi/2} \frac{dP}{\pi^d} \exp(-2iP.y)\, f(P) \tag{2.68}$$

where f(y) is defined on a lattice spacing $2a$ with hypercubes at sites $2y$, the momentum space propagator

$$\Delta^{\alpha a;\beta b}(2P) = \sum_y \exp 2iP.y \langle B^{\alpha a}(y)\, \bar{B}^{\beta b}(0)\rangle \tag{2.69}$$

can be written, using (2.67), as

$$\sum_{\delta\varepsilon} \varphi' \, I_\varrho(P) \prod_{\mu=1}^{4} \left\{ e^{-iP_\mu \varrho_\mu} + (-1)^{\tilde{\varepsilon}} e^{iP_\mu \varrho_\mu} \right\} \Gamma_\delta^{\alpha\beta} \, \Gamma_\varepsilon^{\dagger ba} \qquad (2.70)$$

where

$$\begin{aligned} \tilde{\varepsilon}_\mu &= \varepsilon_\mu \quad \text{if} \quad \sum_\mu \varepsilon_\mu \text{ even} \\ &= 1 - \varepsilon_\mu \quad \text{if} \quad \sum_\mu \varepsilon_\mu \text{ odd} \end{aligned} \qquad (2.71)$$

and

$$I_\varrho(P) = \sum_y e^{iP(2y+\varrho)} \langle B(2y+\varrho)\, \bar{B}(0) \rangle \qquad (2.72)$$

and P′ is a phase dependent on δ and ε only. The second term above comes from the case η = (1,1,1,1). To see how the propagator behaves, we should now look at $I_\rho(P)$.

Now the Susskind action (2.29) is invariant under

$$\begin{aligned} & x_\alpha \longrightarrow -x_\alpha \\ & \chi(\cdots x_\alpha \cdots) \longrightarrow (-1)^{x_\alpha} \chi(\cdots -x_\alpha \cdots) \\ & U_\mu(\cdots x_\alpha \cdots) \longrightarrow \begin{cases} U_\mu(\cdots -x_\alpha \cdots) & \mu \neq \alpha \\ U_\mu^\dagger(\cdots -x_\alpha \cdots) & \mu = \alpha \end{cases} \end{aligned} \qquad (2.73)$$

and because B and $\bar{B}$ transform like χ and $\bar{\chi}$, we must have

$$I_\varrho(\cdots P_\alpha \cdots) = (-1)^{\varrho_\alpha} I_\varrho(\cdots -P_\alpha \cdots) \qquad (2.74)$$

Looking now at the centre of mass frame P = ($\underline{0}$,P_4) for i = 1,2,3 ,we have

$$\begin{aligned} & I_\varrho(P_4) = (-1)^{\varrho_i} I_\varrho(P_4) \qquad (2.75) \\ \Rightarrow \quad & \varrho_i = 0 \quad i = 1,2,3 \end{aligned}$$

In the centre of mass therefore, I_ρ is non-zero only when $\underline{\rho} = \underline{0}$. This fact leads to the following form for the propagator [Morel and Rodrigues (1984)]

$$\Delta(2P_4) = \tfrac{1}{2}\Big[\, i\sin 2P_4\,(\gamma_4 \otimes \mathbb{1}) - (\cos 2P_4 - 1)(\gamma_5 \otimes t_4 t_5)\, F_1(\sin^2 P_4) + 2\,(\mathbb{1}\otimes\mathbb{1})\, F_0(\sin^2 P_4) \tag{2.76}$$

where

$$I_{\underline{\rho},1}(P_4) = i\sin P_4\; F_1(\sin^2 P_4) \tag{2.77}$$

$$I_{\underline{\rho},0}(P_4) = F_0(\sin^2 P_4)$$

from the properties of $I_{\underline{\rho},1}$ and $I_{\underline{\rho},0}$. This has the same structure as a free quark propagator in the centre of mass, with F_0 and F_1 real with poles at the same place.

Using the parity operator as defined in (2.43), we have

$$\mathcal{P}\, B(\underline{y}, y_4)\, \mathcal{P}^{-1} = -(\gamma_4 \otimes \mathbb{1})\, B(-\underline{y}, y_4) \tag{2.78}$$

Looking at the propagator above, we see a term proportional to γ_5 which is parity violating, so the lattice states at finite β are not eigenstates of $\mathcal{P}$. Recall that what is actually measured is

$$\sum_{y,\rho} \langle B(2y+\rho)\, \bar{B}(0)\rangle = \frac{1}{3!}\, \varepsilon_{abc}\, \varepsilon_{ABC} \times \sum_{y,\rho} \langle \chi_a(2y+\rho)\, \bar{\chi}_A(0)\, \chi_b(2y+\rho)\, \bar{\chi}_B(0)\, \chi_c(2y+\rho)\, \bar{\chi}_C(0)\rangle \tag{2.79}$$

and

$$\sum_{y,\rho} \langle B(2y+\rho)\, \bar{B}(0)\rangle = \sum_{y,\rho} \int \frac{dP_4}{\pi}\, e^{-iP_4(2y_4+\rho_4)}\, I_\rho(P_4) \tag{2.80}$$

from the definition of I_ρ. Since $I_\rho(P_4) = 0$ if $\underline{\rho} \neq \underline{0}$, we have

$$\sum_{y\rho} \langle B(2\underline{y}+\underline{\rho}, 2y_4+\rho_4)\, \bar{B}(0)\rangle = 0 \quad \text{if} \quad \underline{\rho} \neq 0 \tag{2.81}$$

and so

$$\sum_{y\rho} \langle B(2y+\rho)\bar{B}(0)\rangle = \sum \langle B(2\underline{y}, 2y+\rho_4)\bar{B}(0)\rangle \qquad (2.82)$$

Performing the inverse Fourier transform on the momentum space propagator, Morel and Rodrigues [*ibid*] obtain for the propagator with $y_4>0$

$$\Delta^{\alpha a;\beta b}(y_4) = \sum_i R_i \left\{ \gamma_4 \otimes \mathbb{1} - \tanh M_i \, (\gamma_5 \otimes t_4 t_5) + \frac{\varepsilon_i}{\cosh M_i} (\mathbb{1}\otimes\mathbb{1}) \right\} \exp -2M_i y_4 \qquad (2.83)$$

where R_i is constant and ε_i is ± 1 according to the sign of R_0/R_1. The sum is over all poles of the functions F_0 and F_1.

$$\sum_{y,\rho_4} \langle B(2y, 2y_4+\rho_4)\bar{B}(0)\rangle$$

$$= \sum_{\rho} \int \frac{dP_4}{\pi} e^{-iP_4(2y_4+\rho_4)} I_\rho(P_4) \qquad \text{from (2.80)}$$

$$= \sum_{\rho} \begin{cases} \int \frac{dP_4}{\pi} e^{-iP_4(2y_4)} F_0(\sin^2 P_4) & \text{for } \rho=(\underline{0},0) \\ \int \frac{dP_4}{\pi} e^{-iP_4(2y_4+1)} i\sin P_4 \, F_1(\sin^2 P_4) & \text{for } \rho=(\underline{0},1) \end{cases} \qquad (2.84a,b)$$

and $F_0(\sin^2 P_4) = F_1(\sin^2 P_4)$ near the poles. This can be used to write an approximate form for the timeslice propagator on the lattice, taking the lowest states only

$$\sum_{\underline{y}\, \rho_4} \langle B(2\underline{y}, 2y_4+\rho_4)\, \bar{B}(0)\rangle = \frac{-R_1^+}{\cosh M_1^+} \exp - M_1^+ t + (-1)^t \frac{R_1^-}{\cosh M_1^-} \exp - M_1^- t \qquad (2.85)$$

This represents a spin 1/2 baryon on the lattice - the nucleon. For a lattice with a finite time extent and Dirichlet boundary conditions, we should use the asymptotic form

$$A_+ \exp(-m_+ t) + (-1)^t A_- \exp(-m_- t) \qquad (2.86)$$

to fit to the propagator

$$\sum_{\underline{y}\, \rho_4} \langle B(2\underline{y}, 2y_4+\rho_4)\, \bar{B}(0)\rangle \qquad (2.87)$$

This is the EVEN nucleon.

We note the following two properties, (which are obtained in the infinite lattice case) :

a) $$\mathrm{Im}\left\{ \sum_{\underline{x}} \langle B(\underline{x})\, \bar{B}(0)\rangle \right\} = 0 \qquad (2.88)$$

This comes from the invariance of the action under complex conjugation which means

$$\langle B(2y+\rho)\, \bar{B}(0)\rangle^* = (-1)^{\rho\cdot\bar{\rho}} \langle B(2y+\rho)\, \bar{B}(0)\rangle \qquad (2.89)$$

where

$$\bar{\rho}_\alpha = \sum_{\mu=1}^{\alpha-1} \rho_\mu \quad ; \quad \bar{\rho}_0 = 0 \qquad (2.90)$$

$$\text{b)}\ \sum_{\underline{x}} (-1)^{\underline{\eta}\cdot\underline{x}} \langle B(x)\,\bar{B}(0)\rangle = (-1)^{\eta_4 x_4} \sum_{y} \langle B(2y, 2y_4+\rho_4)\,\bar{B}(0)\rangle \qquad (2.91)$$
$$= (-1)^{\eta_4 x_4} \sum_{x} \langle B(x)\,\bar{B}(0)\rangle$$

for arbitrary η. This comes from (2.81), so there is no new information to be gained from measuring the left hand side of (2.91), as it is in fact independent of $\underline{\eta}$ - we need only measure at one corner of each hypercube on the lattice. In practice in order to check these relationships we shall also measure the ALL nucleon,

$$\sum_{y\rho} \langle B(2y+\rho)\,\bar{B}(0)\rangle \qquad (2.92)$$

which adds the contribution from all the sites on the x-lattice. The additional sites' contribution should average to zero by (2.81). However, on a finite lattice identity b) may not always hold. In fact, numerical evaluation of the analytic expression for free fermions shows that it holds for periodic boundary conditions but not for antiperiodic boundary conditions [Kenway et al. (1986)] If identity b) is violated in QCD for a particular choice of boundary conditions then it is a finite size effect, and the extent of the violation is a measure of the finite size effects on baryons. This will be further discussed in the interacting theory in chapter four.

For the ALL propagator, we use the same asymptotic form as used to fit to the EVEN nucleon.

2.5 Goldstone Bosons on the Lattice and in the Continuum

In section 2.3 we discussed local lattice operators for mesons, and we saw how there were two states with the same quantum numbers as the $\pi(140)$, viz the $M_{\gamma_4\gamma_5}$ and the M_{γ_5}. If we identify both with the continuum pion, we might hope both to be Goldstone bosons in the continuum limit corresponding to the spontaneously broken full chiral symmetry, a remnant of which is present in the lattice action. In fact, only the γ_5 state is a Goldstone boson at finite a as we show below.

The continuum Lagrangian is invariant under a U(F)⊗U(F) group of

transformations for F flavours, which is broken to $SU(F)_V \otimes SU(F)_A \otimes U(1)_V \otimes U(1)_A$. The lattice action is invariant under a global $U(1) \otimes U(1)$ group of transformations of the χ fields. This comes from the fact that χs at even sites are only coupled to $\bar{\chi}$s at odd sites and vice versa. We can write the transformations as

$$\begin{aligned} \chi(n) &\rightarrow T\,\chi(n) && \text{odd } n \\ \bar{\chi}(n) &\rightarrow \bar{\chi}(n)\,T^{\dagger} && \text{even } n \\ & && T, V \in U(1) \\ \chi(n) &\rightarrow V\,\chi(n) && \text{even } n \\ \bar{\chi}(n) &\rightarrow \bar{\chi}(n)\,V^{\dagger} && \text{odd } n \end{aligned} \qquad (2.93)$$

This symmetry is explicitly broken to the diagonal sub-group U(1) where T=V by the mass term.

$U(1) \otimes U(1)$ has two generators,

$$\begin{aligned} V &= \mathbb{1} \otimes \mathbb{1} \\ A &= \gamma_5 \otimes \gamma_5 \end{aligned} \qquad (2.94)$$

respectively the vector and axial vector generator. Since $\gamma_5 \times \gamma_5$ is traceless in flavour space, it belongs to the axial $SU(F)_A$ and not the axial $U(1)_A$ which is subject to the anomaly in the continuum. Thus if the symmetry is broken we would expect the Goldstone boson to be flavour non-singlet like the pion and unlike the η'. Kluberg-Stern et al. (1983) show that the axial current corresponding to the axial generator above is

$$\begin{aligned} A_\mu^B(y) = {} & \tfrac{1}{2}\{\bar{q}(y)(\gamma_\mu\gamma_5 \otimes T_B)\,q(y+\hat{\mu}) \\ & + \bar{q}(y+\hat{\mu})(\gamma_\mu\gamma_5 \otimes T_B)\,q(y)\} \\ & + \tfrac{1}{2}\{\bar{q}(y)(\mathbb{1} \otimes [t_\mu^{\dagger} t_5^{\dagger}, T_B])\,q(y+\hat{\mu}) \\ & + \bar{q}(y+\hat{\mu})(\mathbb{1} \otimes [t_\mu^{\dagger} t_5^{\dagger}, T_B])\,q(y)\} \end{aligned} \qquad (2.95)$$

where t_μ and T_B represent γ_μ and Γ_B acting in flavour space, and use the point-dependent axial rotations

$$q(y) \longrightarrow q'(y) = \exp\left[i \phi_B(y) (\gamma_5 \otimes T_B)\right] q(y)$$
$$\bar{q}(y) \longrightarrow \bar{q}'(y) = \bar{q}(y) \exp\left[i \phi_B(y) (\gamma_5 \otimes T_B)\right]. \qquad (2.96)$$

to find

$$\frac{1}{2a} \sum_\mu A^B_\mu(y) - A^B_\mu(y-\hat{\mu}) = \frac{a}{2} \sum_\mu \bar{q}(y) \left(\mathbb{1} \otimes \{t^\dagger_\mu t^\dagger_5, T_B\}\right) \delta^\mu q(y)$$
$$+ \delta^\mu \bar{q}(y) \left(\mathbb{1} \otimes \{t^\dagger_\mu t^\dagger_5, T_B\}\right) q(y)$$
$$+ 2m\, \bar{q}(y) (\gamma_5 \otimes T_B)\, q(y) \qquad (2.97)$$

In order that the current be conserved as m -> 0, we require $\{t_\mu t_5, T_B\}$ to vanish, and thus must choose $T_B = t_5$. This choice corresponds to the Goldstone boson of the spontaneously broken generator $\gamma_5 \otimes \gamma_5$. Any other choice of T_B does not give a conserved current. In other words, on the lattice at finite *a* we have one (only) Goldstone boson. Other 'pion' states will only be Goldstone-like in the continuum limit. This fact can be used to test how near the continuum limit our simulations are, as we shall show in chapter four.

2.6 Review of Lattice Hadron Mass Calculations

Hadron mass calculations on the lattice have been in progress since Hamber and Parisi first published results of a simulation on $6^3 \times 10$ and $6^3 \times 12$ lattices at $\beta = 6.0$ [Hamber and Parisi (1981)] This and other early work [Marinari et al(1981), Weingarten (1982a,b), Fucito et al. (1982), Hamber et al. (1982), Bernard et al. (1983a,1983b), Hasenfratz et al. (1982a,1982b)] provided some very encouraging results despite the smallness of the lattices and the fact that we now know they were above the deconfining transition temperature. For example, the spontaneous breaking of chiral symmetry was demonstrated, the pion was certainly the lightest hadron and other states

were well reproduced : the first reported measurement of the ρ mass [Hamber and Parisi 1981] was 800±100 MeV : and it was hoped that by moving up to larger lattices and better statistics, errors would be reduced and the spectrum described more accurately.

However, the next generation of results, on larger lattices, uncovered several problems. [Bowler et al. (1983), Gilchrist et al. (1984a,b), Lipps et al. (1983), Billoire et al. (1984a,b,1985a, Itoh et al. (1984), Bowler et al. (1984a)]. On lattices now of sizes 8^3 and 10^3 in space, finite size effects were still considerable. These were due to the fact that at the values of β chosen, the lattice size corresponded to a physical linear size of about 1fm or less. The electromagnetic radius of the proton is ~ 1.07 fm which suggests that the spatial lattice sizes were still too small. It also became apparent that the time extent of most lattices was not large enough to see true asymptotic decay of the propagators, free from contamination from radial excitations or higher excited states that were not fitted directly. This was especially true for the baryons. The measurements of the ratio of the nucleon mass to the rho mass were systematically too high - by 60% in some cases- and, perhaps most significantly, results using Wilson fermions did not agree with those using Susskind fermions. [Bowler et al. (1984a)]. In the continuum limit we certainly expect the formulations to produce the same results for the hadron masses, because, in the limit a->0 both actions reduce to the continuum QCD action. The discrepancy suggested that calculations were not being done at high enough values of β , and future calculations would need to have $\beta \gtrsim 6.0$. However, increasing β also meant moving up to even larger lattices so that the enclosed physical volume was not correspondingly decreased. The conclusions of these papers were that lattice volumes of at least 16^3 were necessary, and at least 16 units in the time direction (for non-periodic boundary conditions). [Periodic boundary conditions in time mean the propagators decay only as far as the centre if the lattice, before rising again exponentially towards the next time boundary. This reduces the effective distance over which the propagators may be fitted. If non-periodic boundary conditions such as Dirichlet , with G(t=0) = G(t=N+1) = 0, are used then the propagators will decay across the entire lattice and may be fitted over most of the timeslices (removing some near the boundaries to reduce edge effects). At present β values the boundary contaminates about four timeslices, so that for 16 or more timeslices Dirichlet boundary conditions are better than periodic. However, using periodic boundary conditions essentially doubles the

statistical sample by including the reflection in time.]

The latest results involve a variety of new techniques and can be divided into two classes :

i) *Direct Inversion of the Fermion Matrix*

This is now an enormous computational undertaking since the lattice itself contains some 65000 sites for a 16^4 lattice. Powerful computers are required as well as very efficient numerical algorithms to solve the systems of linear equations. Algorithms will be discussed in detail in chapter three. Susskind fermions are preferred now, for as well as their better chiral properties, the fermion matrix is a factor of four smaller than for Wilson fermions. It is then even more important to obtain a clean signal, by measuring over many independent configurations, so that the two parity states described in preceding sections can be 'disentangled'. At present, the only Susskind fermion results published [Barkai et al. (1985a)] apart from [Bowler et al. (1986)] are measured on only five independent gauge configurations. The direct inversion of the Wilson fermion matrix has been performed on a $16^3 \times 48$ lattice recently using a renormalisation group improved pure gauge action at a coupling corresponding to $\beta \sim 5.7$ [Itoh et al. (1986a)]. They have analysed fifteen configurations, and report being able to observe asymptotic decay of the baryon propagators on this size of lattice, which was not the case in their previous work on smaller lattices [Itoh et al. (1986b,1986c)]. They are however unable to fit directly to two independent exponentials to account for the first excited state, and fix the latter to be 500 MeV above the ground state. In chapter four, full details of a simulation on 16^4 and $16^3 \times 24$ lattices using Susskind fermions at a range of β values will be given.

ii) *Indirect Methods*

These include methods using some sort of renormalisation group blocking.

The Wuppertal group uses a 'block diagonalisation' scheme [Konig et al (1984)] which reduces the calculation to inverting an effective fermion matrix on a smaller lattice. They use Wilson fermions and work at $\beta = 6.0$ on a 16^3 spatial lattice with 56 units in the time direction. This allows 28 time steps to observe the decay of the propagators (but only seven after blocking twice) and they report [Konig et al. (1984)] being able to fit the nucleon well with only one exponential - i.e. ground state only - having sufficiently long times

to let any heavier excited states decay. However, there is as yet no test of any systematic errors the block diagonalisation scheme introduces although such a test is in progress at present on a $16^3 \times 28$ lattice. They report observing 'exceptional' configurations, which they suggest [Mutter (1986)] correspond to the fact that the quenched approximation allows large fluctuations in the eigenvalues of the fermion matrix which would be suppressed by the fermionic determinant in the full theory. They claim that three of their 28 configurations are of this type, resulting in propagators whose amplitudes and masses have large deviations from the mean. We will discuss this further in chapter four where we analyse 32 $16^3 \times 24$ configurations to look for such an effect.

A simpler scheme [Kilcup et al (1985)] has also been employed where only the gauge fields are blocked and the standard fermion matrix is inverted on the smaller blocked lattice. However the consequent systematic errors are hard to estimate and so interpretation of the results is difficult.

In summary, then, early results on small lattices produced encouraging results which led to work at higher values of β and larger lattices. Current studies are being done on spatial lattices of 16^3, with up to 56 timesteps for periodic boundary conditions in time or up to 24 timesteps for non-periodic boundary conditions at values of $\beta \gtrsim 6.0$. Current work is mainly concerned with reducing the statistical errors and understanding the systematics. It is especially important to do this in order to expose the failings of the quenched approximation : this means that errors should be controlled to the point where a clear discrepancy with the experimental masses can be established. The next generation of mass calculations will be done with dynamical simulations, and it should be known what size of effects to look for.

CHAPTER THREE

Numerical Techniques

As described in chapter two, the numerical calculation of hadron masses on the lattice can be divided into three main steps :

i) production of a set of gauge configurations with the correct statistical distribution.

ii) inversion of the fermion matrix on the gauge configurations to provide the quark propagators.

iii) averaging gauge invariant combinations of the quark propagators and fitting the averages to analytic formulae in order to extract masses.

In this chapter, we shall discuss the numerical techniques which are used in each of these steps. We will see that the best algorithm to use for the matrix inversion depends on the features of the machine being used, in this case the Distributed Array Processor (DAP), and also on the size of the lattice. Some of the features of the DAP are outlined in Appendix A. Because the matrix inversion is the most time-consuming part of the procedure, it is important to find as efficient an algorithm as possible for this, both in terms of convergence rate and of the balance between cpu time and I/O overhead. Before describing the matrix inversion algorithms and fitting routines however, let us first look at how gauge-field configurations are generated.

3.1 Monte Carlo Methods

Recall that in chapter two, we saw that the expression for the quark propagator was

$$\langle \chi \bar{\chi} \rangle = \sum_{\{C\}} \det(\not{D}+M)\left[\not{D}+M\right]^{-1} \exp - S_G(C) \qquad (3.1)$$

This is a sum over all possible configurations of gauge-field matrices U. Even if we restricted the U matrices to be members of a finite group it would

be impossible to compute this sum directly on anything but minute lattices. However, only a small subset of all the possible states contribute significantly to the expression (3.1) - the $\exp(-S_G(C))$ factor ensures that when the action is large, the contribution to the sum is exponentially small. The idea of Monte Carlo simulations is to sample the ensemble of possible U matrices with a stochastic sequence of configurations C_i, so that the probability of reaching a particular configuration C is proportional to $\exp(-S_G(C))$. This is known as importance sampling. As mentioned in chapter two, we work in the quenched approximation and set the determinant in (3.1) equal to one. We may then use

$$\langle O \rangle = \frac{1}{N} \sum_{c=1}^{N} O(C_i) \qquad (3.2)$$

to approximate the average value of O, where N should be as large as possible. We must find an algorithm for producing such a sequence.

The transition from one configuration C_i to the next one C_{i+1} can be expressed by the transition matrix $W(C_i \rightarrow C_{i+1})$ which must satisfy

$$\begin{aligned} W(C \rightarrow C') &> 0 \\ \sum W(C \rightarrow C') &= 1 \end{aligned} \qquad (3.3)$$

We will use an algorithm which attempts one link update at a time and then moves on to the next one, eventually updating all the links and thus completing one sweep through the lattice. We then really have a collection of transition matrices $W_{n\mu}$ (C->C') representing the transition $U_\mu(n) \rightarrow U'_\mu(n)$ with the other links fixed. They can obviously be combined to give a W (C->C'), in which one (or more) update attempt has been made on every link variable.

If $P(C,t_k)$ denotes the probability of configuration C at time t_k, then

$$P(C,t_k) - P(C,t_{k+1}) = \sum_{\{C'\}} w(C' \to C)\, P(C',t_k) - \sum_{\{C\}} w(C \to C')\, P(C,t_k) \qquad (3.4)$$

For systems in thermal equilibrium, we require both sides to be 0.

$$\sum_{\{C'\}} w(C' \to C)\, P(C,t_k) = \sum_{\{C'\}} w(C \to C')\, P(C,t_k) \qquad (3.5)$$

A sufficient (but not necessary) condition [Binder (1976)] is detailed balance i.e. that this equality holds term by term:

$$\frac{w(C' \to C)}{w(C \to C')} = \frac{P(C,t_k)}{P(C',t_k)} = \frac{\exp - S_G(C)}{\exp - S_G(C')} = \exp - \Delta S \qquad (3.6)$$

where

$$\Delta S = S_G(C') - S_G(C) \qquad (3.7)$$

The algorithm is thus specified by the transition probabilities between states. If we define the distance between two ensembles E and E′ as

$$\| E - E' \| = \sum_C |P(C) - P'(C)| \qquad (3.8)$$

where P(C) denotes the probability density for C in E, P′(C) the probability density for C in E′, and supposing E′ resulted from an application of our Monte-Carlo algorithm to E, then

$$P'(C') = \sum_{C'} W(C' \rightarrow C)\, P(C') \qquad (3.9)$$

and so

$$\| E' - E_{EQ} \| = \sum_{C} \left| \sum_{C'} W(C' \rightarrow C) \left[P(C') - P_{EQ}(C') \right] \right|$$

$$\leq \sum_{CC'} W(C' \rightarrow C) \left| P(C') - P_{EQ}(C') \right| \qquad (3.10)$$

$$= \| E - E_{EQ} \|$$

where E_{EQ} is the equilibrium ensemble. As long as $W(C' \rightarrow C) \neq 0$, the inequality is strict and the algorithm always moves towards equilibrium. The detailed balance condition (3.6) does not not specify completely the actual $W(C' \rightarrow C)$, and so different implementations use different forms for W. The two commonest are the Metropolis [Metropolis et al (1953)] and the Heat-Bath [Creutz (1980), Pietarinen (1981), Cabibbo and Marinari (1982)] which are equivalent for a multi-hit Metropolis where the number of hits$\rightarrow\infty$. The Heat-Bath Algorithm, used to generate the configurations in chapter four, successively touches a heat-bath to each of the links in the lattice. A real thermal source in contact with a link would cause that variable to fluctuate thermally throughout the group manifold, and when the source was removed, the link would be left in any of its allowed states with a probability given by the associated Bolzmann weight. So the algorithm replaces each group element in turn with a new value selected randomly from a set with a probability distribution proportional to $\exp(-S_G)$. The new value is thus independent of the old one, and the detailed balance condition (3.6) is obviously satisfied. The advantage of this method is that there is no possibility that the Monte-Carlo step rejects a change only because a 'bad' new candidate was selected, since all new candidate values for U_{ij} are considered simultaneously. The configurations used for measurement must be separated by many sweeps to ensure they are statistically independent. In the ideal case, our estimates for the quantity being measured by such a procedure

will have associated uncertainties of $\sim N^{-1/2}$ for a sample of size N.

3.2 Properties of the Fermion Matrix

Recall from chapter two that we may write the fermion matrix as

$$\begin{aligned} D_{nm}[U] &= 1/2\ \eta_1(n)\ [\ U_1(n)\delta_{n1+1,m1} - U_1^{\dagger}(m)\delta_{n1-1,m1}\ ]\ \delta_{n2m2}\delta_{n3m3}\delta_{n4m4} \\ &+ 1/2\ \eta_2(n)\ [\ U_2(n)\delta_{n2+1,m2} - U_2^{\dagger}(m)\delta_{n2-1,m2}\ ]\ \delta_{n1m1}\delta_{n3m3}\delta_{n4m4} \\ &+ 1/2\ \eta_3(n)\ [\ U_3(n)\delta_{n3+1,m3} - U_3^{\dagger}(m)\delta_{n3-1,m3}\ ]\ \delta_{n1m1}\delta_{n2m2}\delta_{n4m4} \\ &+ 1/2\ \eta_4(n)\ [\ U_4(n)\delta_{n4+1,m4} - U_4^{\dagger}(m)\delta_{n4-1,m4}\ ]\ \delta_{n1m1}\delta_{n2m2}\delta_{n3m3} \end{aligned} \qquad (3.11)$$

where the $U_\mu(n)$ (μ=1,4) are SU(3) matrices. With **M** = mI, the resulting formula for the quark propagator from the origin 0 to the site n is

$$\langle \chi(0)\bar{\chi}(n)\rangle = \frac{1}{Z}\int [dU]\ \det(\mathbb{D}+M)\ (\mathbb{D}+M)^{-1}_{no}\ \exp -S_G(U) \qquad (3.12)$$

As discussed in the previous chapter, in the quenched approximation the determinant term in the generating functional is neglected, and we use a Monte Carlo algorithm to generate a sequence of configurations distributed with probability $\exp(-S_G)$ so that

$$\langle \chi(0)\bar{\chi}(n)\rangle = \frac{1}{C}\sum_{i=1}^{C} [\mathbb{D}(\{U_i\})+M]^{-1}_{no} \qquad (3.13)$$

For a statistically significant estimate we should calculate $(\mathbf{D}+\mathbf{M})_{nm}^{-1}$ for many independent configurations, and for each configuration that requires solving the following system of linear equations

$$[\mathbb{D}(\{U_i\})+M]^{ac}_{nm}\ x^{c}_{m} = \delta_{no}\ \delta_{ab} \qquad b=1,2,3 \qquad (3.14)$$

where the indices a,b,c refer to colour. For each initial space-time origin 0 we calculate three columns of x, the inverse, corresponding to the three values of the colour index b. In the following sections we shall be concerned

with finding the best way to calculate x for a given configuration of U matrices.

Because the system size is so large compared to the memory of the DAP, we want to restrict the amount we store, so we choose to work in temporal gauge. Recalling from chapter one that link matrices U_{ab} on the lattice represent the gauge transformation

$$\psi_b = U_{ab}\ \psi_a \qquad (3.15)$$

where a and b are the colour labels associated with the sites at each end of the link, and that the $U = \exp(igA_\mu)$, where the A_μ are the Yang-Mills fields, we have under a point-wise gauge transformation Ω

$$U_\mu(n) \longrightarrow \Omega(n+\hat{\mu})\, U_\mu(n)\, \Omega^{-1}(n) \qquad (3.16)$$

where the $\Omega \in SU(3)$, which means $\mathrm{Tr}(U_\square)$ is gauge invariant for a closed path. In other words, lattice gauge theory is invariant under independent SU(3) rotations at each site. In particular we may choose $\Omega(n+\hat{\mu})$ to be the inverse of the time-link at site n i.e.

$$\Omega(n+\hat{\mu}) = U_4^{-1}(n) \ . \qquad (3.17)$$

and perform the transformation (3.16) on all four links there:

$$U_\mu(n) \longrightarrow U_4^{-1}(n)\, U_\mu(n)\, U_4(n-\hat{\mu}) \qquad (3.18)$$

This choice is temporal gauge where the A_0 components of the Yang-Mills fields are zero, giving us time-links equal to the identity:

$$U_4(n) \longrightarrow U_4^{-1}(n)\, U_4(n)\, \mathbb{I} \qquad (3.19)$$

$$= \mathbb{I}$$

since the time links on the previous timeslice are I. So choosing temporal gauge means we use the time-like links as transformation matrices and transform these links themselves to I (in general the links on the last timeslice will not be transformed; choosing Dirichlet boundary conditions however means we do not need these links). This has the advantage that we need not keep the time-like links any more and so have achieved a 25% saving in the amount we have to store. By also storing only two rows of the SU(3) link matrices as scaled 16 bit integers and reconstructing the third row whenever we need it we can compress the storage of the non-zero entries of **D** into 2×10^6 words of 32 bit memory on a 16^4 lattice. This is still four times the total memory of the DAP, so our system must be partitioned into blocks of manageable size which must be repeatedly paged from disk to memory while computation is proceeding. Thus we must look for algorithms with balanced computation and I/O requirements. Many of the standard algorithms for solving large systems of linear equations do not meet this criterion.

The sparse matrix (operator) **D** is not explicitly stored, instead we use the expression

$$(\mathbb{D}x)^a = \frac{1}{2}\sum_\mu \alpha_\mu(n)\left[U_\mu^{ab}(n)\,x^b(n+\hat{\mu}) - U_\mu^{\dagger ab}(n-\hat{\mu})\,x^b(n-\hat{\mu})\right] \tag{3.20}$$

to define its action on a vector x given a set of link matrices {U}. The matrix operator **D** connects a site on the lattice to each of its nearest neighbours, but there is no term from the site itself, so we can divide the lattice up into two classes of sites, even and odd [Bowler et al. (1984a)] (depending on whether $n_1+n_2+n_3+n_4$ is even or odd) in such a way that the calculation of **Dx** on even sites requires data on odd sites only (and vice versa). This allows us to split the propagator equation into two parts

$$\begin{aligned} \mathbb{D}\,x^{odd} + M\,x^{even} &= \delta^{even} \\ \mathbb{D}\,x^{even} + M\,x^{odd} &= \delta^{odd} \end{aligned} \tag{3.21}$$

where $(\mathbf{D}x_{odd})$ is a vector defined on even sites, and $(\mathbf{D}x_{even})$ is defined on odd

sites. By restricting our source term to the even sites we have

$$(-\mathbb{D}^2 + M^2)\, x^{even} = \delta^{even}$$
$$x^{odd} = \frac{-\mathbb{D}\, x^{even}}{m} \qquad (3.22)$$

where $\mathbf{D}^2 = \mathbf{D}^\dagger(\mathbf{D}x) = -\mathbf{D}(\mathbf{D}x)$, and the matrix operator $(-\mathbf{D}^2+\mathbf{M}^2)$ is hermitian and the system (3.22a) is half the size of (3.14).

A convenient partitioning of $(\mathbf{D}+\mathbf{M})$ is into 3-dimensional timeslices i.e.

$$(\mathbf{D}+\mathbf{M})^{(4)} = \begin{vmatrix} (\mathbf{D}_1+\mathbf{M})^{(3)} & \mathbf{T} & & & \\ -\mathbf{T} & (\mathbf{D}_2+\mathbf{M})^{(3)} & \mathbf{T} & & \\ & -\mathbf{T} & (\mathbf{D}_3+\mathbf{M})^{(3)} & \mathbf{T} & \\ & & \cdots\cdots\cdots & & \\ & & & -\mathbf{T} & (\mathbf{D}_{N-1}+\mathbf{M})^{(3)}\ \mathbf{T} \\ & & & & -\mathbf{T}\ (\mathbf{D}_N+\mathbf{M})^{(3)} \end{vmatrix} \qquad (3.23)$$

where $\mathbf{D}_t$ is the 3-dimensional equivalent of (3.11) (i.e. μ runs from 1 to 3) for links on timeslice t, and

$$T = \frac{1}{2}(-1)^{n_1+n_2+n_3+n_4}\, \mathbb{I} \qquad (3.24)$$

We choose boundary conditions on the quark propagator to be Dirichlet in time and anti-periodic in the spatial directions. The advantages of choosing Dirichlet boundary conditions (which set the propagator to zero on the zeroth and N_t+1^{th} timeslices) were mentioned in chapter two (2.6) and they have the additional advantage that, should subsequent work be desired on lattices with larger times, propagators may be extended using the Distant Source Method [Kenway (1985)] as discussed in section 3.7, without having to rerun the whole calculation. We will discuss the spatial boundary conditions further in chapter four.

Each of the blocks $\mathbf{D}_t$ has dimension $6N^3$ and is banded, but with a very large bandwidth due to the anti-periodic boundary conditions in space. Thus $(\mathbf{D}+\mathbf{M})$ is complex, block tridiagonal and sparse, the sum of an anti-hermitean piece and a diagonal piece. For a $16^3\times24$ lattice we must solve a system of 589,824 real linear equations.

When partitioned into timeslices $-\mathbf{D}^2$ in eq.(1.14) has the form

$$\mathbf{D}^2 = \begin{vmatrix} 1/4\mathbf{I}-\mathbf{D}_1^2 & (\mathbf{D}_2-\mathbf{D}_1)\mathbf{T} & -1/4\mathbf{I} & & & \\ (\mathbf{D}_2-\mathbf{D}_1)\mathbf{T} & 1/2\mathbf{I}-\mathbf{D}_2^2 & (\mathbf{D}_3-\mathbf{D}_2)\mathbf{T} & -1/4\mathbf{I} & & \\ -1/4\mathbf{I} & (\mathbf{D}_3-\mathbf{D}_2)\mathbf{T} & 1/2\mathbf{I}-\mathbf{D}_3^2 & (\mathbf{D}_4-\mathbf{D}_3)\mathbf{T} & -1/4\mathbf{I} & \\ \cdots\cdots & & & & & \\ & \cdots\cdots & & & & -1/4\mathbf{I} \\ & & & & 1/2\mathbf{I}-\mathbf{D}_{N-1}^2 & (\mathbf{D}_N-\mathbf{D}_{N-1})\mathbf{T} \\ & & -1/4\mathbf{I} & (\mathbf{D}_N-\mathbf{D}_{N-1})\mathbf{T} & 1/4\mathbf{I}-\mathbf{D}_N^2 & \end{vmatrix} \quad (3.25)$$

It is hermitian, positive definite and (still) very sparse. Again the operator $(-\mathbf{D}^2+\mathbf{M}^2)$ is not stored, but is built up by two applications of the rule (3.14). We will use these partitioning schemes in the following sections.

3.3 The Conjugate Gradient Algorithm.

Our starting point for solving the propagator equation (3.22) is the Conjugate Gradient (CG) Algorithm [Hestenes and Stiefel (1952)], introduced as an exact method for matrix inversion, but now established as an iterative method for solving large sparse systems of equations [Reid (1971), Concus et al (1976)]. The relation between CG and the Lanczos algorithm used by Barbour et al. [Barbour et al. (1985a)] has recently been discussed by Burkitt, who suggests they are step-by-step equivalent [Burkitt (1986)].

To solve **Ax=b** for hermitian **A**

$$
\begin{aligned}
&\text{initial guess } x_0 \\
&p_0 = r_0 = b - Ax_0 \\
&\text{loop while } (r_k,r_k) > \varepsilon \quad \text{for } k = 0,1,2,..... \\
&\qquad \alpha_k = (r_k,r_k) / (p_k,Ap_k) \\
&\qquad x_{k+1} = x_k + \alpha_k p_k \\
&\qquad r_{k+1} = r_k - \alpha_k A p_k \\
&\qquad \beta_k = (r_{k+1},r_{k+1}) / (r_k,r_k) \\
&\qquad p_{k+1} = r_{k+1} + \beta_k p_k \\
&\text{end loop}
\end{aligned}
\tag{3.26}
$$

The choice of CG as a starting point is motivated by properties of the matrix operator **D** . First we must, under all circumstances, preserve its sparsity and structure. Secondly, solutions of (3.24) will be investigated for a range of values of m for each configuration, and we are most interested in the small m region for which $(-\mathbf{D}^2+\mathbf{M}^2)$ is not diagonally dominant. In this limit CG converges significantly faster than relaxation methods [Bowler et al. (1984)].

The CG algorithm is known to converge best for matrices with clustered eigenvalues and low condition number K(**A**) which is defined, for hermitian positive definite **A** by

$$K(A) = \frac{\Lambda_{max}}{\Lambda_{min}} \tag{3.27}$$

where Λ_{max} and Λ_{min} are the highest and lowest eigenvalues of **A** respectively. Earlier work on small lattices [Barbour et al. (1985b)] has shown that the distribution of eigenvalues of **D** for an 8^4 configuration is as in fig 3.1. Let **D** have eigenvalues $i\lambda$, with λ real. The eigenvalues Λ of $(-\mathbf{D}^2+\mathbf{M}^2)$ will be λ^2+m^2. For values of m in our range of interest, $\Lambda_{max} \sim \lambda_{max} \sim 18$. When $m >> \lambda_{min}$ we have $\Lambda_{min} \sim m^2$, and the condition number will be approximately $18/m^2$. However, for very small m, it is the lowest eigenvalue λ_{min} that controls convergence and this eigenvalue is very unstable, varying by many orders of magnitude from one configuration to the next. Hence provided we do not lower m too far we would expect [Concus et al (1976)]

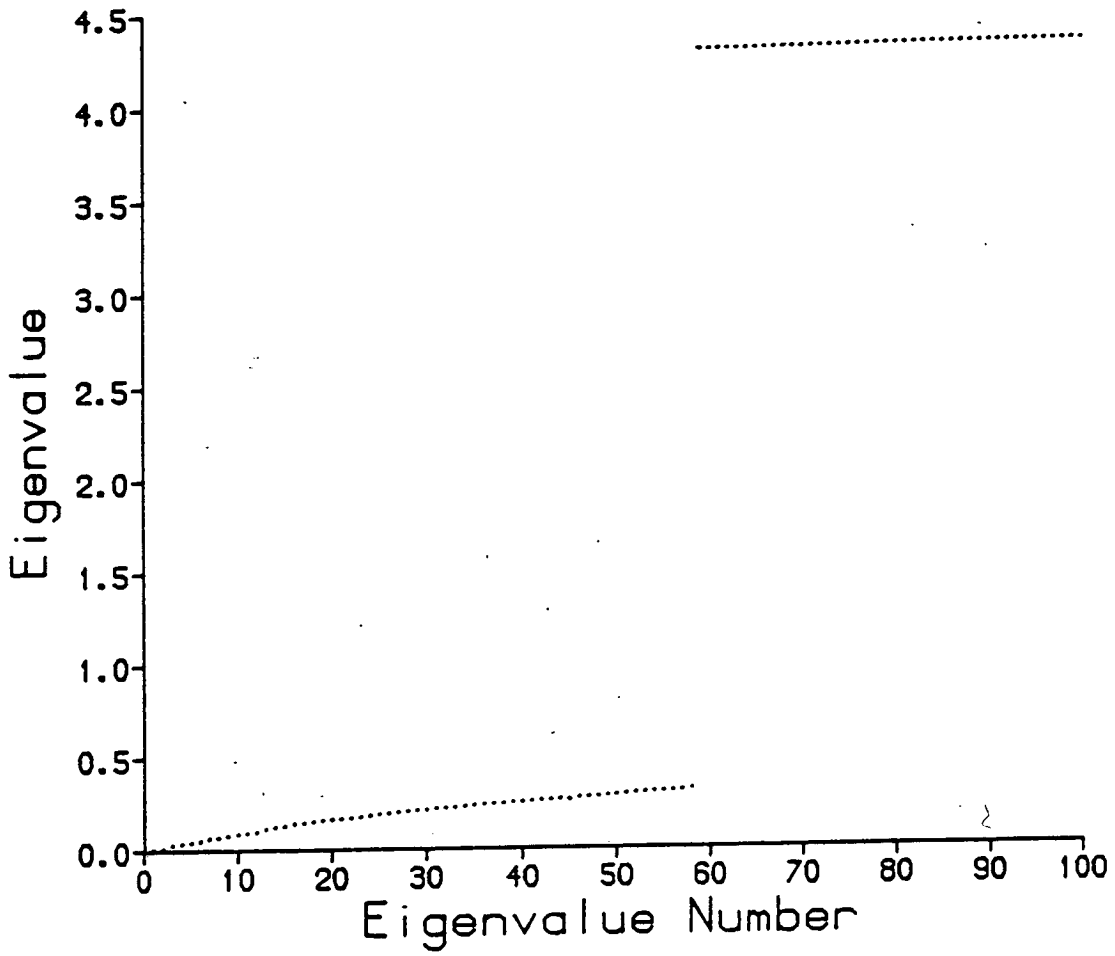

Figure 3.1 Eigenvalues of D on an 8^4 lattice multiplied by -i (the eigenvalues are pure imaginary as D is anti-hermitian). This plots the first 100 eigenvalues to converge using a Lanczos algorithm.

$$\log r_k^{\dagger} r_k \sim k \log\left(\frac{\sqrt{K}-1}{\sqrt{K}+1}\right) \sim -mk \qquad (3.28)$$

i.e. linear behaviour with m.

The CG method is implemented for lattices of size 16^4 on the DAP to solve directly (3.22). The iteration scheme is found to converge smoothly, at a rate approximately proportional to m (for $0.01<m<0.50$), up to some level determined by the precision used to do the calculation. This is shown in fig 3.2 .

The departure of r_k, the iterative residual, from $b-Ax_k$ is a sign of the onset of roundoff errors in the CG algorithm; the importance of such errors can be judged by restarting the system with x_k as the new x_0. We see a marked increase in the residual on restarting after 700 iterations in 32-bit arithmetic at m = 0.01, indicating that round-off errors have become significant. We therefore restart the solver after 500 iterations at the lowest mass and run on for a further 200 iterations, by which time the desired accuracy is achieved (see table 3.1a).

The following criteria are used to decide when to stop the iterations :

1) that baryon propagators should be unchanged in the third decimal place on all timeslices under further iterations.

2) on restarting, baryon propagators should not change and the norm of the residual vector should not increase.

3) the baryon propagator should be unchanged under a random gauge transformation of a given configuration.

Values of (r_k,r_k) sufficient for the above are in table 3.1b. Note that accuracy to 3 decimal places on the last timeslices means accuracy to 4 or 5 decimal places near the source. Some systems of equations require more frequent restarts, e.g. restarts after 50 iterations were necessary even at high mass using the Distant Source Method which is discussed in section 3.6.

The CG algorithm performs well, but is very expensive in terms of storage. Three or four vectors (see next paragraph) have to be stored per colour, each of size $3N_s^3N_t$ words, which together with the $27N_sN_t$ words of links must be paged through the machine on each iteration if the system is too big to be held in memory. This disk-to-DAP paging of timeslices is done

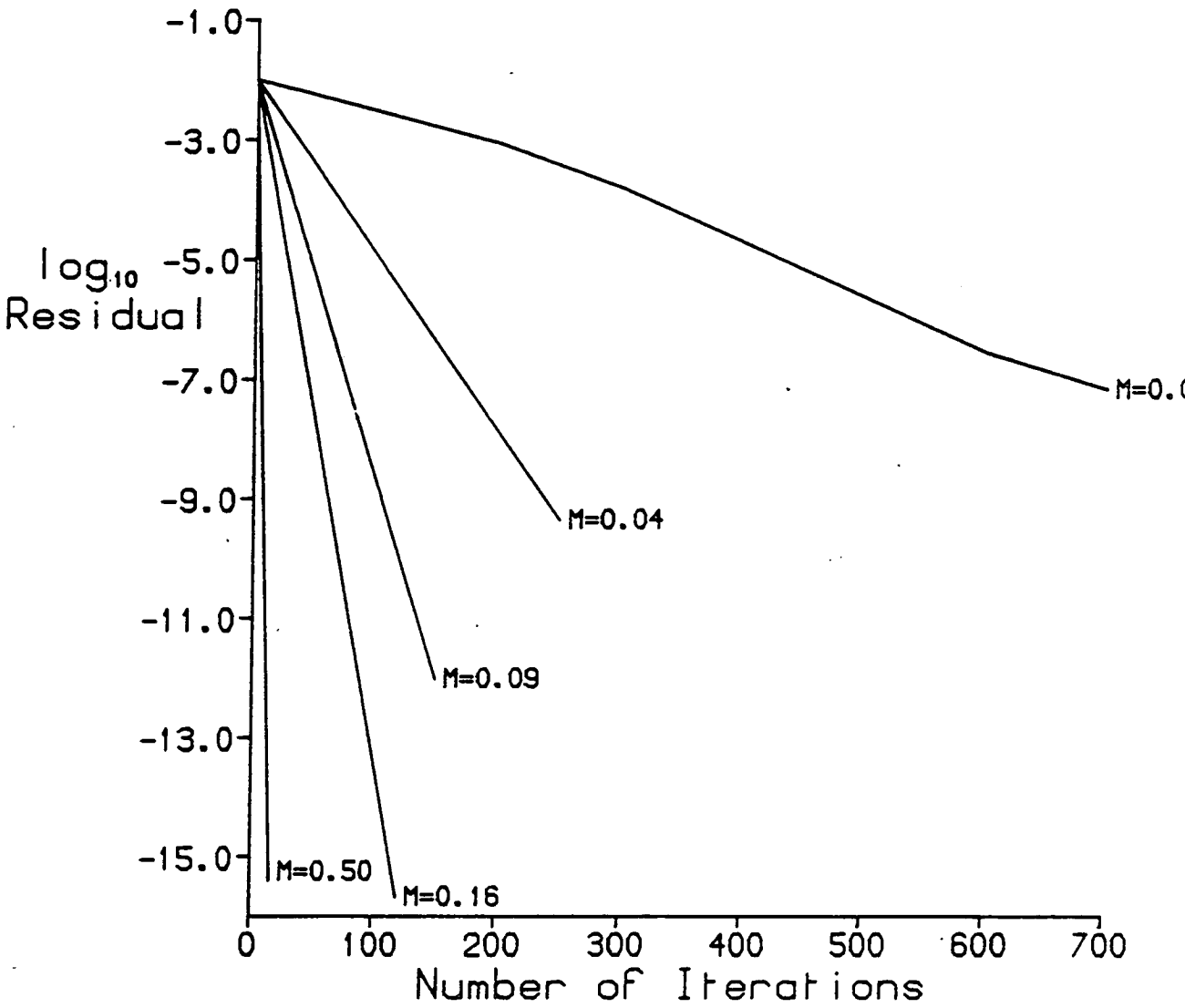

Figure 3.2 Convergence rates of the CG algorithm at the five mass values used on a 16^4 lattice.

number of sweeps	(r_k,r_k)	(r_k,r_k) on restart
100	0.285D-2	
200	0.322E-3	
300	0.406E-4	
400	0.746E-5	
500	0.771E-6	0.780E-6
600	0.903E-7	
700	0.856E-8	0.150E-7

Table 3.1a Residual measurements for CG algorithm on a 16^4 lattice, and effects of restarting. m= 0.01, β = 6.0

m	0.01	0.04	0.09	0.16	0.5
# iterations at β = 5.7	500+200	300	150	120	40
# iterations at β = 6.0	500+200	250	120	100	40
$\log_{10}(r^+ r)$	-8	-9	-12	-15	-15

Table 3.1b Convergence and stopping conditions for odd/even partitioned CG algorithm on a 16^4 lattice.

asynchronously, the links for timeslice (t+1) being paged on while those for timeslice t are being used. The DAP data expansion software, DDX, enables variables held in COMMON areas to be transferred between DAP and disk in parallel with computation.

The CG vectors can only be updated when calculations of the scalars α and β in (3.26) are complete. Barkai et al. (1985b) have proposed a modified CG algorithm which avoids some of the synchronisation problems at the expense of an extra vector. However, because of the DAP's low I/O rate (approximately 250-300 Kbytes/sec compared to a floating-point performance of around 15 Mflops) the matrix multiply step $q_k = \mathbf{A}x_k$ is I/O bound by itself, and so we use the standard algorithm for a hermitian matrix.

The total connect time for a CG propagator calculation running on the DAP is a factor of six longer than the processor time used. Similar I/O stretch factors have been found in other work on a Cyber 205 [Barkai et al (1985)]. The total elapsed time per colour iteration is 48 seconds whereas the cpu time is 8 seconds. The algorithm uses 15 seconds of I/O time per iteration to bring in the links and 30 seconds to bring in the vectors, with a combined I/O overhead of 40 seconds. Almost all the DAP cpu time is used applying the **D** operators, as the cpu time for updating the vectors is insignificant.

The results at β = 5.7 and 6.0 on 16^4 lattices, discussed in chapter four, were generated using the Conjugate Gradient algorithm. However, the method is only really practical for propagator calculations when either (i) the system of equations is small enough to fit within the machine's fast memory, or (ii) the disk-to-fast-memory bandwidth is sufficiently high to keep the processor(s) going all of the time. Systems of equations satisfying (i) are not usually large enough to be of physical significance and machines satisfying (ii) are not widely available. Since we want larger lattices in order to explore the approach to the continuum limit, new algorithms that do not require large numbers of vectors and that use many more floating-point operations per word of I/O transfer would be of great importance.

3.4. Block Gauss Elimination

Bowler et al. (1984b), have proposed that Gauss Elimination be used on the blocks of the matrix $(\mathbf{D}+\mathbf{M})^{(4)}$ for the interacting theory (see eq.(3.23)):

$$\begin{vmatrix} (D_1+M)^{(3)} & T & & & \\ -T & (D_2+M)^{(3)} & T & & \\ & -T & (D_3+M)^{(3)} & T & \\ & & \cdots & \cdots & \cdots \\ & & & -T & (D_N+M)^{(3)} \end{vmatrix} \begin{vmatrix} x_1 \\ x_2 \\ x_3 \\ \cdots \\ x_N \end{vmatrix} = \begin{vmatrix} \delta_1 \\ \delta_2 \\ \delta_3 \\ \cdots \\ \delta_N \end{vmatrix} \qquad (3.29)$$

Consider the first two rows of this operator. Let $P_0 = I$ and $P_1 = 4(D_1+M)T$, and adding row one to P_1.(row two) we obtain

$$\begin{vmatrix} P_1 T & P_0 T & 0 & 0 & \cdots \\ 0 & P_1(D_2+M) + P_0 T & P_1 T & 0 & \cdots \end{vmatrix} \qquad (3.30)$$

Now let $P_2T = P_1(D_2+M) + P_0T$ so that $P_2 = 4P_1(D_2+M)T + P_0$ as $4T^2 = I$. Continuing the process until all the blocks in the lower triangle have been eliminated, we obtain

$$\begin{bmatrix} P_1 T & P_0 T & 0 & \cdots & & 0 \\ 0 & P_2 T & P_1 T & 0 & \cdots & \\ 0 & 0 & P_3 T & P_2 T & 0 & \cdots \\ & & \ddots & \ddots & \ddots & \\ & & & & & 0 \\ \vdots & & & & P_{N-1}T & P_{N-2}T \\ 0 & \cdots & & & 0 & P_N T \end{bmatrix} \begin{bmatrix} x_1 \\ \vdots \\ x_N \end{bmatrix} = \begin{bmatrix} c_1 \\ \vdots \\ c_N \end{bmatrix} \qquad (3.31)$$

where

$$P_t = P_{t-2} + 4P_{t-1}(D_t+M)T \qquad (3.32)$$

and $c_N = 4T\delta_1 + 4P_1T\delta_2 + \cdots 4P_{N-1}T\delta_N$

For a delta function source on timeslice t :

$$\delta_{t'} = \delta_{no} \quad \text{for } t = t' \text{ and } c_N = P_{t-1}\delta_t \qquad (3.33)$$
$$0 \quad \text{otherwise}$$

So, the forward elimination step requires that we solve

$$(P_N T)x_N = c_N \qquad (3.34)$$

x_N is the propagator from the origin to timeslice N, and its calculation is the only non-trivial matrix inversion. Consequently the size of the system of equations that must be solved is reduced by a factor of N, and the resulting system, with 24,576 real linear equations rather than 589,824, might be expected to be easier to invert.

Having solved for x_N, we obtain x_t for $1<t<N$ by back substitution :

$$x_t = -4T\delta_{t'+1} + 4T(D_{t+1} + M)^{(3)} x_{t+1} + x_{t+2} \qquad (3.35)$$

setting $x_{N+1} = 0$.

However, P_N involves all N timeslices, so we must bring the complete set of links through the machine (twice) per iteration of the Bi-Conjugate Gradient algorithm. These transfers are done asynchronously. The stretch factor is of order 2.

When this reduced inversion scheme for the interacting theory was tested at high quark mass (m = 0.5) convergence rates in line with those predicted by Bowler et al. (1984b)were obtained, and pion propagators were consistent with previous results. But when the quark mass was lowered, convergence rates dropped dramatically and pion masses calculated from apparently converged quark propagators were clearly incorrect. At a quark mass of 0.01 the propagator still had not converged after 10,000 sweeps on a $16^3 \times 8$ system (see fig 3.3).

There are two main reasons why the method does not converge :

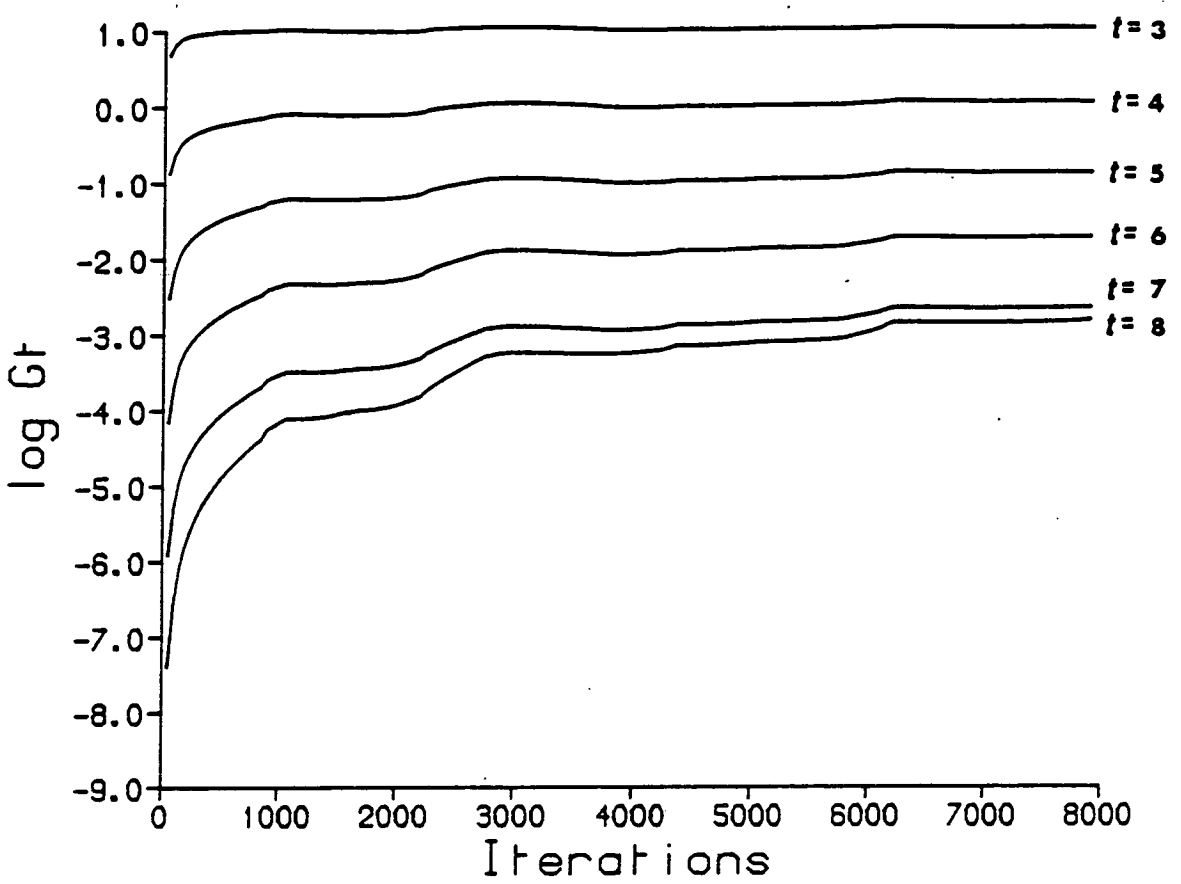

Figure 3.3 Convergence of the pion propagator signal using the block Gauss Elimination algorithm. 8000 iterations on a $16^3 \times 8$ lattice at m=0.01.

i) The operator P_N, although of dimension 24,576 rather than 589,824, is a fully dense matrix, containing terms linking each site of the 16^3 spatial lattice to every other site. It is only diagonally dominant at very high m.

ii) The projection mechanism (3.35) for obtaining x_t on timeslices 1 to N-1 amplifies exponentially any errors present in the solution x_N. In fact the propagator on timeslice N is always the last to converge and so using it as a basis for obtaining x_t for $1<t<N$ is unsound.

To confirm these conclusions let us look at the free fermion data of Bowler et al. for a 16^4 lattice. Here we find the convergence of the propagators to be qualitatively the same, but on a much shorter timescale (see fig 3.4). Pion propagators, given by

$$\langle \pi(0)\,\pi(n)\rangle = \sum_{\underline{n}} |\langle \chi(0)\,\bar{\chi}(n)\rangle|^2 \qquad (3.36)$$

are stable and apparently converged to five or more decimal places for large numbers of iterations : for free fermions, 50 out of a total of 100; for a random gauge transformation of the free (unit) configuration 500 out of a total of 1500 (the disparity in the rates of convergence for these two gauge-equivalent configurations is only observed for this algorithm). The propagators then undergo changes of several orders of magnitude before converging to the analytic result. This seems to indicate that the algorithm is losing track of the long range structure in time of the propagators.

We must therefore conclude that Block Gauss Elimination is intrinsically unreliable; without knowing the answer in advance, it is difficult to know when to stop the iterations when the convergence pattern is like that in fig 3.4. Consequently we cannot use it to produce hadron propagators.

We would like to be able to retain some of the features of this algorithm - in particular, solution of small systems of linear equations (preferably for diagonally dominant matrix operators). But we require a scheme in which an approximation to the correct long range structure of the propagator is obtained quickly. Such a method ,which works well, is discussed in the next section.

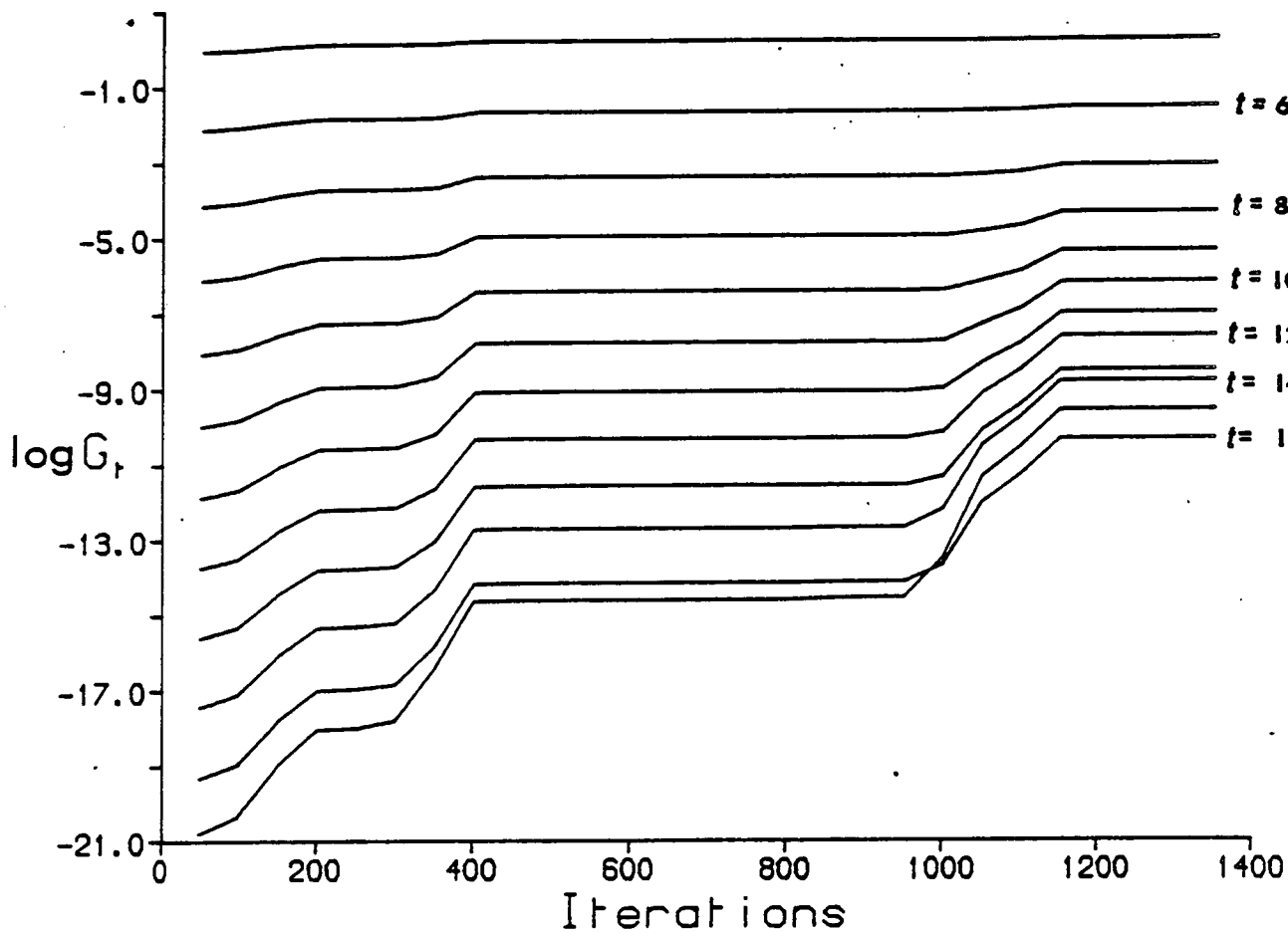

Figure 3.4 Convergence of the free pion propagator signal using block Gauss Elimination. 1400 iterations on a 16^4 lattice at m=0.01

3.5 Block Iterative Methods

Consider the partitioning scheme for (**D**+**M**) in temporal gauge (eq.(3.23)) We can define a Block-Iterative algorithm based on Successive Over-Relaxation (SOR) by regarding each $3N^3$ x $3N^3$ complex block as a component of an N x N linear system of equations. To do this, multiplication is replaced by block matrix-vector products, and division by the solution of a $3N^3$ system of equations.

Then the Iterative Block SOR scheme for solving

$$\begin{vmatrix} (\mathbf{D}_1+\mathbf{M})^{(3)} & \mathbf{T} & & & \\ -\mathbf{T} & (\mathbf{D}_2+\mathbf{M})^{(3)} & \mathbf{T} & & \\ & -\mathbf{T} & (\mathbf{D}_3+\mathbf{M})^{(3)} & \mathbf{T} & \\ & & \cdots & \cdots & \\ & & & -\mathbf{T} & (\mathbf{D}_{N-1}+\mathbf{M})^{(3)} \; \mathbf{T} \\ & & & & -\mathbf{T} \; (\mathbf{D}_N+\mathbf{M})^{(3)} \end{vmatrix} \begin{vmatrix} x_1 \\ x_2 \\ x_3 \\ \cdots \\ x_{N-1} \\ x_N \end{vmatrix} = \begin{vmatrix} \delta_1 \\ \delta_2 \\ \delta_3 \\ \cdots \\ \delta_{N-1} \\ \delta_N \end{vmatrix} \qquad (3.37)$$

is

$$(\mathbb{D}_t+M)\,x_t^{(k+1)} = \omega\left(\delta_t + T\,x_{t-1}^{(k+1)} - T\,x_{t+1}^{(k)}\right) + (1-\omega)\left(\mathbb{D}_t+M\right)x_t^{(k)} \qquad (3.38)$$

where the parameter ω is selected for optimum convergence. We can generalise this to the solution of $(-\mathbf{D}^2+\mathbf{M}^2)x = \delta$ by analogy with 3.25 as follows

$$\begin{aligned} (C-\mathbb{D}^2+M^2)\,x_t^{k+1} &= \beta_t \\ &= \omega\left(\delta_t + \tfrac{1}{4}\,x_{t-2}^{(k+1)} + (\mathbb{D}_{t-1}-\mathbb{D}_t)\,T\,x_{t-1}^{(k+1)}\right. \\ &\quad \left. +(\mathbb{D}_t-\mathbb{D}_{t+1})\,T\,x_{t+1}^{k} + \tfrac{1}{4}\,x_{t+2}^{k}\right) \\ &\quad +(1-\omega)\left(C-\mathbb{D}^2+M^2\right)x_t^{(k)} \end{aligned} \qquad (3.39)$$

where $\mathbf{C}=c\mathbf{I}$.

Working with $\mathbf{D}^2$ reduces the system size by a factor of 2, but requires the use of three sets of links and 5 timeslices of the vector to accumulate β_t. The method can be used for any choice of temporal boundary conditions ; for our choice of Dirichlet boundary conditions, c = 1/4 for x_1 and x_N, and terms on the right-hand side of (3.39) with $t<1$ or $t>N$ are dropped. If we wished to use periodic boundary conditions, we would set c = 1/2 and identify x_0 with x_{N+1}.

We use a Conjugate Gradient algorithm to do the 'divisions' by $(\mathbf{C}-\mathbf{D}^2+\mathbf{M}^2)$: these systems are quite small, a factor of N down on the full system, and diagonally dominant for all values of m, so a CG algorithm is fast and involves no I/O problems.

We might think that this Block SOR scheme would require a huge amount of work, to invert exactly N systems of size $3N^3$ per sweep, but this is not the case. β (the RHS of (3.39)) is accumulated from terms on 5 timeslices and if we assume that the algorithm converges then the error on 3 of these timeslices x_t, x_{t+1}, x_{t+2} is greater than that on the other two x_{t-2}, x_{t-1}. So we should aim to converge the (k+1)'th iterate on timeslice t to a level where the residual on this timeslice is some factor lower than that on (t-1). We should not run the inversion so long that we do work which will be wasted on the next sweep, when x_{t+1} and x_{t+2} have also been upgraded. This fits in with our aim of producing a balanced or cpu-dominated program, if we can do the necessary iterations in the time taken to page out x_{t-2} and page in x_{t+3} and the next set of links. This is the case.

We must tune ω for optimum convergence and determine whether this tuning depends upon our choice of configuration - if it does then the algorithm will be useless as we must calculate propagators on large numbers of configurations. Tuning the parameter ω for mass values 0.50, 0.16, 0.09, 0.04 and 0.01, it turns out that quark mass is the only significant dependent variable. ω is independent of N ($8<N<32$) and does not need re-tuning from one configuration to the next. When we change β (in the small range explored) only slight adjustments are necessary. The range of acceptable ω values narrows with decreasing mass. The values of ω used are shown below.

m	0.50	0.16	0.09	0.04	0.01
ω	1.25	1.55	1.70	1.88	1.955

Fig 3.5 illustrates the variation of the rate of convergence with mass and the slight dependence on configuration (at the lightest mass). The attainable residuals $|b-Ax|^2$ are limited by the precision to which we store the propagator as shown in the first column of table 3.2a. But because the calculation of β is limited to a range of five timeslices and there are no global scalars to be accumulated, the timesliced residual falls off exponentially away from the source, at approximately the same rate as the propagator. We can see this from table 3.2 and fig 3.6. The source term is seen by the algorithm on every sweep, so there is no roundoff-error-induced cumulative drift of the propagator from the correct solution.

The variation of convergence rate with the number of sub-block CG iterations is shown in fig 3.7 for a mass of 0.04. Eight iterations of the CG inverter are more than sufficient at all the mass values. This can be traced to $c>1/4$ in the LHS of (3.39) which guarantees diagonal dominance of the sub-blocks.

32-bit arithmetic is sufficient to converge all our propagators for M=0.01,...,0.50 on a 16^3 x 24 lattice, and the convergence rate is independent of N (for $8<N<32$) . The behaviour of the timesliced residual shown in fig 3.6 is a feature of all mass values.

The algorithm was tested by measuring the number of sweeps necessary to obtain agreement between hadron propagators calculated using the CG algorithm and those obtained using the Iterative Block SOR method. In both cases convergence of the propagators was required on the last timeslice to 3 significant figures (this gives 4 or 5 significant figures near the source) and the results agreed to this accuracy.

When 6 or 8 iterations of the block inverter are used per sweep we find that our stretch factor is 1.02 (compared with about 6 for the full CG algorithm) The time taken to produce a set of 16^4 propagators drops by a factor of around 3.. For a 16^3 x 24 or larger lattice we gain a factor of

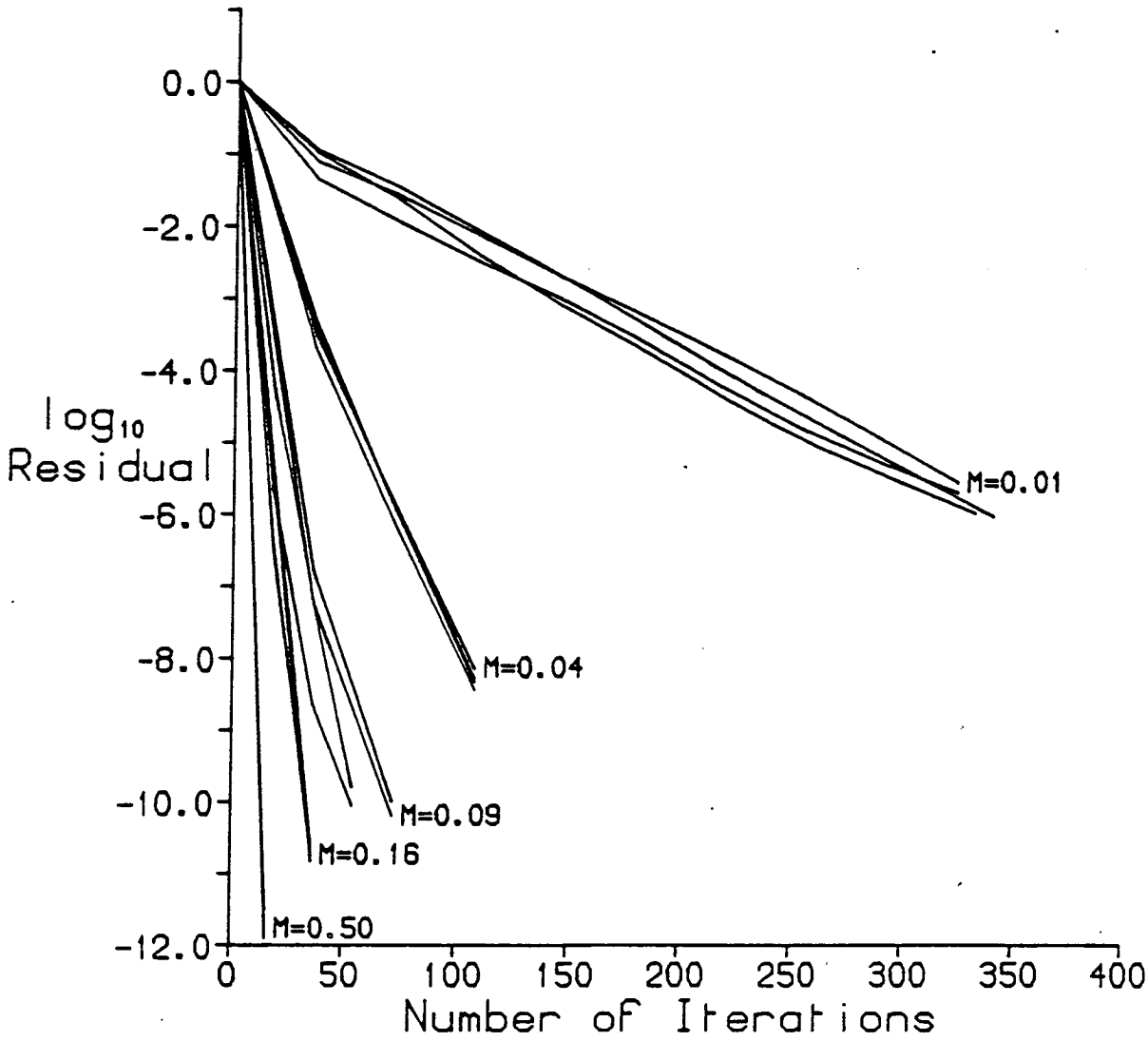

Figure 3.5 Rate of convergence of the block SOR algorithm, showing dependence on mass. $16^3 \times 24$ lattice.

		Limiting Residuals	Timesliced Residuals		
Free Fermions			t_0	t_0+10	
16^4	32 bit	0.14×10^{-13}	0.13×10^{-13}	0.92×10^{-18}	
	64 bit	0.20×10^{-30}	0.18×10^{-30}	0.15×10^{-35}	
Interacting Fermions			t_0+5	t_0+10	t_0+15
$16^3\times24$	m=0.01	0.1×10^{-8}	0.68×10^{-10}	0.35×10^{-10}	0.19×10^{-10}
32 bit	m=0.09	0.3×10^{-10}	0.54×10^{-12}	0.22×10^{-13}	0.10×10^{-14}
	m=0.50	0.1×10^{-12}	0.38×10^{-15}	0.19×10^{-18}	0.86×10^{-22}

Table 3.2a Limiting residuals for block SOR algorithm.

m	0.01	0.04	0.09	0.16	0.5
CG iterations	8	6	6	6	6
SOR iterations	350	105	70	35	15
$\log_{10}(r^+ r)$	-8	-9	-10	-12	-12

Table 3.2b Convergence of block SOR algorithm for a $16^4\times24$ lattice.

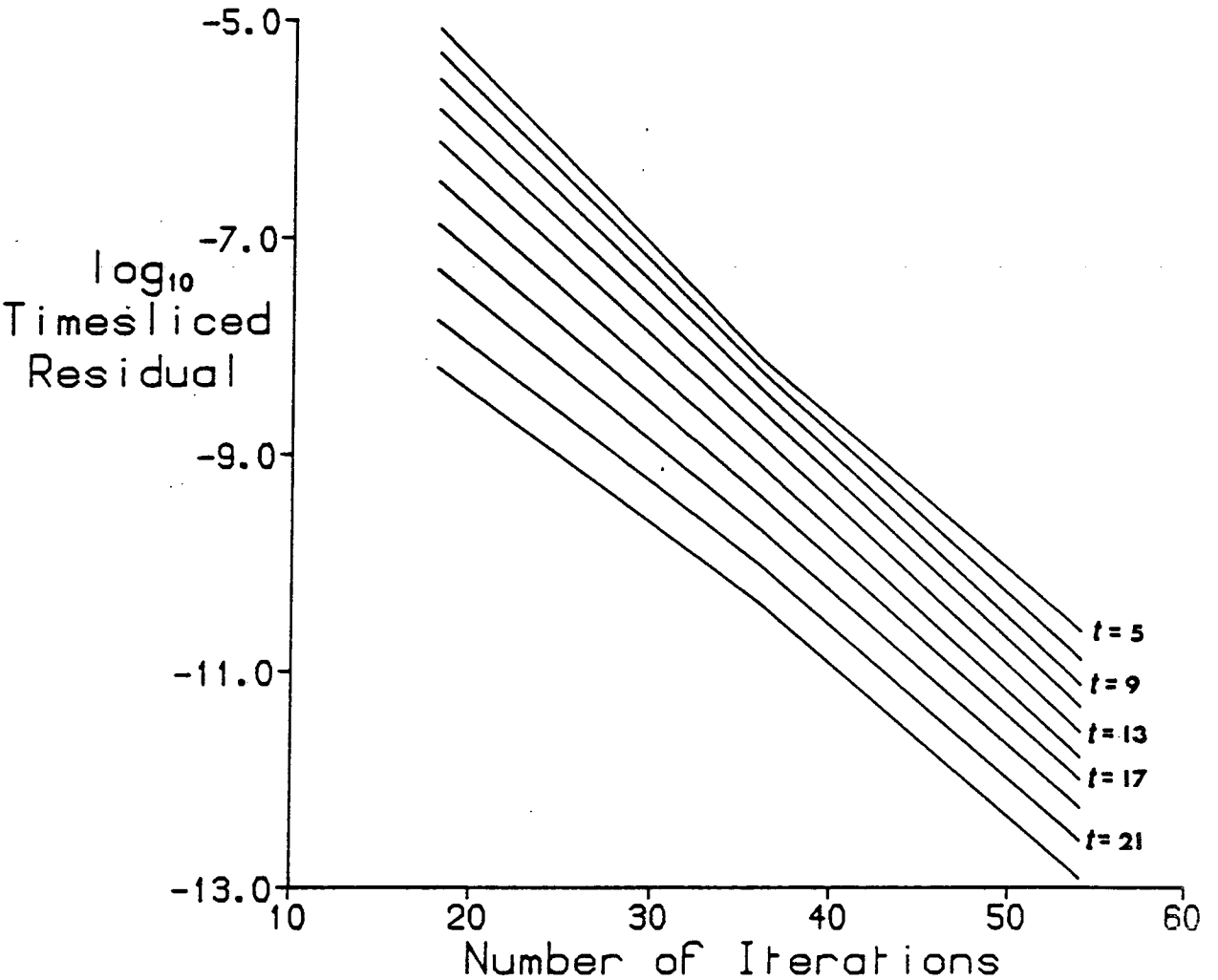

Figure 3.6 Timeslice residuals for the block SOR algorithm on a $16^3 \times 24$ lattice at m=0.09. The figure shows $t_0, t_{0+2} \ldots\ldots t_{0+18}$

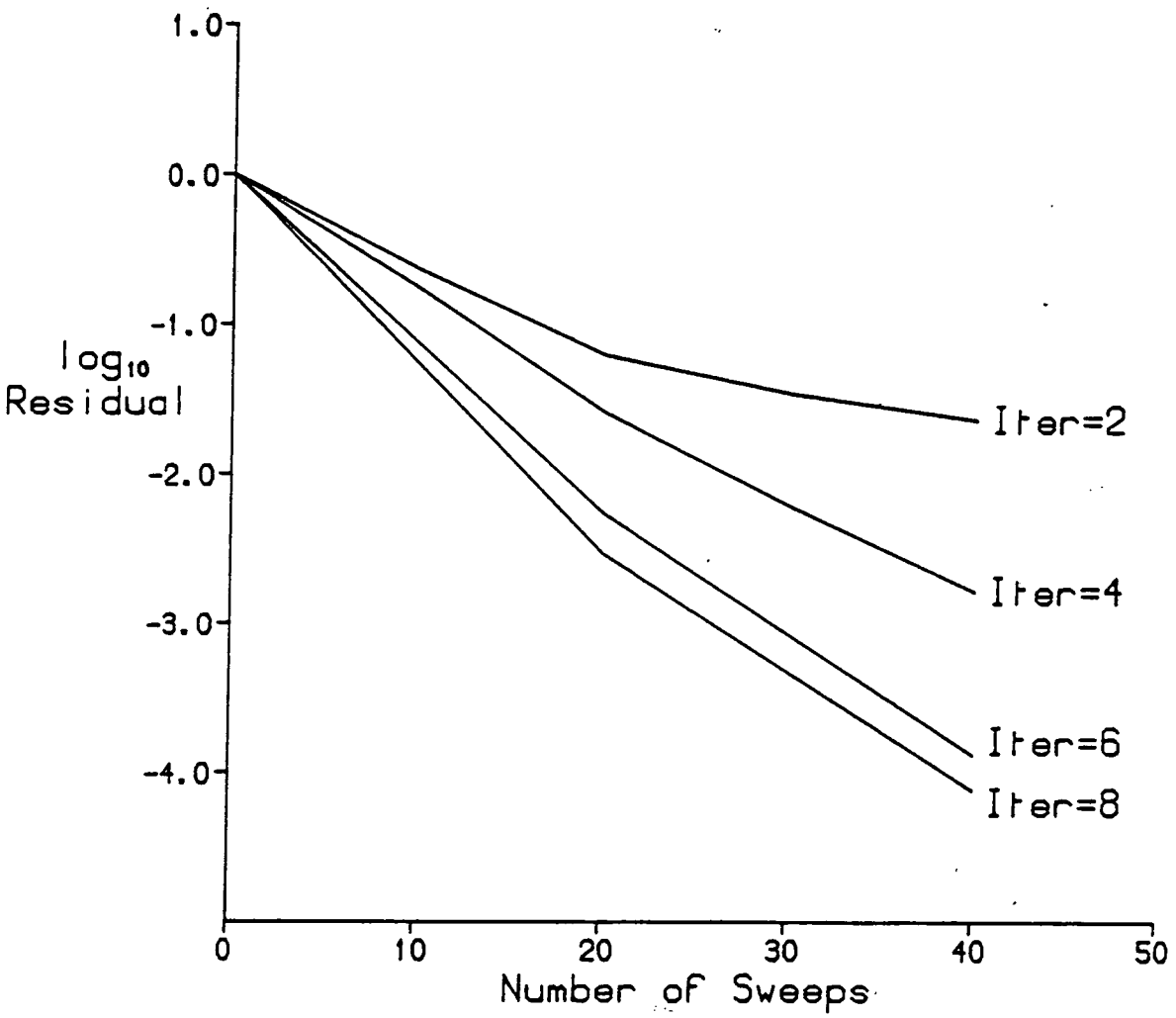

Figure 3.7 Dependence of the convergence rate of block SOR on the number of CG inversion steps. $16^3 \times 24$ lattice at m = 0.04

between 5 and 7 on the CG method, increasing with mass.

3.6 The Distant Source Method.

The Distant Source Method [Kenway (1985)] uses small lattices to calculate the propagator on larger lattices. This is potentially very useful because we are able to alleviate some of the constraints imposed by limited computer memory and speed. This is because we need less data per computation, and also because numerical algorithms tend to converge faster for smaller systems.

If we look again at (3.29) we see that it can be written

$$\begin{vmatrix} (D_1+M)^{(3)} & T & & & & \\ -T & (D_2+M)^{(3)} & T & & & \\ & -T & (D_3+M)^{(3)} & T & & \\ & & \cdots & \cdots & \cdots & \\ & & & -T & (D_{N-1}+M)^{(3)} & T \\ & & & & -T & (D_N+M)^{(3)} \end{vmatrix} \begin{vmatrix} x_1 \\ x_2 \\ x_3 \\ \cdots \\ x_{N-1} \\ x_N \end{vmatrix} = \begin{vmatrix} \delta_1 \\ \delta_2 \\ \delta_3 \\ \cdots \\ \delta_{N-1} \\ \delta_N \end{vmatrix} \qquad (3.40)$$

We have put the source on one of the first J timeslices. With

$$\Delta_{11} = \begin{pmatrix} D_1+M & T & 0 & \cdots & 0 \\ -T & & & & \vdots \\ 0 & & & & \\ \vdots & & & & 0 \\ & & & & T \\ 0 & \cdots & 0 & -T & D_J+M \end{pmatrix} \quad \Delta_{12} = \begin{pmatrix} 0 & \cdots & \cdots & \cdots & 0 \\ \vdots & & & & \vdots \\ & & & & \\ 0 & & & & \\ T & 0 & \cdots & \cdots & 0 \end{pmatrix}$$

$$\Delta_{21} = \begin{pmatrix} 0 & \cdots & \cdots & 0 & -T \\ \vdots & & & & 0 \\ & & & & \vdots \\ 0 & \cdots & \cdots & \cdots & 0 \end{pmatrix} \quad \Delta_{22} = \begin{pmatrix} D_{N-J}+M & T & 0 & \cdots & 0 \\ -T & & & & \vdots \\ 0 & & & & 0 \\ \vdots & & & & T \\ 0 & \cdots & 0 & -T & D_N+M \end{pmatrix} \qquad (3.41)$$

where Δ_{11} is J×J and Δ_{22} is N−J×N−J, and $\underline{x}^T = (x_1,\ldots..x_J)$, $\underline{y}^T = (x_{J+1},\ldots..x_N)$ we

then have

$$\begin{aligned} \Delta_{11}\,\underline{x} + \Delta_{12}\,\underline{y} &= \underline{\delta} \\ \Delta_{21}\,\underline{x} + \Delta_{22}\,\underline{y} &= \underline{0} \end{aligned} \qquad (3.42)$$

Assuming we know, $x_1,\ldots x_J$ from a previous calculation, we may solve for $\underline{y}$ since

$$\Delta_{22}\,\underline{y} = -\Delta_{21}\,\underline{x} = T \begin{bmatrix} x_J \\ 0 \\ \vdots \\ 0 \end{bmatrix} \qquad (3.43)$$

and this is similar to the system of (3.40) but with Tx_J used as the source. We could also divide (3.39) into more than two sets of blocks, in an obvious way. In practice it is necessary to perform the first calculation on a larger lattice than J^4 because the estimate for x_J computed on a J^4 lattice would be contaminated by (time) boundary effects, and so would be a bad choice for the source on the next computation. Thus we take x_J to be well away from the time boundary on the first lattice. For example, with N = 24 and J = 8, we calculate x_8 on a 16^4 lattice, and use Tx_8 as the new source for a calculation on timeslices 9 - 24. A schematic picture of this is shown in fig (3.8).

If we look at table 3.3 we see this method accurately reproduces the analytic results in the free fermion case, at mass of 0.2. Tables 3.4a-d show the results in the interacting case, for a range of mass values. This analysis was done on four configurations, each separated by 1792 sweeps. The Distant Source Method and the Iterative Block SOR were used to invert the fermion matrix, and both sets of results are given for comparison. The algorithm used to invert the 16^4 blocks in the DSM was the Conjugate Gradient, but any algorithm could have been used. At the second stage of the DSM calculation in which a 16^4 propagator is extended to a $16^3\times24$ propagator, the CG algorithm converges more slowly than for the original 16^4 calculation. The iteratively computed residual departs significantly from the actual residual at all mass values, probably due to rounding errors, and it proves necessary to counter this by restarting the CG calculation, as shown in table 3.5, using the latest approximation for the quark propagator as the first guess.

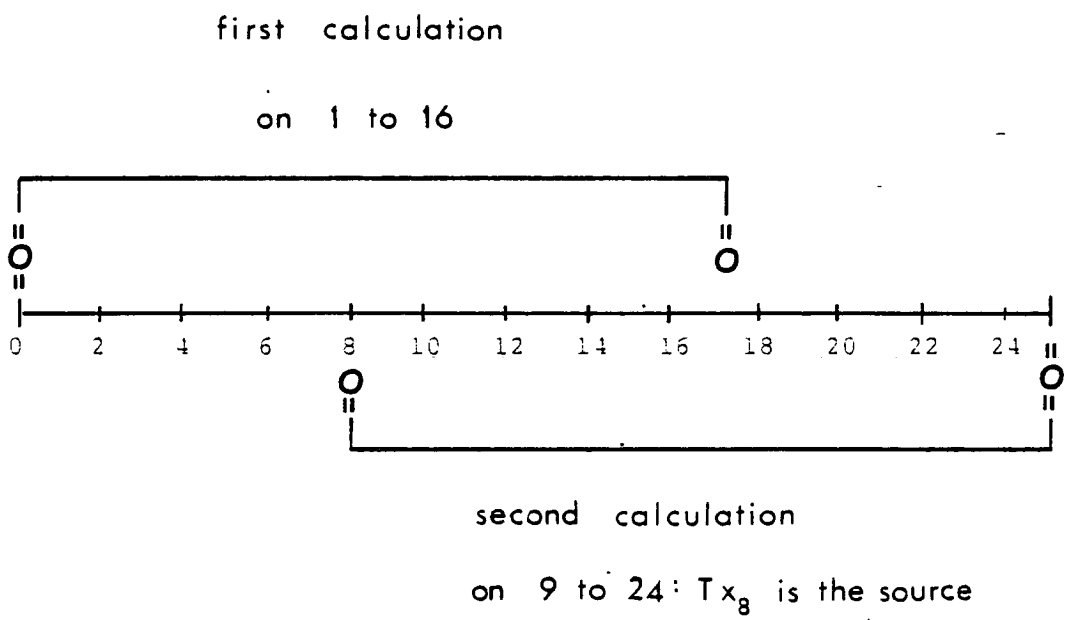

Figure 3.8 Distant Source Method of obtaining $16^3 \times 24$ propagators by calculating on 16^4 lattices

Time	P_{OSM}	$P_{OSM}-P_{anal}$	m_{OSM}	m_{anal}
4	0.41870413E+00	0.00005153E+00	0.18392778E+01	0.18395107E+01
5	0.66545557E-01	0.00023691E-01	0.16280057E+01	0.16284845E+01
6	0.13064271E-01	0.00010903E-01	0.13846450E+01	0.13853500E+01
7	0.32714591E-02	0.00050338E-02	0.11629143E+01	0.11636551E+01
8	0.10225728E-02	0.00023295E-02	0.10026244E+01	0.10032256E+01
9	0.37519753E-03	0.00107971E-03	0.90347962E+00	0.90389831E+00
10	0.15201406E-03	0.00050090E-03	0.84624955E+00	0.84652074E+00
11	0.65217215E-04	0.00232523E-04	0.81361177E+00	0.81378231E+00
12	0.28907807E-04	0.00107978E-04	0.79476142E+00	0.79486765E+00
13	0.13057338E-04	0.00050154E-04	0.78366352E+00	0.78372960E+00
14	0.59636741E-05	0.00232996E-05	0.77702207E+00	0.77706322E+00
15	0.27419372E-05	0.00108249E-05	0.77297678E+00	0.77300247E+00
16	0.12657792E-05	0.00050295E-05	0.77051987E+00	0.77053596E+00
17	0.58576771E-06	0.00233694E-06	0.76894456E+00	0.76895465E+00
18	0.27150451E-06	0.00108590E-06	0.76808517E+00	0.76809153E+00
19	0.12595108E-06	0.00050454E-06	0.76728848E+00	0.76729245E+00
20	0.58475338E-07	0.00234477E-07	0.76734971E+00	0.76735223E+00
21	0.27146697E-07	0.00108922E-07	0.76618079E+00	0.76618238E+00
22	0.12617372E-07	0.00050645E-07	0.76804617E+00	0.76804713E+00
23	0.58534336E-08	0.00235010E-08	0.76362213E+00	0.76362276E+00
24	0.27275569E-08	0.00109526E-08	0.77289031E+00	0.77289073E+00
25	0.12592496E-08	0.00050570E-08	0.75279989E+00	0.75280013E+00
26	0.59316427E-09	0.00238226E-09	0.79602726E+00	0.79602739E+00
27	0.26758683E-09	0.00107471E-09	0.70334800E+00	0.70334812E+00
28	0.13243555E-09	0.00053191E-09	0.90478560E+00	0.90478566E+00
29	0.53587215E-10	0.00215233E-10	0.47972209E+00	0.47972216E+00
30	0.33168095E-10	0.00133222E-10	0.14441381E+01	0.14441381E+01
31	0.78259907E-11	0.00314335E-11	-.48332620E+00	-.48332615E+00
32	0.12689521E-10	0.00050968E-10		

Table 3.3 Timeslice propagator and effective mass for the PS meson composed of free fermions, computed using the DSM on a $16^3 \times 32$ lattice compared with the analytic result. Here timeslice 4 is the source, and m = 0.02.

Quark mass = 0.09			
Time	DSM PS	IBSOR PS	CG 16^4 PS
1	0.8288E-01	0.8291E-01	0.8288E-01
2	0.1014E+00	0.1014E+00	0.1014E+00
3	0.3033E+00	0.3033E+00	0.3033E+00
4	0.8493E+00	0.8493E+00	0.8493E+00
5	0.2724E+01	0.2725E+01	0.2724E+01
6	0.8355E+00	0.8355E+00	0.8355E+00
7	0.2994E+00	0.2995E+00	0.2994E+00
8	0.1115E+00	0.1115E+00	0.1115E+00
9	0.4570E-01	0.4576E-01	0.4570E-01
10	0.1939E-01	0.1951E-01	0.1957E-01
11	0.8733E-02	0.8595E-02	0.8534E-02
12	0.3987E-02	0.3971E-02	0.4049E-02
13	0.1894E-02	0.1884E-02	0.1815E-02
14	0.9092E-03	0.9039E-03	0.1009E-02
15	0.4493E-03	0.4463E-03	0.3777E-03
16	0.2155E-03	0.2140E-03	0.3779E-03
17	0.1030E-03	0.1022E-03	
18	0.5022E-04	0.4981E-04	
19	0.2414E-04	0.2394E-04	
20	0.1176E-04	0.1166E-04	
21	0.5239E-05	0.5193E-05	
22	0.2975E-05	0.2948E-05	
23	0.1101E-05	0.1091E-05	
24	0.1120E-05	0.1109E-05	

Table 3.4a Results from one configuration, comparing the pseudoscalar propagator using the Distant Source method (DS) and the Iterative Block SOR (IBSOR) on a $16^3 \times 24$ lattice and the Conjugate Gradient on a 16^4 lattice.

Quark mass = 0.09			
Time	DSM VT	IBSOR VT	CG 16^4 VT
1	0.2907E-01	0.2909E-01	0.2907E-01
2	0.4892E-01	0.4887E-01	0.4892E-01
3	0.1386E+00	0.1386E+00	0.1386E+00
4	0.6683E+00	0.6683E+00	0.6683E+00
5	0.2114E+01	0.2114E+01	0.2114E+01
6	0.8791E+00	0.8790E+00	0.8791E+00
7	0.1389E+00	0.1389E+00	0.1389E+00
8	0.7283E-01	0.7277E-01	0.7283E-01
9	0.1635E-01	0.1639E-01	0.1635E-01
10	0.7120E-02	0.7368E-02	0.7410E-02
11	0.2622E-02	0.2609E-02	0.2566E-02
12	0.1618E-02	0.1613E-02	0.1655E-02
13	0.4534E-03	0.4514E-03	0.4205E-03
14	0.2562E-03	0.2550E-03	0.2889E-03
15	0.7462E-04	0.7421E-04	0.5760E-04
16	0.2630E-04	0.2612E-04	0.6478E-04
17	0.1136E-04	0.1129E-04	
18	0.5674E-05	0.5634E-05	
19	0.2040E-05	0.2027E-05	
20	0.1560E-05	0.1548E-05	
21	0.4351E-06	0.4326E-06	
22	0.3632E-06	0.3605E-06	
23	0.8494E-07	0.8420E-07	
24	0.1251E-06	0.1241E-06	

Table 3.4b Results from one configuration, comparing the vector propagator using the Distant Source method (DS) and the Iterative Block SOR (IBSOR) on a $16^3 \times 24$ lattice and the Conjugate Gradient on a 16^4 lattice.

Quark mass = 0.09			
Time	DSM vector	IBSOR vector	CG 16^4 vector
1	0.1866E-01	0.1867E-01	0.1866E-01
2	0.4175E-01	0.4173E-01	0.4175E-01
3	0.1189E+00	0.1189E+00	0.1189E+00
4	0.8764E+00	0.8764E+00	0.8764E+00
5	0.1788E+01	0.1788E+01	0.1788E+01
6	0.8116E+00	0.8115E+00	0.8116E+00
7	0.1075E+00	0.1075E+00	0.1075E+00
8	0.5067E-01	0.5064E-01	0.5067E-01
9	0.1065E-01	0.1066E-01	0.1065E-01
10	0.4087E-02	0.4198E-02	0.4222E-02
11	0.1445E-02	0.1435E-02	0.1416E-02
12	0.7451E-03	0.7431E-03	0.7603E-03
13	0.2391E-03	0.2382E-03	0.2254E-03
14	0.1135E-03	0.1130E-03	0.1315E-03
15	0.3694E-04	0.3672E-04	0.2669E-04
16	0.1399E-04	0.1390E-04	0.3004E-04
17	0.5847E-05	0.5812E-05	
18	0.2778E-05	0.2759E-05	
19	0.1009E-05	0.1001E-05	
20	0.6595E-06	0.6539E-06	
21	0.1230E-06	0.1219E-06	
22	0.1548E-06	0.1536E-06	
23	0.3596E-07	0.3565E-07	
24	0.5475E-07	0.5433E-07	

Table 3.4c Column 1 shows the averaged vector (VT) propagator measured with four configurations on a $16^3 \times 24$ lattice using the Distant Source Method; column 2 using the Iterative Block SOR ; and column 3 is the Conjugate Gradient on a 16^4 lattice.

Quark mass = 0.04				
Time	DSM vector	IBSOR vector	CG 16^4	IBSOR SDEV
1	0.2285D-01	0.2291D-01	0.2285D-01	0.1271D-01
2	0.4285D-01	0.4282D-01	0.4285D-01	0.8747D-02
3	0.1208D+00	0.1209D+00	0.1208D+00	0.2566D-01
4	0.8937D+00	0.8940D+00	0.8937D+00	0.1980D+00
5	0.1708D+01	0.1708D+01	0.1708D+01	0.2822D+00
6	0.8625D+00	0.8619D+00	0.8625D+00	0.1226D+00
7	0.1114D+00	0.1116D+00	0.1114D+00	0.2681D-01
8	0.6327D-01	0.6287D-01	0.6327D-01	0.1989D-01
9	0.1453D-01	0.1467D-01	0.1453D-01	0.5356D-02
10	0.5745D-02	0.6915D-02	0.7179D-02	0.4284D-02
11	0.3010D-02	0.2584D-02	0.2427D-02	0.1711D-02
12	0.2014D-02	0.1957D-02	0.2109D-02	0.1836D-02
13	0.7189D-03	0.6937D-03	0.5986D-03	0.7021D-03
14	0.3570D-03	0.3446D-03	0.4782D-03	0.4497D-03
15	0.1700D-03	0.1619D-03	0.1078D-03	0.1913D-03
16	0.4017D-04	0.3825D-04	0.7265D-04	0.9151D-04
17	0.1043D-04	0.1022D-04		0.8322D-04
18	0.1300D-04	0.1204D-04		0.4104D-04
19	-0.3278D-05	-0.3783D-05		0.2782D-04
20	0.1233D-04	0.1123D-04		0.1695D-04
21	-0.8109D-07	-0.2133D-06		0.7149D-05
22	0.6788D-05	0.6160D-05		0.7709D-05
23	0.1689D-05	0.1566D-05		0.1745D-05
24	0.4467D-05	0.4081D-05		0.4173D-05

Table 3.4d Column 1 shows the averaged vector (VT) propagator measured with four configurations on a $16^3 \times 24$ lattice using the Distant Source method; column 2 using the Iterative Block SOR algorithm; column 3 from a 16^4 lattice using the Conjugate Gradient algorithm and column 4 shows the standard deviation of the IBSOR data.

m	# iterations on first (16^4) stage	# iterations on second stage
0.50	40	60+30
0.16	120	100+50
0.09	150	150+50
0.04	300	230+50
0.01	500+200	600+300

Table 3.5 Numbers of iterations used in a DSM calculation on a $16^3 \times 24$ lattice.

In tables 3.4a and 3.4b we can see the results from one configuration for the pseudoscalar and vector propagators at a mass of 0.09. The results at higher masses are of the same or better quality. The two sets of data for the DSM and the IBSOR are in very good agreement. Table 3.4c shows the averaged vector propagator (from the four configurations) and as we might expect, the two sets of data are very close. What is apparent from table 3.4d is that agreement is not quite so good at lower values of the quark mass, although as can be seen from the column of standard deviations, the discrepancy between the two methods is an order of magnitude smaller than the statistical error. A probable explanation for the disagreement is that the second 'source' Tx_8 becomes increasingly contaminated by finite time effects as the quark mass is lowered, due to the lattice only having 16 timeslices.

At a given quark mass, the discrepancy between DSM and the IBSOR results is most marked near the 'join' in the DSM i.e. on timeslices 10 and 11 (as can be seen clearly in table 3.4d). The effect of this join becomes unobservable after two timeslices in our data. However, in high statistics measurements and at low quark masses, it may be sufficiently pronounced to require corrective action. In that case we would replace the bad DSM timeslices (10 and 11) by the corresponding timeslices obtained for the first 16^4 lattice. In this latter data, the effect of timeslice 16 is relatively insignificant whenever finite size effects are small, as is evident from table 3.4d.

To summarise then, we can see that the method works well as long as we do not lower the quark mass too far or, in general, provided finite size effects are small. At the lower quark masses it might be advisable to use three steps on a 16^4 lattice so that, say, x_6 could be used as the source in the second stage, and x_{12} in the third stage, to reduce finite time effects. So far, the IBSOR has proved the more efficient way of obtaining $16^3 \times 24$ propagators on the DAP, and because these lattices are long enough for our present analysis (at least to the extent that signal-noise ratio problems begin around timeslice 19) we do not need to extend these lattices. However, in future work with higher statistics it might be beneficial to extend the propagators in time to $16^3 \times 32$ for example, where we might then be able to use up to timeslice 24 for fitting. Given the existence of a large set of $16^3 \times 24$ propagators, the DSM would be a more efficient way of accomplishing this than starting from scratch.

3.7 Fitting the Data

We saw in chapter two that the propagators are expected to have the functional forms

$$\begin{aligned} & A_1 \exp -m_1(t-t_0) && \text{(PS)} \\ & A_1 \exp -m_1(t-t_0) + (-1)^{t-t_0} \tilde{A}_1 \exp -\tilde{m}_1(t-t_0) && \text{(EV, ALL, VT, SC, PV)} \end{aligned} \qquad (3.44)$$

accounting for the ground state only. We can allow for the first excited state for the PS fit in general because we have sufficient degrees of freedom, so we need a routine to fit to two types of function :

$$\begin{aligned} & 1.\ A_1 \exp -m_1(t-t_0) + A_2 \exp -m_2(t-t_0) \\ & 2.\ A_1 \exp -m_1(t-t_0) + (-1)^{t-t_0} \tilde{A}_1 \exp -\tilde{m}_1(t-t_0) \end{aligned} \qquad (3.45)$$

Fit 2 can be written

$$B(t_i) = A_1 f(t_i, m_1) + \tilde{A}_1 g(t_i, \tilde{m}_1) \qquad (3.46)$$

where

$$f(t_i, m_1) = \exp -m_1(t-t_0) \qquad (3.47)$$

and

$$g(t_i, \tilde{m}_1) = (-1)^{t-t_0} \exp -\tilde{m}_1(t-t_0) \qquad (3.48)$$

For fit 1 we have g replaced by f in (3.46). Let us look at fit 2 and see how to implement a routine. We have data y_i and σ_i at each timeslice t_i, the result of averaging the propagators over the configurations, so we define

$$\chi^2 = \sum_{i=1}^{n_d} \frac{(y_i - B(t_i))^2}{\sigma_i^2} \qquad (3.49)$$

where n_d = number of data points included. We wish to minimise this expression with respect to the parameters $m_1, \tilde{m}_1, A_1, \tilde{A}_1$. Looking first at $\frac{\partial \chi^2}{\partial A_1}$, we have

$$\frac{\partial \chi^2}{\partial A_1} = \sum_{i=1}^{n_d} \frac{-2}{\sigma_i^2} [y_i - B(t_i)] \frac{\partial B(t_i)}{\partial A_1} \qquad (3.50)$$

$$= \sum_{i=1}^{n_d} \frac{-2}{\sigma_i^2} \{ y_i f(t_i, m_1) - A_1 f^2(t_i, m_1) - \tilde{A}_1 f(t_i, m_1) g(t_i, \tilde{m}_1) \} \qquad (3.51)$$

so the minimum values are given by

$$A_1 \sum_{i=1}^{n_d} \frac{1}{\sigma_i^2} f^2(t_i, m_1) + \tilde{A}_1 \sum \frac{1}{\sigma_i^2} f(t_i, m_1)\, g(t_i, \tilde{m}_1)$$

$$= \sum_{i=1}^{n_d} \frac{-2}{\sigma_i^2} y_i f(t_i, m_1) \qquad (3.52)$$

and similarly for $\frac{\partial \chi^2}{\partial \tilde{A}_1}$. Using the notation

$$\langle F \rangle = \sum_{i=1}^{n_d} \frac{1}{\sigma_i^2} F(t_i) \qquad (3.53)$$

we have

$$\begin{aligned} A_1 \langle f^2 \rangle + \tilde{A}_1 \langle fg \rangle &= \langle yf \rangle \\ \tilde{A}_1 \langle g^2 \rangle + A_1 \langle fg \rangle &= \langle yg \rangle \end{aligned} \qquad (3.54)$$

or

$$A_1 = \frac{1}{\langle f^2 \rangle \langle g^2 \rangle - \langle fg \rangle^2} \left\{ \langle g^2 \rangle \langle yf \rangle - \langle fg \rangle \langle yg \rangle \right\} \qquad (3.55)$$

$$\tilde{A}_1 = \frac{1}{\langle f^2 \rangle \langle g^2 \rangle - \langle fg \rangle^2} \left\{ \langle f^2 \rangle \langle yg \rangle - \langle fg \rangle \langle yf \rangle \right\}$$

so the linear parameters A_1 and $\tilde{A}_1$ may be treated as dependent variables. We need only vary m_1 and $\tilde{m}_1$ independently. In practice, the first stage of the fitting procedure takes the form of a series of user-determined histograms of the χ^2 in the $(m_1, \tilde{m}_1)$ space. The region round the minimum may be successively enlarged to obtain as good a starting point as possible for the second stage, the steepest descent. This also ensures we can study several

regions of the space interactively to search for new minima.

In the second stage of the fitting a steepest descent algorithm is performed :

$$(ml_{n+1}, \tilde{m}l_{n+1}) = \left(ml_n - k\frac{\partial\chi^2}{\partial ml}\Big|_n, \tilde{m}l_n - k\frac{\partial\chi^2}{\partial \tilde{m}l}\Big|_n\right) \qquad (3.56)$$

where k is some (small) step size chosen as follows:

$$ml_{n+1} = ml_n - k_{n+1}\frac{\partial\chi^2}{\partial ml}\Big|_n \qquad (3.57)$$

and define

$$\Delta m_{n+1} = |m_{n+1} - m_n| = \sqrt{(ml_{n+1} - ml_n)^2 + (\tilde{m}l_{n+1} - \tilde{m}l_n)^2} \qquad (3.58)$$

Then we expect $\Delta m_{n+1} < \Delta m_n$ if the system is converging, so

$$k_{n+1}\sqrt{\left(\frac{\partial\chi^2}{\partial ml}\Big|_n\right)^2 + \left(\frac{\partial\chi^2}{\partial \tilde{m}l}\Big|_n\right)^2} < \Delta m_n \qquad (3.59)$$

$$k_{n+1}\left|\frac{\partial\chi^2}{\partial m}\Big|_n\right| < |m_n - m_{n-1}| \qquad (3.60)$$

We take

$$k_{range} = k_{r_{n+1}} = \frac{|m_n - m_{n-1}|}{\left|\frac{\partial\chi^2}{\partial m}\Big|_n\right|} \qquad (3.61)$$

and use 1/20 k_r for k. We perform the steepest descent until $\frac{\partial\chi^2}{\partial m}$ begins to increase again, signalling that we have reached a minimum, and then interpolate between the last three points as shown in fig 3.9.

The programme is designed so that it is easy to vary the range of timeslices used to fit with. We can thus find out the effect of timeslices near

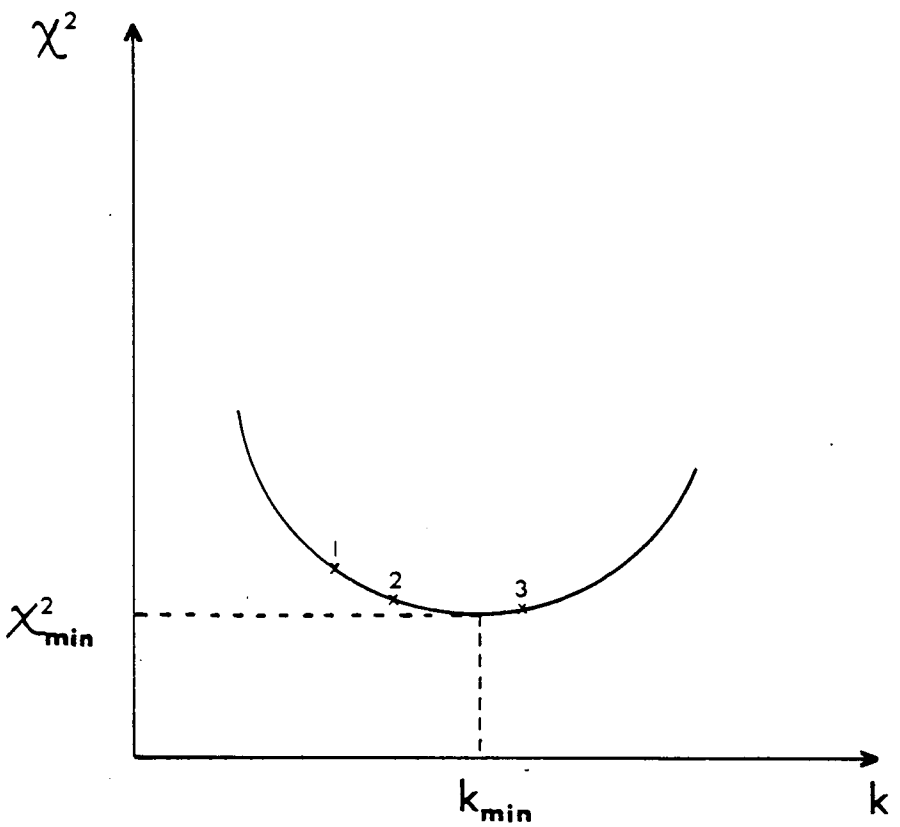

Figure 3.9 Location of the minimum χ^2 as k varies

the boundary and locate the onset of asymptotic decay of the propagators. It also divides the configurations up into N_B blocks of N_C configurations and performs the fit on these averaged data as well. This is used to estimate the errors: we use

$$\sqrt{\frac{\sum_{i=1}^{N_B} x^2 - \frac{1}{N_B}\left(\sum_{i=1}^{N_B} x\right)^2}{N_B(N_B-1)}} \qquad (3.62)$$

as the error in m_F, calculated from the full data, for each parameter m_1, $\tilde{m}_1, A_1, \tilde{A}_1$.

In principle, if the lattice is long enough in the time direction, we could use timeslices far enough away from the origin that only have ground states remain in the signal. However, there are various factors to consider which mean this may not be an appropriate procedure in practice. Timeslices near the boundary will be edge-affected, the signal-to-noise ratio may be very low so that we cannot go to as long times as we would like, and we might have a situation where the lowest mass (ground state) has a very small amplitude and so only becomes dominant at very large times, beyond the effective extent of the lattice, in which case we would not be seeing the ground state at the range of timeslices we have. For these reasons, we have to find ways of accounting for excited states. We use two approaches.

1. Rely on the lattices being long enough for asymptotic decay to set in i.e. when only the signals from the lightest mass in the direct and oscillating channel remain. In this case a sequence of two exponential fits is performed, in which successively more points are dropped near the source until the resulting masses stabilise. In certain cases, for example the baryons at β=6.0, this procedure is not sufficient to give us the lowest mass state and we must use the second approach.

2. Explore an eight-parameter space by using a sequence of two-exponential (four-parameter) fits. Here one excited state is included in both the direct and oscillating channel and the aim is to refine the data interactively by subtracting out successively better approximations to these excitations. In this case, because we are accounting for excitations, we can include points close to the source, in general dropping only one point as well as the source itself. An example of this procedure is

i) fit to one direct and one oscillating term.

ii) subtract the direct part from the data and fit the remainder to two oscillating exponentials

iii) subtract the two oscillating exponentials from the data and fit the remainder to two direct exponentials.

iv) subtract the estimates for the excitations in ii) and iii) from the data and repeat fit i).

We may then continue the procedure until the masses are stable. In some cases there is no measureable oscillating exponential in which case a simpler procedure can be used. The χ^2 falls during the steps above, usually to a point significantly lower than the corresponding two-exponential fit. The disadvantage of this method is that we must perform a large number of fits at each mass value - this is quite a consideration since the error estimation needs analysis on blocks of data as well. However, we are able to include as much of the propagator data as possible in the fits, and we do obtain an estimate for the excited state mass (this will not be very reliable however due to contamination by higher excitations). Where the data is of sufficient quality, we use both these procedures in chapter four.

3.8 Conclusions

In this chapter, we have discussed a variety of numerical techniques which have been used in obtaining the results presented in the next chapter. The most time-consuming part of a hadron mass calculation is the inversion of the fermion matrix and it is thus very important to find as efficient an algorithm as possible to do this.

The Conjugate Gradient Algorithm works well, but is expensive in terms of storage and needs a large amount of data transfer each iteration. This means, because of the low I/O rate of the DAP, that the connect time is about six times the cpu time. The method is only really practical where the disk-to-fast-memory bandwidth is very high - so that the calculation is continuous - or for systems small enough to fit within the machine's fast memory. As far as our calculations are concerned, the former does not apply to the DAP and so, for the lattice sizes we wish to use, we had to look for an alternative [Chalmers et al. (1986a)].

The Distant Source Method computes quark propagators on large lattices via two or more calculations on smaller lattices. Use of the DSM does involve a systematic error, which is due mainly to finite size effects on the small lattice. It has already been shown that this is insignificant for free fermions [Kenway (1985)] and we saw that the systematic error introduced by the DSM in quenched QCD is much smaller than the statistical error in an average over four gauge configurations [Chalmers et al. (1986b)]. This systematic error grows with decreasing quark mass, but is likely to remain acceptably small, relative to the level of statistical accuracy of present hadron mass calculations, whenever finite size effects are themselves acceptably small. The DSM is not competitive with other algorithms for generating quark propagators from scratch; its usefulness lies in permitting the extension of an existing set of propagators in time where analysis shows that this is desirable.

The investigation of the Block Gauss Elimination method proposed by Bowler et al (1984) forced us to conclude that this method was unreliable - the scheme reduces to inverting an ill-conditioned fully dense matrix, and the projection mechanism of (3.35) amplifies any errors present in the x_N solution; indeed, using x_N to obtain the solutions on the other timeslices is unwise as x_N is always the last to converge.

On the other hand, the iterative Block SOR scheme described in section 5 proved to be ideal for our system. The stretch factor when this scheme is implemented is now only 1.02 and we gain a factor of around six in elapsed time as compared with the Conjugate Gradient algorithm on the $16^3 \times 24$ lattice. At present the Block SOR algorithm requires slightly more cpu time than CG at low masses, but there is no I/O overhead. The algorithm work in this chapter has been developed and tested for the DAP, whose performance peaks at around 15 Mflops and whose asynchronous I/O rate is around 250-300 Kbytes/sec. The conclusions however are valid for most memory-limited supercomputers on which the Conjugate Gradient algorithm has high I/O overheads. The Iterative Block SOR algorithm in its present form has between 1/3 and 1/4 of the vector I/O per sweep, and generally fewer sweeps are needed. Consequently, performance is determined by the cpu speed, not the disk-to-fast-memory transfer rate. Further, the removal of synchronising scalars means that the Iterative Block SOR algorithm can run at very close to 100% efficiency on multiprocessor systems, such as the Cray XMP/4. If processor 1 is inverting the (k)'th block equation for x_t then processor 2 can work in parallel on the (k+1)'th equation for x_{t-3} without any

danger of write conflicts arising. Extending this idea we can fully utilise an n-processor system when our lattice has temporal extent 3n or larger.

In general, we conclude that when the calculations are small the Conjugate Gradient algorithm remains the best way of obtaining columns of the inverse fermion matrix, but for large systems the Iterative Block SOR algorithm is more efficient. In addition the roundoff problems in accumulating the CG scalars have been avoided, and so bigger systems can be studied in 32-bit arithmetic than is possible with CG. Thus for the work on lattices of $16^3 \times 24$ the Iterative Block SOR algorithm was used.

CHAPTER FOUR

Results

In this chapter, results of hadron mass calculations at four different values of β are presented and discussed. We use the quenched approximation, with pure gauge configurations on 16^4 lattices at β = 5.7, 6.0 and 6.3 (which we periodically-extend to $16^3 \times 24$) and, on $16^3 \times 24$ lattices at β = 6.15. The Susskind formulation of lattice fermions and local hadron operators are used (see chapter two), and we invert the fermion matrix using either the even/odd partitioned Conjugate Gradient algorithm or the Iterative Block SOR depending on lattice size. Before looking at the hadron mass results in sections 2-6, first we discuss propagator distributions.

4.1 Propagator Distributions

It has been suggested [Mutter (1986)] that the quenched approximation allows large fluctuations in the eigenvalues of the fermion matrix which would be suppressed by the fermionic determinant in the full theory. The corresponding 'exceptional' gauge configurations have been associated with unusual behaviour of quenched hadron propagators. As mentioned in chapter three, the Wuppertal group have claimed that three of their sample of 28 β = 6.3, $24^3 \times 48$ gauge configurations are of this type, and result in hadron propagators whose amplitudes and masses have large deviations from the mean. Let us look at how the timeslice propagators for the various hadrons in this calculation are distributed. We perform a simple statistical analysis of our $16^3 \times 24$, β = 6.0 propagators to check whether or not they display any evidence of 'exceptional' behaviour. This consists of taking the data for one hadron at a particular quark mass, consisting of 32 timeslice propagators, and constructing histograms of the deviations of the 32 measurements from the mean *at each time*, scaled by the sample standard deviation. We then add together the histograms for times n_4 = 9 to 19 in order to increase the statistics. These 11 sets of data are, of course, correlated. The histograms plotted in figs 4.1-4.3 use 1/2 σ bins.

Fig. 4.1 shows the logarithm of the pseudoscalar (PS) meson, or pion,

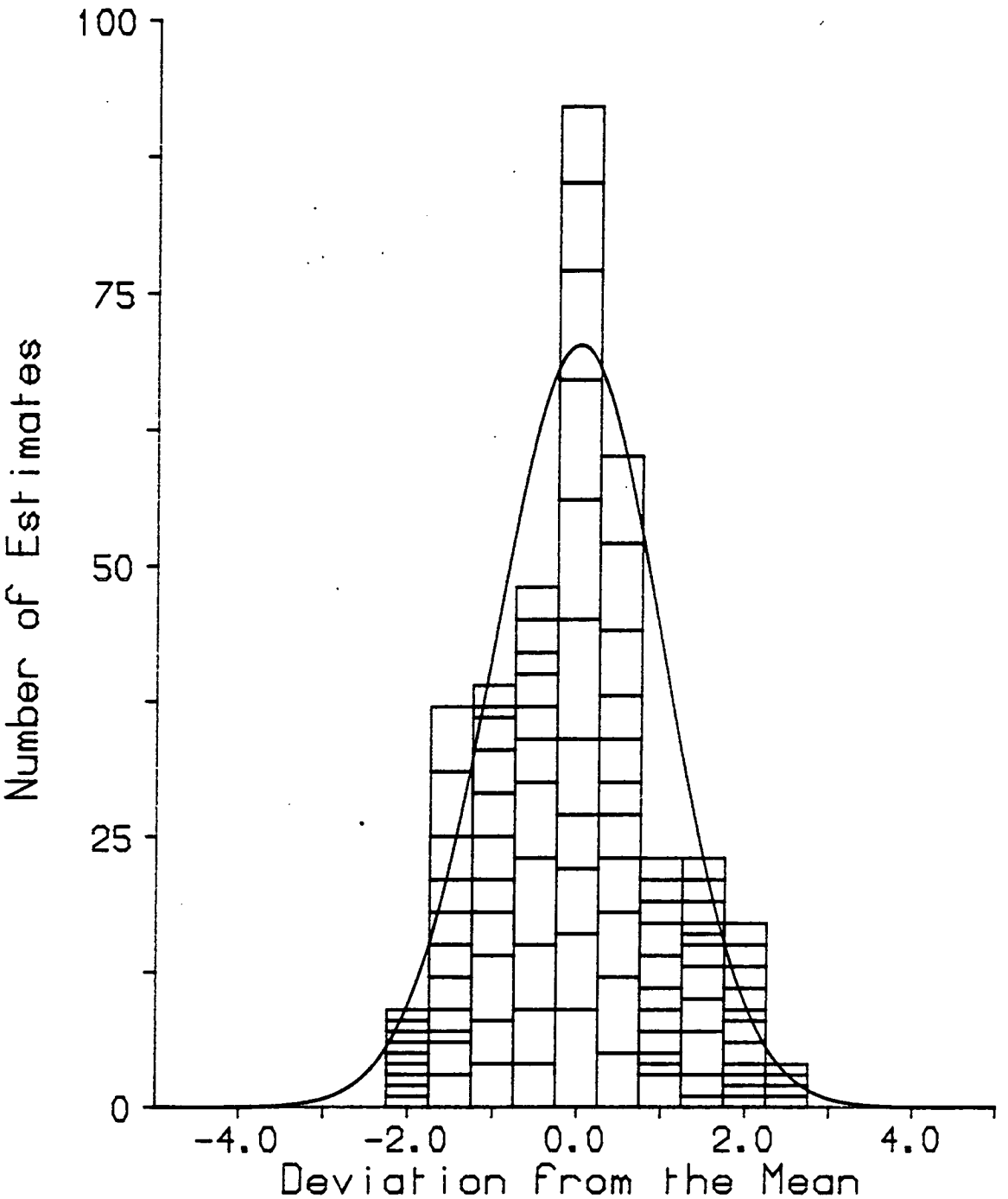

Fig. 4.1 Histogram of the deviation of the log of the pion propagator from the mean at time n_4 , scaled by the standard deviation and summed over n_4 = 9-19, in 1/2 σ bins. β = 6.0 and the quark mass is 0.04. Superimposed is an appropriately normalised Gaussian.

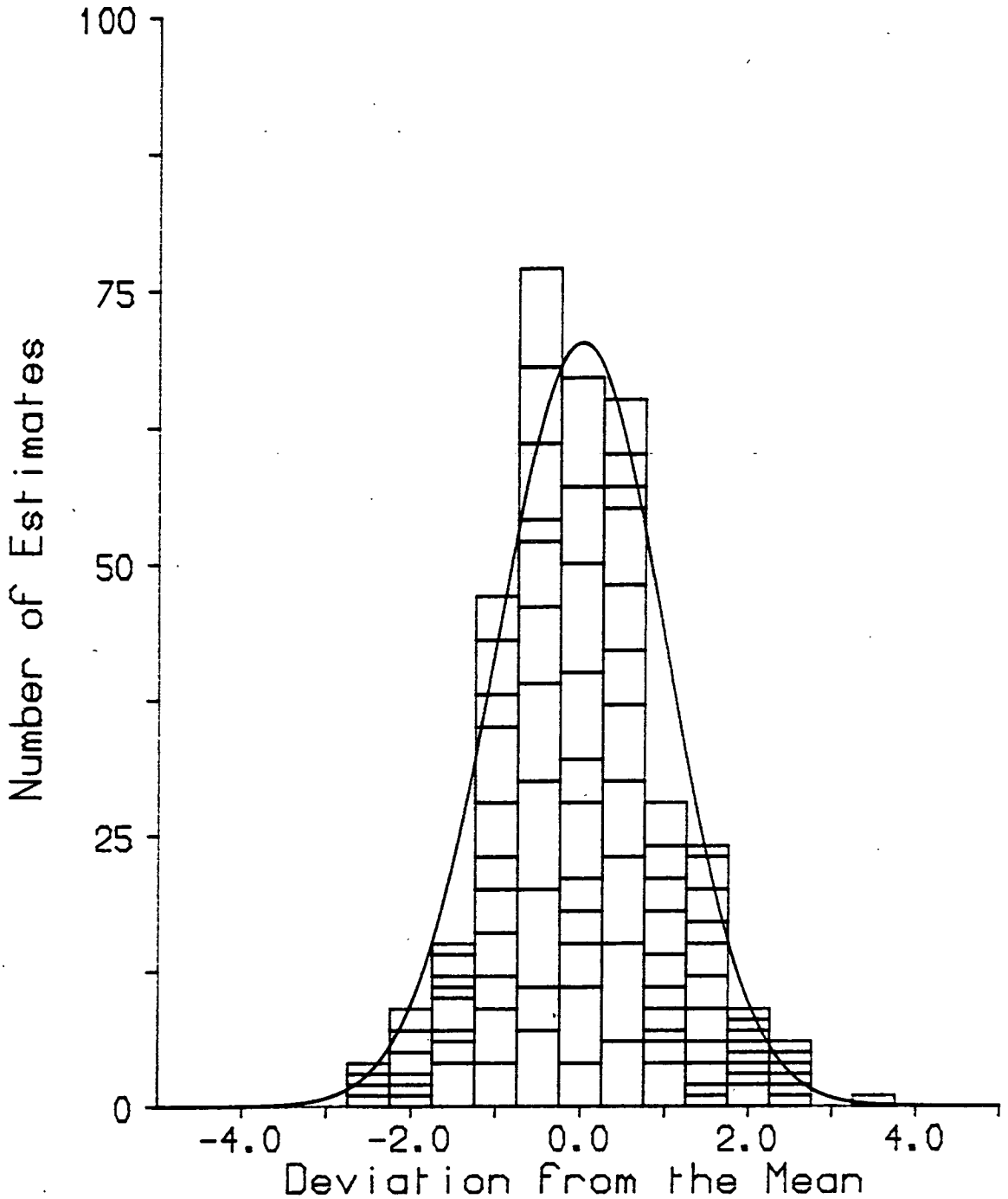

Fig. 4.2 Histogram of the deviation of the vector meson propagator from the mean at time n_4, scaled by the standard deviation and summed over n_4 = 9–19, in 1/2 σ bins. β = 6.0 and the quark mass is 0.04. Superimposed is an appropriately normalised Gaussian.

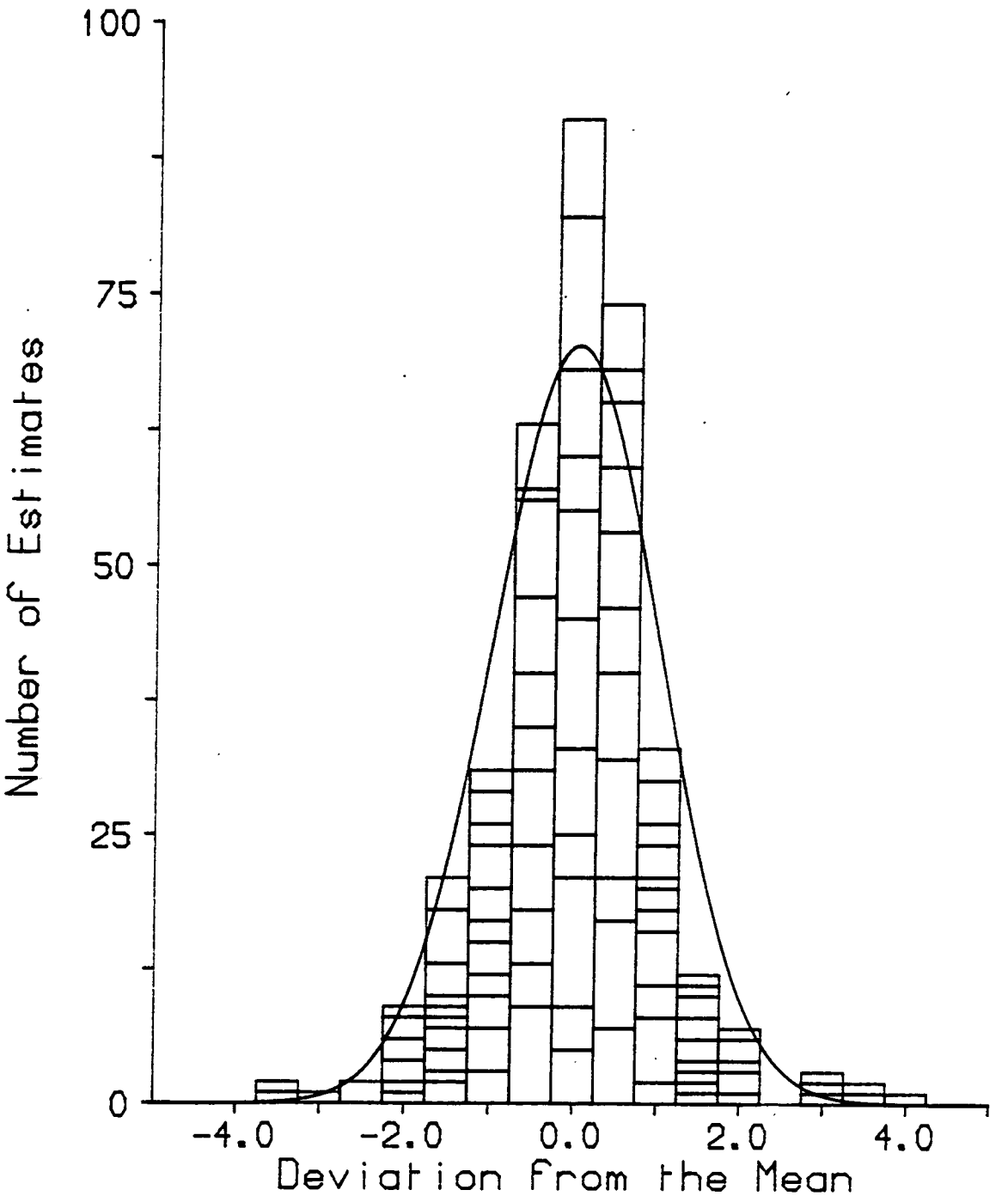

Fig. 4.3 Histogram of the deviation of the EVEN baryon propagator from the mean at time n_4, scaled by the standard deviation and summed over n_4 = 9–19, in 1/2 σ bins. β = 6.0 and the quark mass is 0.04. Superimposed is an appropriately normalised Gaussian.

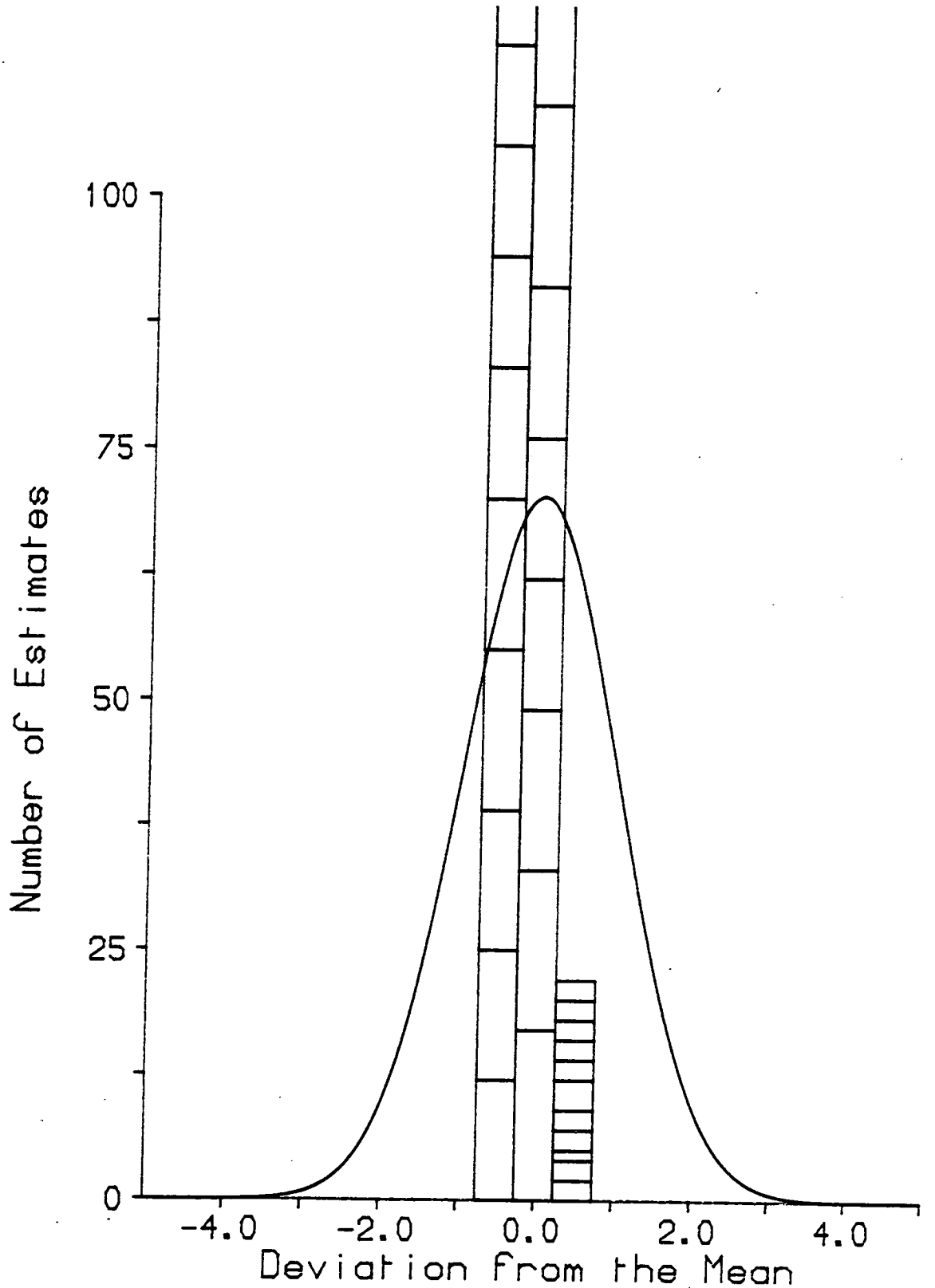

Fig. 4.4a As fig. 4.1, but with one of the 32 propagators multiplied by 10

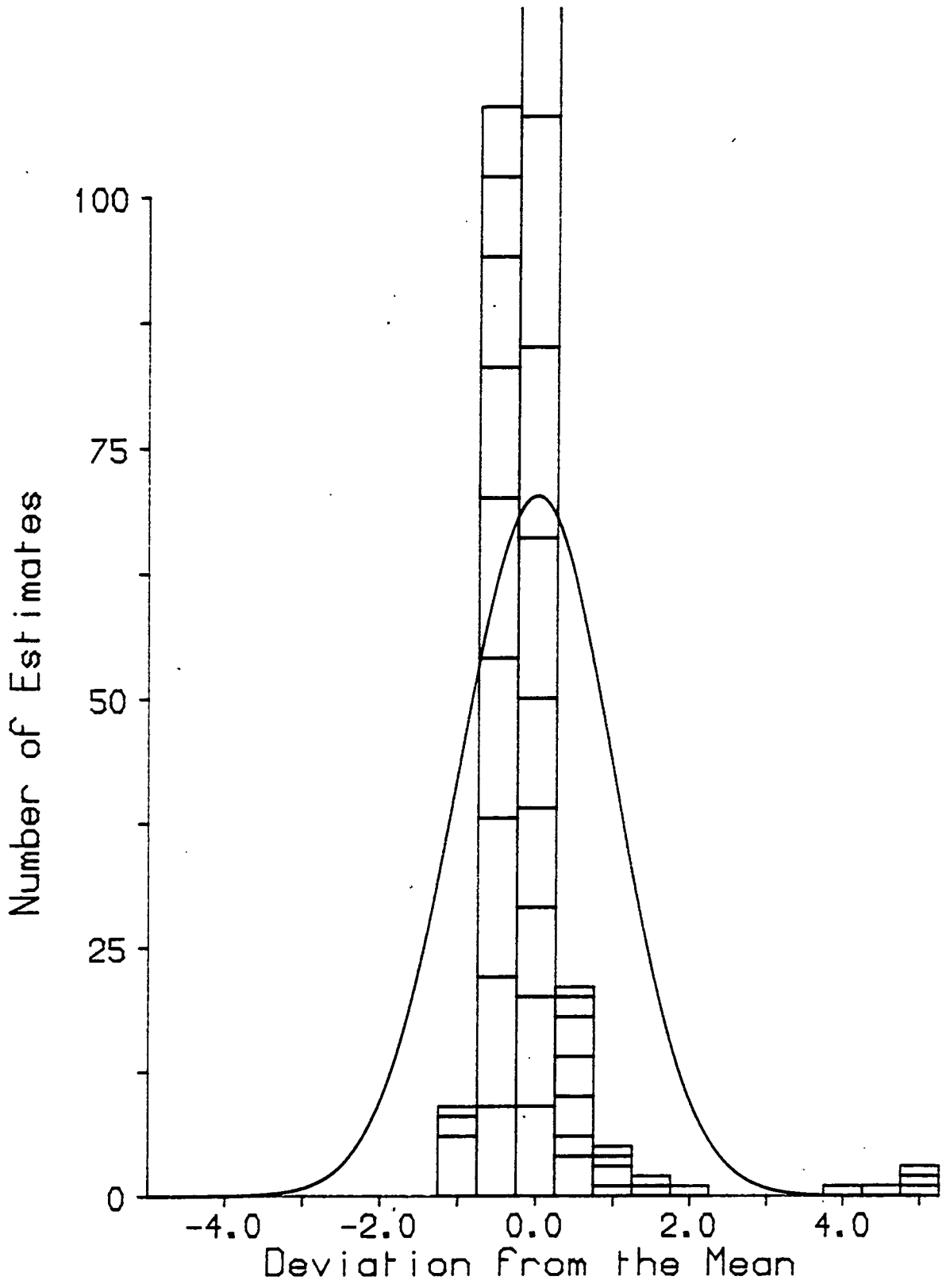

Fig. 4.4b As fig. 4.1, but with one of the 32 propagators replaced by a propagator with quark mass 0.01.

propagator data at m = 0.04 together with a superimposed, appropriately normalised Gaussian, included for the purpose of comparison only. We plot the logarithm of the data because the raw data itself is asymmetrically distributed, because the PS propagator is strictly positive from (2.56a). Our measurements are approximately consistent with a normal distribution in the pion mass estimates.

Figs 4.2 and 4.3 are the histograms for the vector (VT) meson propagator and for the EVEN baryon propagator at m = 0.04, together with the corresponding Gaussians. Again the agreement is reasonable and, for example, the number of data points more than 2σ from the mean is roughly in accordance with the normal distribution. The same comments apply at other quark mass values. While we cannot be sure of the correct distribution of hadron propagators, this qualitative agreement with normal distributions suggests that we do not have any exceptional configurations in our sample. We can further test this assertion by replacing one of the pion propagators in fig. 4.1 with a 'rogue' propagator and observing the effect on our histograms. In fig. 4.4a we show the effect of multiplying the amplitude of one propagator in the sample by 10, and in fig 4.4b we show the effect of replacing one propagator by a propagator at m = 0.01. Both have dramatic effects on the distribution, producing a narrow peak due to the artificially increased σ. In both cases the peak is shifted below the mean. When one propagator has an exceptionally low mass, there is also a second peak in the distribution approximately 5σ above the mean. We therefore conclude that there is nothing obviously exceptional about our propagators.

4.2 Results at $\beta = 5.7$ on a 16^4 lattice

At $\beta = 5.7$ we have quark propagators at five mass values on eight gauge configurations separated by 896 pseudo-heatbath sweeps. We use Dirichlet boundary conditions in time on a 16^4 lattice (with the source on timeslice 5) and work with the odd/even partitioned CG algorithm, with the gauge configurations in temporal gauge. The hadron propagators which result are not of sufficient quality to support more than 2-exponential fits, so we attempt to remove excitations at short times by successively dropping data points near the source, looking for the resulting masses to stabilize. For the PS propagator there is no signal in the oscillating channel and so we are able

to include a radial excitation in the fit. The full results are given in table 4.1. At the lighter quark masses there is no evidence of an excited state in the pseudoscalar propagator.

These results may be compared with previous results at $\beta = 5.7$ using 8^4 gauge configurations, which were duplicated in time for the calculation of $8^3 \times 16$ quark propagators [Bowler et al. (1984a)]. Those on the small lattice have been accumulated from a variety of measurements, described in detail in [Bowler et al. (1984a)]. Fig. 4.5 shows our best estimates for the pion masses, along with the $8^3 \times 16$ results, plotted against $\sqrt{m}$. On the 16^4 lattice these are taken from the single exponential fits. Any spatial finite size effect in the pion data is apparently small.

The full data for pion, rho and $(1/2)^+$ nucleon are shown in fig. 4.6 together with the $8^3 \times 16$ results. The rho and nucleon masses at small quark mass are systematically lower on the smaller lattice, although the statistical errors are large. However, since we have only eight propagators on the 16^4 lattice, the error estimation is crude (the spread in the measurements from two consecutive bins of 4).

The local meson operators and the corresponding timeslice propagators permit the measurement of two different flavour combinations of the pion and the rho, as we saw in chapter two. This therefore provides a means of testing the restoration of flavour symmetry. From table 4.1 we can see that there is some agreement between the mass estimates for the two rhos at high quark mass, but not at $m = 0.01$. There is no agreement between the two pions, although the errors on the state in the scalar (SC) propagator are large and this state may be contaminated by excitations. We conclude that there is no compelling evidence for flavour symmetry restoration. Where both yield successful fits, the two nucleon propagators give consistent mass estimates. However, as can be seen from fig. 4.7, the behaviour of the ALL and EVEN propagators themselves is different especially at the lowest quark masses, although the general quality of the data (with only eight configurations) is poor.

In fig. 4.8 we plot the nucleon/rho mass ratio versus the pion/rho ratio. The numerical values are given in table 4.2.

	Mq	A1	m1		
	0.50	1.616 (36)	1.661 (1)		
PS	0.16	2.366 (38)	1.022 (3)		
1-exp	0.09	2.672 (42)	0.795 (5)		
	0.04	3.264 (94)	0.550 (1)		
	0.01	5.543 (6)	0.273 (1)		
	Mq	A1	m1	A2	m2
	0.50	0.120 (146)	1.639 (7)	1.487 (153)	1.662 (72)
PS	0.16	0.119 (1096)	0.894 (260)	2.285 (1148)	1.035 (194)
	0.09	2.654 (189)	0.794 (8)	0.216 (229)	1.938 (670)
	0.04	3.251 (224)	0.549 (15)	3.470 (6903)	4.409 (1504)
	0.01	0.726 (2497)	0.165 (78)	5.036 (5535)	0.305 (2092)*
	Mq	A1	m1	$\widetilde{A1}$	$\widetilde{m1}$
	0.50	3.111 (47)	1.930 (9)	0.009 (6641)	1.583 (1115)
VT	0.16	4.022 (44)	1.558 (3)	0.559 (-)	1.761 (1795)
	0.09	4.642 (302)	1.471 (27)	4.761 (2558)	2.114 (673)
	0.04	3.340 (1867)	1.242 (75)	6.807 (-)	2.037 (2127)
	0.01	4.354 (743)	1.055 (7)	2.1D+3 (9)	3.391 (701)
	Mq	A1	m1	$\widetilde{A1}$	$\widetilde{m1}$
	0.50	2.083 (173)	2.048 (27)	-1.394 (395)	2.458 (320)
PV	0.16	1.022 (1118)	1.459 (249)	-1.405 (-)	1.776 (785)
	0.09	0.862 (2393)	1.306 (424)	-1.512 (3449)	1.596 (385)
	0.04	1.273 (-)	1.348 (2067)	-1.761 (-)	1.435 (450)
	0.01	2.048 (349)	1.480 (28)	-1.473 (586)	1.214 (165)
	Mq	A1	m1	$\widetilde{A1}$	$\widetilde{m1}$
	0.50	0.643 (37)	2.256 (163)	-0.547 (16)	2.277 (157)
SC	0.16	0.291 (57)	1.586 (170)	-1.521 (145)	1.650 (19)
	0.09	0.257 (156)	1.418 (563)	-1.766 (74)	1.386 (75)
	0.04	0.129 (103)	1.105 (512)	-2.332 (99)	1.224 (27)
	0.01	-	-	-	-
	Mq	A1	m1	$\widetilde{A1}$	$\widetilde{m1}$
	0.5	0.858 (70)	3.040 (11)	-0.509 (262)	3.495 (378)
EVEN N	0.16	0.858 (293)	2.550 (165)	-0.962 (103)	2.875 (18)
	0.09	1.020 (518)	2.543 (263)	-0.897 (94)	2.643 (17)
	0.04	0.965 (51)	2.448 (4)	-1.086 (318)	2.593 (179)
	0.01	0.945 (242)	2.359 (89)	-1.089 (373)	2.466 (196)
	Mq	A1	m1	$\widetilde{A1}$	$\widetilde{m1}$
	0.5	0.920 (9)	3.042 (44	-0.403 (59)	3.514 (211)
ALL N	0.16	1.329 (214)	2.703 (70	-0.512 (31)	2.748 (28)
	0.09	1.420 (245)	2.627 (104	-0.566 (158)	2.625 (92)
	0.04	0.988 (464)	2.368 (274	-1.490 (109)	3.031 (141)
	0.01	-	-	-	-

Table 4.1

Amplitudes and masses from 2-exponential fits to hadron propagators on a 16^4 lattice at β=5.7. The PS and SC were fitted using timeslices 6-13, the VT and 1-exp PS using 8-13 and the PV used 7-13. The baryons were obtained from 6-13 . The starred point should be not be regarded as a reliable estimate.

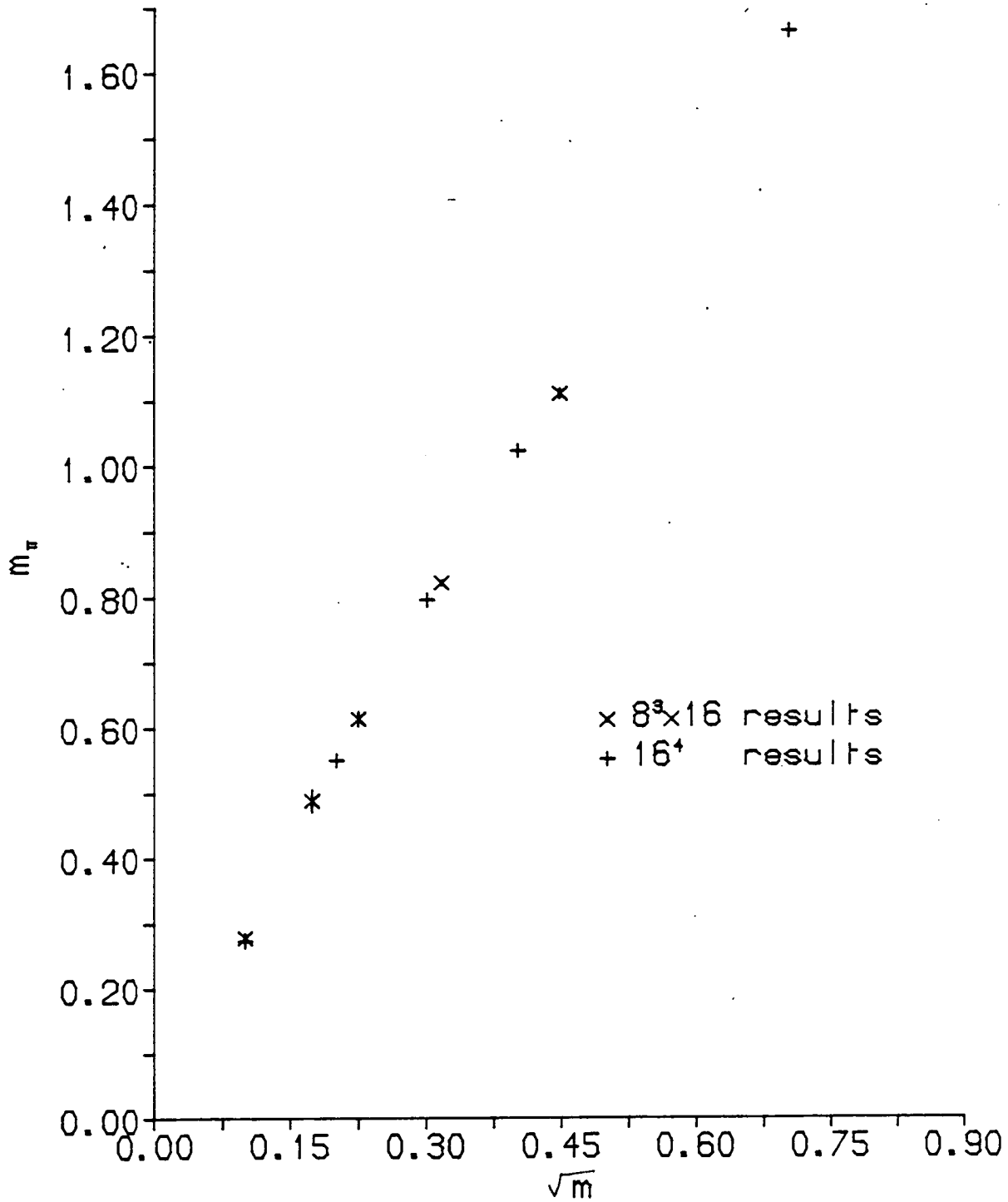

Fig. 4.5 The pion mass in lattice units at β = 5.7. The error bars are smaller than the symbol size.

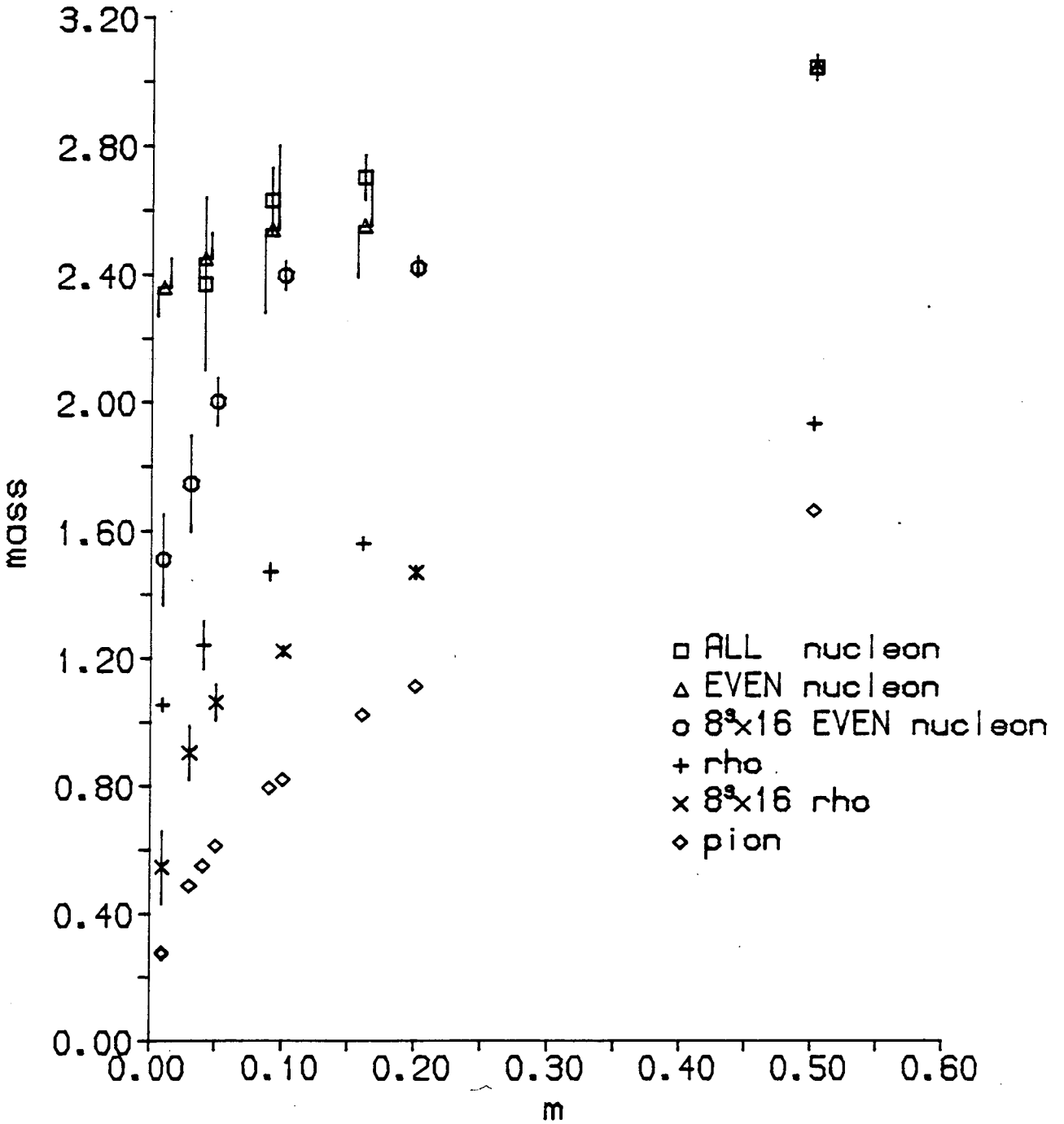

Fig. 4.6 Hadron masses in lattice units at $\beta = 5.7$. The pion error bars are smaller than the symbol size.

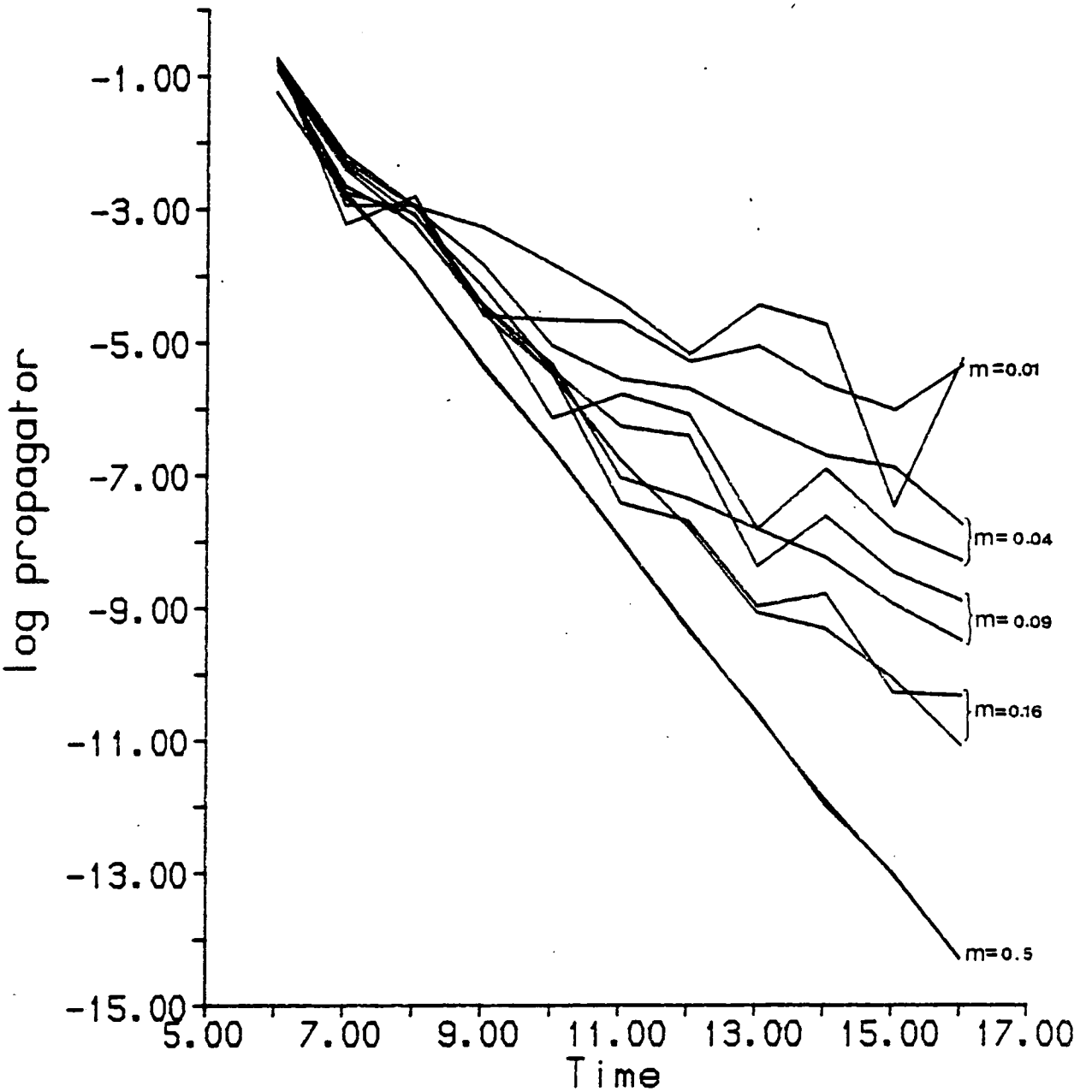

Fig. 4.7 EVEN and ALL baryon timeslice propagators for five different quark masses on a 16^4 lattice at β = 5.7, using antiperiodic spatial boundary conditions. (8 configurations)

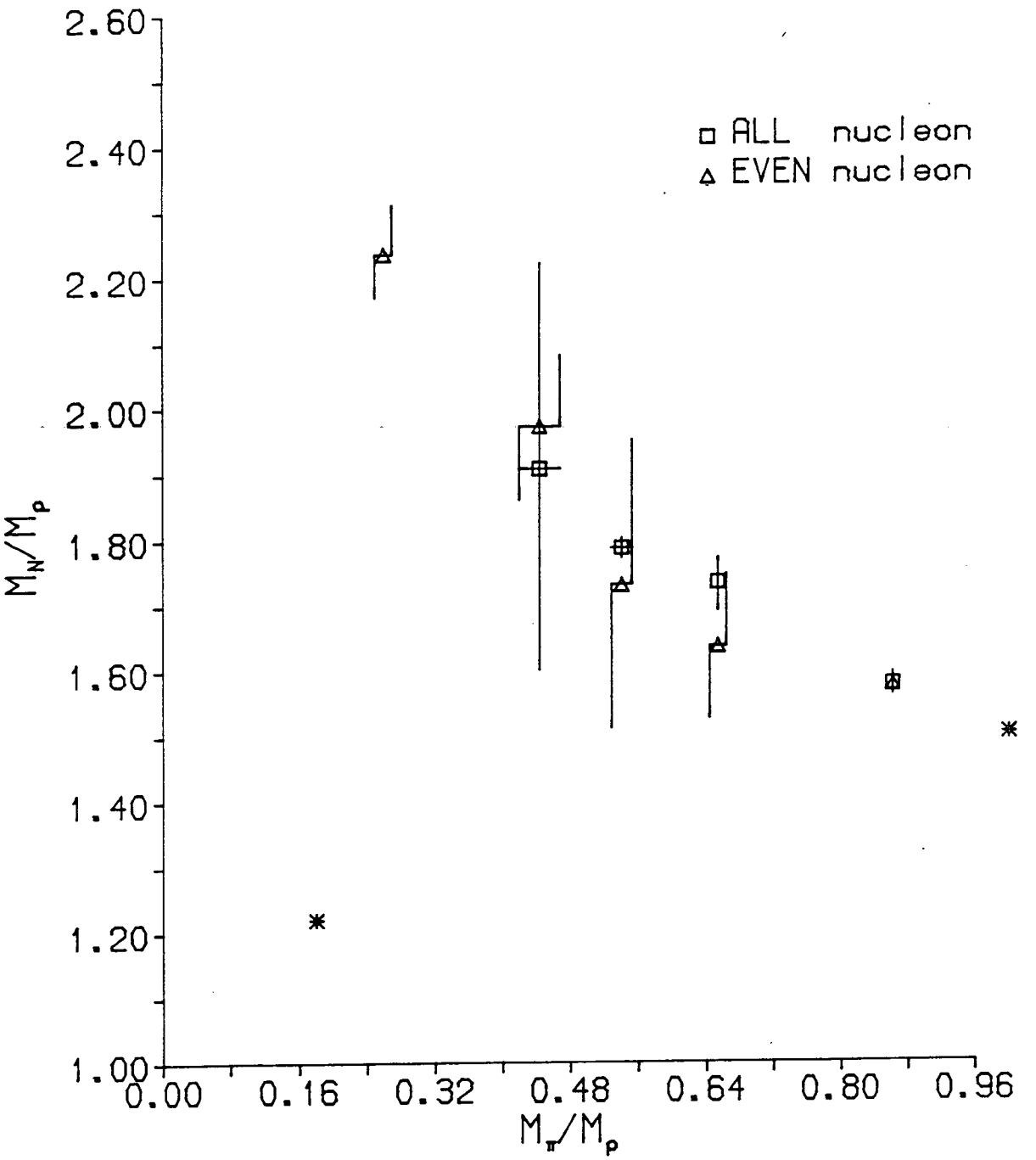

Fig. 4.8 Mass ratios at $\beta = 5.7$; the starred points are the experimental and infinitely-heavy quark values.

m_q	m_π/m_ρ	m_N/m_ρ
0.50	0.861 (4)	1.575 (1)
0.16	0.653 (2)	1.635 (110)
0.09	0.540 (12)	1.729 (217)
0.04	0.443 (24)	1.971 (107)
0.01	0.259 (3)	2.236 (71)

Table 4.2 Ratios of hadron masses at β = 5.7.

The spatial finite size effects in the rho and nucleon masses appear approximately to cancel in the ratios and both spatial lattice sizes support the conclusion that $M_{nucleon}/ M_{rho}$ increases as M_{pion} /M_{rho} decreases and that there is no crossover to the light quark regime necessary for agreement with the experimental values. More importantly, this ratio is not consistent with that at β = 6.0 (see later), indicating that quenched hadron masses are not scaling at 5.7. Consequently, no further analysis was done at β = 5.7.

4.3 Results at β = 6.0 on a 16^4 lattice

We have propagators on eight 16^4 configurations separated by 896 pseudo-heatbath sweeps. The same boundary conditions, quark masses, conjugate gradient algorithm and convergence criteria as at β = 5.7 were used, although convergence is slightly faster, as we saw in table 3.1b.

The results from 2-exponential fits to the hadron propagators are given in table 4.3. As before, only the pion fit includes an excitation and, except at the highest quark mass, we observe a clear signal for the excited state in this channel. There is no evidence that the masses of other hadrons are stabilizing as data near the source is dropped from the fits. This is not surprising given the smallness of the lattice and makes the results of little significance in themselves, but they are valuable for comparison with the β = 5.7 results and with the larger lattice results at β = 6.0.

The pion mass estimates obtained from 2-exponential fits to the pseudoscalar propagator are plotted against $\sqrt{m}$ in fig. 4.9. They deviate from the estimates of [Barkai et al. (1985a)] as the quark mass decreases, being almost 20% higher at m = 0.01. A linear fit through our data supports a larger intercept at m = 0 than on the 16^4 lattice at β = 5.7, which suggests larger finite size effects [Billoire et al. (1985b)]. We also see a signal for the pion in the scalar propagator with masses in rough agreement with those in fig. 4.9 for all but the lightest quark mass. The estimates from the scalar propagator are systematically higher, probably due to the presence of remnants of excited states, and agree better with estimates from 1-exponential fits to the pseudoscalar propagator. This is indicative of flavour symmetry restoration at the higher quark masses. The other hadron masses are shown in fig. 4.10. As remarked for our β = 5.7 data, the error bar estimation is poor.

There is a signal for the rho in the pseudovector propagator, with a mass within 8% of the first, except at the lowest quark mass, although the lack of evidence for asymptotic decay means we can attach little significance to this observation. The nucleon mass estimates from the two types of propagator analysed are in agreement. However, both our rho and nucleon masses are higher than those of [Barkai et al. (1985a)] and are certainly over-estimated by our fitting procedure. Even so, it is tempting to conclude on the basis of the stronger evidence for flavour symmetry in the spectrum, that these measurements show significantly better indications of continuum behaviour than we observed at β = 5.7. Nothing can be concluded about mass ratios because it is certain we have not properly been able to remove the effects of excitations.

	Mq	A1	m1		
	0.50	1.450 (65)	1.665 (4)		
PS	0.16	1.396 (50)	1.016 (1)		
1-exp	0.09	1.249 (74)	0.793 (4)		
	0.04	1.063 (89)	0.561 (17)		
	0.01	1.013 (44)	0.319 (29)		
	Mq	A1	m1	A2	m2
	0.50	1.365 (59)	1.658 (4)	0.214 (28)	2.083 (54)
PS	0.16	1.101 (102)	0.985 (7)	1.056 (37)	1.525 (38)
	0.09	0.928 (67)	0.754 (8)	1.352 (16)	1.389 (14)
	0.04	0.800 (71)	0.523 (21)	1.596 (26)	1.228 (23)
	0.01	0.833 (15)	0.300 (22)	1.746 (30)	1.223 (82)
	Mq	A1	m1	$\widetilde{A1}$	$\widetilde{m1}$
	0.50	2.202 (22)	1.839 (1)	-5.082 (-)	2.843 (1166)
VT	0.16	0.917 (1)	1.196 (8)	-186.7 (-)	3.226 (390)
	0.09	0.580 (103)	0.981 (19)	-183.5 (145.1)	3.045 (855)
	0.04	0.564 (44)	0.873 (15)	-2.803 (1.823)	1.640 (323)
	0.01	0.958 (124)	0.959 (25)	-0.140 (-)	0.739 (1184)*
	Mq	A1	m1	$\widetilde{A1}$	$\widetilde{m1}$
	0.50	1.437 (13)	1.913 (5)	-2.407 (2727)	2.398 (287)
PV	0.16	0.582 (8)	1.265 (1)	-2.427 (250)	1.736 (20)
	0.09	0.386 (88)	1.059 (40)	-1.809 (480)	1.464 (96)
	0.04	0.249 (70)	0.870 (51)	-1.570 (255)	1.265 (55)
	0.01	1.682 (42)	0.732 (39)	-1.340 (131)	1.095 (13)
	Mq	A1	m1	$\widetilde{A1}$	$\widetilde{m1}$
	0.50	0.344 (19)	1.880 (13)	-0.607 (470)	2.080 (269)
SC	0.16	0.102 (14)	1.070 (48)	-1.187 (56)	1.305 (5)
	0.09	0.071 (11)	0.848 (71)	-1.266 (120)	1.044 (8)
	0.04	0.034 (10)	0.582 (71)	-1.169 (138)	0.775 (11)
	0.01	0.125 (58)	0.511 (87)	-0.677 (96)	0.399 (38)
	Mq	A1	m1	$\widetilde{A1}$	$\widetilde{m1}$
	0.50	0.599 (30)	2.921 (11)	-0.707 (545)	3.323 (232)
EVEN N	0.16	0.442 (40)	2.370 (11)	-0.547 (321)	2.524 (175)
	0.09	0.340 (15)	2.193 (49)	-0.510 (230)	2.344 (142)
	0.04	0.286 (138)	2.062 (132)	-0.351 (80)	2.128 (83)
	0.01	0.193 (282)	1.881 (298)	-0.203 (71)	1.894 (137)
	Mq	A1	m1	$\widetilde{A1}$	$\widetilde{m1}$
	0.50	0.648 (11)	2.924 (6)	-0.432 (40)	3.239 (65)
ALL N	0.16	0.511 (150)	2.370 (27)	-0.354 (527)	2.427 (249)
	0.09	0.382 (112)	2.178 (13)	-0.342 (313)	2.245 (178)
	0.04	0.166 (97)	1.907 (327)	-0.977 (-)	2.409 (1155)
	0.01	0.431 (327)	2.066 (221)	-0.281 (245)	2.056 (1258)

Table 4.3

Amplitudes and masses from 2-exponential fits to hadron propagators on a 16^4 lattice at β=6.0. The VT,PV and 1-exp PS mesons were fitted using timeslices 8-13 ; the SC used 7-13 and the PS used 6-13. The baryons were obtained from 8-13. The starred point should be not be regarded as a reliable estimate.

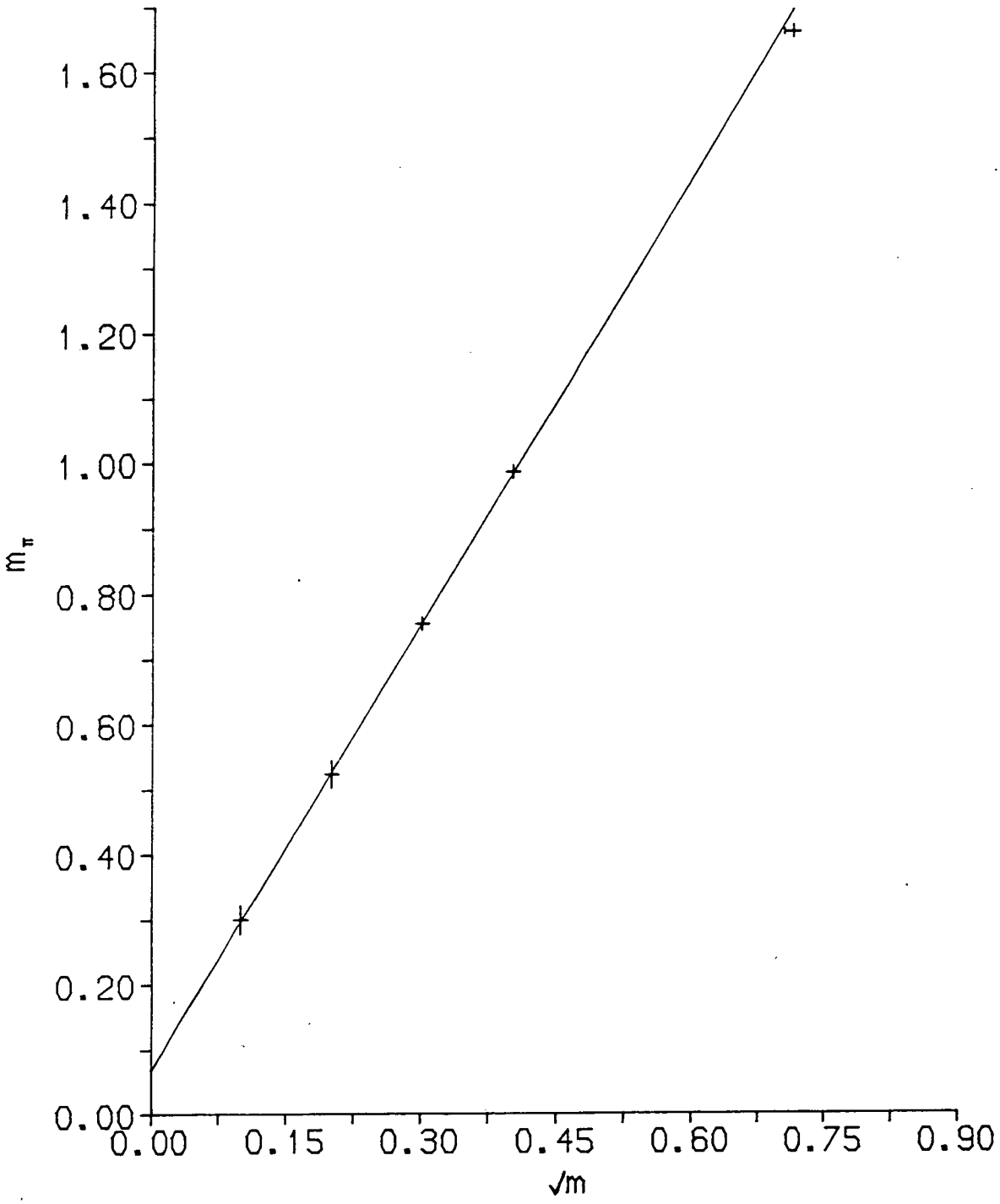

Fig. 4.9 The pion mass in lattice units on a 16^4 lattice at $\beta = 6.0$.

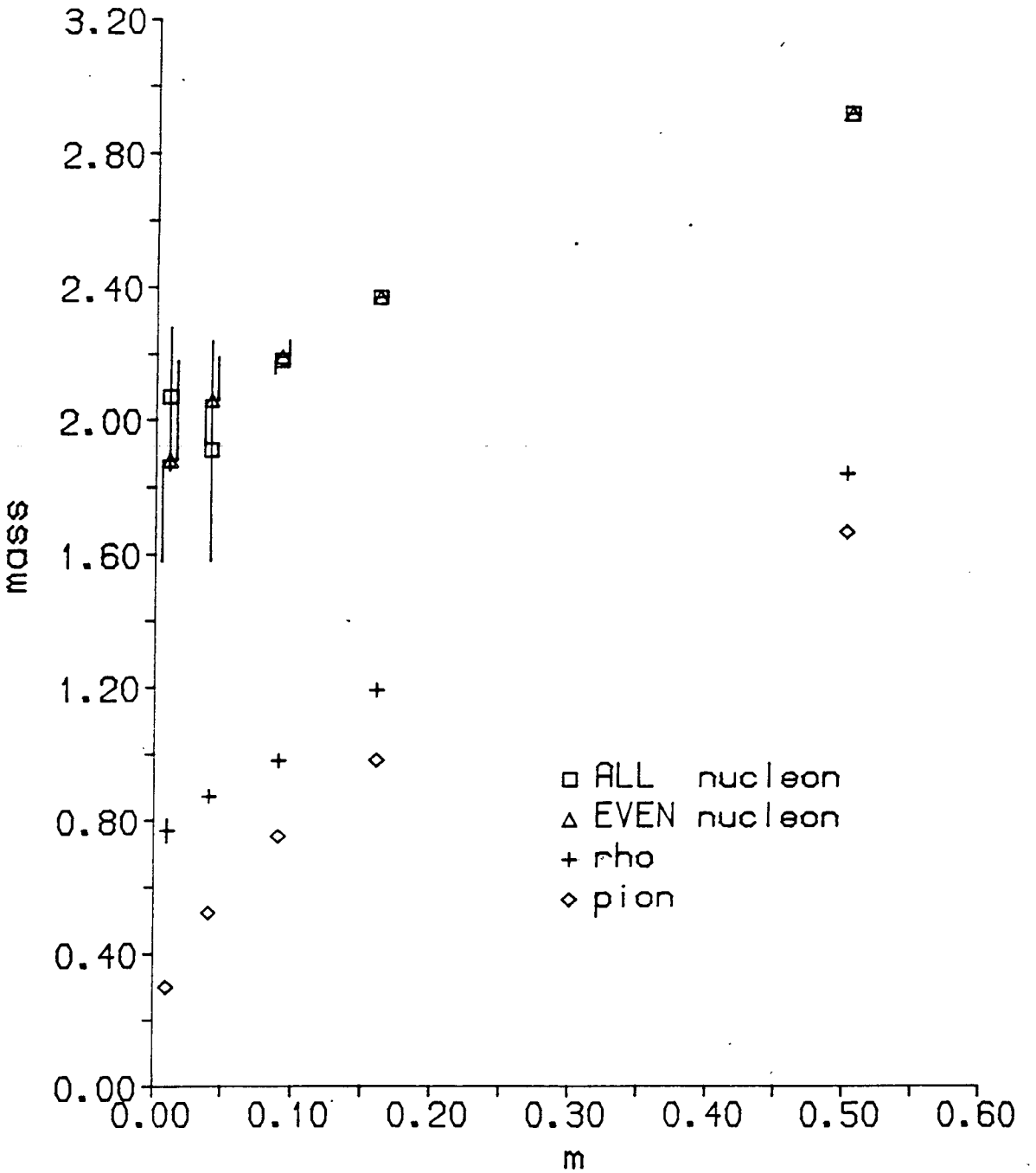

Fig. 4.10 Hadron masses in lattice units on a 16^4 lattice at $\beta = 6.0$. The pion and rho error bars are smaller than the symbol sizes.

4.4 Results at $\beta = 6.0$ on a $16^3 \times 24$ lattice

These $16^3 \times 24$ gauge configurations are constructed by periodically extending 16^4 configurations in time. Since hadron propagation over more than 16 timeslices is unobservable at our level of statistical accuracy, we do not expect this procedure to introduce any observable effects. We analyse propagators on 32 configurations, separated by 224 pseudo-heatbath sweeps. We impose Dirichlet boundary conditions in time and antiperiodic boundary conditions in space on the quark propagators (with the source on timeslice 5), and use the Iterative Block SOR algorithm described in chapter three. In all cases, our quoted errors are the standard deviation in the mean estimated from dividing the data into four consecutive bins. We perform a variety of fits to the timeslice hadron propagators in order to try to extract estimates of the ground state masses in each channel. This involves fits to sums of as many as four exponentials. A fairly clear picture emerges for the meson sector. The baryon propagators are more difficult to fit and it is unclear how reliable the resulting mass estimates are.

4.4.1 The meson sector

The results are given in table 4.4. Where comparable fits have been performed, the estimates are in very good agreement with [Barkai et al. (1985a)]. We include in tables 4.4a, b and c results from both fitting techniques described in chapter three. Typically, we see no evidence for an excitation in the oscillating channel. Consequently, we include either one or two exponentials for the direct channel (in the former case restricting the data to 'asymptotic' times) and just a single excitation in the oscillating channel. Usually, the 3-exponential fits give lower estimates for the ground state mass in the direct channel, and so we regard these as the most reliable. The pion mass estimates from 2-exponential fits to the pseudoscalar meson propagator (i.e. including an excitation) are shown in fig. 4.11. Linear dependence on $\sqrt{m}$ persists even at $m = 0.01$, from which we conclude that finite size effects are very small. We find

$$m_\pi = (2.400 \pm 0.038)\sqrt{m} + (0.006 \pm 0.014) \qquad (4.1)$$

	Mq	A1	m1		
	0.50	1.288 (8)	1.650 (1)		
PS	0.16	1.033 (17)	0.972 (1)		
1-exp	0.09	0.806 (20)	0.733 (2)		
	0.04	0.639 (29)	0.492 (2)		
	0.01	0.651 (37)	0.247 (3)		
	Mq	A1	m1	A2	m2
	0.50	1.262 (287)	1.648 (11)	0.174 (293)	2.089 (394)
PS	0.16	0.953 (63)	0.966 (5)	1.144 (257)	1.468 (779)
	0.09	0.736 (68)	0.725 (6)	1.497 (171)	1.287 (44)
	0.04	0.611 (83)	0.488 (8)	2.380 (1238)	1.252 (166)
	0.01	0.640 (264)	0.245 (13)	2.356 (3555)	1.135 (241)
	Mq	A1	m1	$\widetilde{A1}$	$\widetilde{m1}$
	0.50	2.049 (128)	1.823 (10)	-4.307 (2143)	2.497 (134)
VT	0.16	0.687 (68)	1.132 (15)	-1.378 (5586)	1.672 (172)
	0.09	0.399 (36)	0.893 (11)	-0.901 (-)	1.426 (395)
	0.04	0.272 (18)	0.709 (15)	-0.139 (5927)	0.959 (330)
	0.01	0.260 (251)	0.617 (71)	-0.010 (5)	0.317 (87)
	Mq	A1	m1	$\widetilde{A1}$	$\widetilde{m1}$
	0.50	1.350 (212)	1.896 (24)	-0.372 (127)	1.937 (37)
PV	0.16	0.326 (58)	1.147 (21)	-0.614 (836)	1.368 (98)
	0.09	0.174 (41)	0.895 (33)	-0.639 (195)	1.184 (69)
	0.04	0.097 (25)	0.686 (31)	-0.750 (292)	1.052 (62)
	0.01	0.129 (1233)	0.661 (180)	-0.775 (3677)	0.912 (182)
	Mq	A1	m1	$\widetilde{A1}$	$\widetilde{m1}$
	0.50	0.189 (177)	1.814 (61)	-0.343 (285)	1.895 (77)
SC	0.16	0.087 (29)	1.070 (36)	-0.802 (91)	1.218 (22)
	0.09	0.051 (4)	0.800 (16)	-0.872 (94)	0.984 (19)
	0.04	0.031 (10)	0.540 (19)	-0.788 (50)	0.752 (11)
	0.01	0.029 (9)	0.312 (47)	-0.266 (42)	0.366 (60)
	Mq	A1	m1	$\widetilde{A1}$	$\widetilde{m1}$
	0.50	0.551 (42)	2.922 (6)	-0.761 (698)	3.224 (104)
EVEN N	0.16	0.148 (56)	2.168 (41)	-0.746 (-)	2.523 (291)
	0.09	0.017 (18)	1.727 (93)	-0.032 (9)	1.892 (156)
	0.04	0.003 (1)	1.314 (152)	-0.004 (1)	1.401 (110)
	0.01	0.017 (124)	1.418 (341)	-0.016 (161)	1.400 (370)
	Mq	A1	m1	$\widetilde{A1}$	$\widetilde{m1}$
	0.50	0.504 (62)	2.909 (11)	-8.447 (-)	3.683 (407)
ALL N	0.16	0.156 (565)	2.174 (143)	-0.859 (382)	2.541 (143)
	0.09	0.025 (349)	1.797 (209)	-0.004 (1.717)	1.602 (371)
	0.04	0.001 (45)	1.055 (146)	-0.8d+5(87.25)	4.512 (454)
	0.01	0.026 (2)	1.332 (255)	0.5d-6(-)	0.158 (809)

Table 4.4a

Amplitudes and masses from 2-exponential fits to hadron propagators on a $16^3 \times 24$ lattice at β=6.0. The 1-exp PS and the SC were fitted using timeslices 11-19, the VT and the PV using 10-19, the PS using 9-19 and the baryons were obtained from 11-19.

Mq	m1	m2	$\widetilde{m1}$	$\widetilde{m2}$
0.50	2.882 (150)	3.024 (35)	3.177 (233)	3.547 (217)
0.16	1.752 (158)	2.373 (54)	1.190 (284)	2.404 (72)
0.09	1.193 (106)	2.219 (76)	0.893 (142)	2.239 (81)
0.04	1.018 (86)	2.140 (99)	1.055 (213)	2.140 (117)
0.01	0.935 (136)	1.801 (111)	0.594 (487)	1.798 (158)

EVEN N

Mq	A1	A2	$\widetilde{A1}$	$\widetilde{A2}$
0.50	0.263 (40)	0.417 (33)	-0.587 (-)	0.355 (-)
0.16	0.002 (800)	0.459 (107)	0.379D-5(-)	-0.400 (121)
0.09	0.772D-4(293)	0.392 (139)	0.108D-5(-)	-0.379 (140)
0.04	0.128D-3(103)	0.375 (132)	-0.945D-4(-)	0.370 (-)
0.01	0.213D-4(419)	0.212 (641)	-0.795D-5(7100)	-0.211 (597)

Mq	m1	m2	$\widetilde{m1}$	$\widetilde{m2}$
0.50	2.722 (128)	3.011 (47)	3.153 (63)	4.840 (293)
0.16	1.799 (225)	2.520 (67)	2.264 (56)	2.989 (125)
0.09	1.517 (264)	2.412 (63)	1.904 (108)	2.716 (106)
0.04	1.068 (189)	2.329 (29)	1.938 (218)	2.668 (126)
0.01	0.904 (237)	2.157 (81)	1.749 (516)	1.749 (308)

ALL N

Mq	A1	A2	$\widetilde{A1}$	$\widetilde{A2}$
0.50	0.036 (136)	0.756 (176)	-0.376 (56)	-0.697 (260)
0.16	0.005 (132)	0.848 (113)	-0.128 (57)	-0.909 (170)
0.09	0.002 (33)	0.856 (67)	-0.035 (24)	-0.955 (56)
0.04	0.428D-3 (-)	0.845 (67)	-0.066 (56)	-0.941 (96)
0.01	0.859D-3 (-)	1.553 (264)	1.046D+3(3)	-1.047D+3(2)

Table 4.4*b*

Amplitudes and masses from 4-exponential fits to baryon propagators on a $16^3 \times 24$ lattice at β=6.0. The EVEN baryons were fitted from timeslices 7-16, and the ALL using 6-16.

VT 3-exp	Mq	m1	m2	$\widetilde{m1}$
	0.50	1.806 (60)	1.966 (87)	2.062 (24)
	0.16	1.104 (37)	1.527 (55)	1.454 (18)
	0.09	0.862 (54)	1.354 (80)	1.228 (25)
	0.04	0.648 (65)	1.182 (121)	1.042 (100)
	0.01	0.352 (82)	0.845 (212)	0.530 (111)
	Mq	A1	A2	$\widetilde{A1}$
	0.50	1.534 (459)	0.909 (389)	-0.325 (31)
	0.16	0.480 (147)	1.472 (137)	-0.335 (17)
	0.09	0.271 (80)	1.288 (119)	-0.259 (14)
	0.04	0.141 (60)	1.100 (177)	-0.217 (31)
	0.01	0.015 (239)	0.669 (2395)	-0.050 (13)
SC 3-exp	Mq	m1	m2	$\widetilde{m1}$
	0.50	1.849 (63)	3.307 (630)	1.942 (58)
	0.16	1.048 (98)	2.799 (481)	1.230 (15)
	0.09	0.778 (19)	2.608 (274)	0.997 (13)
	0.04	0.525 (14)	4.236 (652)	0.773 (10)
	0.01	0.280 (54)	4.745 (684)	0.550 (41)
	Mq	A1	A2	$\widetilde{A1}$
	0.50	0.252 (78)	5.971 (-)	-0.504 (183)
	0.16	0.069 (21)	0.177D+2 (179)	-0.889 (45)
	0.09	0.040 (7)	0.196D+2 (1055)	-0.972 (51)
	0.04	0.027 (4)	0.489D+4 (6570)	-0.933 (45)
	0.01	0.032 (54)	-0.108D+4 (-)	-0.896 (2215)
PV 3-exp	Mq	m1	m2	$\widetilde{m1}$
	0.01	0.574 (154)	1.668 (447)	1.177 (49)
		A1	A2	$\widetilde{A1}$
		0.057 (898)	1.677 (383)	-1.831 (679)

Table 4.4c

Amplitudes and masses from 3-exponential fits to meson propagators on a $16^3 \times 24$ lattice at β=6.0. The VT and SC mesons were fitted from timeslices 7-18, and the 0.01 PV was 6-16.

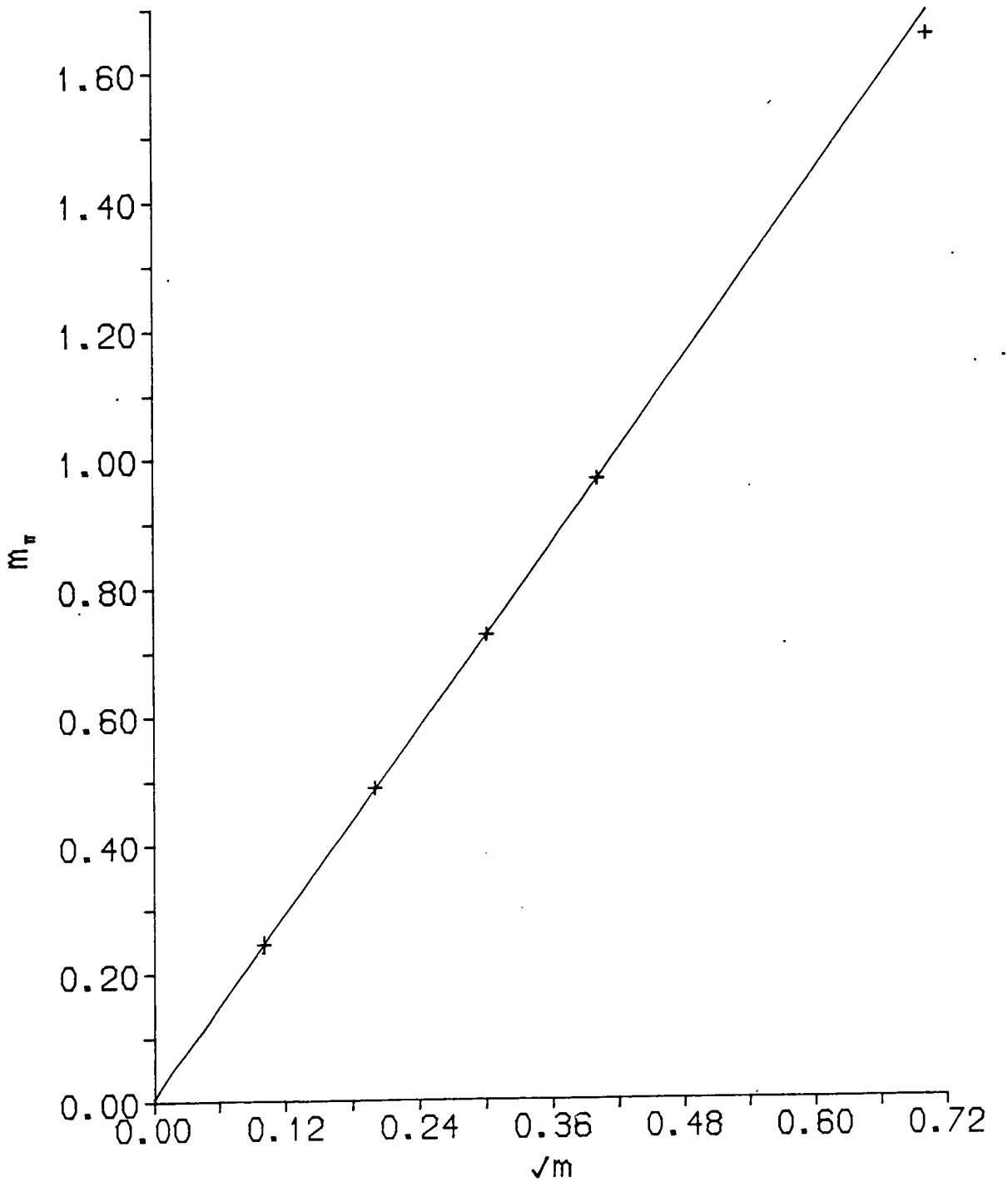

Fig. 4.11 Pion mass in lattice units on a $16^3 \times 24$ lattice at $\beta = 6.0$ plotted against $\sqrt{m}$. The error bars are smaller than the symbol size.

Comparison of these results with the 16^4 estimates in fig. 4.9 and table 4.3, reveals a finite-time effect at small quark masses, which is the origin for the discrepancy with [Barkai et al. (1985a)] mentioned in the previous section. On the longer lattice our pion mass estimates are in complete agreement with [*ibid*]. In spite of our better statistics, our quoted errors are lárger than those of [*ibid*]; this may be due to correlations in their data.

As discussed in section 2.5, the member of the pion multiplet obtained from the scalar meson propagator is not a Goldstone boson at nonzero lattice spacing, but should become degenerate with the pion from the pseudoscalar propagator (which is a Goldstone boson at $m = 0$ and non-zero lattice spacing) in the continuum limit. So the extent to which these two pion mass estimates agree is a measure of our proximity to the continuum limit. There is an oscillating channel in the scalar propagator (identified with the 0^{++}), and so in order to be able to perform a proper comparison between the two pion mass estimates, we should include at least an excitation in the direct channel. For this reason we perform 3-exponential fits to the scalar meson propagator. The two pion mass estimates thus obtained are shown in fig. 4.12. Flavour symmetry holds to about 10% for $m \leqslant 0.16$ and furthermore, the pion mass estimate from the scalar propagator extrapolates linearly in $\sqrt{m}$ to a small value which is consistent with zero within errors.

For the rho meson in the vector propagator, where we saw no evidence for asymptotic decay on the shorter lattice, the extra timeslices appear to expose the ground state. The 2-exponential fits at large times provide evidence that the resulting mass estimates are stabilizing. There is a slight drop in the rho mass when we include an excitation explicitly in that channel, although, except at $m = 0.01$, agreement with estimates from 2-exponential fits is very good. These results are in table 4.4c. The big drop in the rho mass at $m = 0.01$ from a 3-exponential fit is probably due to instability in this procedure when the data is poor. As for the pion, we obtain mass estimates for two rho mesons with different flavour components, the second one coming from the pseudovector propagator. We have performed 2-exponential fits at 'asymptotic' times for both of these and the results are shown in fig. 4.13 (the numerical values are in table 4.4a). We see that flavour symmetry has been restored to a good accuracy, in fact to within 7% at all quark masses, in agreement with the conclusions from the shorter lattice. We conclude that there are signs that flavour symmetry is beginning to be restored in the meson sector at $\beta = 6.0$. To this extent, we may be

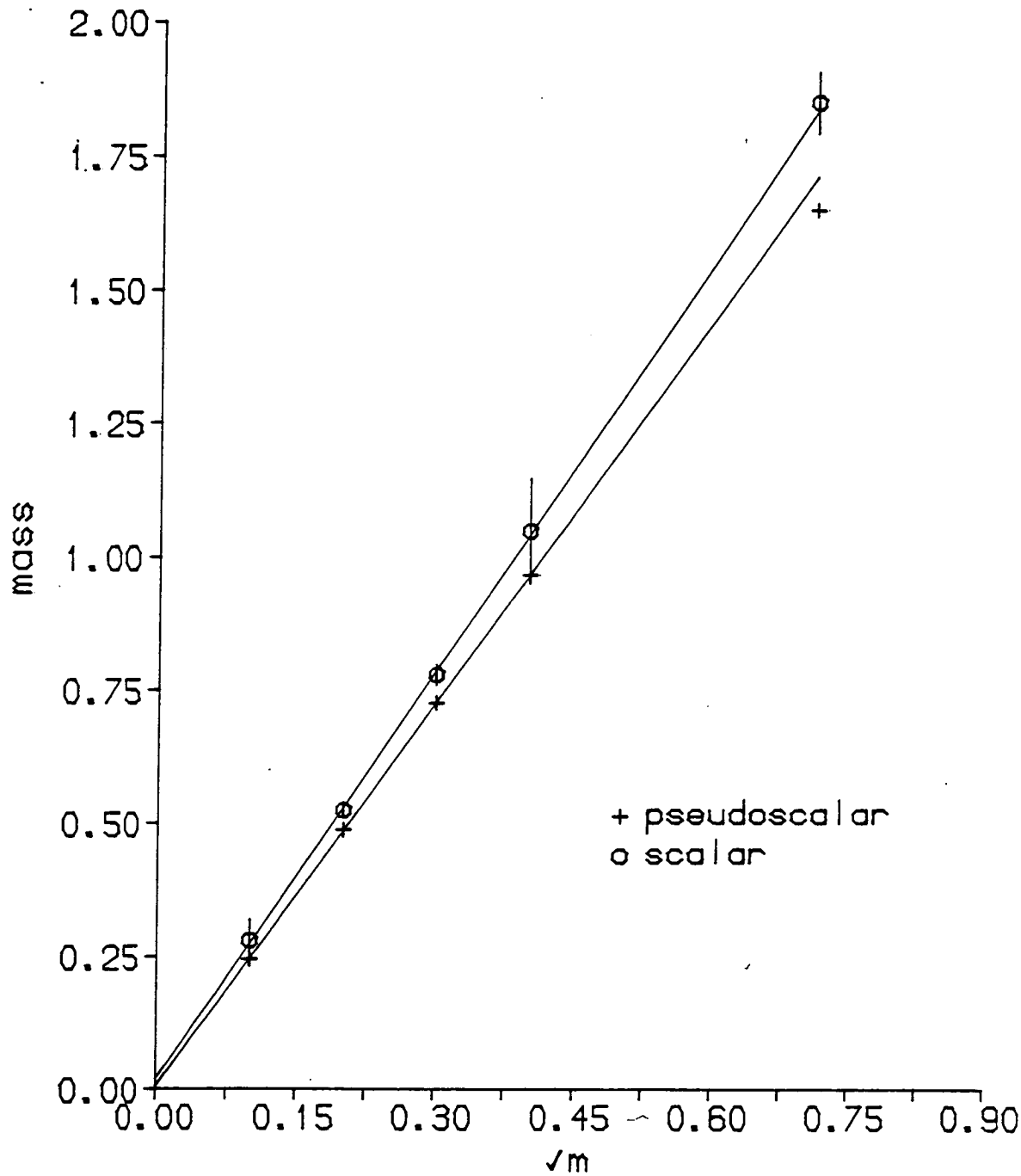

Fig. 4.1.2 Extent of flavour symmetry restoration in the pion sector on a 16^3 x 24 lattice at β = 6.0.

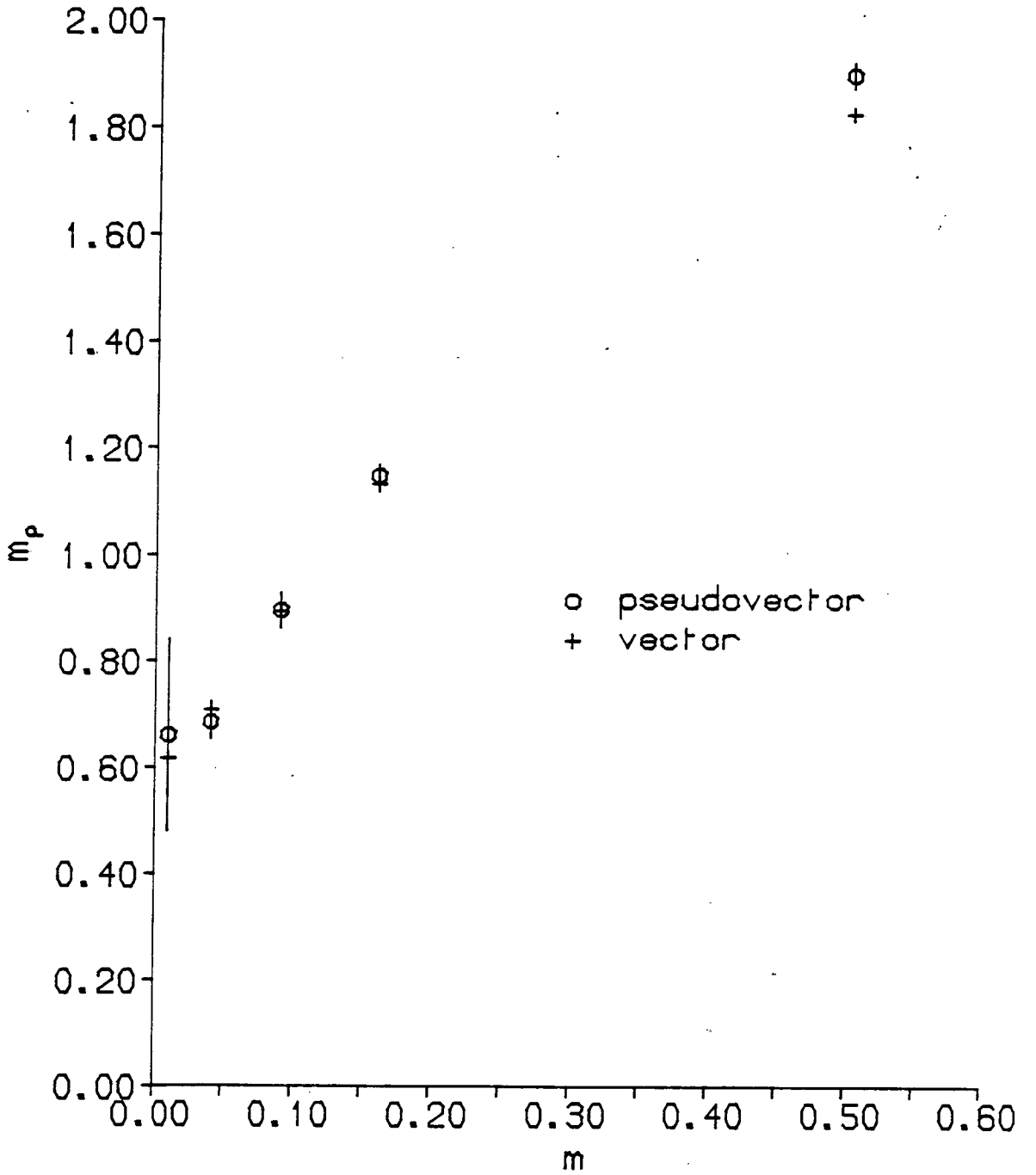

Fig. 4.13 Extent of flavour symmetry restoration in the rho meson sector on a $16^3 \times 24$ lattice at $\beta = 6.0$.

approaching the continuum limit.

4.4.2 The baryon sector

The situation in the baryon sector is not so clear. The problems appear to be exaggerated by the antiperiodic boundary conditions in space, suggesting that finite size effects are large.

We measure two baryon timeslice propagators ALL and EVEN, as described in section 2.4. According to [Morel and Rodrigues (1984)], these should be identical on an infinite lattice. Our results are plotted for the five different quark masses in fig 4.14. It is obvious that the discrepancy between ALL and EVEN increases with decreasing quark mass. However, it appears from this figure that asymptotic decay of the two propagators is similar. We find this to be true of the mass estimates from our fits, as can be seen in table 4.4.

As we found for the rho meson, there is better evidence for asymptotic decay of the baryon propagator on the longer lattice (see fig. 4.14). The mass estimates from the 2-exponential fits do appear to be stabilizing at large times, although errors become large because of a low signal-to-noise ratio. However, as can be seen from the values in table 4.4a, the resulting nucleon mass estimates are in serious disagreement with [Barkai et al. (1985a)], the discrepancy getting worse as the quark mass decreases. The only significant difference between [*ibid*] and the present study is their use of periodic boundary conditions in space. Given the difference, mentioned above, between the EVEN and ALL propagators when antiperiodic boundary conditions are used, it is possible that this is the reason for the discrepancy. This will be investigated in the next section.

In order to investigate the baryons more thoroughly, we perform 4-exponential fits on both the EVEN and ALL baryon propagators, with the results given in table 4.4b. We find a large contribution coming from the excited states in both the direct and oscillating channels for both propagators. For the EVEN propagator the two excitations are degenerate in mass and amplitude to a surprising accuracy. Notwithstanding the relative size of the amplitudes of the ground and excited states, fig 4.14 indicates that asymptotic decay with the ground state mass is just observable on the $16^3 \times 24$ lattice. However, the excitation dominates over most of the range for which we are able to obtain reliable fits and so is responsible for the overly high mass

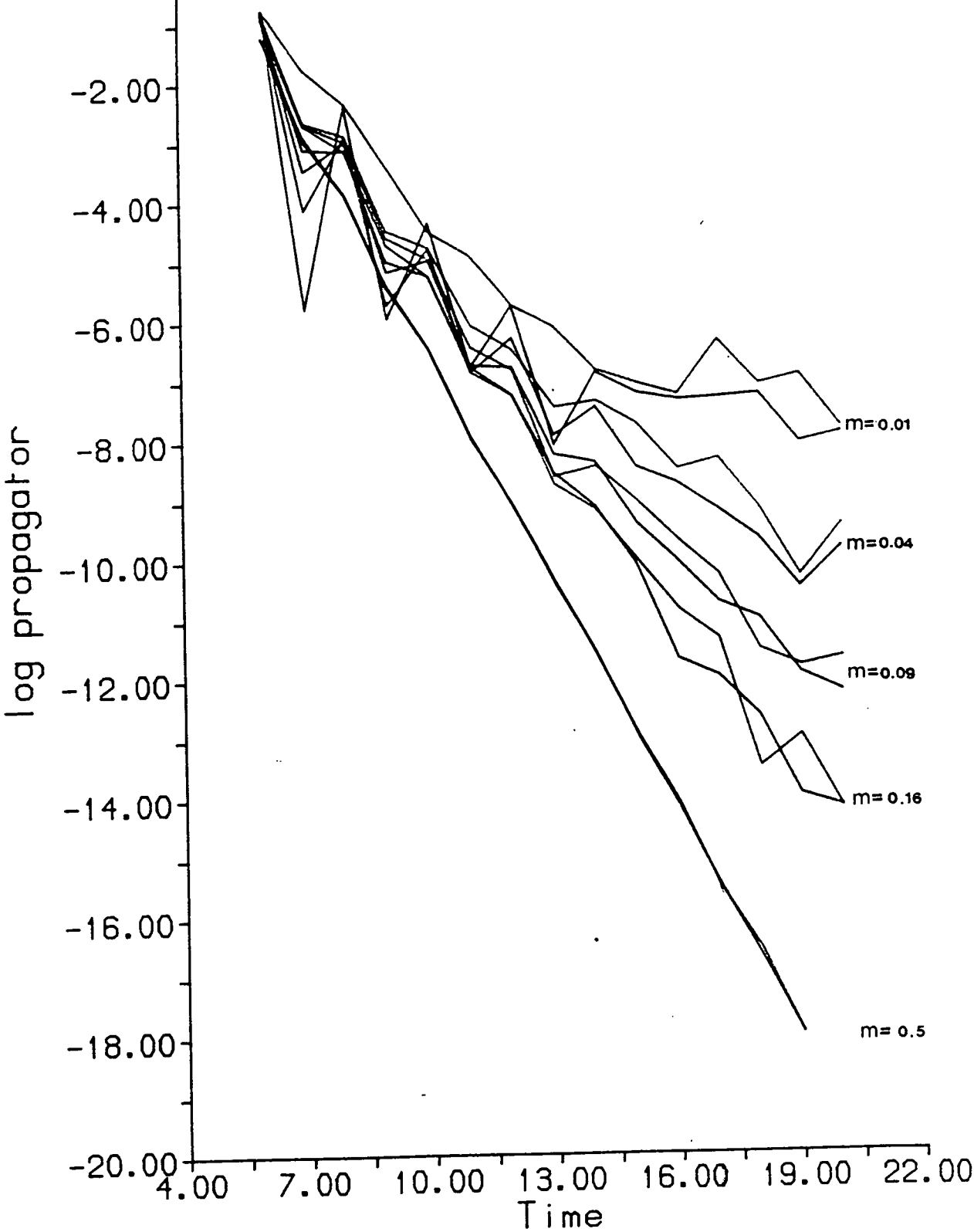

Fig. 4.14 EVEN and ALL baryon timeslice propagators for five different quark masses on a $16^3 \times 24$ lattice at $\beta = 6.0$, using antiperiodic spatial boundary conditions. (32 configurations)

estimates found with only 2-exponentials (this phenomenon has also been observed with periodic boundary conditions [Itoh et al. (1986d)]). The ground state amplitudes and masses that we get from the 4-exponential fits are in agreement with [Barkai et al. (1985a)]. Hence it appears that imposing antiperiodic boundary conditions in space enhances a large 'parity-doublet' excitation in the local EVEN baryon propagator. The contributions of the excitation in the ALL propagator are also large, but appear not to be degenerate in mass, although this propagator is noisier, so that the excitations are not so easy to extract. The ground state masses obtained from 4-exponential fits to the ALL propagator are in good agreement with those from the EVEN propagator, so it may be that the symmetry of [Morel and Rodrigues (1984)] is manifested only in the ground states in our data.

The full results for the pion, rho and nucleon masses are shown in fig. 4.15, plotted against quark mass. The ratio of the nucleon to rho mass is plotted versus the ratio of the pion to rho mass in fig. 4.16. The numerical values are given in table 4.5.

m_q	m_π/m_ρ	m_N/m_ρ
0.50	0.913 (36)	1.596 (111)
0.16	0.875 (29)	1.587 (156)
0.09	0.841 (49)	1.384 (129)
0.04	0.753 (107)	1.571 (108)
0.01	0.427 (93)	1.629 (630)

Table 4.5 Ratios of hadron masses at β = 6.0 (the ρ mass is taken from VT propagator except at m = 0.01 where it is from the PV propagator)

We see that, compared to our results at β = 5.7, the nucleon to rho mass ratio

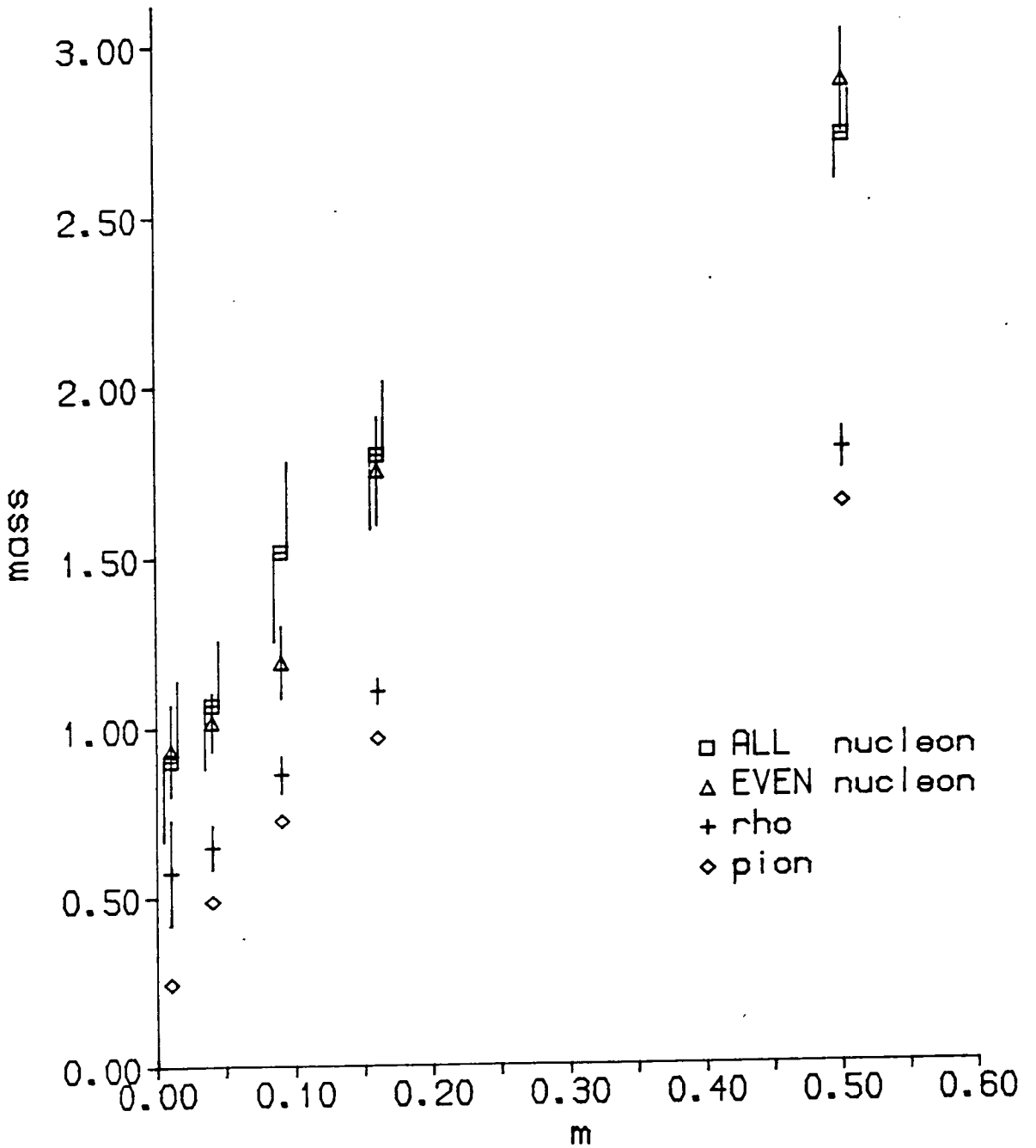

Fig. 4.15 Hadron masses in lattice units on a $16^3 \times 24$ lattice at $\beta = 6.0$. The pion error bars are smaller than the symbol size.

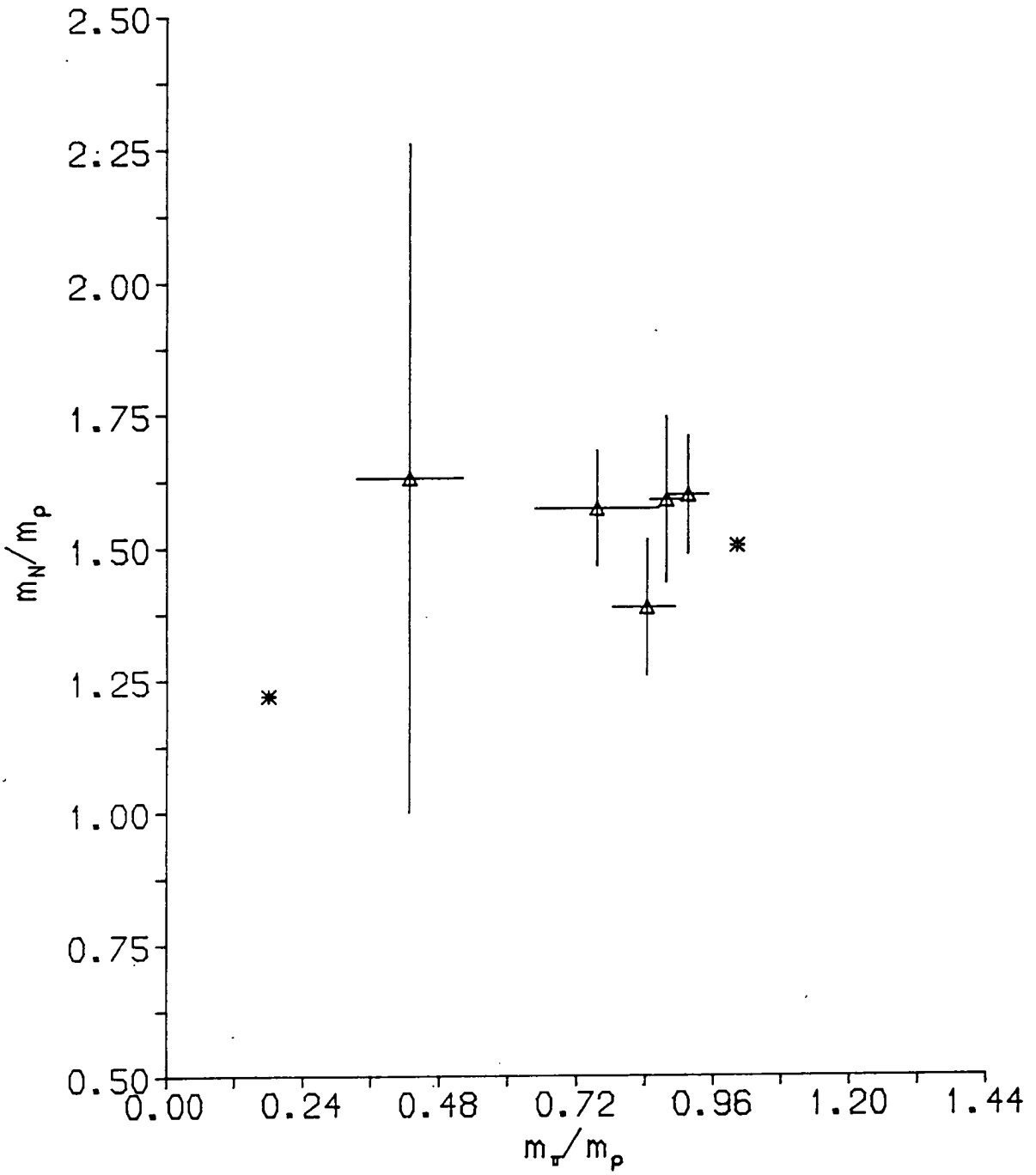

Fig 4.16 Mass ratios at $\beta = 6.0$; the starred points are the experimental and infinitely-heavy quark values.

is lower at β = 6.0 and may be showing signs of crossing over from the heavy quark limit, but the errors are still too large to draw firm conclusions.

4.5 Results at β = 6.15 on a $16^3 \times 24$ lattice

The results in this section were obtained from a set of twenty-four full $16^3 \times 24$ gauge configurations with periodic boundary conditions, separated by 176 pseudo-heat bath sweeps, and gauge fixed to temporal gauge. We imposed periodic spatial boundary conditions and Dirichlet boundary conditions in time on the quark propagators. In order to assess the effect of the spatial boundary conditions (any effect being a finite size effect) we also recomputed quark propagators on eight of the twenty-four configurations using *antiperiodic* boundary conditions.

4.5.1 The meson sector

The PS propagator averaged over twenty-four configurations is fitted using both 1-exponential and 2-exponential fits and the data is shown in table 4.6. Excitations appear to be still present in the data at timeslice 12 (i.e. seven timeslices from the source), so that the 2-exponential fit is necessary to extract the ground state. These estimates for the pion mass are plotted in fig 4.17 and lie on a curve through the origin suggesting that finite size effects are very small at these quark masses. From a fit to data at the lowest four quark masses we find

$$m_\pi = (0.725 \pm 0.236)\, m + (2.003 \pm 0.122)\sqrt{m} + (-0.006 \pm 0.016) \qquad (4.2)$$

Unlike the results at β = 6.0, there is now a term quadratic in $\sqrt{m}$ but this term is less important at low quark mass, and we must remember that because we have chosen to keep the values of the quark mass fixed in lattice units, the corresponding physical values are now *higher* than at β = 6.0 since a, the lattice spacing, has decreased. We would thus expect linear behaviour with $\sqrt{m}$ to set in at correspondingly lower values of the quark mass in lattice units. Looking now at fig 4.18, where the PS propagators from the eight configurations on which we have computed propagators both for periodic and

	Mq	A1	m1	A2	m2
	0.50	1.159 (32)	1.640 (1)		
PS	0.16	0.679 (13)	0.930 (1)		
1-exp	0.09	0.452 (7)	0.680 (1)		
	0.04	0.300 (10)	0.436 (3)		
	0.01	0.250 (13)	0.206 (7)		
	Mq	A1	m1	A2	m2
	0.50	1.129 (145)	1.638 (7)	0.408 (1272)	2.065 (277)
PS	0.16	0.528 (40)	0.911 (5)	1.260 (210)	1.301 (50)
	0.09	0.356 (17)	0.661 (2)	1.402 (264)	1.130 (41)
	0.04	0.256 (8)	0.423 (2)	1.510 (293)	1.004 (33)
	0.01	0.238 (14)	0.202 (6)	1.926 (611)	1.049 (111)
	Mq	A1	m1	$\widetilde{A1}$	$\widetilde{m1}$
	0.50	1.421 (82)	1.764 (6)	-1.889 (3624)	2.325 (169)
VT	0.16	0.351 (35)	1.017 (15)	-0.011 (12)	0.971 (120)
	0.09	0.189 (12)	0.764 (12)	-0.014 (6)	0.764 (92)
	0.04	0.105 (12)	0.543 (18)	-0.008 (86)	0.493 (174)
	0.01	0.062 (47)	0.384 (77)	-0.011 (-)	0.340 (892)
	Mq	A1	m1	$\widetilde{A1}$	$\widetilde{m1}$
	0.50	0.793 (46)	1.801 (11)	-0.160 (196)	1.823 (102)
PV	0.16	0.119 (22)	0.991 (25)	-0.108 (39)	1.089 (60)
	0.09	0.069 (5)	0.741 (13)	-0.101 (30)	0.861 (55)
	0.04	0.049 (50)	0.532 (8)	-0.058 (72)	0.607 (78)
	0.01	0.029 (197)	0.344 (130)	-0.025 (12)	0.333 (42)
	Mq	A1	m1	$\widetilde{A1}$	$\widetilde{m1}$
	0.50	0.150 (53)	1.771 (53)	-0.443 (173)	1.929 (51)
SC	0.16	0.045 (5)	0.970 (10)	-0.560 (50)	1.141 (12)
	0.09	0.025 (5)	0.686 (13)	-0.571 (26)	0.902 (6)
	0.04	0.016 (4)	0.426 (17)	-0.611 (126)	0.705 (36)
	0.01	0.013 (8)	0.224 (34)	-0.238 (-)	0.398 (201)
	Mq	A1	m1	$\widetilde{A1}$	$\widetilde{m1}$
	0.50	0.326 (44)	2.805 (6)	-0.071 (11)	2.880 (52)
EVEN N	0.16	0.012 (1)	1.627 (19)	-0.008 (3)	1.723 (49)
	0.09	0.004 (1)	1.226 (21)	-0.003 (1)	1.332 (40)
	0.04	0.110(13)D-2	0.865 (24)	-0.120(18)D-2	0.960 (29)
	0.01	0.366(235)D-3	0.568 (63)	-0.765(118)D-2	0.688 (24)
	Mq	A1	m1	$\widetilde{A1}$	$\widetilde{m1}$
	0.50	0.294 (48)	2.797 (14)	-0.041 (10)	2.798 (74)
ALL N	0.16	0.014 (2)	1.643 (23)	-0.009 (8)	1.753 (69)
	0.09	0.358(52)D-2	1.242 (21)	-0.416(303)D-2	1.390 (63)
	0.04	0.970(213)D-3	0.862 (32)	-0.328(472)D-2	1.103 (97)
	0.01	0.229(18)D-3	0.510 (240)	-0.732(455)D-3	0.669 (82)

Table 4.6

Amplitudes and masses from 2-exponential fits to hadron propagators on a $16^3 \times 24$ lattice at β=6.15. The 1-exp PS was fitted using timeslices 12-19; the PS using 9-19 and the SC using 11-19. The VT was obtained from 12-19 for m = 0.5,0.16 and 0.09, and 11-19 for m = 0.04 and 0.01. The PV and ALL both used 11-19 for m = 0.5,0.16 and 0.09, and 12-19 for 0.04 and 0.01. EVEN was obtained from 11-19 apart from the lowest mass where 12-19 was used.

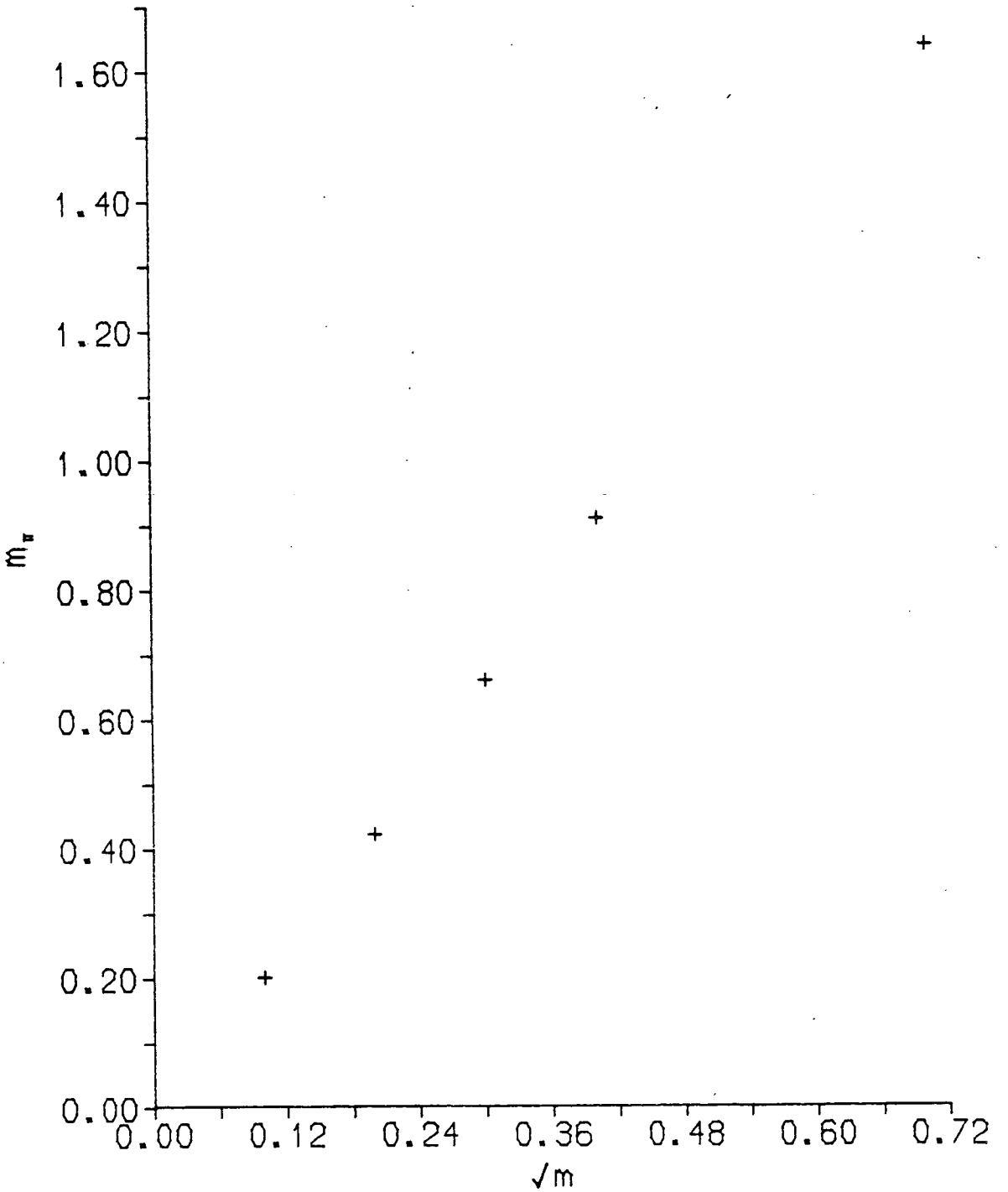

Fig. 4.17 The pion mass in lattice units at β = 6.15. The error bars are smaller than the symbol size.

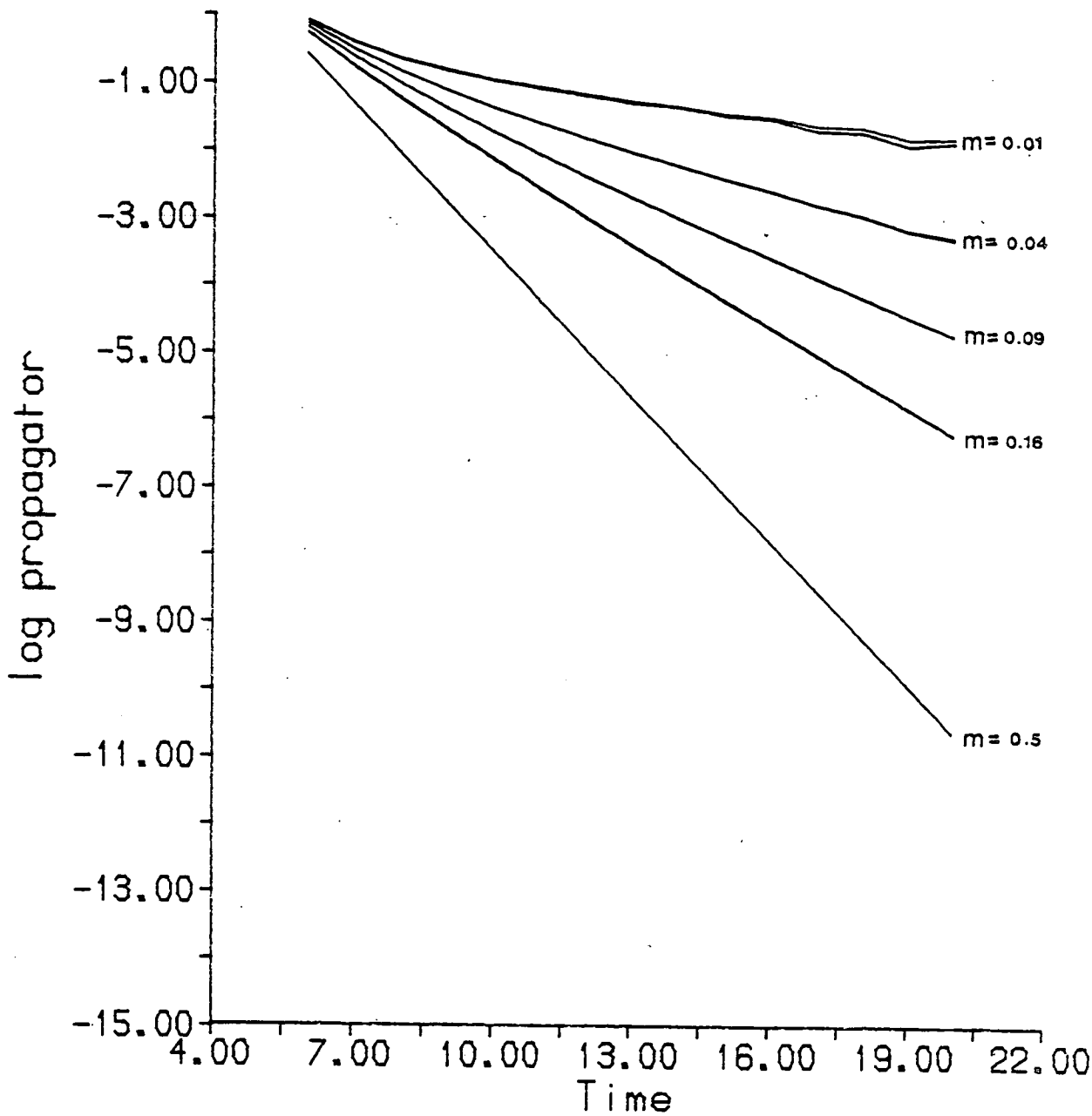

Fig. 4.18 The PS meson timeslice propagator at five different values of the quark mass for both periodic and antiperiodic spatial boundary conditions at β =6.15.

antiperiodic boundary conditions are plotted, we see that the choice of boundary conditions has no effect on the PS propagator, confirming the absence of finite size effects. Fig 4.19 shows the pion from both the PS and the SC propagators, and we see that flavour symmetry holds better than at at $\beta = 6.0$; for $m \lesssim 0.16$ the symmetry holds to within 6%. The SC data does extrapolate to zero within errors but has a higher curvature than the PS data and appears to be more affected by finite size effects - as we can see from fig 4.20 (however, the SC propagator also contains the δ meson so we cannot compare directly the effect of the boundary conditions on the pion content). From a similar fit to (4.2), we find for the SC pion

$$m_{\pi}(SC) = (2.050 \pm 1.259)m + (1.473 \pm 0.733)\sqrt{m} + (0.054 \pm 0.092) \qquad (4.3)$$

The large errors in these coefficients are almost entirely due to the relatively large error in the pion mass estimate at $m = 0.01$.

Fig. 4.21 indicates that, as for the PS propagator, the finite size effects on the VT propagator are small and any discrepancies at low quark mass may well be statistical, due to this comparison using only eight configurations. For the full twenty-four configurations 2-exponential fits were sufficient to extract estimates for the rho mass from both the VT and the PV propagators, and the results are given in table 4.6. Fig. 4.22 demonstrates that flavour symmetry is excellent - there is a 2% discrepancy at $m = 0.5$ which however corresponds to a very high physical quark mass. This effect is also observed at all other β values and lattice sizes in this chapter and the 2% discrepancy compares well with the figure of 7% seen at $\beta = 6.0$.

4.5.2 Baryons and finite size effects

Here we use the same set of eight configurations to obtain EVEN baryon propagators using both periodic and antiperiodic spatial boundary conditions. Obviously, if we had large enough lattices the choice of boundary conditions (BC) would have a negligible effect, so a comparison between the propagators obtained from each choice is an important indication of the extent of the finite size effects. Carpenter and Baillie [Carpenter and Baillie (1985)] have shown that for free Wilson fermions on lattices infinite in the time direction the propagator is bounded above and below by the periodic BC propagator and the antiperiodic BC propagator respectively. This is shown in fig. 4.23, taken

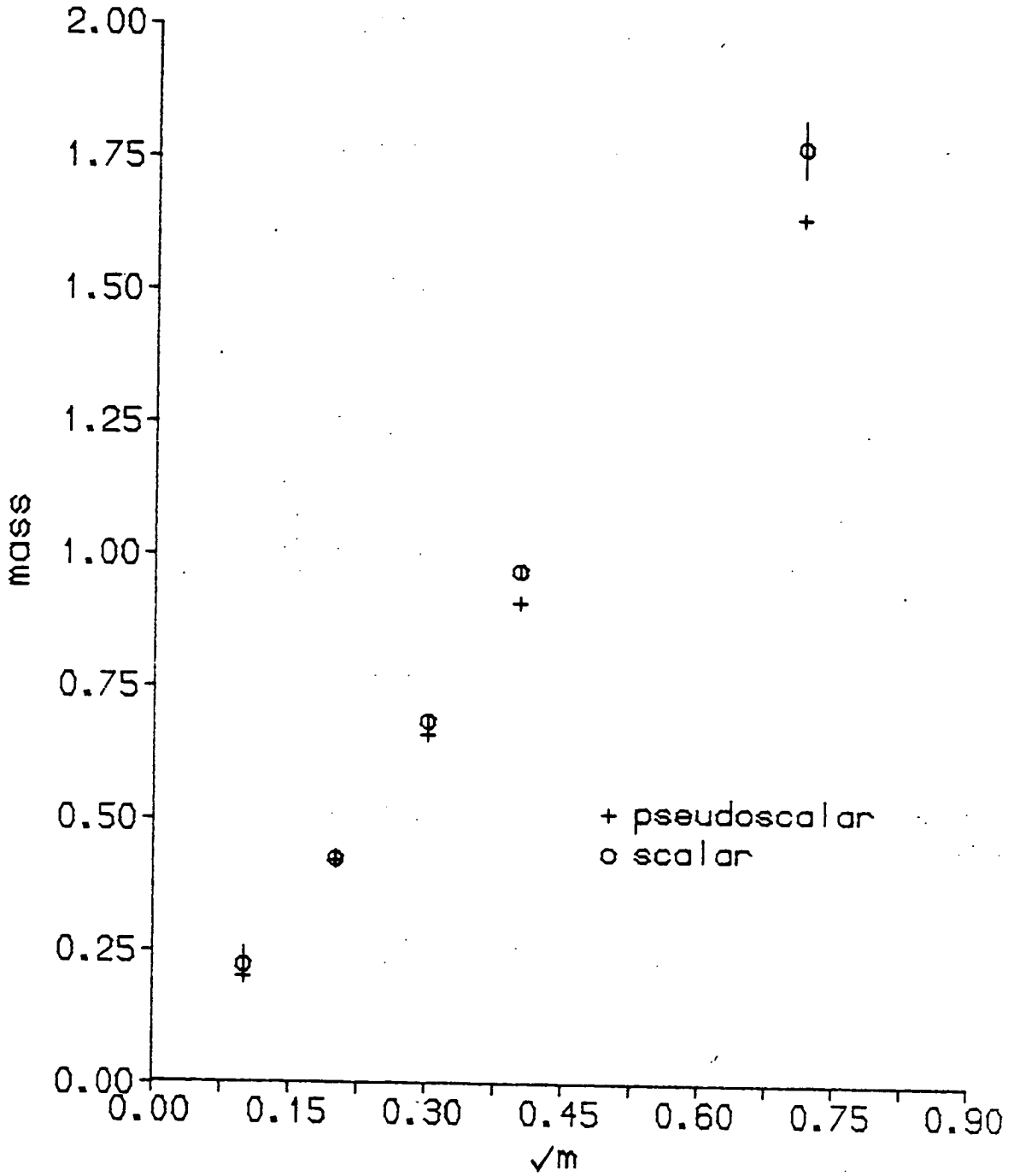

Fig. 4.19. Extent of flavour symmetry restoration in the pion sector at $\beta = 6.15$.

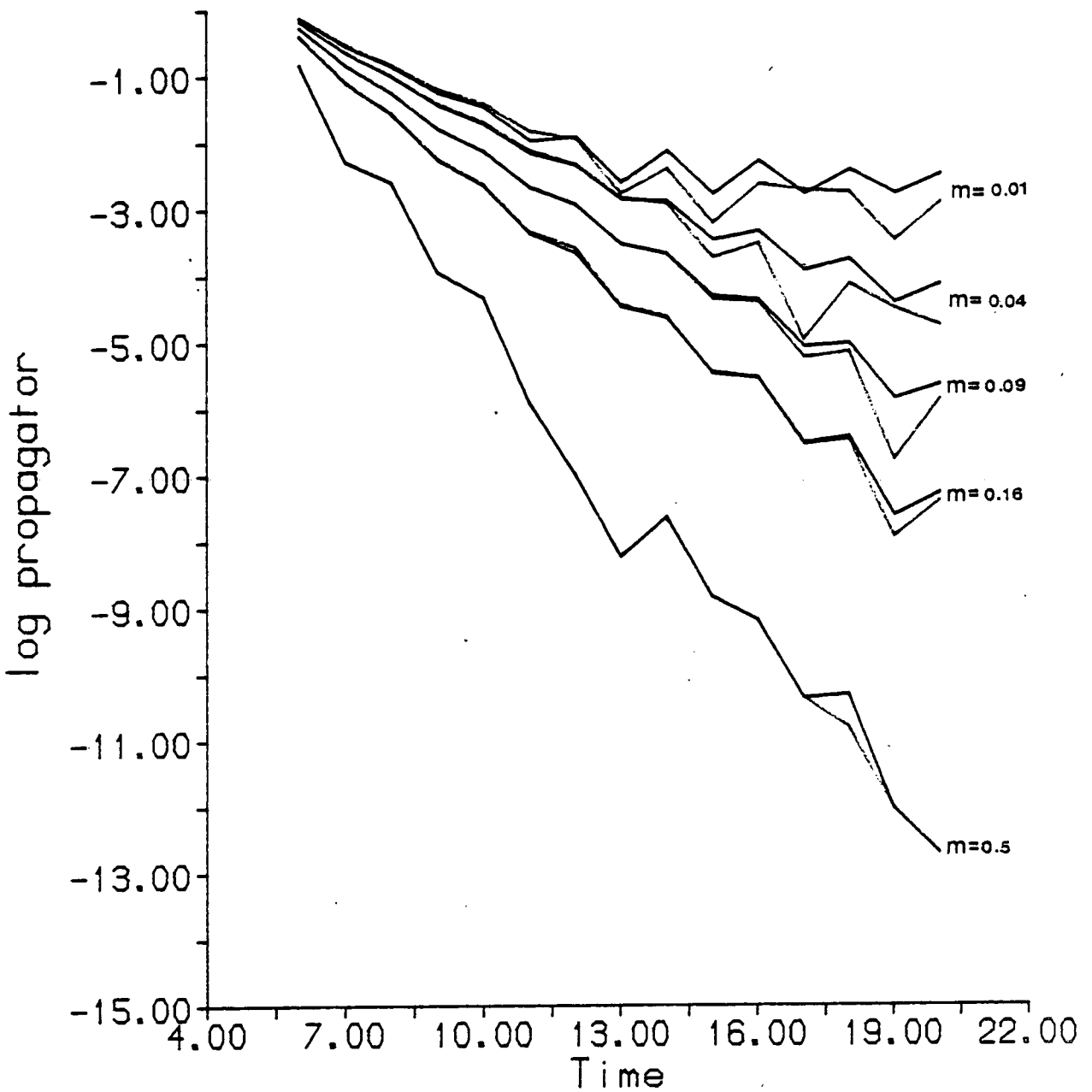

Fig 4.20 SC meson timeslice propagator at five different values of the quark mass for periodic and antiperiodic boundary conditions at $\beta = 6.15$

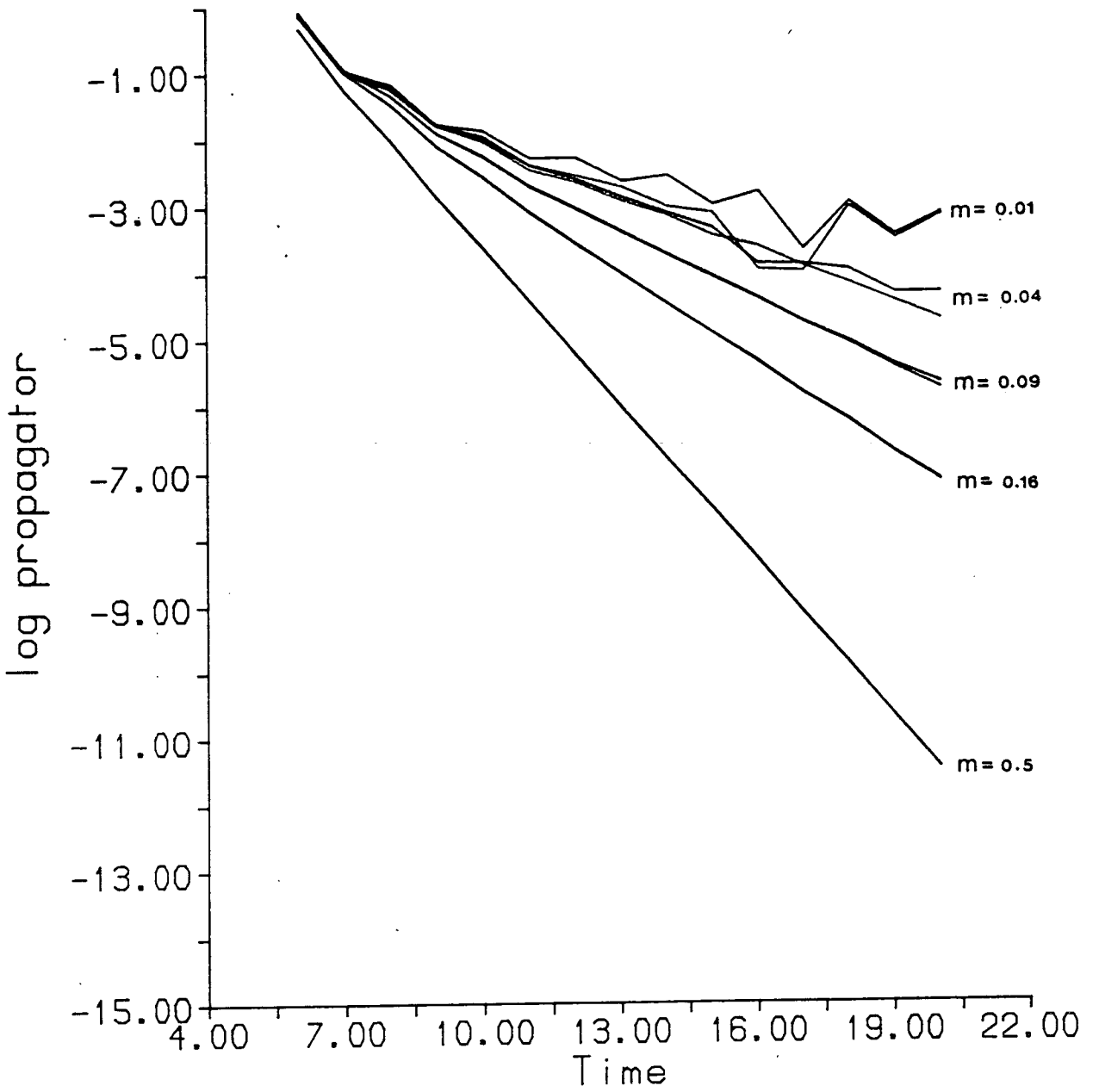

Fig. 4.21. VT meson timeslice propagator at five different values of the quark mass for periodic and antiperiodic boundary conditions at $\beta = 6.15$.

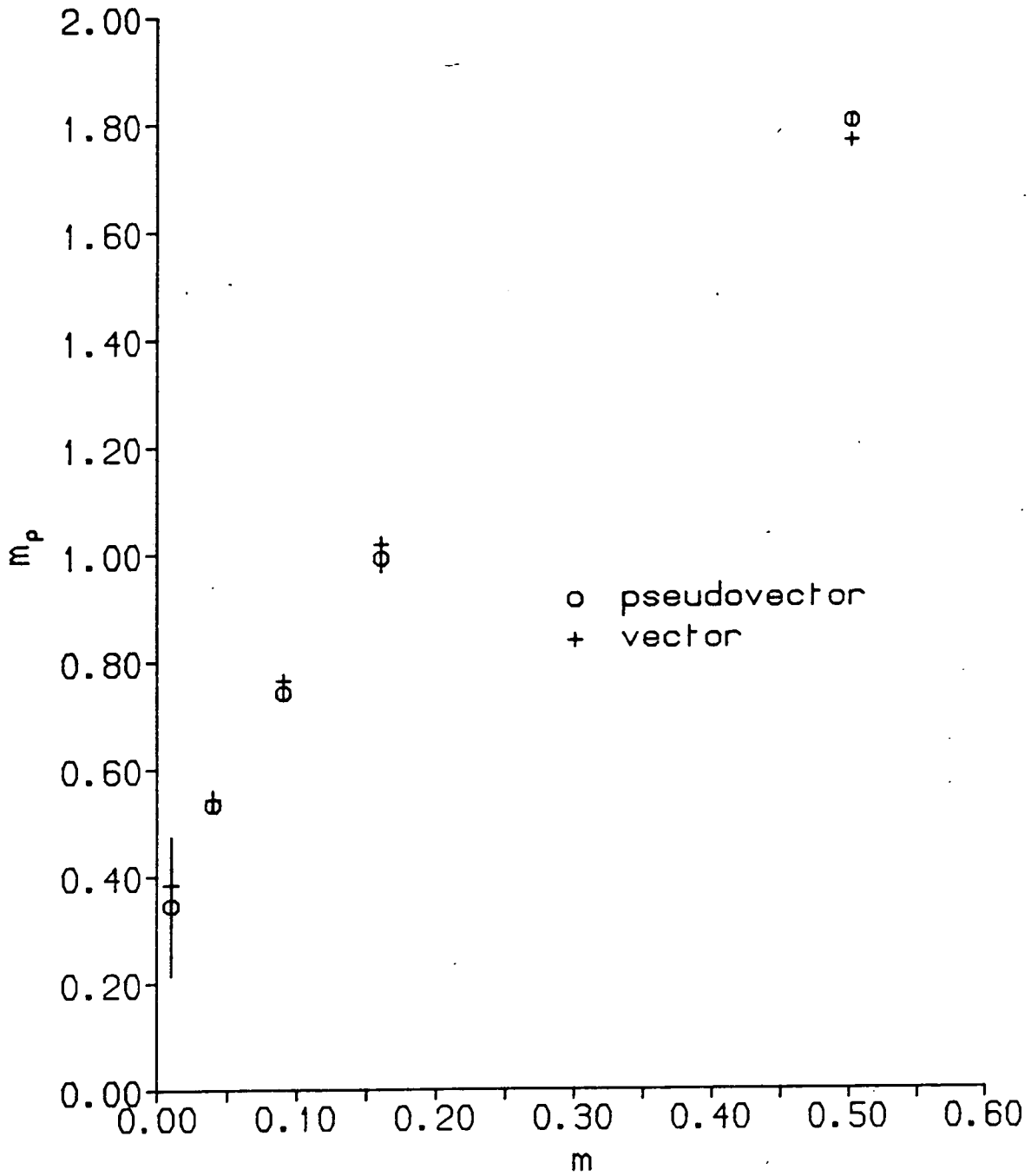

Fig. 4.22. Extent of flavour symmetry restoration in the rho meson sector at β = 6.15.

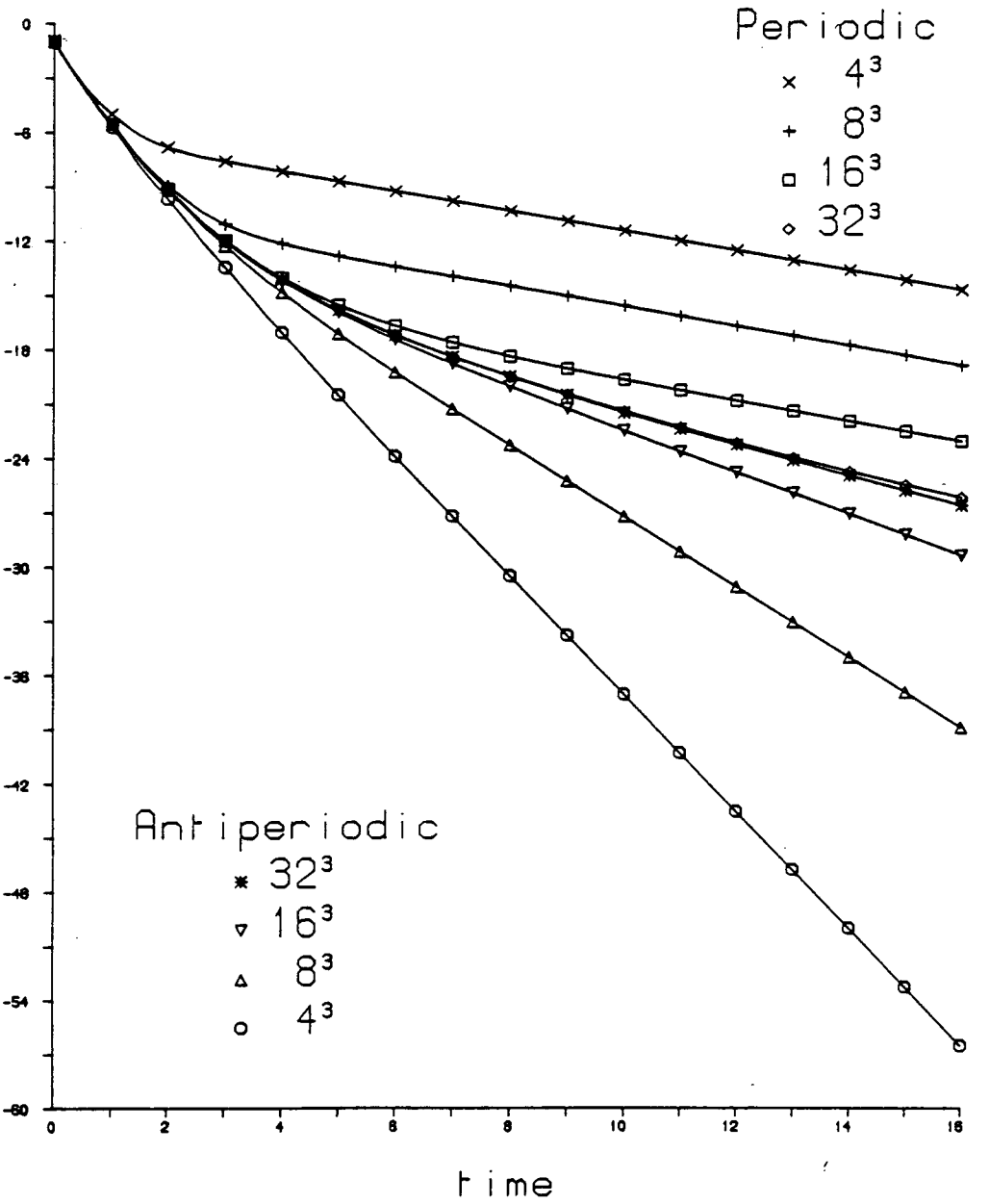

Fig 4.23 Natural log of the proton propagator for free Wilson fermions at a quark mass of 0.2 for t $=\infty$ and various spatial lattice sizes.

from [Carpenter and Baillie (1985)]. Figs 4.24a-e show the corresponding results on a $16^3 \times 24$ lattice at $\beta = 6.15$ for the EVEN propagator using five values of the quark mass. There appear to be large finite size effects, and the disagreement in the propagators obtained from the two choices of BC increases as we lower the quark mass. The signal from the periodic BC propagator is larger than from the antiperiodic BC propagator at all values of the quark mass, as found in the free fermion case by [Carpenter and Baillie (1985)]. The antiperiodic propagator is noisier than the periodic but taking statistical fluctuations into account the asymptotic decays are similar. At short times, the antiperiodic propagators fall much faster and this shows up in the fits as a larger contamination by excited states.

Another important estimate of the finite size effects is the degree to which the EVEN and ALL propagators are equal. As we saw in chapter two, on an infinite lattice the two propagators should be identical, but for free fermions on finite lattices this identity does not hold for antiperiodic boundary conditions. For a confining theory, violation of this identity must be a finite size effect : if our box size is about the size of a proton, then the quarks inside are approximately free and we would expect to see the same sort of violation of the identity as for free fermions. The proton size presumably increases as the quark mass decreases. As we can see from fig. 4.25, the identity appears to be satisfied for periodic boundary conditions in this case. However, fig 4.26 shows that for antiperiodic BC EVEN and ALL are not the same, the discrepancy increasing with decreasing quark mass, and becoming very pronounced at short times. We are thus forced to conclude from these two independent estimates, that finite size effects are considerable for this choice of $\beta = 6.15$ and 16^3 lattices.

4.5.2 Baryon mass estimates at $\beta = 6.15$

We have EVEN and ALL propagators for 24 gauge configurations using periodic spatial boundary conditions, and fig. 4.27 indicates that the two are almost identical (with the exception of one point which we take to be a statistical fluctuation). Not surprisingly therefore, the mass estimates for the nucleon obtained from each propagator are in complete agreement. This is shown in table 4.6 and fig 4.28. 2-exponential fits appeared to be sufficient to expose the ground state as, where tested, 4-exponential fits gave similar

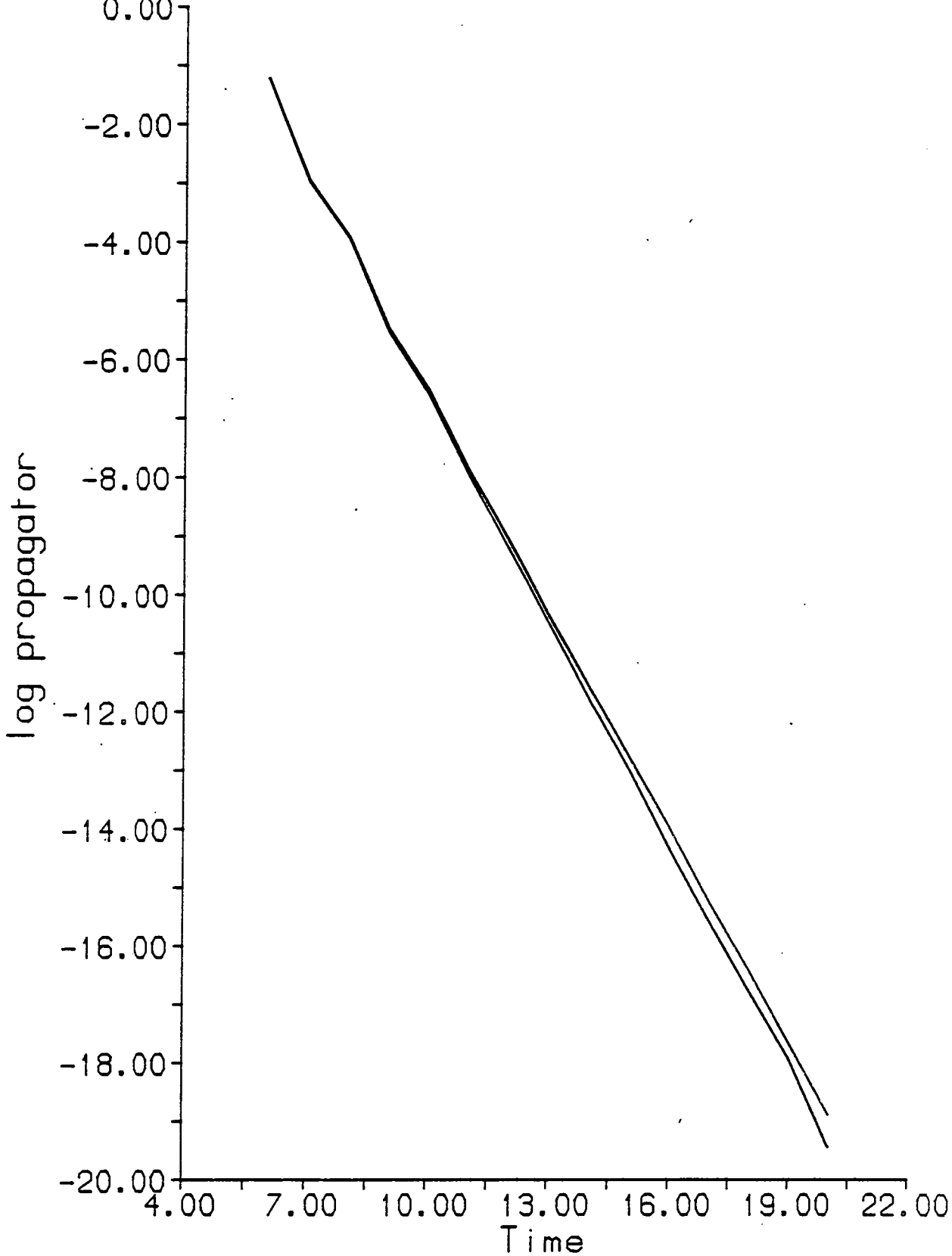

Fig. 4.24a The EVEN baryon timeslice propagator at a quark mass of 0.5 for both periodic and antiperiodic spatial boundary conditions at β =6.15.

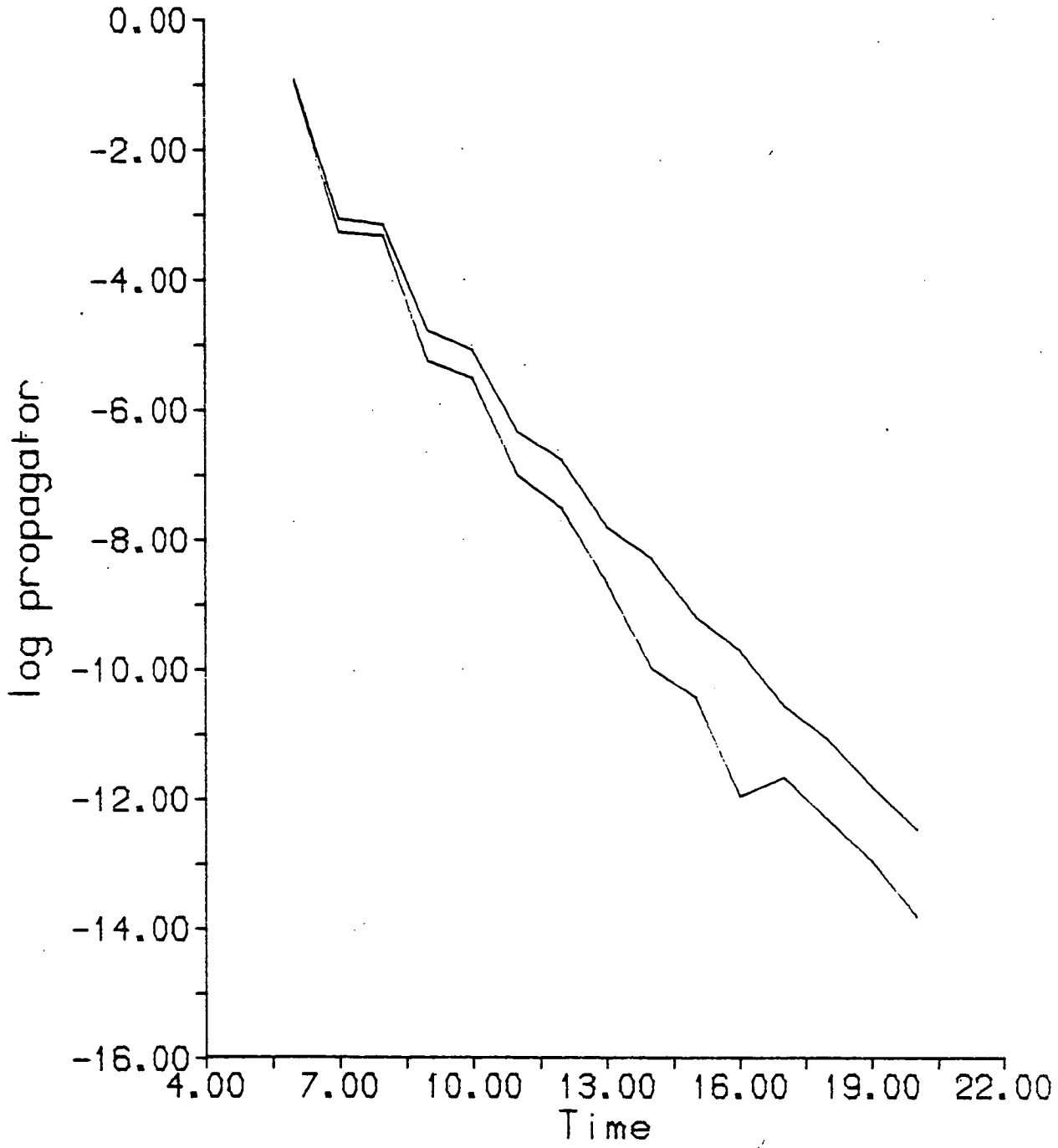

Fig. 4.24b The EVEN baryon timeslice propagator at a quark mass of 0.16 for both periodic and antiperiodic spatial boundary conditions at β =6.15. The numerically higher propagator is from periodic boundary conditions.

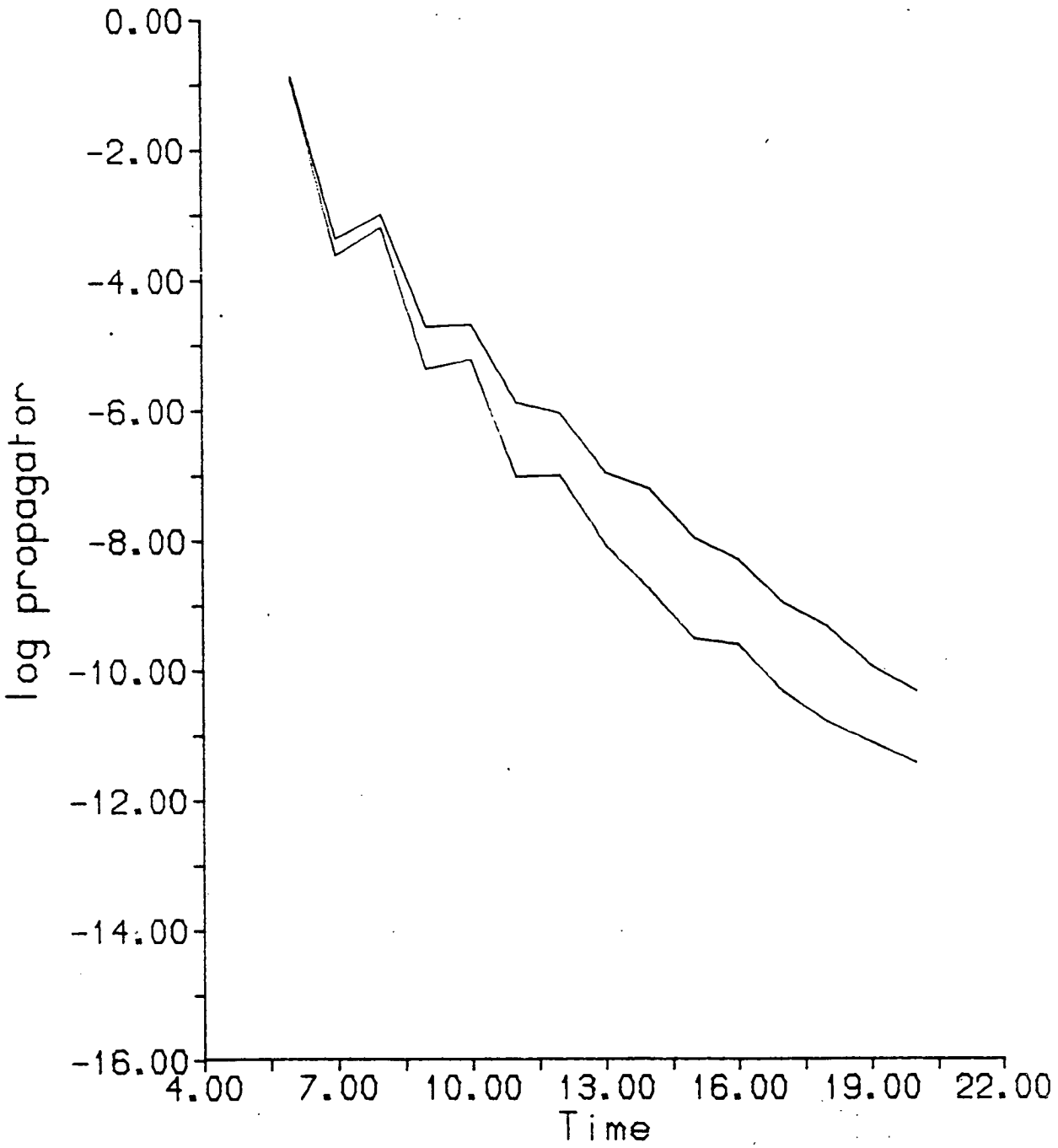

Fig. 4.24c The EVEN baryon timeslice propagator at a quark mass of 0.09 for both periodic and antiperiodic spatial boundary conditions at β =6.15. The numerically higher propagator is from periodic boundary conditions.

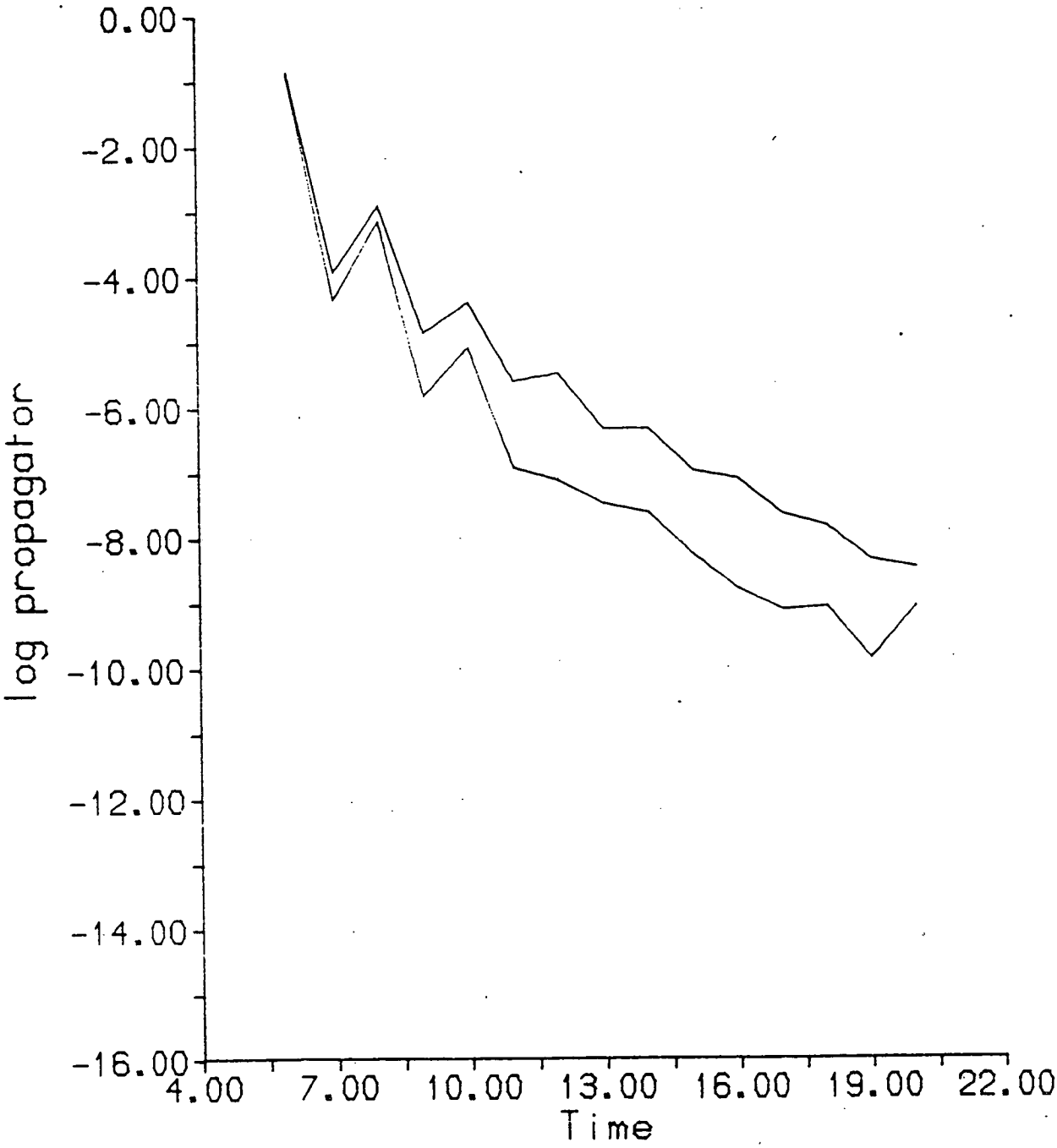

Fig. 4.24d The EVEN baryon timeslice propagator at a quark mass of 0.04 for both periodic and antiperiodic spatial boundary conditions at β =6.15. The numerically higher propagator is from periodic boundary conditions.

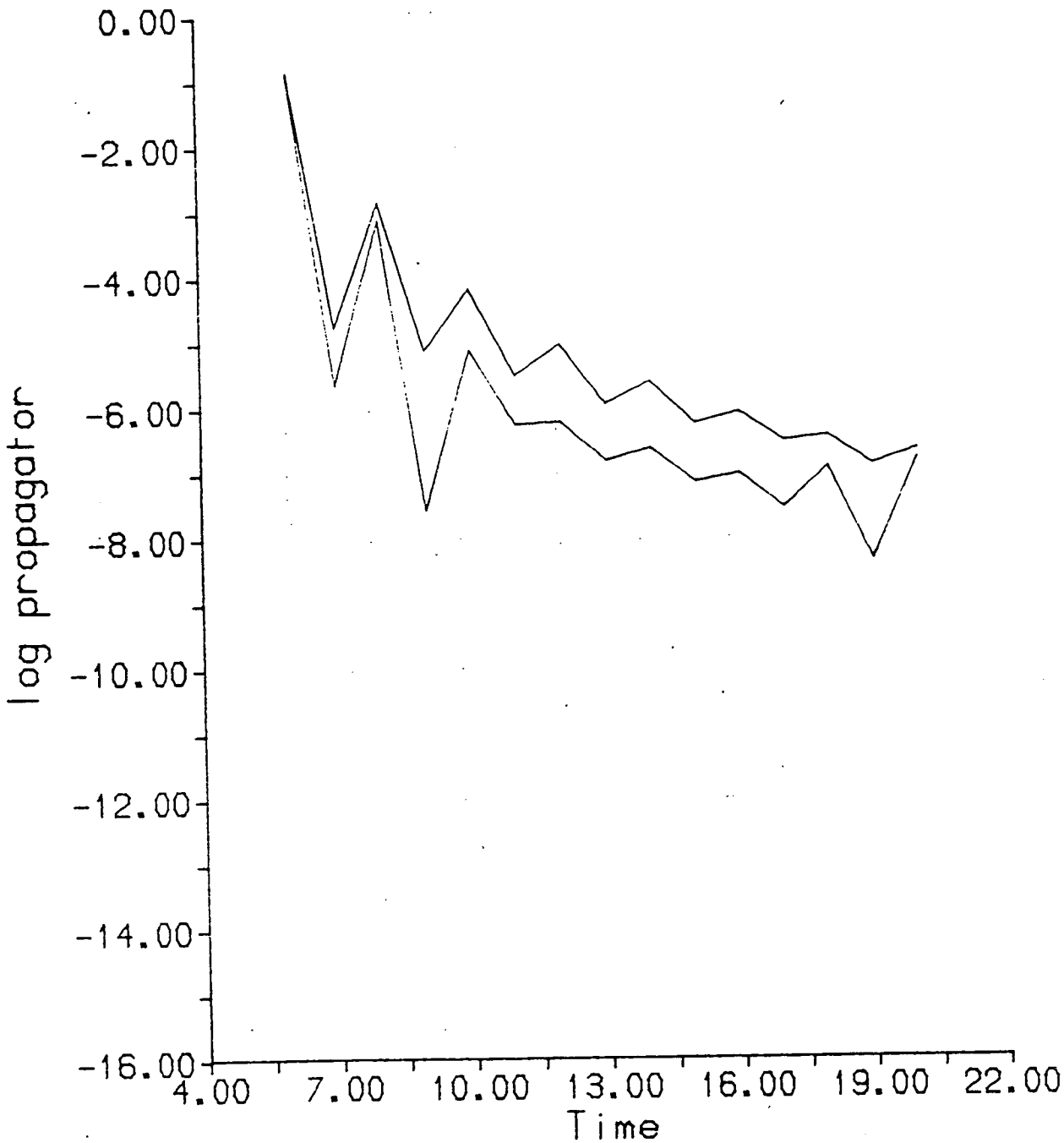

Fig. 4.24e The EVEN baryon timeslice propagator at a quark mass of 0.01 for both periodic and antiperiodic spatial boundary conditions at β =6.15. The numerically higher propagator is from periodic boundary conditions.

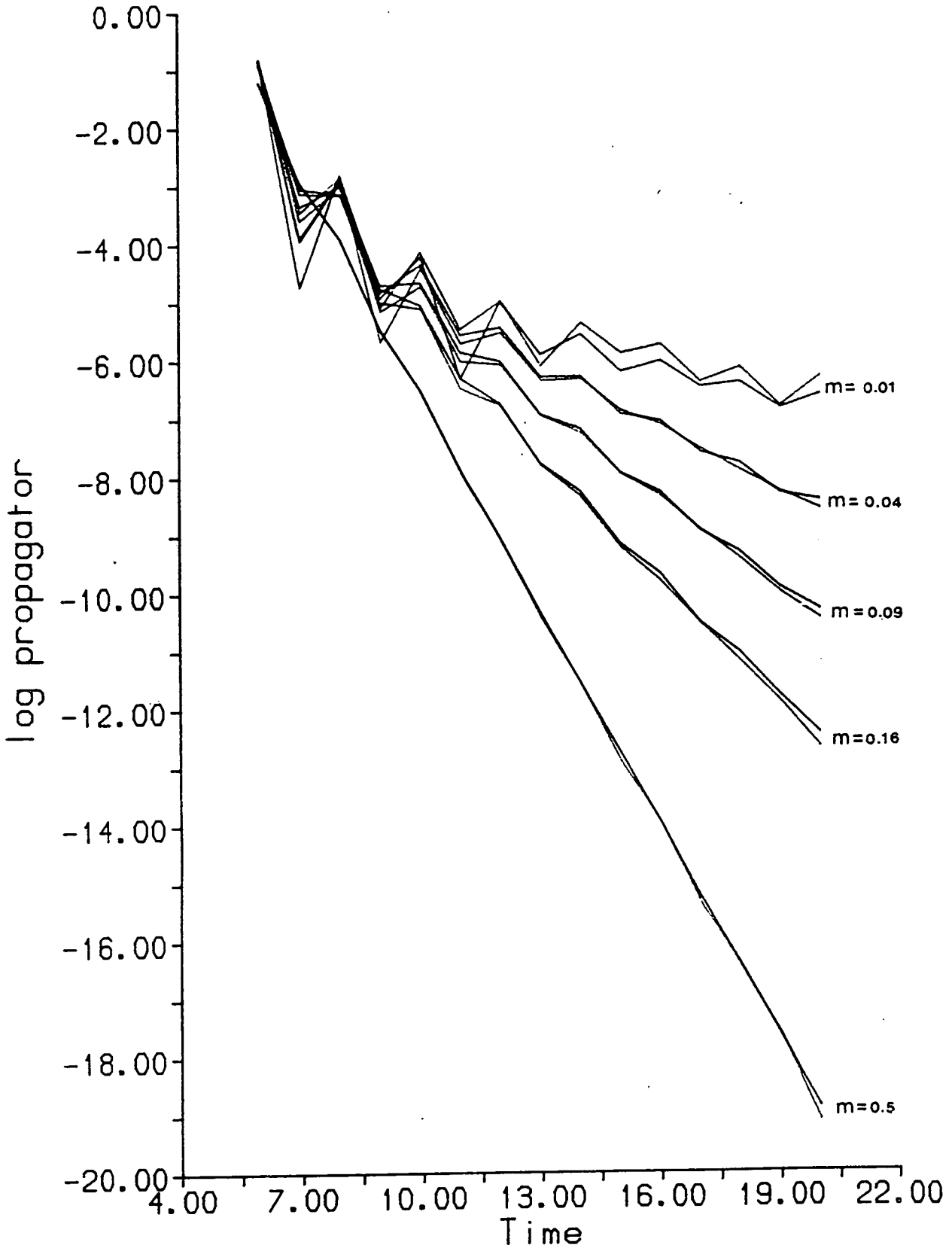

Fig. 4.25 The EVEN and ALL baryon timeslice propagator at five quark masses for periodic boundary conditions in space at β =6.15.

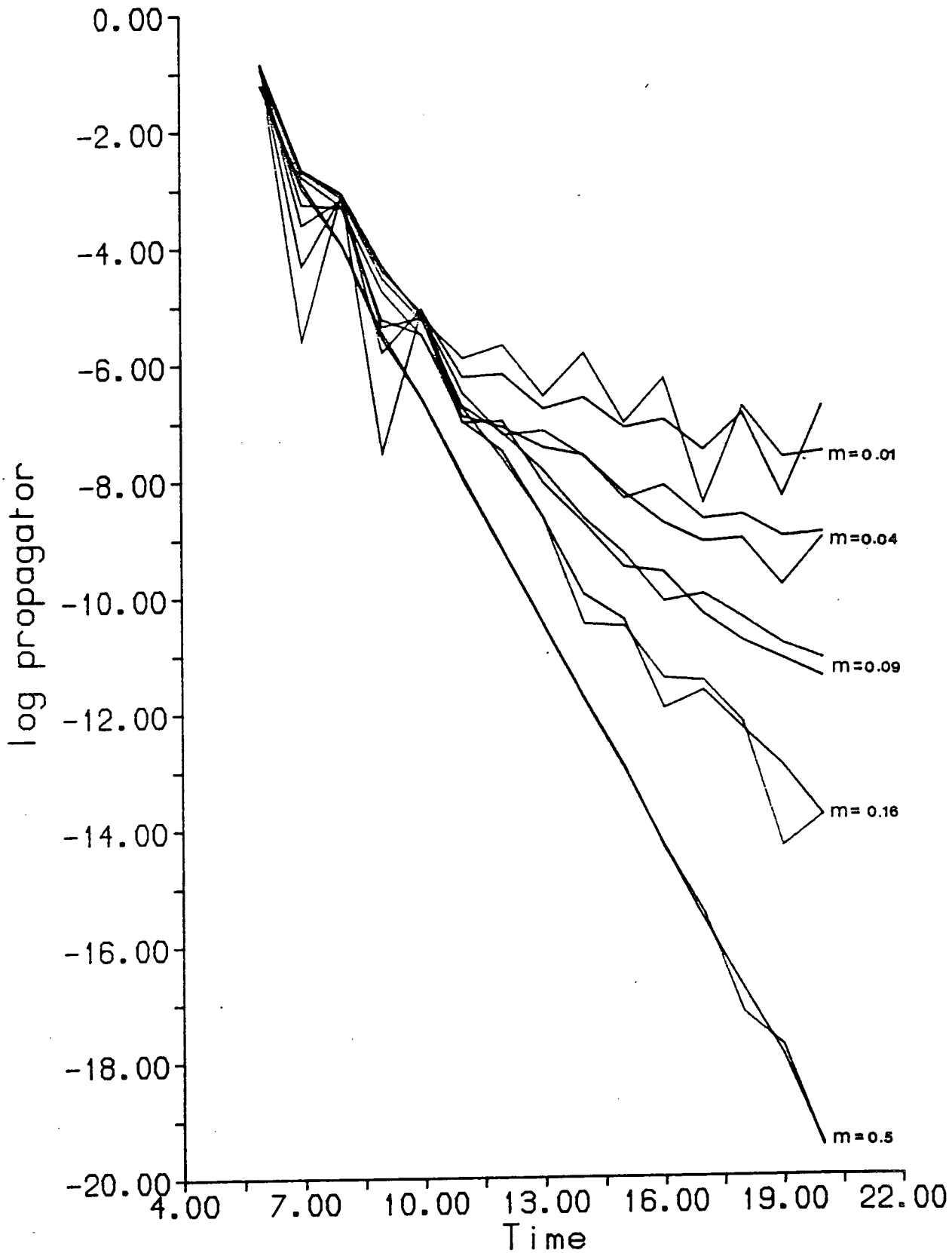

Fig. 4.26 The EVEN and ALL baryon timeslice propagators at five quark masses for antiperiodic boundary conditions at $\beta = 6.15$. The large oscillations near the source are in the EVEN propagator.

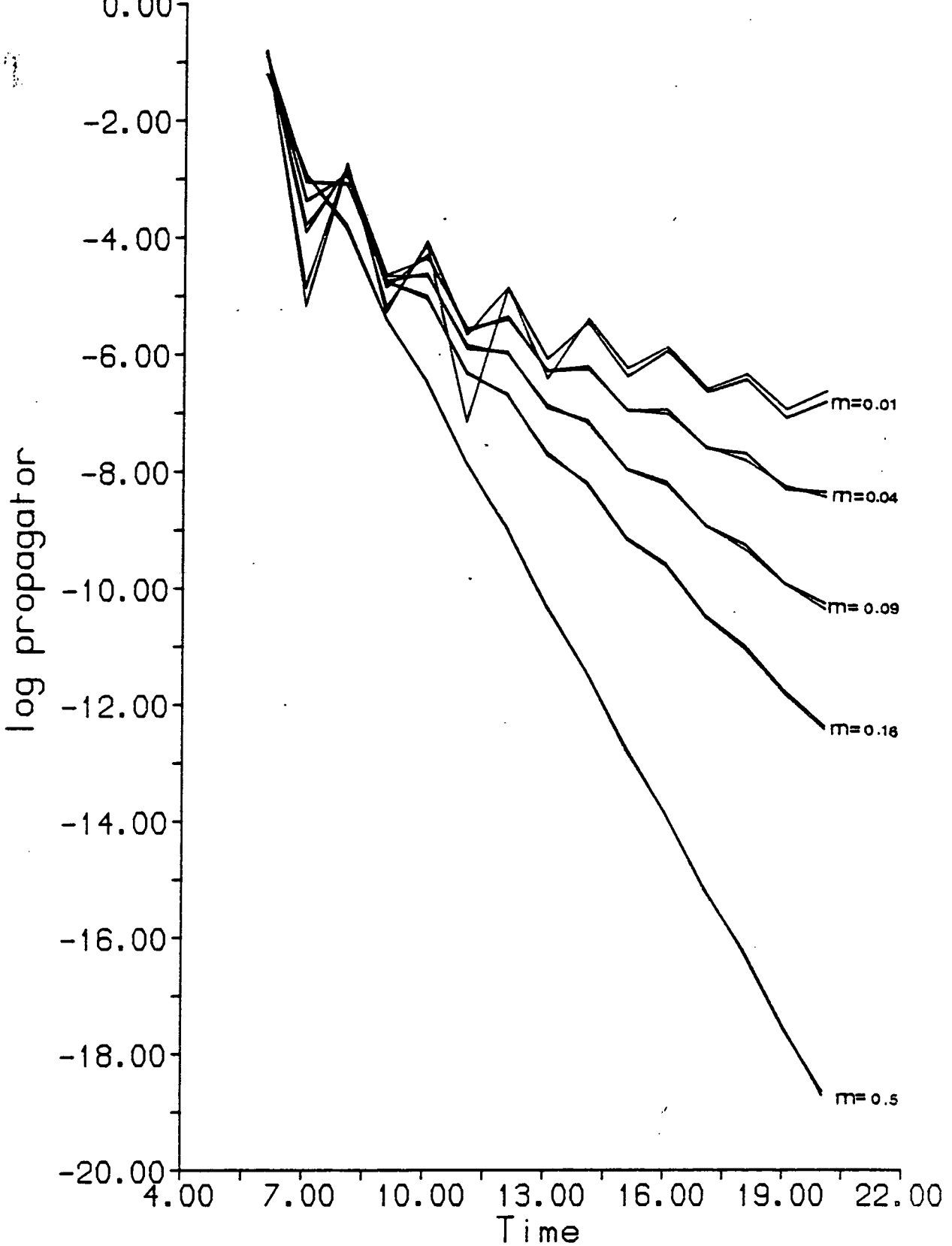

Fig. 4.27 EVEN and ALL baryon timeslice propagators for five different quark masses on a $16^3 \times 24$ lattice at $\beta = 6.15$ using periodic spatial boundary conditions. (24 configurations)

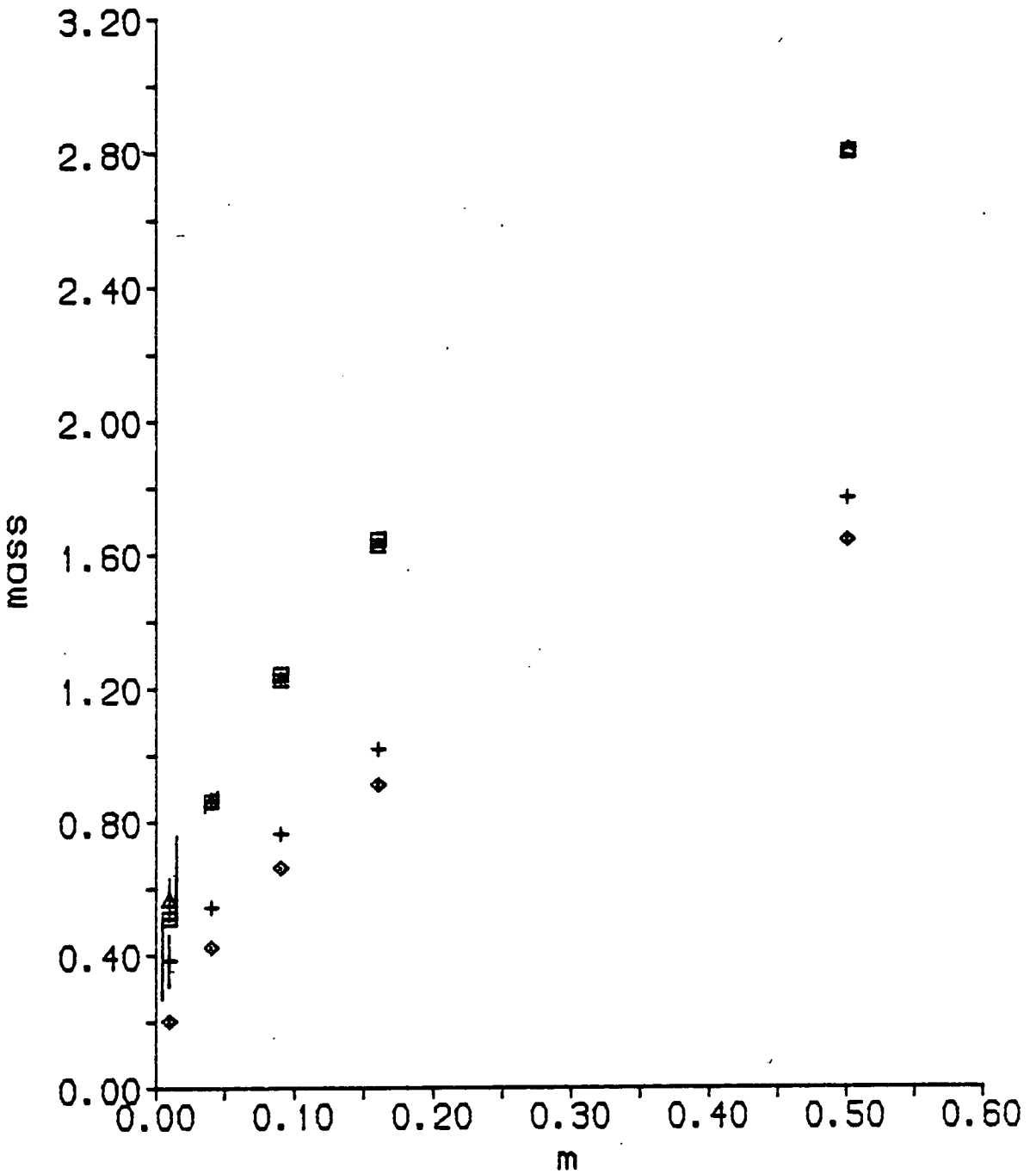

Fig. 4.28 Hadron masses in lattice units at $\beta = 6.15$. The pion error bars are smaller than the symbol size.

masses for the lowest state and higher χ^2 per degree of freedom. The errors in the estimates are very much smaller than for the β = 6.0 (antiperiodic BC) results. The mass ratios shown in table 4.7 below are plotted in figure 4.29.

m_q	m_π/m_ρ	m_N/m_ρ
0.50	0.929 (7)	1.590 (9)
0.16	0.896 (16)	1.600 (8)
0.09	0.866 (15)	1.605 (17)
0.04	0.779 (22)	1.592 (43)
0.01	0.526 (106)	1.480 (307)

Table 4.7 Ratios of hadron masses at β = 6.15

These results show much clearer evidence of crossover between the heavy and light quark regimes, and again the errors are lower than we saw at β = 6.0. However, we have already seen that the baryons are more seriously affected by the finite size of this lattice than are either the pion or the rho, so that these ratios are presumably also finite size affected. The mass ratio linearly extrapolated to zero quark mass using the lowest three data points is

$$\frac{m_N(0)}{m_\rho(0)} = 1.446 \pm 0.146 \qquad (4.4)$$

We can also see that, as the lowest value of the pion to rho mass ratio is 0.51, that the values of the quark mass we have been using are still rather high to justify such an extrapolation.

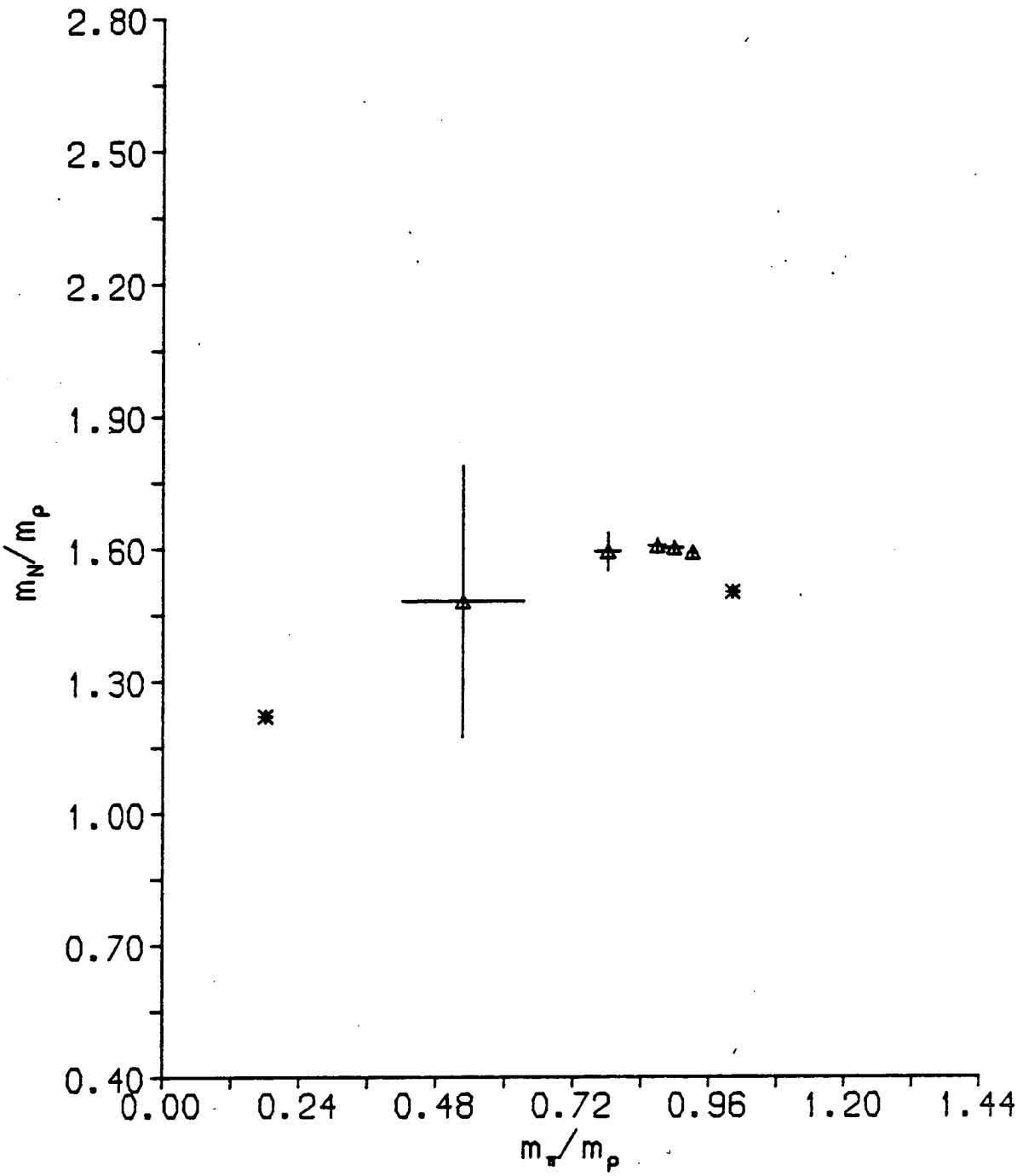

Fig. 4.29 Mass ratios at $\beta = 6.15$; the starred points are the experimental and infinitely-heavy quark values.

4.6 Results at $\beta = 6.3$ on a$16^3 \times 24$ lattice

This section describes the results of a study performed before that of the previous section; having seen that the baryon data at $\beta = 6.15$ is finite size affected, we expect more severe problems at $\beta = 6.3$. However, while we should not expect sensible baryon physics, it is important to establish whether the mesons are now also affected.

We have thirty-two gauge configurations, separated by 224 pseudo-heatbath sweeps and gauge-fixed to temporal gauge. We impose Dirichlet boundary conditions in time and anti-periodic spatial boundary conditions on the quark propagators. Although the foregoing suggests that the signal-to-noise ratio for baryons is much worse with these spatial boundary conditons, our choice does enable us to use the discrepancy between the EVEN and ALL baryon propagators as a measurement of finite size effects. Since we do not expect sensible baryon masses, the poor signal does not matter.

4.6.1 The meson sector

The results of the meson analysis are presented in table 4.8a. The PS propagator was again fitted using both one and two exponentials, and as can be seen from the table, the two-exponential fit was necessary to expose the ground state. Fig. 4.30 shows that there are large finite size effects in the PS data, giving a curvature which persists to low quark mass. The points at a quark mass of 0.005 and 0.0 were obtained from only four configurations, hence we have no error estimates at these points. A fit to the data for $0.01 \leq m \leq 0.16$ gives

$$m_{\pi} = (1.975 \pm 0.131)m + (1.152 \pm 0.132)\sqrt{m} + (0.113 \pm 0.038) \qquad (4.5)$$

where now the intercept is non-zero and the term in m is much bigger than at $\beta = 6.15$. The data at m =0.005 and 0.0 are consistent with this curve. Note that it is the presence of large finite size effects which permits the calculation of quark propagators down to zero quark mass, by producing a non-zero lower bound to the eigenvalues of the fermion matrix which is responsible for ensuring convergence of our iterative linear equation solver.

	Mq	A1	m1		
	0.50	1.142 (15)	1.636 (1)		
PS	0.16	0.586 (18)	0.912 (1)		
1-exp	0.09	0.376 (18)	0.666 (5)		
	0.04	0.243 (20)	0.437 (15)		
	0.01	0.199 (39)	0.250 (30)		
	Mq	A1	m1	A2	m2
	0.50	1.074 (28)	1.632 (3)	0.330 (145)	1.962 (233)
PS	0.16	0.427 (28)	0.888 (4)	1.104 (78)	1.288 (32)
	0.09	0.277 (25)	0.642 (8)	1.181 (92)	1.125 (33)
	0.04	0.190 (5)	0.417 (17)	1.202 (318)	1.002 (83)
	0.01	0.197 (44)	0.250 (26)	2.286 (1145)	1.185 (244)
	Mq	A1	m1	$\widetilde{A1}$	$\widetilde{m1}$
	0.50	1.591 (76)	1.759 (9)	-0.055 (503)	1.859 (153)
VT	0.16	0.328 (16)	0.975 (4)	-0.030 (7)	1.074 (9)
	0.09	0.166 (15)	0.719 (11)	-0.016 (6)	0.776 (32)
	0.04	0.085 (19)	0.496 (28)	-0.006 (6)	0.442 (79)
	0.01	0.044 (19)	0.329 (58)	-0.008 (9)	0.269 (89)
	Mq	A1	m1	$\widetilde{A1}$	$\widetilde{m1}$
	0.50	0.807 ( )	1.789 (20)	-0.188 ( )	1.823 (146)
PV	0.16	0.142 ( )	0.969 (8)	-0.207 ( )	1.116 (6)
	0.09	0.074 (6)	0.715 (10)	-0.154 (10)	0.865 (23)
	0.04	0.036 (6)	0.491 (26)	-0.085 (56)	0.606 (23)
	0.01	0.020 (4)	0.337 (46)	-0.044 (20)	0.370 (51)
	Mq	A1	m1	$\widetilde{A1}$	$\widetilde{m1}$
	0.50	0.172 (49)	1.768 (24)	-0.628 (114)	1.925 (26)
SC	0.16	0.043 (10)	0.938 (25)	-0.478 (58)	1.091 (16)
	0.09	0.023 (2)	0.656 (15)	-0.384 (90)	0.825 (30)
	0.04	0.012 (3)	0.402 (12)	-0.253 (141)	0.563 (61)
	0.01	0.005 (2)	0.152 (17)	-0.136 (40)	0.281 (42)
	Mq	A1	m1	$\widetilde{A1}$	$\widetilde{m1}$
	0.50	0.465 (44)	2.894 (11)	-0.320 (498)	3.064 (111)
EVEN N	0.16	0.057 (214)	2.041 (118)	-0.165 (-)	2.292 (548)
	0.09	0.017 (174)	1.735 (193)	-0.084 (-)	2.043 (690)
	0.04	0.001 (11)	1.254 (206)	-0.006 (-)	1.571 (407)
	0.01	0.007 (10)	1.486 (344)	-4.213 (368)	2.567 (420)*
	Mq	A1	m1	$\widetilde{A1}$	$\widetilde{m1}$
	0.50	0.441 (52)	2.909 (11)	-0.042 (118)	2.805 (121)
ALL N	0.16	0.095 (11)	2.072 (41)	-1.564 (1)	2.759 (340)
	0.09	0.018 (41)	1.708 (143)	0.26D-5(-)	0.882 (508)
	0.04	0.003 (5)	1.304 (99)	0.51D-4(-)	0.983 (426)
	0.01	0.002 (-)	1.099 (764)	-0.15D-6(-)	0.227 (95)

Table 4.8a

Amplitudes and masses from 2-exponential fits to hadron propagators on a $16^3 \times 24$ lattice at β=6.3. The mesons were fitted using timeslices 11-19 (except the 2-exponential fit to the PS which used 9-19) and the baryons were obtained from 11-18. The starred point should be not be regarded as a reliable estimate.

Mq	m1	m2	$\widetilde{m1}$	$\widetilde{m2}$
0.50	2.677 (82)	3.003 (34)	3.113 (71)	4.220 (399)
0.16	1.778 (107)	2.549 (55)	2.178 (193)	2.648 (180)
0.09	1.504 (143)	2.456 (71)	1.983 (50)	2.547 (401)
0.04	1.141 (278)	2.384 (45)	1.821 (179)	2.478 (377)
0.01	1.138 (326)	2.381 (81)	2.257 (212)	1.609 (838)

EVEN N

Mq	A1	A2	$\widetilde{A1}$	$\widetilde{A2}$
0.50	0.027 (36)	0.699 (31)	-0.414 (96)	-0.317 (32)
0.16	0.005 (5)	0.788 (43)	-0.041 (132)	-0.780 (204)
0.09	0.002 (4)	0.791 (80)	-0.034 (1)	-0.828 (410)
0.04	0.335(1070)D-3	0.769 (37)	-0.023 (1)	-0.842 (33)
0.01	0.223(9750)D-3	0.784 (95)	-0.379 (2)	-0.476 (937)

Mq	m1	m2	$\widetilde{m1}$	$\widetilde{m2}$
0.50	2.751 (189)	3.018 (143)	2.673 (165)	3.261 (80)
0.16	1.555 (184)	2.318 (78)	1.862 (267)	2.328 (308)
0.09	1.136 (161)	2.140 (80)	1.539 (289)	2.085 (132)
0.04	0.985 (139)	2.175 (98)	1.602 (281)	2.091 (179)
0.01	0.820 (334)	2.101 (253)	1.835 (370)	1.836 (287)

ALL N

Mq	A1	A2	$\widetilde{A1}$	$\widetilde{A2}$
0.50	0.087 (127)	0.665 (133)	-0.009 (12)	-0.438 (55)
0.16	0.379D-3 (-)	0.428 (134)	0.005 (-)	-0.238 (104)
0.09	0.42 D-4 (-)	0.330 (182)	0.003 (-)	-0.161 (-)
0.04	0.142D-3 (-)	0.462 (293)	0.014 (-)	-0.268 (348)
0.01	0.109D-3 (-)	0.407 (211)	3.28D+1(-)	-3.30D+1 (-)

Table 48b

Amplitudes and masses from 4-exponential fits to baryon propagators on a $16^3 \times 24$ lattice at β=6.3. The EVEN baryons were fitted from timeslices 6-16, and the ALL using 7-16.

	Mq	m1	m2	$\widetilde{m1}$
	0.50	1.693 (37)	1.886 (301)	2.059 (24)
	0.16	0.925 (29)	1.373 (102)	1.259 (44)
	0.09	0.677 (11)	1.214 (6)	1.020 (45)
VT	0.04	0.456 (31)	1.075 (28)	0.801 (32)
3-exp	0.01	0.296 (75)	0.969 (299)	0.567 (82)
	Mq	A1	A2	$\widetilde{A1}$
	0.50	0.535 (289)	1.808 (301)	-0.344 (13)
	0.16	0.172 (42)	1.392 (102)	-0.206 (46)
	0.09	0.096 (7)	1.147 (40)	-0.162 (30)
	0.04	0.053 (12)	0.951 (14)	-0.162 (19)
	0.01	0.028 (42)	0.821 (-)	-0.088 (65)

Table 4.8c

Amplitudes and masses from 3-exponential fits to the VT propagator on a $16^3 \times 24$ lattice at β=6.3. It was fitted using timeslices 7-18.

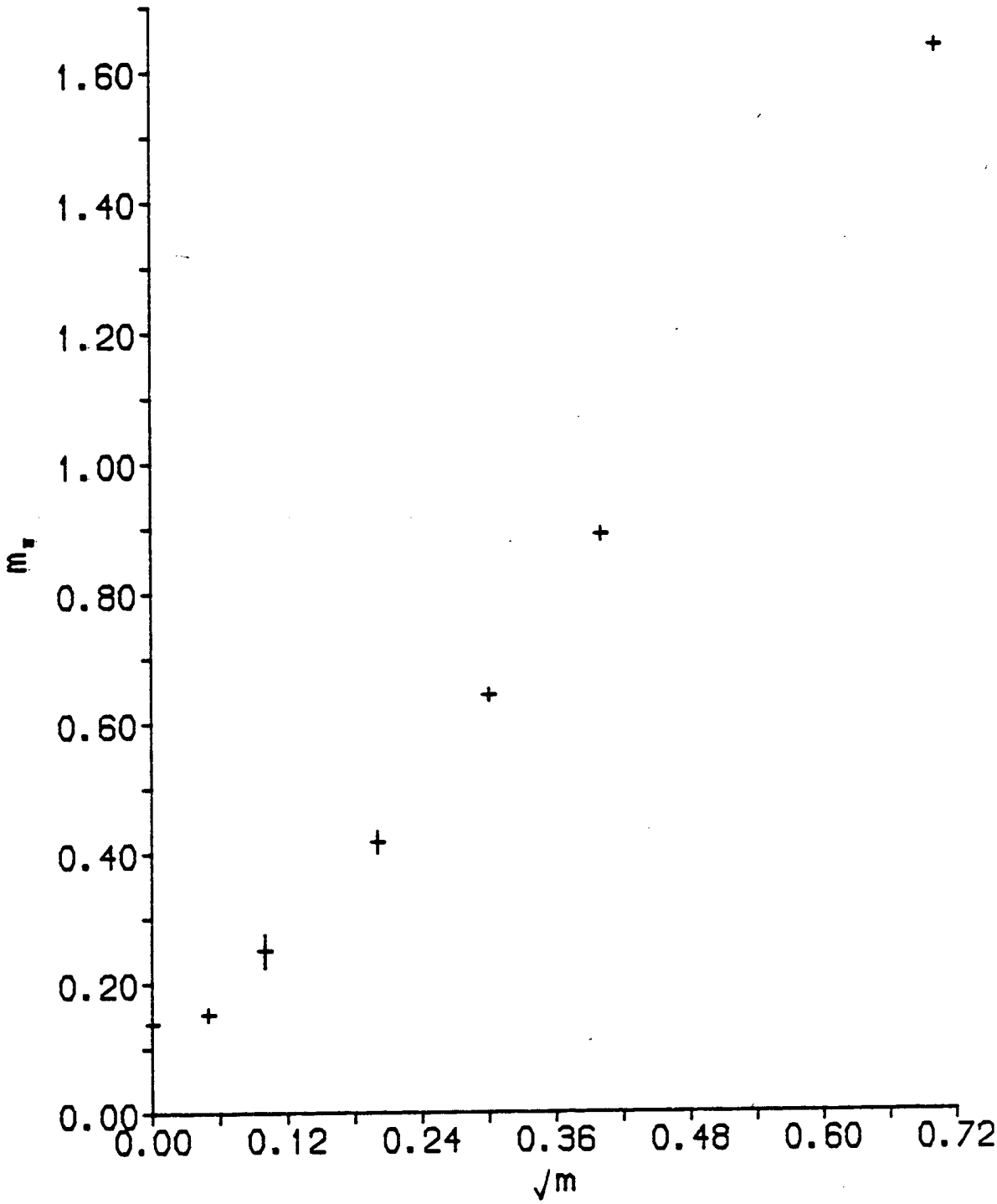

Fig. 4.30 Pion mass in lattice units at β = 6.3 plotted against √m.

Fig. 4.31 shows the pion mass estimates obtained from both the PS and SC propagators. The line is a best fit through the SC data. At the lowest mass, the lightest particle is the SC pion. In the absence of severe finite size effects, the lightest particle on the lattice should be the Goldstone pion (from the PS) however, it could be that the small physical size of this lattice is affecting this state most and forcing it to have a much higher value. At the other values of the quark mass ($0.01 < m \leqslant 0.5$), flavour symmetry is better than at the lower values of β, especially when we take into account the relatively high physical quark masses.

If we turn now to the rho sector, we see from fig 4.32 that we have almost perfect flavour symmetry. The VT propagator has also been fitted using three exponentials because these give slightly lower mass estimates than the two-exponential fits. These results are in table 4.8c. We have no direct measurement of finite size effects in the rho sector, however fig 4.33 shows signs of a pion-rho degeneracy which has previously been observed [Bowler and Pendleton (1984), Bowler et al (1984a)] as a symptom of finite-size effects. The VT can also be fitted using three exponentials, and here a slight decrease in mass occurs at all but the lowest quark mass. These results are in table 4.8c.

4.6.2 The baryon sector

As we might anticipate, due to the boundary conditions and the shrinking of the physical lattice size due to the higher β, the nucleon is harder to extract than at $\beta = 6.15$. We can see from tables 4.8a and b that the four exponential fits are necessary to extract the ground states and achieve good fits. Fig. 4.33 shows that the ALL and EVEN mass estimates agree within errors at all but $m = 0.09$, but this is mainly due to the fairly large error bars on all the points. The decay of the two propagators shown in fig. 4.34 is quite different, especially near the source, (where the large oscillations are present in the EVEN propagator). This serves to confirm that finite size effects are large. The nucleon to rho mass ratios shown in fig. 4.35 and in table 4.9 below are thus poor, and clustered near the heavy quark limit.

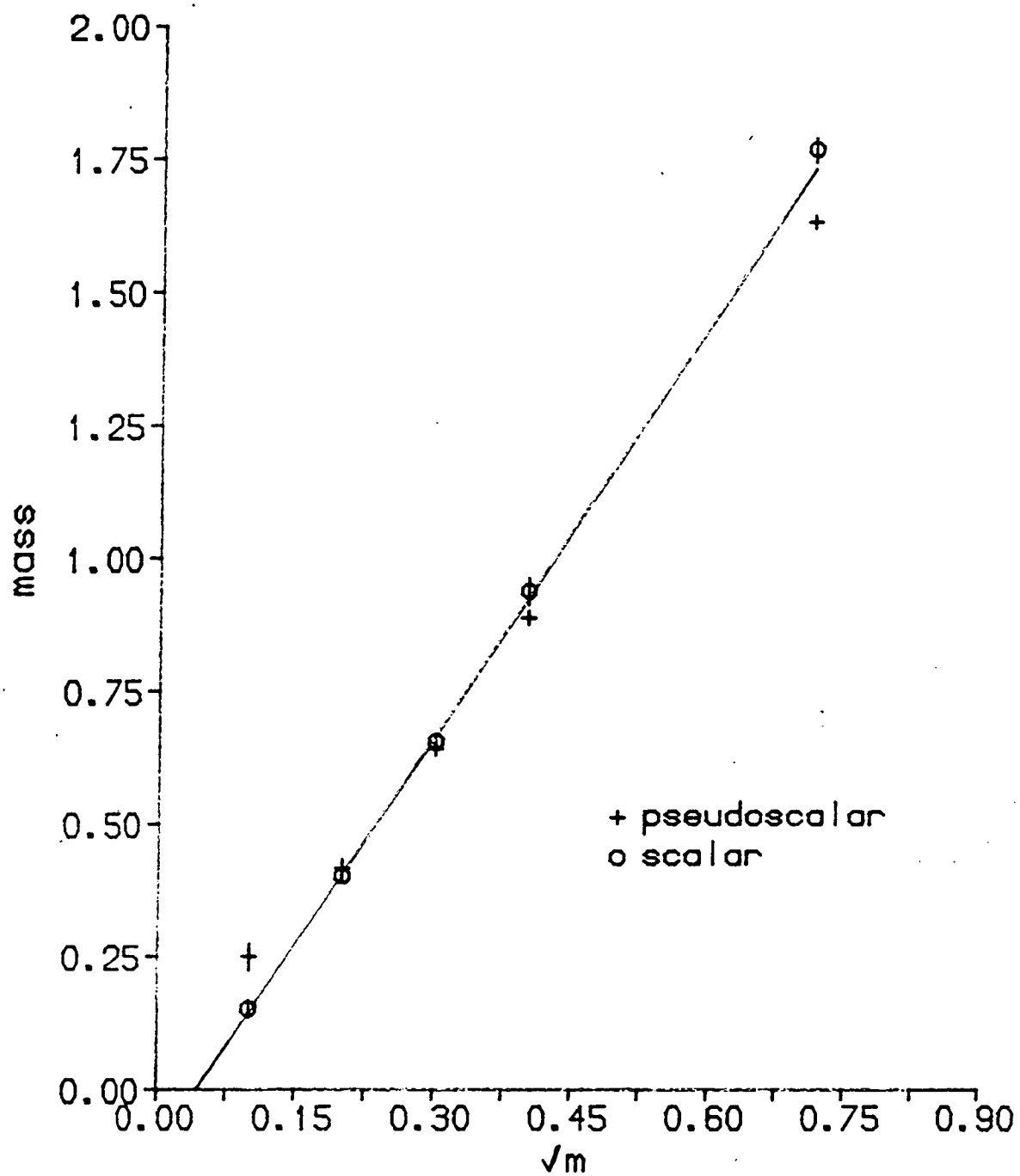

Fig. 4.31 Extent of flavour symmetry restoration in the pion sector at $\beta = 6.3$

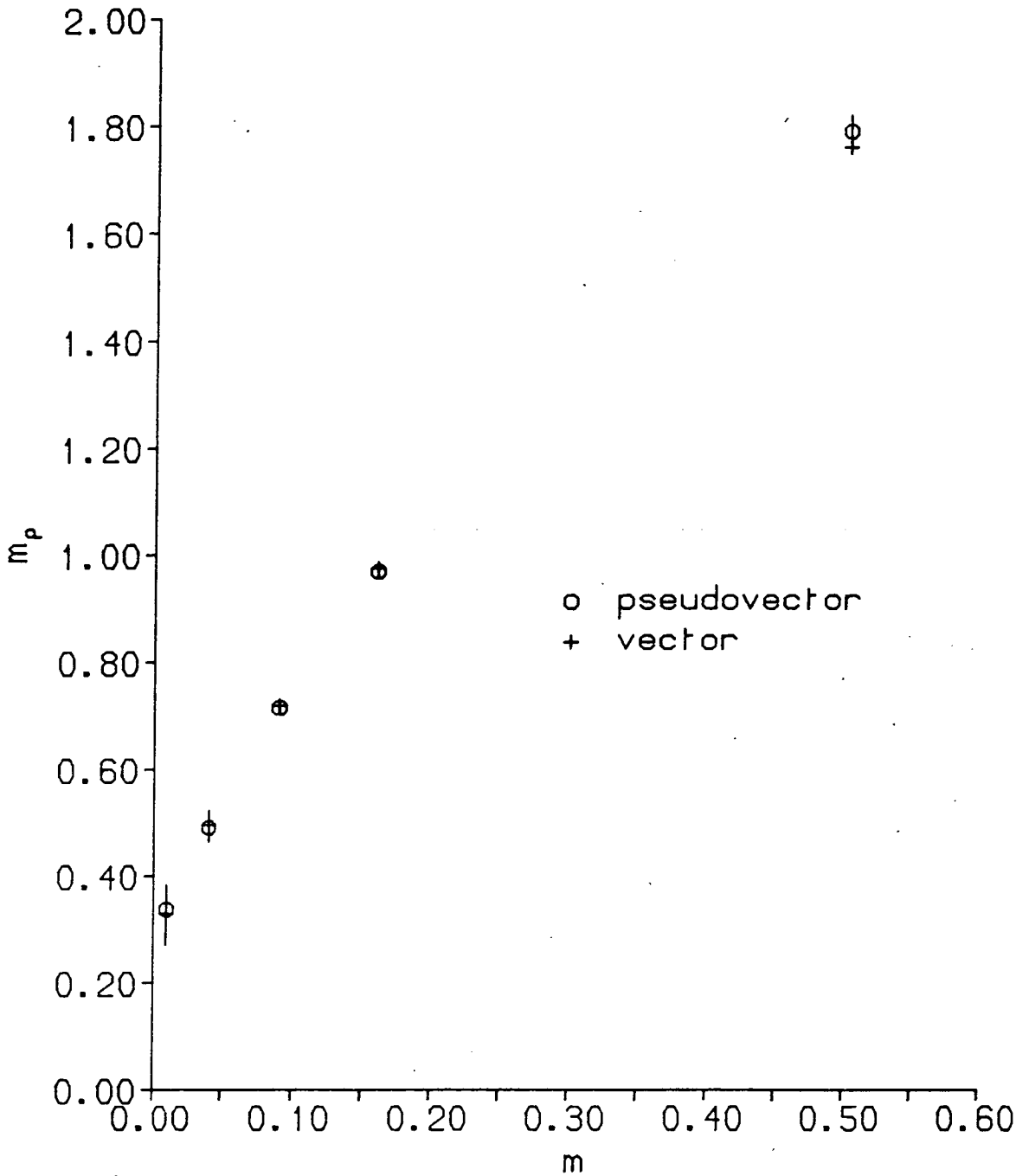

Fig. 4.32 Extent of flavour symmetry restoration in the rho meson sector at β = 6.3.

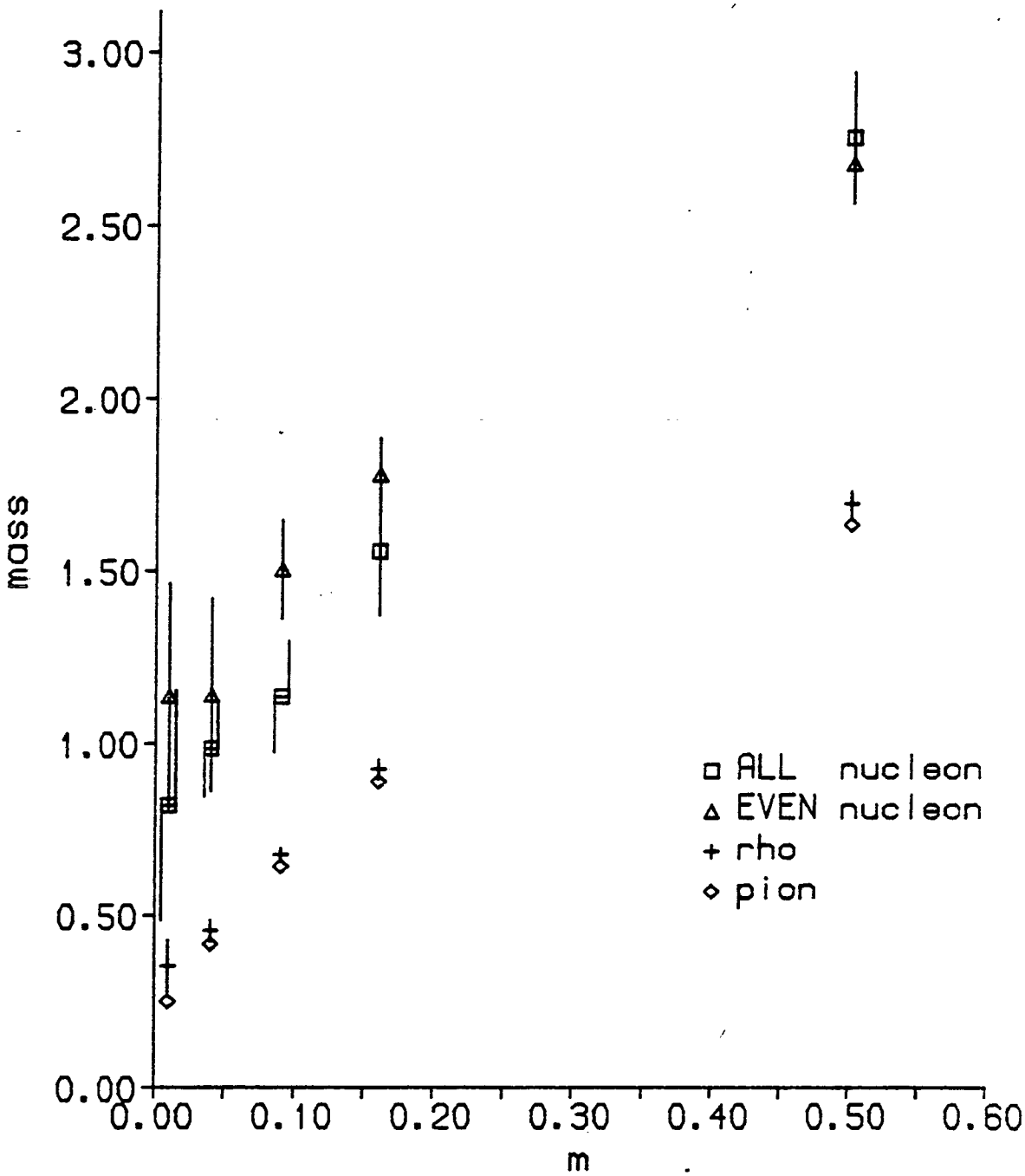

Fig. 4.33 Hadron masses in lattice units at $\beta = 6.3$.

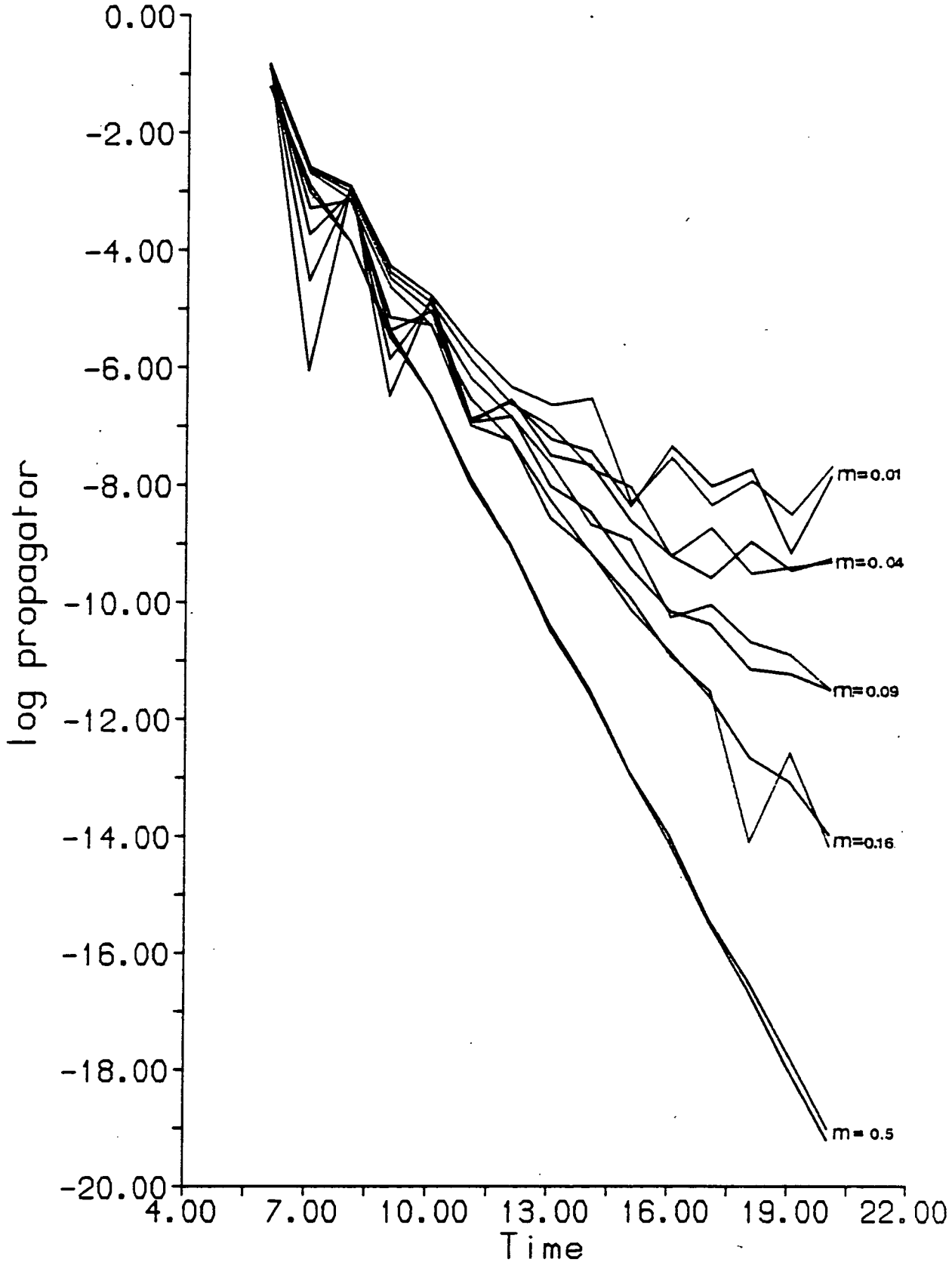

Fig. 4.34 EVEN and ALL baryon timeslice propagators for five different quark masses on a $16^3 \times 24$ lattice at $\beta = 6.3$, using antiperiodic spatial boundary conditions. (32 configurations)

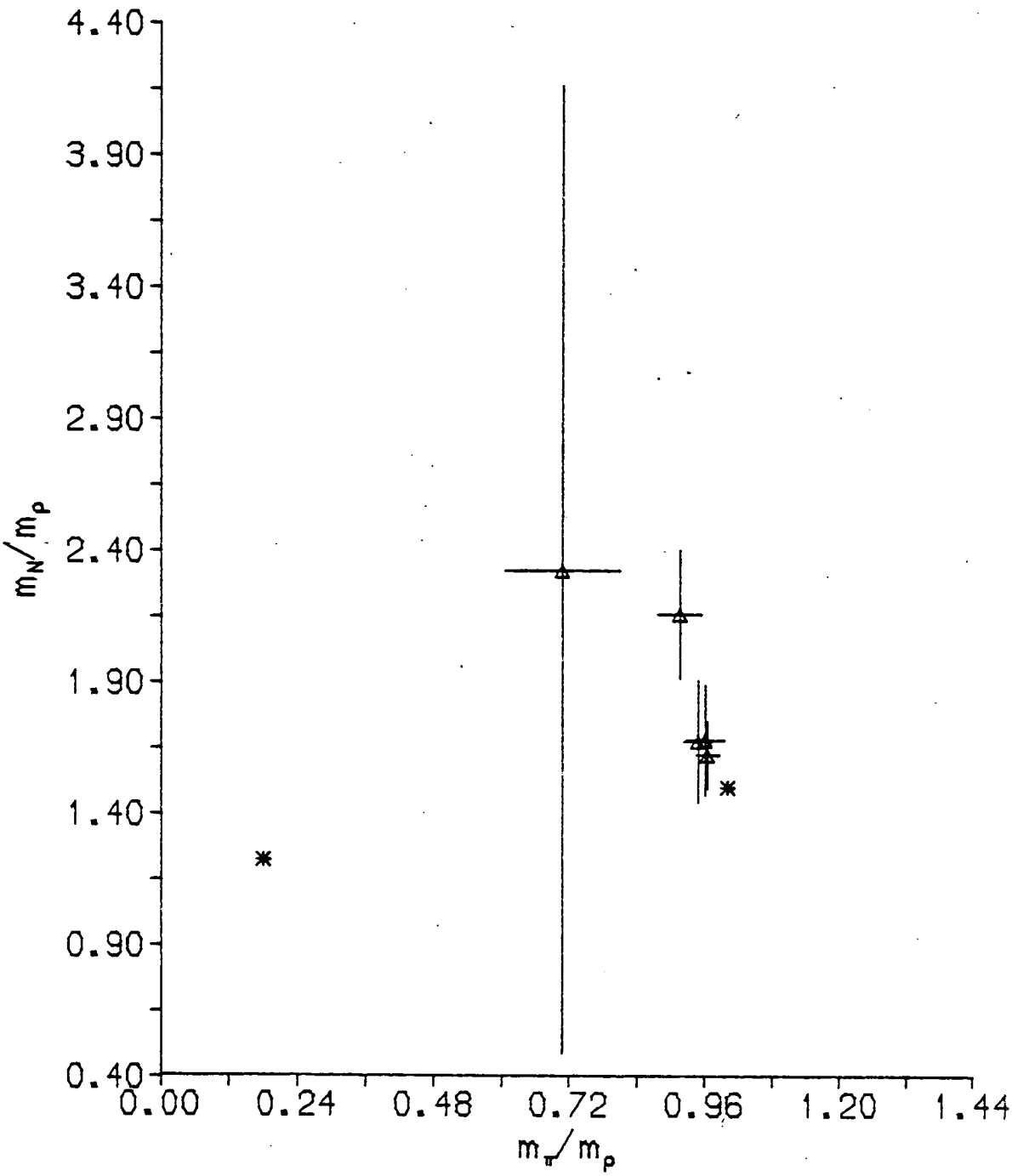

Fig. 4.35 Mass ratios at $\beta = 6.3$; the starred points are the experimental and infinitely-heavy quark values.

m_q	m_π/m_ρ	m_N/m_ρ
0.50	0.964 (21)	1.625 (126)
0.16	0.960 (34)	1.682 (208)
0.09	0.947 (24)	1.677 (232)
0.04	0.915 (38)	2.160 (244)
0.01	0.708 (102)	2.326 (1836)

Table 4.9 Ratios of hadron masses at β = 6.3, measured using the ALL nucleon obtained from a 4-exponential fit and the ρ from a 3-exponential fit.

As we have seen, the baryons seem to be most affected by the finite size of the lattice, but we also saw that the lowest mass pion from the PS propagator (used in this plot) is badly affected. If instead, the pion mass from the SC propagator is used, the lowest point is pushed down to a value for the pion to rho ratio of 0.431(49).

4.7. Conclusions

The aim of the work presented here was to perform high statistics measurements of hadron masses at several values of the gauge coupling, extending upwards from β = 6.0.

As a precursor to this, low statistics measurements at β = 5.7 on a 16^4 lattice were performed . Here the matrix inversion is relatively more costly to perform than at higher β, and our results do not show any indications of

perform than at higher β, and our results did not show any indications of continuum behaviour setting in at this value of the coupling; flavour symmetry was broken in the meson sector, and the nucleon-to-rho mass ratio did not cross over from the heavy to light quark regimes, but continued to grow as the pion-to-rho mass ratio decreased. For this reason we chose to begin high statistics measurements at β = 6.0 [Bowler et al. (1986b)].

Preliminary results at β = 6.0 on a 16^4 lattice suggested that we should extend the lattice in the time direction, so subsequent work used $16^3 \times 24$ lattices. Using 32 configurations on this size of lattice at β = 6.0, we observed signs of flavour symmetry restoration in the meson sector, particularly for the rho meson. The pion multiplet is a more severe test for the lattice calculation because only one pion is a Goldstone boson at zero quark mass and nonzero lattice spacing. Only in the continuum limit will the other 15 pions be driven to zero mass at zero quark mass. It is perhaps not surprising then that the non-Goldstone pion mass which we measured is 2-3 standard deviations higher than the Goldstone pion mass at nonzero quark mass; although it does extrapolate to a value consistent with zero at zero quark mass. We conclude that there is a marked improvement in flavour symmetry in going from β = 5.7 to 6.0, and that the latter β value may be close to the onset of continuum behaviour in the meson masses.

The results for baryon masses at β = 6.0 were less conclusive. It is important to comment that, at our level of statistics i.e. 32 gauge configurations, the baryon propagators with antiperiodic spatial boundary conditions become submerged in the noise before reaching the time boundary. So a lattice of 24 timeslices, with Dirichlet boundary conditions in time, is long enough; higher statistics are what is needed for improvement. In spite of observing a difference between the EVEN and ALL baryon timeslice propagators, the ground state masses extracted from them are in very good agreement and the resulting nucleon-to-rho mass ratio shows some sign of crossing over from the heavy to light quark regime, although errors are large and the pion-to-rho mass ratio is probably not small enough for this crossover to be clearly visible. Because the difference between the EVEN and ALL propagators increases with decreasing quark mass, and has not been reported for periodic spatial boundary conditions, we tentatively interpreted the difference as a finite-size effect which has somehow been highlighted by our choice of antiperiodic spatial boundary conditions.

At β = 6.15, we tested directly the effects of the spatial boundary conditions by obtaining propagators on the same eight configurations with both periodic and antiperiodic boundary conditions [Bowler et al. (1986c)]. For the mesons, there is good agreement between the two sets of propagators which indicates that the mesons are not significantly affected by the finite size of the 16^3 lattice at this value of β. The two pions, from the PS and SC propagators, are in good agreement and both lie on a straight line through zero. The two measurements of the rho agree to within 2% at all values of the quark mass, an improvement in flavour symmetry from the situation at β = 6.0.

On the other hand, there is a significant difference between the baryon propagators measured for the two choices of spatial boundary conditions and the discrepancy increases as the quark mass decreases. In addition, the disagreement between EVEN and ALL propagators noted for β = 6.0 persists at β = 6.15 for antiperiodic boundary conditions but is not present for periodic boundary conditions. We ascribe these differences to finite size effects.

We note that with antiperiodic boundary conditions on a finite lattice a three-quark state cannot have zero momentum : the timeslice projection does not single out a zero momentum baryon state; however the smallest momentum corresponds to only a 5% effect in the lightest baryon mass we measure, which is much less than the statistical error, so this fact alone does not account for the discrepancy between the data for the two choices of boundary conditions. In future high statistics work using antiperiodic spatial boundary conditions however, it might be advisable to take account of the non-zero minimum momentum by projecting onto a single non-zero momentum state and subtracting out the momentum contribution from the resulting mass estimates.

Using periodic boundary conditions, the signal appears to be cleaner and it is easier to extract masses. The mass ratios we obtain at β = 6.15 suggest that we may have reached the asymptotic scaling region, but we must remember that these ratios are calculated from data which may be finite-size-affected.

At β = 6.3 we find that now, at the lowest quark mass, the mesons are also finite-size-affected. The PS propagator seems to be the worst affected - the masses are no longer a linear function of the square root of the quark mass and the intercept is non-zero. However, for $0.04 \leqslant m \leqslant 0.5$, there is a

further improvement in flavour symmetry, due to the smaller value of a. Although we only have measurements for antiperiodic spatial boundary conditions, we conclude from the discrepancy between EVEN and ALL propagators that baryon propagators are badly finite-size-affected for $m < 0.16$. Hence we do not expect reliable nuceon-to-rho mass ratios at this value of β. The values of the physical quark mass that we have used are high because, although our quark propagator algorithm converges for all quark masses, significant finite size effects are observed in all hadron massses for quark masses below 0.01 in lattice units. So there is little to be gained by working at lower quark masses.

Finally, we look at the evidence for scaling in our hadron mass measurements. In fig 4.36, we plot the nucleon-to-rho mass ratio versus the pion-to-rho mass ratio obtained from three different sets of measurements - those of this chapter at β = 6.0 and 6.15 and also those of [Barkai et al. (1985a)] at β = 6.0. If meson and baryon masses are scaling between these β-values, then these data should all lie on a single universal curve. We can see that the data of [Barkai et al.], which was obtained using a $16^3 \times 32$ lattice with periodic boundary conditions, is in excellent agreement with our β = 6.15 results using periodic spatial boundary conditions. Our β = 6.0 results, obtained using antiperiodic boundary conditions, are also consistent with the other data, and all three sets of points lie approximately on the same curve. Thus it may be the case that there is a " scaling window " between β = 6.0 and β = 6.15. From fig. 4.35 it is clear that this window does not extend up to β = 6.3, except at high quark masses. It is therefore of interest to perform higher statistics measurements at β = 6.15 and to explore smaller quark masses in order to obtain mass estimates closer to the physical value of the pion-to-rho mass ratio. This work indicates that fairly accurate measurements of meson masses are possible using 16^3 spatial lattices and $6.0 \leqslant \beta \leqslant 6.15$. In particular, flavour symmetry holds to a good approximation in this range. These measurements should be extended to mesons other than the pion and rho. The situation in the baryon sector is less clear, and further analysis of finite-size and non-zero momentum effects is needed in order to intepret our results properly. Bearing this caveat in mind, we conclude that on the basis of fig. 4.36 and the observed flavour symmetry in the meson sector, predictions for continuum quenched hadron masses are possible using $16^3 \times 24$ lattices between β = 6.0 and 6.15.

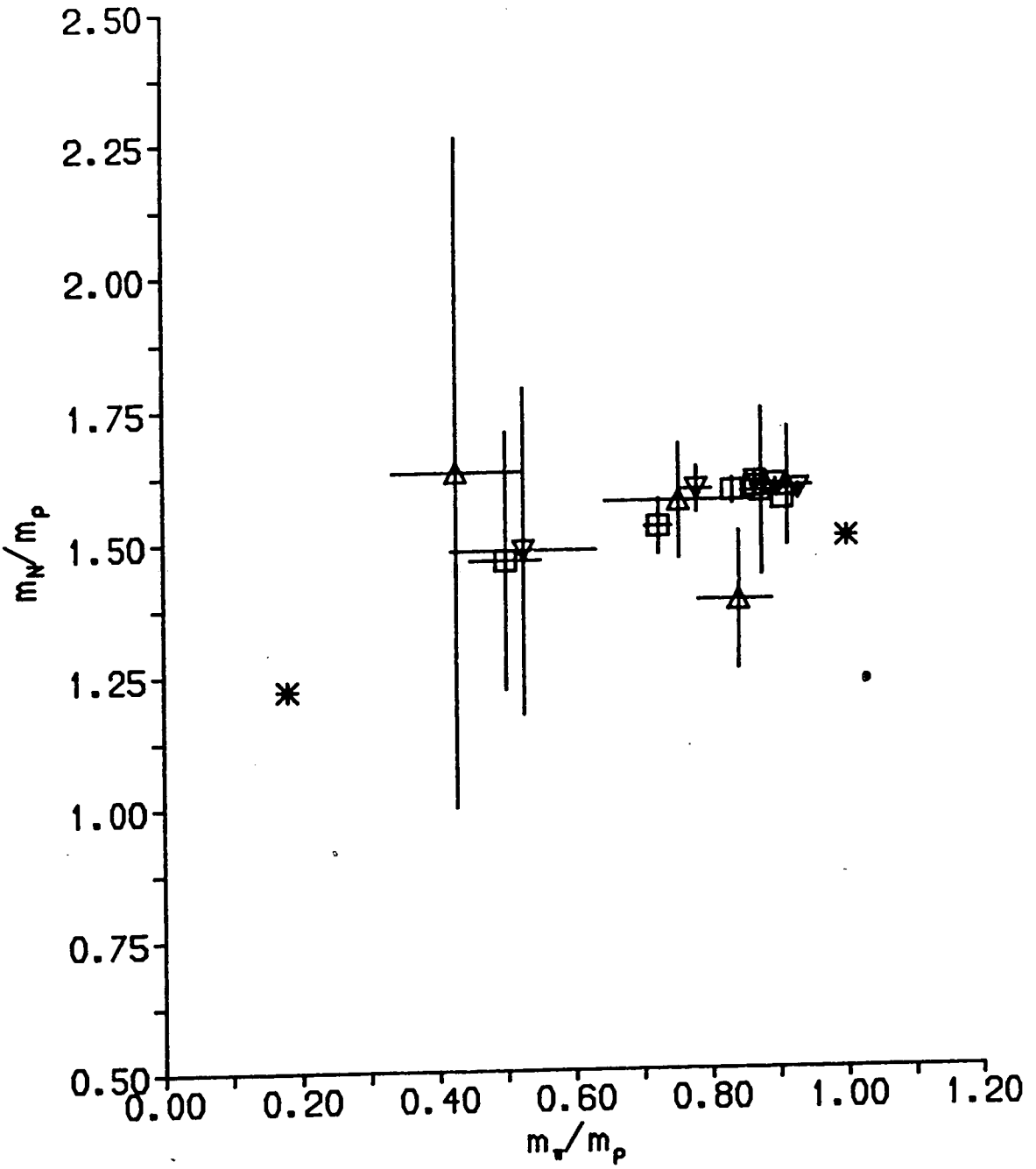

Fig 4.36 Mass ratios from :

△ - β = 6.0 [Bowler et al. (1986b)]
□ - β = 6.0 [Barkai et al. (1985a)]
▽ - β = 6.15 [Bowler et al. (1986c)]

Appendix

The DAP

The Distributed Array Processor (DAP) is a square array of 4096 processing elements (PEs), each with 4kbits of store, giving a total of 2 Mbytes.

It is accessed through an ICL 2900 mainframe (known in this context as the host) and it can also be used as normal store for the host when it is not acting as a parallel processor. Figure A.1 is a diagram of the DAP.

The 64×64 array is connected two-dimensionally with each processing element linked to its four neighbours. These are identified by N,S,E and W in an obvious way, and the connections at the edges of the array depend on whether planar or cyclic geometry is in operation : cyclic geometry connects the edges N to S and E to W to form a torus, whereas planar defines a zero input at the edges. Each processing element has its own one-bit processor with three registers. Two of these are an accumulator store and a 'carry' store, and the third, the activity register (A-register) allows programmable control of the PEs : only if the A-register is set will certain store instructions be implemented.

The DAP is programmed in a development of fortran, DAP fortran. Any DAP program is composed of two parts - a host fortran program and a DAP fortran program which is called as a subroutine from the host. The two parts are linked by the shared COMMON blocks which are loaded into DAP store. The processing begins in the host, where the input routines and data are set up and any initial processing completed, before control is passed over to the DAP using a DAP entry subroutine which can call other DAP subroutines in the usual way. When the parallel processing is complete, control is passed back to the host for final processing.

DAP fortran has three types of variable - scalars, vectors and matrices- which may be Real (3-8bytes), Integer (1-8bytes) or Logical. Scalars are like the ordinary fortran variables whereas vectors and matrices are arrays of 64 and 64×64 entries respectively. The parallelism means that for example to add two numbers at every PE we use

```
DIMENSION A(,),B(,),C(,)
A = B + C
```

and the calculation and assignment is performed simultaneously at every processing element. The fact that the matrices are 64x64 is made implicit in the DIMENSION statement by using (,).

There are two important features of DAP fortran which are fully exploited in efficient QCD programs. These are the SHIFT functions and logical MASKing. The shift functions are used to bring information stored at one PE to another. A variant of the illustration above would be

```
DIMENSION A(,),B(,),C(,)
A = B + SHEC(C,4)
```

whose effect would be to add to B at each PE the value of C at the PE four sites away in the west direction, and assign the sum to A. SHEC SHifts East Cyclically, so at the western boundary data is moved on from the eastern one. There are eight shifting functions, corresponding to the four directions and the two choices of geometry : SHEC,SHWC,SHNC,SHSC,SHEP,SHWP,SHNP and SHSP. There are also functions which perform shifts in long vector mode.

Operations may be made conditional on the value of a logical matrix (MASK) at the particular PE. These MASKs set the A-register mentioned above, and may be set up using built-in functions such as ALTR(n) and ALTC(n). ALTR(n) sets the first n rows and every alternate n rows to .FALSE. and the rest of the entries to .TRUE. ,as shown in fig A.2. Then we can use

```
LOGICAL LCHESS(,)
LCHESS = ALTR(1).LEQ.ALTC(1)
```

for example to set up a 'chessboard' MASK , as shown in fig A.2. Then the statement

```
A(LCHESS) = B
```

assigns B only to the corresponding values of A which are at .TRUE. PEs, or alternatively, using the MASKs in combination with MERGE statements, we have

```
A = MERGE(B,C,LCHESS)
```

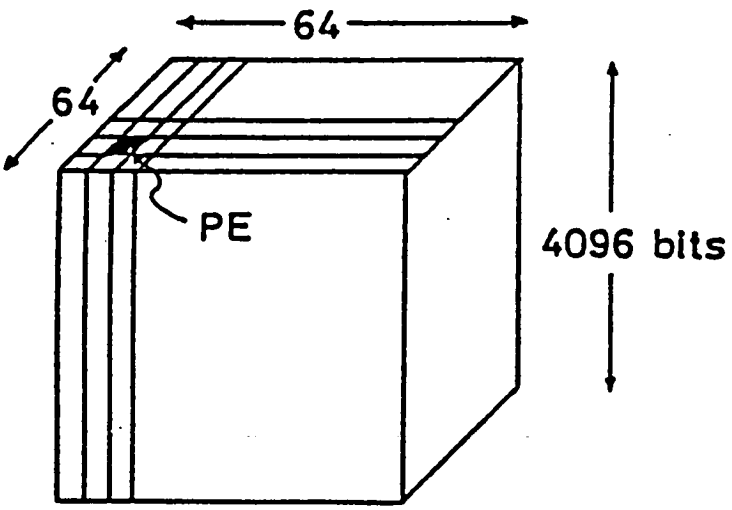

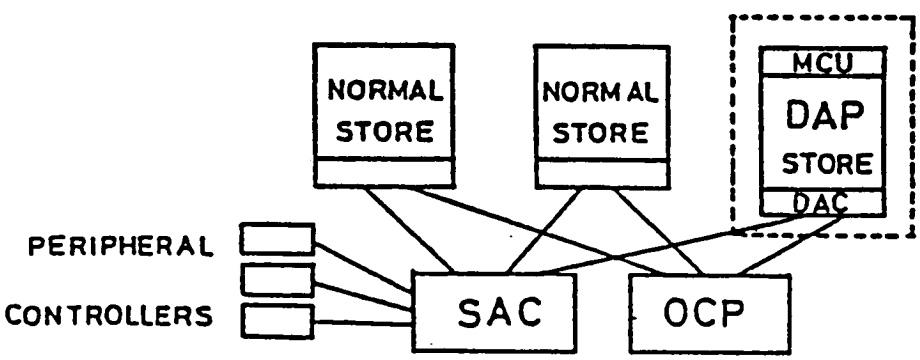

MCU - Master Control Unit

DAC - DAP Access Controller

SAC - Store Access Controller

OCP - Order Code Processor

Fig A.1 Schematic diagram of the DAP

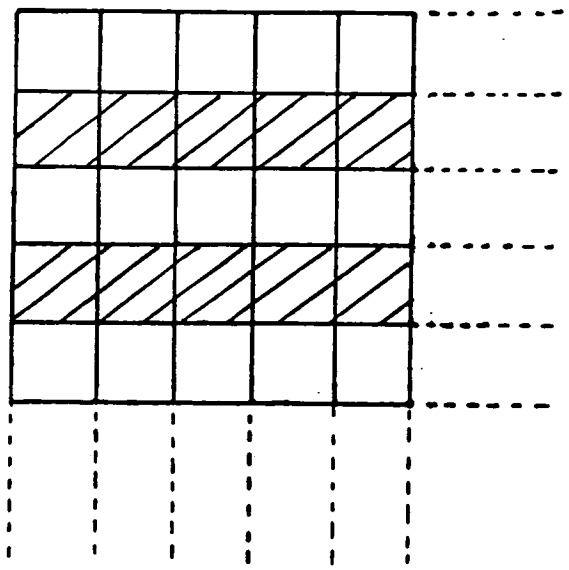

shaded boxes represent .TRUE. PEs

a ALTR(1)

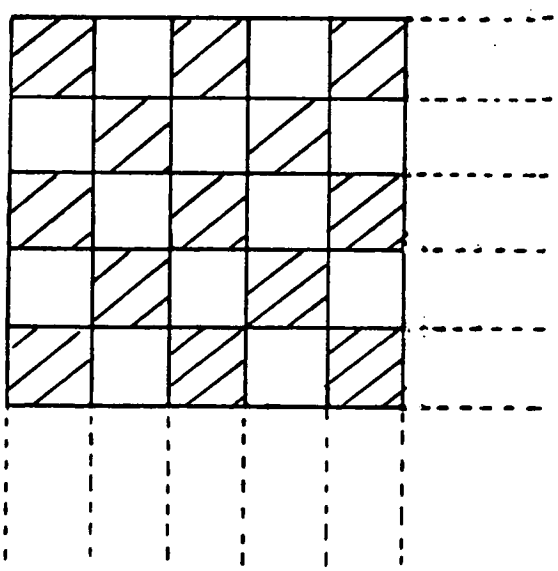

b ALTR(1).LEQ.ALTC(1)

Fig A.2

where now A is assigned the value of B at sites where LCHESS is .TRUE. and C where it is .FALSE..

In using the DAP for QCD programs, we map one 16^3 timeslice onto the 64x64 structure in the way shown in fig A.3 : thus for example, the data for site (1,1,5) of the 16^3 timeslice is held at position (2,4) on the 64x64 array since the 3-direction is packed into a 4x4 square for each (1-direction,2-direction) coordinate. This means shifts in the 1 and 2 directions are straightforward but for the shifts in the 3-direction we need a series of masks as shown in Fig A.4. These masks allow us to link the data at a given site with that one point away in the 3-direction; as we can see the .TRUE. sites are the ones on the array which are adjacent to the neighbouring lattice site in the given direction (L3FS = L3FSouth etc).
So the following code will shift W 'back' in the 3-direction onto WS.

```
WS(L3FNG1) = - SHNC(W,1)
WS(L3FNG2) =   SHNC(W,1)
WS(L3FS)   =   SHSC(W,1)
WS(L3FE)   =   SHEC(W,1)
WS(L3FW)   =   SHWC(W,1)
```

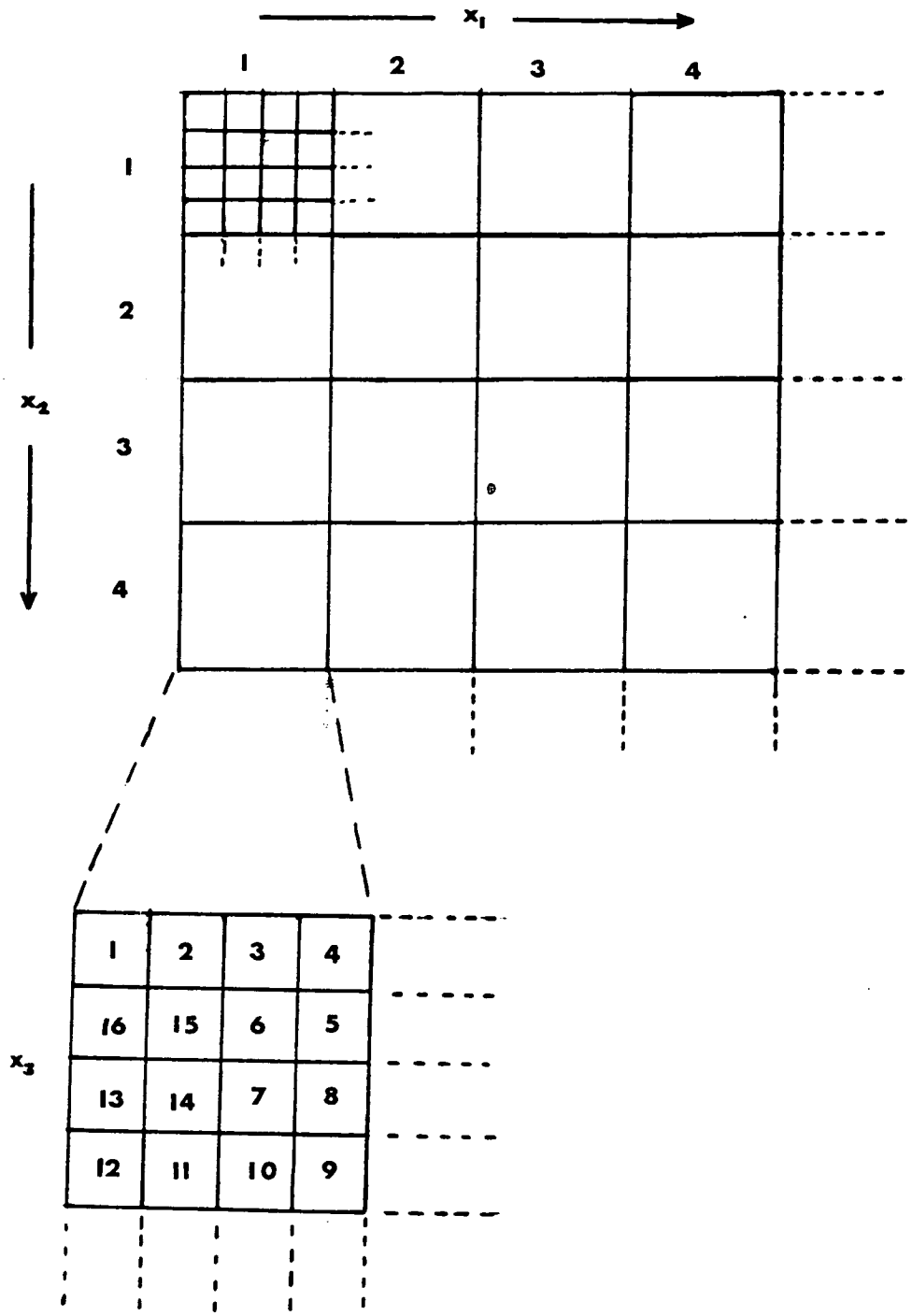

Fig A.3 How a 16^3 timeslice is mapped onto the 64×64 array,using 4×4 squares to store the x_3 data.

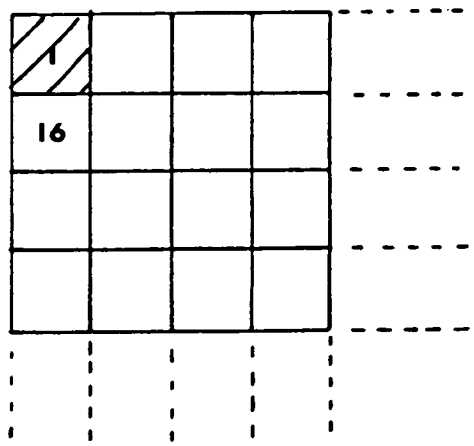

L3FN1

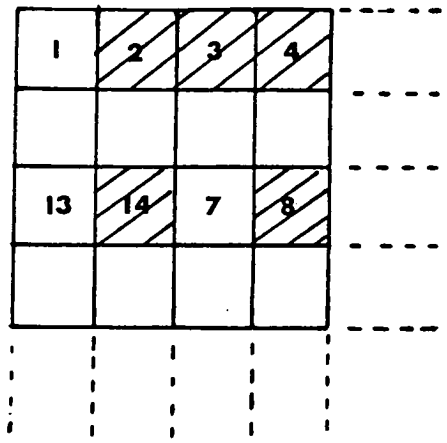

L3FE

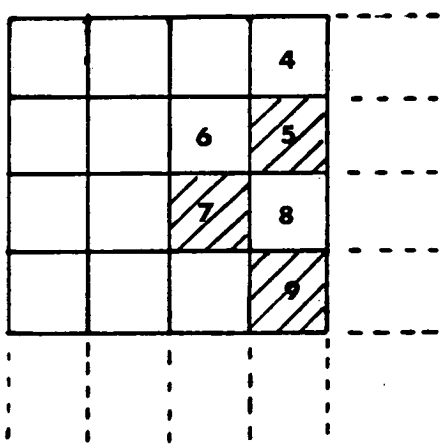

L3FS

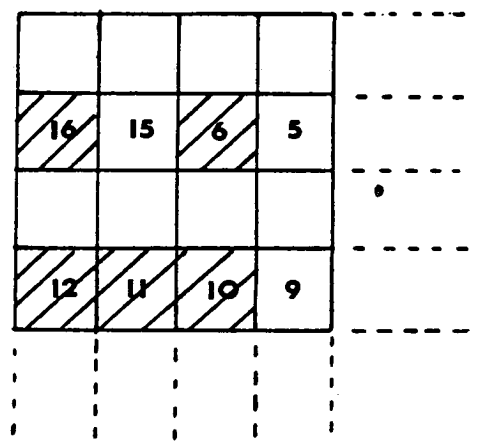

L3FW

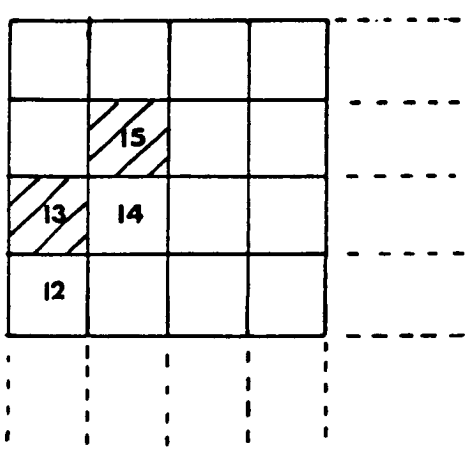

L3FN2

Fig A.4 Masks needed for shifting back in the x_3 direction

References

Arnison, G. *et al* { UA1 collaboration } (1983a) Phys. Lett. 122B 103

Arnison, G. *et al* { UA1 collaboration } (1983b) Phys. Lett. 126B 398

Arnison, G. *et al* { UA1 collaboration } (1983c) Phys. Lett. 122B 273

Bagnaia, P. *et al* { UA2 collaboration } (1983) Phys. Lett. 129B 130

Banner, M. *et al* { UA2 collaboration } (1983) Phys. Lett. 122B 476

Barbour, I.M., N.E. Behilil, P. Gibbs, G. Schierholz and M. Teper (1985a) in The Recursion Method and its Applications, ed. D.G. Pettifor and D.L. Weaire (Springer-Verlag, Berlin) p149-164

Barbour, I.M., P. Gibbs, K.C. Bowler and D. Roweth (1985b) Phys. Lett 158B 61

Barkai, D., K.J. Moriarty and C. Rebbi (1985a) Phys. Lett. 156B 385

Barkai, D., K.J. Moriarty and C. Rebbi (1985b) Comput. Phys. Commun. 36 1

Bernard, C., T. Draper, K. Olynyk and M. Rushton (1983a) Nucl. Phys. B220 508

Bernard, C., T. Draper and K. Olynyk (1983b) Phys. Rev. D27 227

Billoire, A., R. Lacaze, E. Marinari and A. Morel (1984a) Phys. Lett. 136B 418

Billoire, A., R. Lacaze, E. Marinari and A. Morel (1985b) The Goldstone Pion in SU(2) Lattice QCD at Low Quark Mass : Scaling and Finite Size Effects, Saclay preprint PhT 85-180

Billoire, A., E. Marinari, A. Morel and J.P. Rodrigues (1984b) Phys. Lett. 148B 169

Billoire, A., E. Marinari and R. Petronzio (1985a) Nucl. Phys. B251 141

Binder, K. (1976) in Phase Transitions and Critical Phenomena, ed. C. Domb and M.S. Green (Academic Press, New York) vol 5.

Bowler, K.C., C.B. Chalmers, R.D. Kenway, G.S. Pawley and D. Roweth (1986b) Hadron Mass Calculations Using Susskind Fermions at β = 5.7 and 6.0, to be published in Nucl. Phys. B

Bowler, K.C., C.B. Chalmers, R.D. Kenway, G.S. Pawley, D. Roweth and D.B. Stephenson (1986c) Hadron Mass Calculations Using Susskind Fermions at β = 6.15 and 6.3, in preparation

Bowler, K.C., D.L. Chalmers, A. Kenway, R.D. Kenway, G.S. Pawley and D.J. Wallace (1984a) Nucl. Phys. B240 213

Bowler, K.C., A. Hasenfratz, P. Hasenfratz, U. Heller, F. Karsch, R.D. Kenway, G.S. Pawley and D.J. Wallace (1986a) The SU(3) β-function at Large β, Illinois preprint ILL(TH) 86-44

Bowler, K.C., R.D. Kenway, G.S. Pawley and D.J. Wallace (1984b) Phys.Lett. 145B 88

Bowler, K.C., E. Marinari, G.S. Pawley, F. Rapuano and D. J. Wallace (1983) Nucl. Phys. B220 137

Bowler, K.C. and B.J. Pendleton (1984) Nucl. Phys. B230 [FS10] 109

Burkitt, A.N. (1986) private communication

Cabibbo, N. and E. Marinari (1982) Phys. Lett. 119B 387

Carpenter, D.B. and C.F. Baillie (1985) Nucl. Phys. B260 103

Chalmers, C.B., R.D. Kenway and D. Roweth (1986a) Algorithms for Calculating the Quark Propagator on Large Lattices, Edinburgh preprint 86/361, to be published in J. Comput. Phys.

Chalmers, C.B., R.D. Kenway and D. Roweth (1986b) Extending Quark Propagators in Time, Edinburgh preprint 86/386, submitted to Phys. Lett.

Cheng, T-P. and L-F. Li (1984) Gauge Theory of Elementary Particle Physics, (Clarendon Press,Oxford)

Concus, P., G.H. Golub and D.P. O'Leary (1976) in Sparse Matrix Computations ed. J.R. Bunch and D.J. Rose (Academic Press, New York)

Creutz, M. (1980) Phys. Rev. D21 2308

Feynman, R.P. (1948) Rev. Mod. Phys. 20 367

Fucito, F., G. Martinelli, C. Omero, G. Parisi, R. Petronzio and F. Rapuano (1982) Nucl. Phys. B210 407

Fukugita, M., Y. Oyanagi and A. Ukawa (1986) Phys. Rev. Lett. 57 953

Gilchrist, J.P., H. Schneider, G. Schierholz and M. Teper (1984a) Phys. Lett. 136B 87

Gilchrist, J.P., H. Schneider, G. Schierholz and M. Teper (1984b) Nucl. Phys B248 29

Gell-Mann, M. (1964) Phys. Lett. 8 214

Glashow, S.L. (1961) Nucl. Phys. B22 579

Guerin, F. and R.D. Kenway (1980) Nucl. Phys. B176 168

Hamber, H. and G. Parisi (1981) Phys. Rev. Lett. 47 1792

Hamber, H., E. Marinari, G. Parisi and C. Rebbi (1982) Phys. Lett. 108B 314

Han, M., and Y. Nambu (1965) Phys. Rev. B189 1006

Hasenfratz, A., P. Hasenfratz, Z. Kunszt and C.B. Lang (1982a) Phys. Lett. 110B 289

Hasenfratz, A., P. Hasenfratz, Z. Kunszt and C.B. Lang (1982b) Phys. Lett. 117B 81

Hasenfratz, P. and I. Montvay (1984) Nucl. Phys. B237 237

Hestenes, M.R. and E. Stiefel (1952) J. Res. Nat. Bur. Standards 49 409

Itoh, S., Y. Iwasaki, Y. Oyanagi and T. Yoshie (1984) Phys. Lett. 148B 153

Itoh, S., Y. Iwasaki and T. Yoshie (1986a) 'Hadron Masses in Quenched QCD', University of Tokyo preprint UTHEP-155

Itoh, S., Y. Iwasaki and T. Yoshie (1986b) Phys. Lett. 167B 443

Itoh, S., Y. Iwasaki, Y. Oyanagi and T. Yoshie (1986c) Nucl. Phys. B (in press)

Itoh, S., Y. Iwasaki, Y. Oyanagi and T. Yoshie (1986d) The Hadron Spectrum in Quenched QCD on a $12^3 \times 24$ Lattice, University of Tsukuba preprint UTHEP-150

Kawamoto, N. and J. Smit (1981) Nucl. Phys. B192 100

Kennedy, A.D. (1986) Deconfining Transition in Lattice QCD, Florida State preprint FSU-SCRI 86-46

Kenway, R.D. (1985) Phys. Lett. B158 327

Kenway, R.D., B.J. Pendleton and D. Roweth (1986), forthcoming Edinburgh preprint

Kilcup, G.W., S.R. Sharpe, R. Gupta, G. Guranlik, A. Patel and T. Warnock (1985) Phys. Lett. 164B 347

Kluberg-Stern, H., A. Morel, O. Napoly and B. Petersson (1983) Nucl. Phys. B220 [FS8] 447

Kogut, J.B. (1983) Rev. Mod. Phys. 55 775

Kogut, J. and L. Susskind (1975) Phys. Rev. D11 395

Konig, A., K-H. Mutter and K. Schilling (1984) Phys. Lett. 147B 145

Konig, A., K-H. Mutter, K. Schilling and J. Smit (1985) Phys. Lett. 157B 421

Lipps, H., G. Martinelli, R. Petronzio and F. Rapuano (1983) Phys. Lett. 126B 250

Marinari, E., G. Parisi and C. Rebbi (1981) Phys. Rev. Lett. 47 1795

Matthews, P.T. and A. Salam (1954) Nuovo Cim. 12 563

Matthems, P.T. and A. Salam (1955) Nuovo Cim. 2 120

Metropolis, N.A., M.N. Rosenbluth, A.H. Rosenbluth, E. Teller and J. Teller (1953) J. Chem. Phys. 21 1087

Morel, A. and J.P. Rodrigues (1984) Nucl. Phys. B247 44

Mutter, K-H (1986) Talk at Cosener's House Lattice Gauge Theory Meeting (March)

Nielsen, H.B. and M. Ninomiya (1981) Nucl. Phys. B185 20 and Nucl. Phys. B193 173

Pietarinen, E. (1981) Nucl. Phys. B190 [FS3] 349

Reid, J.K. (1971) in Proc. of Conference on Large Sparse Sets of Linear Equations, (Academic Press, New York)

Salam, A. (1968) in Elementary Particle Theory, ed. N. Svartholm (Almquist, Forlag AB, Stockholm)

Susskind, L. (1977) Phys. Rev. D16 3031

Tomboulis, E. (1983) Phys. Rev. Lett. 50 885

Weinberg, S. (1967) Phys. Rev. Lett. 19 1264

Weingarten, D. (1982a) Phys. Lett. 109B 57

Weingarten, D. (1982b) Nucl. Phys. B215 1

Wilson, K.G. (1974) Phys. Rev. D10 2445

Wilson, K.G. (1977) in New Phenomena in Subnuclear Physics (Erice 1975) ed. A. Zichichi, Plenum, New York

Yang, C.N. and R. Mills (1954) Phys. Rev. 96 191

Zweig, G. (1964) CERN preprints TH401, 412 (unpublished)